Scuola Normale Superiore

Ph.D. Thesis in Methods and Models for Molecular Science

Understanding molecular phenomena and mechanisms occurring in the lipid membranes through molecular dynamics simulations

Candidate

Muhammad Jan Akhunzada

Advisor

Prof. Giuseppe Brancato

Academic Year 2018-2019

This thesis is dedicated to

My beloved parents

"Prof. Dr. Iftikhar. H. Qari and Fehmidah Iftikhar"

For providing me with everything and for making me who I am today

with their continuous affection, backing and guidance

My teachers from my primary education to Ph.D.

Who taught me, corrected me and shaped my future

My mentors

Who inspired me and motivated me

My ever supporting and loving siblings

Waleed Jan, Faiza Jan, Osman Jan, Wardah Jan

My sweet Nieces and Nephews

Malaak, Awatif, Nofal

Ibrahim, Abdul Mannan, Ayaan, Hassan

Noah

My Friends

Ishaq Badshah, Farhan Haq, Nabeel Ahmed, Saad Ali, Nabeel Khalid

for brightening the dull and mundane moments

and

My amazing and lovely wife

"Dr. Amna Farrukh"

For believing in me and for standing by my side

Thank you all for the life I love and being a part of it

Acknowledgement

First of all, I am deeply grateful to Allah Almighty for the ability and strength to complete my research work, publications and this thesis. Working as a Ph.D. student in Scuola Normale Superiore, Pisa, was a magnificent as well as a challenging experience. During these years, many people were instrumental, directly or indirectly, in shaping up my academic career. It was impossible to thrive in my doctoral work without the precious support of these personalities. Here is a small tribute and word of thanks to all those people.

I would like to specially thank my supervisor ***Professor Giuseppe Brancato*** for the opportunity he has given me to undertake my doctorate at Scuola Normale Superiore, Pisa, Italy, which is one of the most prestigious institutes in Italy and highly ranked among European universities. I express my gratitude for all the academic support, help and guidance he provided to me throughout my Ph.D. degree. It was only due to his valuable guidance, cheerful enthusiasm and ever friendly nature that I was able to complete my research work in a respectable and timely manner. His confidence, patience and encouragement has paved my way to understanding, planning and executing the undertaken projects and delineate them into a written form. I am really thankful to him for being such a nice teacher, an exemplary mentor and I shall remain indebted to him for life.

My special thanks to my friend and lab colleague ***Dr. Balasubramaniam Chandramouli*** without whom I could not have grasped the very concepts of MD simulations and research in general. I am also thankful to him for introducing me to python and his help in formulating many analysis scripts and correcting them for me. He was a source of continuous help and moral support in the starting days of my Ph.D. degree.

I wish to express gratitude to my experimental collaborator at NEST SNS, ***Francesco Cardarelli***. He and his group members provided me with valuable and insightful experimental results and comments which were used as the experimental evidence for the computational studies I conducted and was able to publish later on. I would like to specially thank one of his

Ph.D. students late ***Dr. Carmine Di Rienzo*** who started Rhodamine work with me and provided initial results related to the study but he unfortunately passed away prematurely and couldn't see the final published paper.

I express thanks to the ***Scuola Normale Superiore, Pisa, Italy*** for all the facilities including food, accommodation, research funding and academic support that assisted working in a congenial environment. I extend my gratitude to respected ***Prof. Vincenzo Barone*** for providing me the Ph.D. scholarship at the Scuola Normale Superiore, Pisa. I am thankful to ***Dr. Giordanno Mancini*** for providing assistance and submission scripts for Avogadro computing clusters. Appreciation also goes out to the technical support team especially to ***Alberto Coduti*** for providing robust computer and technical assistance and simplifying the submission of MD Jobs on the clusters. I am thankful to all the office staff of the Scuola Normale Superiore especially ***Emanuela Brustolon***, ***Silvia Zappulla, Luca de Francesco*** and ***Lucia Monacci*** who were always there to solve all the non-academic problems and that too on a very short notice and were always happy to help on such issues. Special thanks to all the funding sources including ***Scuola Normale Superiore*** and ***INFN*** for funding my projects, workshops and conferences. I would also like to thank ***Cineca,Italy*** for providing access to different HPC clusters.

I appreciate ***Dr. Balasubramaniam Chandramouli, Dr. Nuno Barbosa, Dr. Nicolous Bhattacharjee*** and ***Dr. Tommaso d'Agostino*** for giving me such a nice and friendly time, I am thankful to you guys for bucking me up that kept me energized and focused and for valuable advices over a cup of coffee.

I would like to acknowledge my lab colleague especially ***Dr. Andrea Catte*** for sharing work space and his valuable knowledge on membranes and Ion channels. I am also thankful to him for having fruitful discussions on the projects related to Ion channels and I acknowledge his contributions in various analysis in the Ion channel studies.

I would like to extend my sincere thanks in advance to the PhD committee and the external examiners who will evaluate my thesis and hopefully will give their constructive comments. I am really thankful to them for investing their precious time in reading and assessing my work.

I am thankful to my M.Phil. supervisor ***Dr. Syed Sikander Azam*** who introduced me to Molecular modeling and without his support and guidance I would not be able to come this far. I am really indebted for life to all my teachers since the beginning of my school days up to this day, without their sincere efforts none of this would have been possible.

I acknowledge the efforts of my family members during my degree. I am thankful from the core of my heart to my brothers and sisters who have always encouraged me in all my endeavors. Their reassuring remarks have always kept me on the right track and their special interests in my studies have made this thesis possible today. My nieces and nephews have made my Ph.D. times much easier with their sweet talks. I would also like to thank my brother in law ***Asad Ali Rajput*** for the moral and financial help he provided me during my stay in Italy and also gave me a place in his home at the start and end of my Ph.D. degree. Lastly I would not shy away without thanking the Italian people for their kind and hospitable attitude. Indeed Italy, its food and people will always have special place in my heart.

I am deeply grateful to my beautiful wife, ***Dr. Amna Farrukh*** for the support and care she provided me during my Ph.D. and the writing of this thesis. She continuously encouraged me with her motivating remarks and curbed any anxiety and doubts during this stressful time.

Finally, I owe a special thanks to my parents ***Dr. Iftikhar H Qari*** and ***Fehmidah Iftikhar***, this journey would have never been accomplished without their continuous support and unconditional love. I am, indeed the most blessed to have my beloved parents around me whose prayers and endless kindness has not only comforted me in times of stress and respite but also strengthened me with vigor to move forward at every stage. My father's valuable comments and constructive remarks have encouraged me to be a better person and to do good in life and my mother's efforts for trying to discipline me would always be appreciated and respected.

I hope this Ph.D. furthers my quest for scientific learning and enables me to achieve technological advances that may benefit the scientific community. May Allah help me in all my future pursuits. (Amen).

The work in this thesis is based upon the following publications:

Akhunzada, M.J., Chandramouli, B., Bhattacharjee, N., Macchi, S., Cardarelli, F., Brancato, G., 2017. The role of Tat peptide self-aggregation in membrane pore stabilization: insights from a computational study. Phys. Chem. Chem. Phys. 19, 27603–27610. https://doi.org/10.1039/C7CP05103D

Akhunzada, M.J., D'Autilia, F., Chandramouli, B., Bhattacharjee, N., Catte, A., Rienzo, R.D., Cardarelli, F., Brancato, G., 2019. Interplay between lipid lateral diffusion, dye concentration and membrane permeability unveiled by a combined spectroscopic and computational study of a model lipid bilayer. Scientific Reports 9, 1508. https://doi.org/10.1038/s41598-018-37814-x

Akhunzada, M.J., Sagresti, L., Catte, A., Bhattacharjee, N., D'Agostino, T., Brancato, G., 2019. Temperature Dependence of the Structure and Dynamics of a Dye-Labeled Lipid in a Planar Phospholipid Bilayer: A Computational Study. J Membrane Biol. https://doi.org/10.1007/s00232-019-00081-6

Catte, A., Ferbel, L., Bhattacharjee, N., Akhunzada, M.J., D'Agostino, T., Brancato, G., 2019. In silico investigation of the interaction between the voltage-gated potassium channel Kv4.3 and its auxiliary protein KChIP1. Manuscript submitted.

Del Frate, G., Macchiagodena, M., Akhunzada, M.J., D'Autilia, F., Catte, A., Bhattacharjee, N., Cardarelli, F., Brancato, G., 2019. Probing liquid-ordered and disordered phases in lipid membranes: a combined theoretical and spectroscopic study of a fluorescent molecular rotor. Manuscript in preparation.

Akhunzada, M.J., Bhattacharjee, N., Catte, A., Kocer, A., Brancato, G., 2019. Ion conductance in a voltage-gated potassium channel is tuned by a single mutation in proximity of the selectivity filter. Manuscript in preparation.

Table of Contents

Acknowledgement *3*

List of Figures *11*

List of Tables *22*

Chapter 1 Introduction *25*

Chapter 2 Biological Background *31*

2.1 Overview **31**

2.2 Plasma Membranes: Models and Structural Composition **31**

2.3 Mode of transport in biomembranes and role of proteins in transportation **35**

2.4 Cell Penetrating Peptides **36**

2.5 Voltage-gated potassium ion channels **38**

2.6 Molecular rotors as probes for membrane properties **40**

Chapter 3 Theoretical and Computational Methods *45*

3.1 Molecular Dynamics Simulations **45**

3.2 Statistical Mechanics **46**

3.2.1 Classical Mechanics, Newton's Second Law of Motion 47

3.2.2 Verlet Algorithm 49

3.3 Molecular Mechanics **50**

3.4 Trajectory Analysis **51**

3.4.1 Radial Distribution Function 51

3.4.2 Mean Square Displacement 51

3.4.3 Lipid Order Parameter 52

3.4.4 Normalized Water Density 52

3.4.5 Pulling Simulation and pulling force analysis 52

3.4.6 Average Pore Radius 53

3.4.7 Permeation and Conductance 54

Chapter 4 Insights into the interplay between dye concentration, lipid lateral diffusion and membrane permeability in lipid bilayers *55*

4.1 Introduction **55**

4.2 Computational Details **58**

4.2.1 Molecular models of DOPC and dye-labelled lipid 58

4.2.2 Molecular model of an aggregated cluster of dye-labeled lipids 66

4.2.3 Molecular dynamic simulation parameters 66

4.2.4 Data analysis 67
4.3 Results 69
4.3.1 Structural properties of the RHB-DOPC bilayer 69
4.3.2 Lipid lateral dynamics: DOPC vs RHB-DOPC 72
4.3.3 FCS measurements of lipid lateral diffusion effects of RHB concentration 74
4.3.4 High RHB concentration aggregation and membrane permeability change 75
4.3.5 Modelling RHB aggregation structural effects and lipid diffusion 77
4.3.6 Modelling RHB aggregation water permeation into the membrane 78
4.4 Discussion 80
4.5 Conclusions 83
Chapter 5 Temperature dependence of the structure and dynamics of a dye-labeled lipid in a planar phospholipid bilayer, a computational study 85
5.1 Introduction 85
5.2 Computational Details 88
5.2.1 Molecular models of DOPC and dye-labeled lipid 88
5.2.2 Molecular dynamic simulation parameters 89
5.2.3 Data analysis 90
5.3 Results 92
5.3.1 Temperature effects on the structural properties of the RHB-DOPC bilayer 92
5.3.2 Lipid lateral diffusion in pure DOPC and RHB-DOPC membranes 100
5.3.3 Partitioning of RHB lipids into the membrane 101
5.3.4 Local hydration at the RHB-DOPC membrane surface 109
5.3.5 Orientation of the RHB fluorescent headgroups 112
5.4 Discussion 114
5.5 Conclusions 115
Chapter 6 Probing liquid-ordered and disordered phases in lipid membranes, a combined theoretical and spectroscopic study of a fluorescent molecular rotor 117
6.1 Introduction 117
6.2 Computational details 120
6.2.1 Force field parameterization and QM calculations 120
6.2.2 Molecular dynamic simulation parameters 122
6.3 Results 123
6.3.1 Structure analysis and FF development 123
6.3.2 Model validation in organic solvents 128
6.3.3 Probing lipid phase in model bilayers through DPAP fluorescence lifetime 135
6.3.4 DPAP molecular dynamics in different lipid phases 137
6.4 Discussion 139
6.5 Conclusions 142
Chapter 7 The role of Tat peptide self-aggregation in membrane pore stabilization 154
7.1 Introduction 154
7.2 Computational Details 156
7.2.1 Model system generation 156
7.2.2 Molecular dynamic simulation parameters 160
7.3 Results 162
7.3.1 Membrane pore formation and stabilization 162

7.3.2 Tat_{11} and Tat_{11}-TAMRA peptide translocation....163
7.3.3 Tat_{11}-TAMRA monomer versus dimer translocation....166
7.4 Discussion....170
7.5 Conclusions....172
Chapter 8 Tuning the ion conductance in a voltage-gated potassium channel through a single mutation....174
8.1 Introduction....174
8.2 Computational Details....177
8.2.1 Kv4.3 Shal K+ channel system set up in the open state....177
8.2.2 Molecular dynamic simulation parameters....178
8.2.3 Data analysis....180
8.3 Results....180
8.3.1 Wild-type Kv4.3....181
8.3.2 Comparison of WT, M373I and M373E....182
8.4 Discussion....189
8.5 Conclusions....191
Chapter 9 In silico investigation of the interaction between the voltage-gated potassium channel Kv4.3 and its auxiliary protein KChIP1....192
9.1 Introduction....192
9.2 Computational Details....195
9.2.1 Kv4.3 T1-KChIP1 complex model....195
9.2.2 Molecular dynamic simulation parameters....196
9.2.3 Data analysis....197
9.3 Results....197
9.3.1 Wild-type Kv4.3 T1-KChIP1 complex....197
9.3.2 The first interface and its destabilization by the W8E-P10E-A15E Kv4.3 triple mutant....199
9.3.3 The second interface: structure, energy stability and effect of mutations....205
9.3.4 The third interface....217
9.4 Discussion....219
9.5 Conclusions....221
Chapter 10 Conclusions....223
References....228

List of Figures

Figure 2.1: Fluid mosaic model proposed by Jonathan Singer and Garth Nicholson in the year 1972. 32
Figure 2.2: Structure of lipid molecules used in this thesis. 34
Figure 2.3: Schematic of different mode of transports mediated by channel, carrier and transport proteins. 36
Figure 2.4: Cell penetrating peptide (CPP) along with cargo molecule can take direct penetration pathway to permeate through lipid bilayer, the toroidal pore model a direct penetration pathway is shown. 37
Figure 2.5: a) Top view of the KV gated ion channel embedded inside the POPC lipid bilayer b) Side view of the KV gated ion channel embedded inside the POPC lipid bilayer. 40
Figure 2.6: structures of probes used in experimental and computational studies mentioned in this thesis, a) Rhodamine B linked to 1,2-dioleoyl-sn-3-phosphatidylehanolamine (RHB) b) tetramethylrhodamine-5-maleimide (TAMRA) dye c) 4-(diphenylamino)phthalonitrile (DPAP) d) 6-Dodecanoyl-N,N-dimethyl-2-naphthylamine (LAURDAN). 42
Figure 2.7: Snapshots from atomistic molecular dynamic simulations of different systems with the chromophores. a) DPAP embedded inside the DPPC bilayer containing cholesterol, b) RHB embedded inside DOPC bilayer and c) is TAMRA dye embedded inside the DOPC lipid bilayer. 43
Figure 4.1: a) Scheme of the RHB lipid. b) Side and c) top view of a MD simulation snapshot of the RHB-DOPC lipid bilayer. d) Side and e) top view of a MD simulation snapshot of the RHB-DOPC bilayer displaying RHB self-aggregation. RHB lipids are shown in yellow, with nitrogen in blue, while DOPC lipids are in gray with corresponding phosphate atoms in red; water is omitted for clarity. 57
Figure 4.2: a) P-P radial distribution functions (RDFs) obtained considering only DOPC-DOPC pairs as issuing from MD simulations of DOPC (black), RHB-DOPC (red) and RHBAgg-DOPC (blue, RHB self-aggregation) lipid bilayers. b) P-P RDFs obtained from DOPC (black, DOPC-DOPC pairs), RHB-DOPC (red, RHB-DOPC pairs) and RHBAgg-DOPC (blue, RHBAgg-DOPC pairs) bilayer simulations. c,d) Deuterium order parameters (SCD) evaluated for lipid acyl chains (i.e., sn-1 and sn-2) as issuing from MD simulations of DOPC (black, DOPC lipids), RHB-DOPC (red, RHB lipids) and RHBAgg-DOPC (blue, RHBAgg lipids) lipid bilayers. e,f) Deuterium order parameters (SCD) from MD simulations of DOPC (black, DOPC lipids) and RHBAgg-DOPC (blue, only DOPC lipids within 5 Å from any RHBAgg lipid) lipid bilayers. In all diagrams, error bars correspond to standard errors. 71
Figure 4.3: a) Mean square displacement (MSD) evaluated as a function of time from MD simulations of DOPC (black, DOPC lipids), RHB-DOPC (red, RHB lipids) and RHBAgg-DOPC (blue, RHBAgg lipids) lipid bilayers. Error bars correspond to standard errors. b) Mean square displacement (MSD) evaluated as a function of time from MD simulations of DOPC (black, DOPC lipids), RHB-DOPC (red, DOPC lipids) and RHBAgg-DOPC (blue, DOPC lipids) lipid bilayers. Error bars correspond to standard errors. c) Schematic representation of a FCS measurement. d) Confocal microscopy image of a GUV DOPC - 0.1% RHB, scale bar 1 micron. e) Effect of fluorophore concentration on the diffusion of RHB lipids in GUVs. f) Emission spectra of Rhodamine B at different

concentration (0.1% and 10%) in GUVs, the aggregation of Rhodamine B induces an emission spectra red shift of 8 nm, from 583 to 591 nm. *73*

Figure 4.4: P - Na^+ radial distribution functions (RDFs) obtained considering DOPC (black line) and RHB (red line) lipids as issuing from the RHB-DOPC MD simulation with 0.5M NaCl. Sodium ions are observed to penetrate the phosphate region of the lipid bilayer in a similar way with respect to both RHB and DOPC lipids. *74*

Figure 4.5: a) Diffusion coefficient of LAURDAN increases with increasing concentration of RHB (blue dots), G0 remains constant (black dots). b) Confocal microscopy images of GUVs labelled with LAURDAN, the emission signal was split in two channels and polarity maps were obtained from these images using GP equation. c) GP values obtained in GUVs at different concentration of RHB. d) Water density distribution evaluated along a direction normal to the membrane surface as issuing from MD simulations of DOPC (black), RHB-DOPC (red) and RHBAgg-DOPC (blue, water within 5 Å in XY plane from the center of the RHB cluster) lipid bilayers. Origin was set to the average position of P atoms in one leaflet, negative values correspond to the inner bilayer region, positive values to the outer region and bulk solution. Water density was normalized with respect to bulk density. e) MD snapshot of the RHB cluster: RHB lipids are shown in orange, DOPC phosphate groups in red, water molecules within 5 Å from the RHB aggregate are in blue, while remaining water molecules at the membrane-water interface are in gray. f) Average water dipole moment evaluated along a direction normal to the membrane surface as issuing from MD simulations of DOPC (black) and RHBAgg-DOPC (red, water within 5 Å in XY plane from the center of the RHB cluster) lipid bilayers. *76*

Figure 4.6: a,b) Deuterium order parameters (S_{CD}) evaluated for lipid acyl chains (i.e., sn-1 and sn-2) as issuing from MD simulations of DOPC (black, DOPC lipids), RHB^{Agg}-DOPC (blue, only DOPC lipids within 5 Å from any RHB lipid) and RHB^{Agg}-DOPC (green, only DOPC lipids within 7.5 Å from any RHB lipid) lipid bilayers. Small differences in DOPC order parameters appeared as caused by the local interaction with RHB lipids. In all diagrams, error bars correspond to one standard errors. Error bars of pure DOPC system (black lines) are negligible and then omitted for clarity in all plots. *78*

Figure 4.7: 2D electrostatic potential maps as issuing from MD simulations of a) DOPC and b) RHBAgg-DOPC lipid bilayers evaluated on a lateral plane (i.e, XZ) of the simulation cell. Electrostatic potential evaluated along a direction normal to the membrane surface as issuing from MD simulations of c) DOPC and d) RHBAgg-DOPC lipid bilayers. In the latter case, the normal was selected to pass through the center of the RHB cluster. Origin was set to the center of the bilayer in both cases. Overall, the electrostatic potential can change by up to 0.6 V across the lipid bilayer, but RHBAgg-DOPC system shows a high degree of asymmetry with a peak at about 30 Å in correspondence to the RHB aggregate. *80*

Figure 5.1: a) Molecular structure of the RHB lipid with the definition of vertical (v1) and horizontal (v2) molecular axes of the fluorescent polar headgroup. RHB sn-1 and sn-2 acyl chains are labeled together with significant carbon atoms of hydrophobic lipid tails on the sn-2 chain. Carbon, hydrogen, sulphur, phosphorus, oxygen and nitrogen atoms are shown in cyan, white, yellow, tan, red and blue, respectively. b) Side and c) top view of a MD simulation snapshot of the RHB-DOPC lipid bilayer with a 0.02 mol% RHB concentration. d) Side and e) top view of a 155 ns MD simulation snapshot of the RHB-DOPC lipid bilayer displaying RHB self-

aggregation. Carbon atoms of RHB lipids inserted into the DOPC lipid bilayer are shown in magenta, with the other atoms having the same color code of panel a, while DOPC lipids glycerol backbone and hydrophobic acyl chains are in green with corresponding polar headgroups in orange. For clarity, water and ions are not displayed. 86

Figure 5.2: Atoms selected to define horizontal (v1, red) and vertical (v2, blue) axes of the RHB fluorescent polar headgroup. Horizontal and vertical axes of the RHB polar fluorescent headgroup form angles α and β, respectively, with the lipid bilayer normal n, which is assumed to be coincident with the z-axis. A side view of a MD simulation snapshot of the RHB-DOPC lipid bilayer with a 2 mol% RHB concentration is shown in the right panel of the figure. The same color code of Fig. 1 is used for DOPC and RHB molecules..... 91

Figure 5.3: RHB P-P distances from AA MD simulations of RHB-DOPC lipid bilayers with a 2 mol% RHB concentration performed at a), b) 320 K, c), d) 303 K and e), f) 293 K. Different colors are used for different P-P distances between all possible pairs of RHB molecules in upper and lower leaflets of the RHB-DOPC lipid bilayer. The formation of RHB aggregates is not observed at any temperature (RHB P-P distance > 2 nm)..... 95

Figure 5.4: P-P radial distribution functions (RDFs) of DOPC-DOPC and RHB-DOPC pairs from MD simulations of DOPC and RHB-DOPC lipid bilayers at three different temperatures. a) P-P RDFs of DOPC-DOPC pairs from MD simulations of DOPC (blue: 293 K, turquoise: 303 K and cyan: 320 K) and RHB-DOPC (violet: 293 K, magenta: 303 K and purple: 320 K) lipid bilayers. Note that the six lines appear as superimposed on one another. b) P-P RDFs of DOPC-DOPC (blue: 293 K, turquoise: 303 K and cyan: 320 K) and RHB-DOPC pairs (purple: 293 K, red: 303 K and green: 320 K) from DOPC and RHB-DOPC lipid bilayer simulations. Error bars of P-P RDFs DOPC-DOPC pairs in pure DOPC and RHB-DOPC systems are negligible and omitted for clarity in panel a. In all diagrams of panel b error bars correspond to standard deviations..... 96

Figure 5.5: Deuterium order parameters (SCD) evaluated for sn-1 and sn-2 lipid acyl chains from MD simulations of DOPC and RHB-DOPC lipid bilayers at three different temperatures (solid, dashed and dotted lines: 293 K, 303 and 320 K, respectively). SCD of a), b) sn-1 and c), d) sn-2 acyl chains of DOPC and RHB molecules, respectively, from MD simulations of DOPC (blue, DOPC lipids) and RHB-DOPC (red, RHB lipids) lipid bilayers. Errors were estimated as standard deviations. 97

Figure 5.6: Deuterium order parameters (S_{CD}) evaluated for sn-1 and sn-2 lipid acyl chains from MD simulations of DOPC and RHB-DOPC lipid bilayers at three different temperatures (solid, dashed and dotted lines correspond to 293 K, 303 and 320 K, respectively). S_{CD} of a), c), e) sn-1 and b), d), f) sn-2 acyl chains of DOPC and RHB molecules, respectively, from MD simulations of pure DOPC (blue) and RHB-DOPC (DOPC and RHB order parameters are shown in green and red, respectively) lipid bilayers. Errors were estimated as one standard deviation. 99

Figure 5.7: a) Mean square displacement (MSD) of DOPC lipids evaluated as a function of time from MD simulations of DOPC (blue) and RHB-DOPC (green) lipid bilayers at three different temperatures (solid, dashed and dotted lines: 293 K, 303 and 320 K, respectively). b) MSD evaluated as a function of time from MD simulations of DOPC (DOPC lipids MSDs are shown in blue) and RHB-DOPC (RHB lipids MSDs are shown in red) lipid bilayers at three different temperatures (solid, dashed and dotted lines: 293 K, 303 and 320 K,

respectively). Error bars correspond to standard errors. Differences in error bars reflects mainly the different number of systems (i.e., 400 DOPC lipids and 8 free RHB lipids).....101
Figure 5.8: Partial density profiles across the lipid bilayer for different lipid components of DOPC and RHB lipids from MD simulations of RHB-DOPC lipid membranes at three different temperatures. Blue, green and red lines correspond to 293 K, 303 and 320 K, respectively, for a) DOPC phosphate (PO_4^-), b) RHB sulfonate (SO_3^-), c) DOPC glycerol (OCH2-CHO-CH2) and d) RHB headgroup (NH-sulforhodamine B) groups. The partial density of each lipid moiety was initially averaged over the last 50 ns of the simulation and, then, the final average was performed over the four replicas at each temperature.....103
Figure 5.9: Partial density profiles across the lipid bilayer for different lipid components of DOPC and RHB lipids from MD simulations of RHB-DOPC lipid membranes at three different temperatures. Solid, dashed and dotted lines correspond to 293 K, 303 and 320 K, respectively. DOPC choline (CH_2-CH_2-N-$(CH_3)_3^+$), phosphate (PO_4^-), carbonyl (C=O), glycerol (OCH_2-CHO-CH_2), methylene (CH_2), double bond (C=C) and methyl (CH_3) groups are shown with blue, orange, light green, green, red, yellow and black lines. RHB fluorescent polar headgroups (NH-sulforhodamine B) are shown with magenta lines. The partial density of each lipid moiety was initially averaged over the last 50 ns of the simulation and, then, the final average was performed over the four replicas at each temperature. 104
Figure 5.10: Partial density profiles across the lipid bilayer for different lipid components of DOPC lipids from MD simulations of RHB-DOPC lipid membranes at three different temperatures. Blue, green and red lines correspond to 293 K, 303 and 320 K, respectively, for DOPC a) phosphate (PO_4^-), b) choline (CH_2-CH_2-N-$(CH_3)_3^+$), c) glycerol (OCH_2-CHO-CH_2) and d) carbonyl (C=O) groups. The partial density of each lipid moiety was initially averaged over the last 50 ns of the simulation and, then, the final average was performed over the four replicas at each temperature.....105
Figure 5.11: Partial density profiles across the lipid bilayer for different lipid components of DOPC lipids from MD simulations of RHB-DOPC lipid membranes at three different temperatures. Blue, green and red lines correspond to 293 K, 303 and 320 K, respectively, for DOPC a) methylene (CH_2), b) double bond (C=C) and c) methyl (CH_3) groups. The partial density of each lipid moiety was initially averaged over the last 50 ns of the simulation and, then, the final average was performed over the four replicas at each temperature.....106
Figure 5.12: Partial density profiles across the lipid bilayer for different lipid components of RHB lipids from MD simulations of RHB-DOPC lipid membranes at three different temperatures. Blue, green and red lines correspond to 293 K, 303 and 320 K, respectively, for RHB a) phosphate (PO_4^-), b) fluorescent polar head (NH-sulforhodamine B), c) glycerol (OCH_2-CHO-CH_2) and d) carbonyl (C=O) groups. The partial density of each lipid moiety was initially averaged over the last 50 ns of the simulation and, then, the final average was performed over the four replicas at each temperature.....107
Figure 5.13: Partial density profiles across the lipid bilayer for different lipid components of RHB lipids from MD simulations of RHB-DOPC lipid membranes at three different temperatures. Blue, green and red lines correspond to 293 K, 303 and 320 K, respectively, for RHB a) methylene (CH_2), b) double bond (C=C) and c) methyl (CH_3) groups. The partial density of each lipid moiety was initially averaged over the last 50 ns of the simulation and, then, the final average was performed over the four replicas at each temperature.....108

Figure 5.14: Snapshots of a single RHB molecule at a) 293 K, b) 303 and c) 320 K show the effect of temperature on the hydration of the RHB fluorescent headgroup. The lower panel of the figure reports the temperature and the average number of water molecules within one hydration layer (0.28 nm) of any atom of the RHB fluorescent headgroup from MD simulations of RHB-DOPC lipid membranes at three different temperatures. The number of water molecules was averaged over the last 50 ns of each simulation at each temperature. The errors are standard deviations. The same color code of Fig. 1 is used for DOPC and RHB molecules. Oxygen and hydrogen atoms of water molecules are shown in skyblue and cyan, respectively. *109*

Figure 5.15: Water density distribution evaluated along a direction normal to the membrane surface from MD simulations of DOPC (solid lines) and RHB-DOPC (dashed lines) lipid bilayers at three different temperatures. a) Blue, green and red lines correspond to 293 K, 303 and 320 K, respectively. The origin was set to the average position of P atoms in both leaflets. Negative and positive values until ~2.5 nm correspond to lower and upper leaflets bilayer regions including water-membrane interfaces, respectively. Negative and positive values above ~2.5 nm refer to the bulk solution. b) A zoomed view in the region defined by the highest peak intensity of partial density profiles of DOPC glycerol and carbonyl groups (1.5 nm) show a higher water density in RHB-DOPC (dashed lines) lipid bilayers as compared to DOPC membranes (solid lines) at every temperature. *110*

Figure 5.16: Water partial density profiles in the region defined by the highest peak intensity of partial density profiles of DOPC glycerol and carbonyl groups (1.5 nm) from MD simulations of DOPC (solid lines) and RHB-DOPC (dashed lines) lipid bilayers at a) 293 K (blue lines), b) 303 K (green lines) and c) 320 K (red lines). Snapshots of single RHB molecules at different temperatures show the increase in the hydration around RHB fluorescent headgroups below the DOPC glycerol backbone region. The same color code of Fig. 6 is used for DOPC, RHB and different types of water molecules. *111*

Figure 5.17: Angle distributions of a) horizontal (v1) and b) vertical (v2) axes of RHB fluorescent polar headgroups at three different temperatures. Blue, green and red lines correspond to angle distributions at 293 K, 303 and 320 K, respectively. Horizontal and vertical axes of the RHB polar fluorescent headgroup forming angles α and β, respectively, with the lipid bilayer normal, which is assumed to be the z-axis, are also shown in the molecular representations of specific RHB molecules in right panels of the figure. The same color code of Fig. 1 is used for DOPC and RHB molecules. *113*

Figure 6.1: 4-(diphenylamino)phthalonitrile (DPAP) 2D molecular structure a) and a con- figuration of the DPAP rotor (in magenta) in the DPPC:CHOL system b) highlighting in yellow the cholesterol molecules, in red and gray the polar head and non-polar tails, respectively. *119*

Figure 6.2: DPAP propeller-like conformation as optimized in butanoic acid (solvent effect modeled by the PCM). Flexible dihedral are indicated with green vectors. The ipso (C1, C1' and C''), the ortho (C2, C2' and C2'') carbon atoms are labeled in black together with the nitrogen (N' and N'') and the carbon (C3 and C3') atoms of the two cyano groups. *124*

Figure 6.3: Frontier molecular orbitals of DPAP: HOMO a) and LUMO b). An isosurface value of 0.02 a.u. has been used. *125*

Figure 6.4: Potential energy curve of dihedral angle 1 (panel a)) and 2/3 (panel b)). QM data, black points; MM data, continuous lines. *127*

Figure 6.5: Radial distribution functions between DPAP and acetonitrile (blue), cyclohexane (green) and o-xylene (magenta) center of mass. *129*
Figure 6.6: Dihedral distribution function of the three dihedral angles in acetonitrile: in solid red line dihedral angle 1, in blue dashed line dihedral angle 2 and in solid green line dihedral angle 3. ..... *130*
Figure 6.7: Time dependent dihedral distribution function for dihedral angle 1 for the first 5 ns of simulation in acetonitrile (ACN) a), cyclohexane b), o-xylene c). *131*
Figure 6.8: Time dependent dihedral angle distribution function in acetonitrile (in red results for dihedral angle 1, in blue for dihedral angle 2 and in green for dihedral angle 3). The first 5 ns of simulation are reported. *132*
Figure 6.9: Distribution of the emission wavelengths computed for 200 DPAP geometries extracted from the MD trajectories in cyclohexane a), o-xylene b) and acetonitrile c). The solid lines represent the fitting to a Gaussian curve. For sake of clarity a different number of bins have been used in the three panels. *135*
Figure 6.10: Conformational dependence of the fluorescence wavelength computed in acetoni- trile. a) Energy profile of dihedral angle 1. b) Relation between DPAP emission energy and dihedral angle 1 amplitude. c) Dihedral 1 distribution for the selected conformations taken from the MD trajectory and used for fluorescence wavelength calculation. *136*
Figure 6.11: ph-FLIM of multilamellar vesicles characterized by homogeneous lipid phases. a) Fluorescence image of a multilamellar vesicle characterized by homogeneous Lo phase. b) Fluorescence image of a multilamellar vesicle characterized by homogeneous Ld phase. c) Phasor plot relevant to vesicles a) and b): the segment connecting the averages of the two reference phasor clouds is depicted in red. *137*
Figure 6.12: Deuterium order parameter for a) DOPC and b) DPPC lipid, the lipid nomenclature is indicated inside the inset of the graph. The first order parameter corresponds to the first CH_2 group of the acyl chain (position 2). *138*
Figure 6.13: Correlation between DPAP rotational correlation time (ps) and experimental fluorescence lifetimes (ns) in the considered environments. *141*
Figure 6.14: DPAP atom labelling. *143*
Figure 7.1: Transduction of Tat_{11} peptide, originating from spatially restricted zones (NZs) on the plasma membrane (white arrows). Time-lapse confocal microscopy at room temperature (with frames recorded every 30 seconds) for a free serum growth medium 15 μM solution of Tat_{11}-TAMRA administered to CHO-K1 cells. Five frames recorded at 1, 2, 3, 5 and 10 min are shown; transmitted-light channel recorded at 10 min is shown in the last frame. Scale bars: 10 μm. *154*
Figure 7.2: Chemical structure of TAMRA dye covalently linked to the Tat_{11} peptide. *157*
Figure 7.3: Representative initial configurations of a) Tat_{11} and b) Tat_{11}-TAMRA dimer peptides as embedded into a DOPC membrane pore. Peptide backbone is depicted in vdW representation, O atoms in red and N atoms in blue. Lipid chains are depicted in gray, phosphate groups in yellow. c) Top and d) side views of an equilibrated molecular configuration of the membrane pore. Lipid chains are depicted in gray, phosphate groups in yellow and lipid head groups shaping the pore in blue. *161*

Figure 7.4: Snapshot configurations issuing from a) Tat_{11} and c) Tat_{11}-TAMRA MD simulations taken at different time intervals. Peptides are depicted in red with TAMRA dye in green. (b-d) Corresponding translocation distance of monomer center of mass along the longitudinal pore axis (i.e., Z-coordinate). *164*

Figure 7.5: (a,c) Snapshot configurations issuing from Tat_{11} replica simulations taken at different time intervals. Peptides are depicted in red. (b,d) Corresponding translocation distance of monomer center of mass along the longitudinal pore axis (i.e., Z-coordinate)..... *165*

Figure 7.6: (a,c) Snapshot configurations issuing from Tat_{11}-TAMRA replica simulations taken at different time intervals. Peptides are depicted in red with TAMRA dye in green. (b,d) Corresponding translocation distance of monomer center of mass along the longitudinal pore axis (i.e., Z-coordinate). *166*

Figure 7.7: a) Snapshot configurations issuing from Tat_{11}-TAMRA dimer MD simulation taken at different time intervals. Peptides are depicted in red with TAMRA dye in green. b) Corresponding translocation distance of dimer center of mass along the longitudinal pore axis (i.e., Z-coordinate). *167*

Figure 7.8: (a,c) Snapshot configurations issuing from Tat_{11}-TAMRA dimer replica simulations taken at different time intervals. Peptides are depicted in red with TAMRA dye in green. (b,d) Corresponding translocation distance of dimer center of mass along the longitudinal pore axis (i.e., Z-coordinate). *168*

Figure 7.9: Initial (top) and final (after 40 ns, bottom) configurations issuing from Tat_{11}-TAMRA a) monomer and b) dimer SMD simulations. Peptide are depicted in red with TAMRA dye in green. Red arrow shows the direction of applied pulling force along the longitudinal pore axis (i.e., Z-coordinate). *169*

Figure 7.10: Average pulling force applied to gently move the Tat_{11}-TAMRA peptide (both monomeric and dimeric forms) out of the membrane pore as a function of distance from the lipid bilayer center. The resulting force profile is evaluated as the average of four SMD simulations for each system under consideration. Peptide (yellow) at various distances from pore center is depicted in the insets, with lipid head groups in blue. Standard error is 25 pN...... *170*

Figure 7.11: Role of Tat peptide self-aggregation to direct transduction in cells is highlighted in a computational study of dimer versus monomer. *173*

Figure 8.1: Top and side views of the open conformation of the transmembrane domain of wild-type Kv4.3 in its tetrameric (top panels) and monomeric (bottom panels) forms. The location of VSDs (residues 182-307), PD (residues 321-402) and SF (residues 367-372) are indicated by arrows. The sites of the single point mutation in residue M373 skyblue licorice representations, respectively. S4, S4-S5 linker, S5 and S6 helices are shown in red, blue and green, respectively. Crystallographic K^+ ions are shown in magenta space filling representation. All remaining residues are shown in white. *177*

Figure 8.2: (a) Sequence alignment of the transmembrane PD (residues 321-402) of human wild-type Kv4.3 with Kv1.2 PD from Rattus norvegicus shows high sequence similarity. (b) Sequence alignment of the transmembrane PD domains (residues 359-411) of human wild-type Kv4.3 with different Kv channels from Homo sapiens. The SF domain of Kv4.3 exhibits high sequence similarity with all human Kv channels, indicating that this region of the protein is highly conserved...... *181*

Figure 8.3: Average pore radius along the channel axial position (z-coordinate) for human WT, M373I and M373E Kv4.3 TMDs embedded in a POPC lipid bilayer and simulated with an applied voltage of 1 V. The S6

gating helices become increasingly constricted in mutated forms of Kv4.3 as it can be seen from the structural alignment of PDs for WT (red), M373I (blue) and M373E (cyan). *182*
Figure 8.4: Water coordination number and distribution of K^+ ions of human WT and M373E Kv4.3 TMDs embedded in a POPC lipid bilayer and simulated with an applied voltage of 1 V at 310.15 K for 1 μs. The SF of WT Kv4.3 TMD is shown in silver with highlighted carbonyl groups and T367 sidechains in licorice representation. Water molecules and permeating K^+ ions (green) are shown in space filling representation. The different binding sites inside the SF are separated by dashed lines. The analysis was performed over the whole trajectory. *184*
Figure 8.5: Contact maps of a region of the transmembrane PD domain in close proximity of the SF (residues 350-375) of human WT, M373E and M373I Kv4.3 TMDs embedded in a POPC lipid bilayer and simulated with an applied voltage of 1 V at 310.15 K for 350 ns. *184*
Figure 8.6: Number of contacts residue 373 with residues 350-375 of human WT, M373E and M373I Kv4.3 TMDs embedded in a POPC lipid bilayer and simulated with an applied voltage of 1 V at 310.15 K for 710 ns. In M373I the mutated residue 373 exhibits a higher average number of contacts to residues 350-375 than in the WT and M373E model. The cutoff used for the calculation of the number of contacts was 3.0 Å. Averages and standard deviations of the number contacts for each chain are measured over the last 40% of each trajectory. *185*
Figure 8.7: The average number of contacts of residue 373 of human WT, M373E and M373I Kv4.3 TMD with residues 350-372. The average number of contacts was measured by averaging the total number of contacts over the four chains and it was normalized dividing by the total number of frames from the whole trajectory. Top views of WT (red), M373E (cyan) and M373I (blue) SFs are shown with residues 350-363 (WT: orange and M373I: cyan). In the inset a side view of M373I SF shows the interaction of I373 with Y360. The cutoff for considering a residue in contact with residue 373 was 3.0 Å. The analysis was performed over the whole trajectory. *186*
Figure 8.8: a) Average distances of residue 373 Cαs of human WT, M373E and M373I Kv4.3 TMDs embedded in a POPC lipid bilayer and simulated with an applied voltage of 1 V at 310.15 K for 710 ns. b-d) indicating average distance between SF of chains A, B, C and D for all three Kv models, in the M373I model the average distances d1 and d3 are shorter than those in the WT and M373E models, indicating a tighter packing of the SF in proximity of residue 373. (e,f) A top view of the SF is shown together with a CPK representation of residue 373 and the set of distances of residue 373 Cαs in WT (red) and M373I (blue) models. Cαs are shown in orange and purple for WT and M373I models, respectively. The average distances were measured over the last 40% of each trajectory. *187*
Figure 8.9: Solvent accessible surface areas (SASAs) of (a) residues 367-373 and (b) residue 373 of human WT, M373E and M373I Kv4.3 TMD embedded in a POPC lipid bilayer and simulated with an applied voltage of 1 V at 310.15 K for 710 ns. In both WT and M373E model the SF including residue 373 show larger SASAs compared to the M373I system, whereas the SASA for residue 373 in M373E is also larger than WT model indicating that the presence of the mutation affects the overall SF hydration. Average SASAs for residues 367-373 and residue 373 with their errors estimated as standard deviations over the analyzed trajectory are reported in the right panel of the figure. The probe radius used for the calculation of SASAs was 1.4 Å. The analysis was performed over the last 40% of each trajectory. *188*

Figure 8.10: RMSF of alpha carbons of human WT (RED), M373I (blue) and M373E (Cyan) Kv4.3 models calculated for VSD, PD and SF region of the Kv4.3 channel TMD. *189*
Figure 9.1: a) Side view of the full-length atomistic model of human wild-type (WT) Kv4.3 open state in its tetrameric form showing transmembrane (TMD), intracellular (ICD) domains and KChIP1 auxiliary subunits. Black lines indicate the lipid bilayer. S4, S4-S5 linker and S5/S6 helices are shown in yellow, blue and green, respectively. Crystallographic potassium, zinc and calcium ions are shown in magenta, green and purple space filling representations, respectively. Kv4.3 TMD (residues 165-411) and Kv4.3 residues 142-164 are shown in white. KChIP1 residues are shown in skyblue. For clarity, only two of the four KChIP1 auxiliary subunits are shown. Kv4.3 T1 domain and KChIP1 auxiliary subunits are shown in red and skyblue ribbon representations, respectively. b) Top view of the WT Kv4.3 T1-KChIP1 complex with a dashed line enclosing a c) zoomed view of two Kv4.3 monomers (red and light blue) interacting with one KChIP1 auxiliary subunit (blue). First, second and third sites of interaction between Kv4.3 and KChIP1 are indicated by arrows. d) Side view of Kv4.3 T1 domain (red) showing residues involved in the W8E-P10E-A15E Kv4.3 triple mutant complex (orange). e) Top and f) side views showing sites of mutations in the first (orange) and second (Kv4.3 and KChIP1 residues are shown in magenta and cyan, respectively) interfaces. *194*
Figure 9.2: a) Side and b) top views of a KChIP1 auxiliary subunit showing all its α-helical domains in different colors. H1 (residues 39-45) and H2 helices (residues 50-63) mainly mediate the second interface interaction among Kv4.3 residues 70-78 and KChIP1. H1, H2, H3, H4, H5, H6, H7, H8, H9, H10 are shown in cyan, celeste, skyblue, red, orange, yellow, blue, green, purple and magenta, respectively. The remaining residues are in white. Calcium ions are shown in purple spacefilling representation. *199*
Figure 9.3: Average number of contacts of a) W8 (purple), b) F11 (green) and c) W19 (purple) residues of the WT Kv4.3 T1-KChIP1 complex. The cutoff used to define a contact was 3 Å. The Kv4.3 N-terminus (residues 1-20) and the KChIP1 subunit of the starting model are shown in red and transparent skyblue ribbon representations, respectively. W8, W19 and F11 amino acids are shown in purple and green licorice representations, respectively. Residues displaying the largest average number of contacts are also shown for W8 (top right, panel a), F11 (middle right, panel b) and W19 (bottom right, panel c). *200*
Figure 9.4: a) Average interaction energy of Kv4.3 residues 8-15 with KChIP1 from 100 ns MD simulations of WT (red) and W8E-P10E-A15E (purple) Kv4.3 T1-KChIP1 complex models. Energies were computed and averaged over the whole trajectory, saved every 50 ps. Errors correspond to one standard deviation. Electrostatic potential surfaces of the Kv4.3 N-terminus (residues 3-20) of b) WT and c) W8E-P10E-A15E Kv4.3 T1-KChIP1 complex models. *202*
Figure 9.5: a) Average interaction energy of Kv4.3 residues 8-15 with KChIP1 from 100 ns MD simulations of WT (red) and W8E-P10E-A15E (purple) Kv4.3 T1-KChIP1 complex models. Energies were computed and averaged over the whole trajectory, saved every 50 ps. Errors correspond to one standard deviation. Electrostatic potential surfaces of the Kv4.3 N-terminus (residues 3-20) of b) WT and c) W8E-P10E-A15E Kv4.3 T1-KChIP1 complex models. *204*
Figure 9.6: Average pulling forces applied to move a single KChIP1 subunit out of a Kv4.3 T1-KChIP1 octameric complex from 100 ns SMD simulations of WT (red) and W8E-P10E-A15E (purple) Kv4.3 T1-KChIP1 complex

models using a constant velocity pulling of 0.25 Å·ns^{-1}. Pulling force is reported as a function of Kv4.3-KChIP1 distance. The Kv4.3 T1 domain (red) and the pulled KChIP1 subunit (green) structures are shown as insets at different distances. The overall force profile is given as an average over two SMD simulations. Standard deviation is 35 pN. *205*

Figure 9.7: The average number of contacts of Kv4.3 amino acid residues 70-78 with KChIP1 residues 37-61 from 100 ns AA MD simulations of Kv4.3 T1-KChIP1 complexes: a) WT (red), Y57A-K61A KChIP1 (orange) and Y57A KChIP1 (cyan); b) WT (red), E70A-F73E Kv4.3 (blue) and E70A-F73E Kv4.3 + L39E-Y57A-K61A KChIP1 (green). The number of contacts were measured and averaged over the whole trajectory. The cutoff used to define a contact was 3 Å. *206*

Figure 9.8: a) Average number of contacts of Kv4.3 residue 73 with KChIP1 residues from MD simulations of WT (red), E70A-F73E Kv4.3 (blue), E70A-F73E Kv4.3 + L39E-Y57A-K61A KChIP1 (green), Y57A-K61A KChIP1 (orange) and Y57A KChIP1 (cyan) Kv4.3 T1-KChIP1 complexes. b) Average number of contacts of KChIP1 residue 57 with Kv4.3 residues from MD simulations of WT and mutated Kv4.3 T1-KChIP1 complex models. The cutoff used to define a contact was 3 Å. *209*

Figure 9.9: Salt bridges of the second interface formed between Kv4.3 (green) and KChIP1 (blue) amino acid residues from MD simulations of WT, E70A-F73E Kv4.3, E70A-F73E Kv4.3 + L39E-Y57A-K61A KChIP1, Y57A-K61A KChIP1, and Y57A KChIP1 Kv4.3 T1-KChIP1 complexes displayed on the 100 ns structure. The cutoff used to define a salt bridge was 5 Å. Kv4.3 monomers (omitting residues 3-40) and KChIP1 subunits of each model are shown with the same color code of Fig. 1. Salt bridges are shown in yellow connecting alpha carbons of Kv4.3 and KChIP1 residues. The percentage of persistence of salt bridges of the WT Kv4.3 T1-KChIP1 complex are reported in the top, right table (see also Table 9.1). *210*

Figure 9.10: a) Solvent accessible surface areas (SASAs) of residues interacting in the second interface, namely Kv4.3 residues E70, F73, F74 and D78 and KChIP1 residues M37-E40, L42, K50, R51, L53, Q54, Y57, R58, K61 and F108, from 100 ns AA MD simulations of WT (red, 892 ± 33 Å^2), Y57A-K61A KChIP1 (orange, 853 ± 30 Å^2), Y57A KChIP1 (cyan, 880 ± 40 Å^2), E70A-F73E Kv4.3 (blue, 1018 ± 31 Å^2) and E70A-F73E Kv4.3 + L39E-Y57A-K61A KChIP1 (green, 1235 ± 45 Å^2), Kv4.3 T1-KChIP1 complexes. Mutations in the second interface side of Kv4.3 induce an increase in the SASA as compared to WT, KChIP1 mutants and Kv4.3 triple mutant systems. All SASAs were computed over the last 40% of each trajectory, saved every 50 ps. The errors are reported as standard deviations. b) Side and c) top views of residues interacting in the second interface. The same color code of Fig. S1 is used for helices of the KChIP1 subunit. The region of the Kv4.3 T1 domain interacting with H2 helix of KChIP1 is shown in yellow. *212*

Figure 9.11: a) Top view of the structural alignment of starting and 100 ns structures of the E70A-F73E Kv4.3-L39E-Y57A-K61A KChIP1 Kv4.3 T1-KChIP1 complex. The starting structure is shown with the same color code of Fig. 1 except for KChIP1 auxiliary subunits, which are shown in blue. In the 100 ns structure, Kv4.3 T1 domain and KChIP1 auxiliary subunits are shown in orange and celestial blue ribbon representations, respectively. Cysteine and histidine amino acid residues involved in the Zn^{2+} ion (silver) binding site are highlighted in lime and celestial blue licorice representations, respectively. Two Kv4.3 monomers interacting with one KChIP1

subunit are enclosed with a dashed line and a b) zoomed view of them highlights the loss of second interface interactions, as confirmed by the large average C_α atoms RMSD of KChIP1 auxiliary subunits. 214
Figure 9.12: a) Average interaction energy of Kv4.3 amino acid residues 70-78 with KChIP1 residues 37-61 from MD simulations of WT (red), Y57A-K61A KChIP1 (orange), Y57A KChIP1 (cyan), E70A-F73E Kv4.3 (blue) and E70A-F73E Kv4.3 + L39E-Y57A-K61A KChIP1 (green) complex models. All energies were computed and averaged over the whole trajectory, saved every 50 ps. The errors are reported as standard deviations. b) Average pulling forces applied to move a single KChIP1 subunit out of a Kv4.3 T1-KChIP1 complex from 100 ns SMD simulations of WT (red), E70A-F73E Kv4.3 (blue) and Y57A-K61A KChIP1 (orange) complex models using a constant velocity pulling of 0.1 $Å \cdot ns^{-1}$. Pulling forces are reported as a function of the Kv4.3-KChIP1 distance. Kv4.3 T1 domain (red) and the pulled KChIP1 subunit (green) are shown in the insets at different distances. The overall force profile is given as an average over two SMD simulations. Standard deviation is 25 pN. 216
Figure 9.13: Salt bridges of the third interface formed between Kv4.3 (red) and KChIP1 (blue) residues from MD simulations of WT, E70A-F73E Kv4.3, E70A-F73E Kv4.3 + L39E-Y57A-K61A KChIP1, Y57A-K61A KChIP1, and Y57A KChIP1 complex models. The cutoff used to define a salt bridge was 5 Å. Salt bridges are shown as yellow bond connecting Kv4.3 and KChIP1 residues. The percentage of persistence of the salt bridges of the WT Kv4.3 T1-KChIP1 complex are reported in the top, right table (see also Table 9.2). 219

List of Tables

Table 4.1: List of atoms of the RHB lipid model reporting atom types and atomic charges. 59
Table 4.2: Structural and dynamical properties of the DOPC and RHB-DOPC bilayer systems as issuing from corresponding MD simulations. 70
Table 4.3: FCS measurements of RHB and LAURDAN, diffusion coefficients (D) and G0 75
Table 5.1: Structural and dynamical properties of DOPC and RHB-DOPC lipid bilayers from AA MD simulations at three different temperatures. 94
Table 5.2: Average tilt angles of horizontal and vertical axes of RHB fluorescent polar headgroups from AA MD simulations of RHB-DOPC lipid bilayers at three different temperatures. 113
Table 6.1: Comparison between ground state (GS) and electronically excited state (EES) DPAP geometry optimized. Atom labeling in Figure 6.2. 125
Table 6.2: Dynamic properties of DPAP in solvents. 132
Table 6.3: Experimental and theoretical maximum emission peak wavelength (nm) and Stokes shift of DPAP in different environments. In parenthesis the dielectric constant of the solvent. Stoke shift values are computed by considering the absorption peak wavelength determined in our previous work. [58] *For DOPC bilayer no experimental counterpart is available.* 133
Table 6.4: Dynamic properties of DPAP in DOPC and DPPC:CHOL bilayers. Errors are in brackets. 139
Table 6.5: Comparison between GS and EES atom charges (e) of DPAP in acetonitrile. For atom labeling see Figure 6.14 143
Table 6.6: DPAP force field non-bonded parameters for atom labelling see Figure 6.14 145
Table 6.7: DPAP force field stretching parameters for atom labeling see Figure 6.14 146
Table 6.8: DPAP force field bending parameters. 147
Table 6.9: DPAP force field stiff torsional parameters. 150
Table 6.10: DPAP force field improper dihedral angles parameters. 152
Table 6.11: DPAP force field flexible torsional parameters. 153
Table 7.1: List of atoms of TAMRA model reporting atom type and atomic charge (i.e., standard CHARMM format is adopted). 158
Table 7.2: Molecular dynamics simulation details. 160
Table 7.3: Interaction energy and H-bond analysis of Tat_{11} and Tat_{11}-TAMRA peptides with DOPC 163
Table 8.1: Number of permeation events and conductance of K^+ ions for WT, M373I and M373E Kv4.3 estimated from MD simulations and electrophysiological measurements at single-channel level. 183
Table 9.1: Salt bridges of the second interface from MD simulations of WT and mutated Kv4.3 T1-KChIP1 complexes. 208
Table 9.2: Salt bridges of the third interface from MD simulations of WT and mutated Kv4.3 T1-KChIP1 complexes. 218

Chapter 1 Introduction

Plasma membranes not only provide the necessary compartmentalization to protect living cells, but also are directly involved in a variety of vital cellular processes such as signaling, transport of biomaterial, cell adhesion and cell communication. For their multiple biological roles, plasma membranes do require a high degree of plasticity to modulate the perception and transduction of extracellular and intracellular signals. Dynamic lateral assembly of protein complexes combined with an independent compositional lipid patterning in both membrane leaflets provide cells the opportunity to decorate this interface with specific molecules in an organized but dynamic manner. For such reasons, in recent years a great effort has been directed towards the understanding, at molecular level, of lipid diffusion, self-organization, phase change, raft formation, and so on. In my PhD thesis, I am presenting different computational approaches based on molecular dynamics (MD) techniques, which have been fruitfully used as complementary tools with respect to experimental methodologies to shed light onto some relevant phenomena and processes occurring within the lipid bilayers. Briefly, the topics covered in my research work include the study of lipid lateral diffusion and membrane permeability, the study of the role of self-aggregation in promoting cell-penetrating peptides translocation across a lipid membrane (Tat11 peptide, either or not covalently-linked to a common fluorescent dye), the dynamic and photophysical properties of a molecular rotor used to probe lipid order in lipid bilayers of different composition, and the detailed mechanisms through which single point mutations affect the gating and ion translocation in a voltage-gated potassium channel (Kv4.3) and also how the mutations inside the Kv4.3-KChIP1 complex affect the overall structural stability of the ion channel.

The biological membranes and their diverse constituents play key roles in cellular physiology and there has been a significant progress in experimental techniques over the last few decades to study lipid bilayers and their structures. Yet, lipid membranes, due to their complexity, continue to pose major challenges to experimental techniques, whereas computational modeling methods, specifically molecular dynamics simulations, have been utilized quite

effectively to fill the gap in the structural and dynamical description of biological membranes, not readily accessible to standard experimental methodologies. Moreover, the work presented in this thesis illustrates in some detail the molecular structures, dynamics and mechanisms characterizing molecules like fluorophores, molecular rotors, carrier peptides and ion channels when embedded inside biological membranes. This work also highlights the possible role and effect that such molecules could have on the physical and chemical properties of the biological membranes. In all studies included in this thesis, results helped to gain new and relevant insights into subtle features of lipid membranes and of protein channel behavior. To better interpret and support our findings from molecular dynamics simulations, parallel experimental investigations were carried out by external collaborators. These studies were conceived towards a more accurate prediction of structural and dynamical properties of biological membranes. In addition, the choice of probes described in this work could also be applied to other biological membrane systems and could help in predicting correct dynamics as well as structural properties of more general lipid membranes and plasma membranes. This thesis comprises also a detailed study of a voltage-gated potassium channel (Kv), along with a mutation that could cause channelopathies and its interaction with an important auxiliary protein. The work on the channel mutation affecting the gating mechanism and the functioning of the ion channel could serve as an illustrative application for researchers interested in analyzing various other mutations in similar ion channels. Overall, the work presented here has also implication in fluorophore designing, transport of drugs to its target and to understand the role of certain amino acids in the normal functioning of ion channels. This in turn could lead to cure various disorders associated specifically with the ion channels. All the above-mentioned phenomena are discussed and described in separate chapters of this thesis, where a short summary of each chapter is sketched below.

In chapter 2 and 3 of this thesis, the basic biological background and the description of the computational methodology which has been used throughout the present research work is reported. Chapter 4 and 5 discusses the role of dye-labelled lipids as molecular probes for lipid diffusion studies. When molecular probes are used, two major points of concern arises: 1) the incomplete understanding of the probe behavior inside the lipid bilayers and the perturbation of the latter resulting from probe incorporation 2) Another concern is the dye concentration and how it could affect the lipid bilayers. In this study, for the first time the effect of self-aggregation of Rhodamine labeled lipid was studied in comparison to non-labeled lipids. To

study this effect, molecular dynamics simulations represent a valuable way to characterize the location and dynamics of bilayer-inserted membrane probes, by providing a detailed atomic-scale information. As well, the magnitude of the induced perturbation on the host lipid structure can be effectively investigated, in fact several important classes of reporter molecules have been studied in recent years. It has been now widely recognized that our understanding of complex biological processes, such as protein folding, ion transport through bio-channels and molecular recognition, can greatly benefit from the use of computer simulations in conjunction with conventional laboratory techniques. The aim of the present studies, as detailed in these chapters, is to use state-of-the-art computational tools to shed light on lipid dynamics and to support experimental evidence issuing from advanced fluorescence microscopy techniques. Given the high number of experimental systems and imaging approaches used, it is now difficult to rationalize all collected results into a unified picture of membrane heterogeneity regulation. In particular, experimental results inevitably suffer from the effect of the fluorophore used for lipid/protein labeling. Moreover, the bias introduced by the optical probes is not easily predictable and biological conclusions must be carefully interpreted in light of possible perturbative effects by the probes. Molecular dynamics simulations offer a unique opportunity to quantitatively investigate the effect of lipid labeling through fluorescent probes of different size and physico-chemical characteristics. While several computational studies have recently investigated dynamical properties of lipids in homogeneous and heterogeneous model bilayer membranes, the plan in the current study was to assess the optimal computational methodology (ensemble conditions, force fields, mechanical stress) for studying diffusion and self-organization processes. Moreover, the use of appropriate kinetic models helped to establish diffusion laws that hold well beyond the time limit of the computer simulations. Then, the dependence of dynamical properties on temperature and composition, a somewhat overlooked yet important physical condition, were studied to gather significant information transferable to more realistic vesicles and plasma membranes. In this thesis, a large effort has been put to assess the influence of the fluorophore probes on the lipid dynamics and clustering properties. The hydrodynamic effect of a Rhodamine-labeled lipid along with its ability to self-aggregate at different concentration levels was scrutinized and compared to the experimentally observed dynamics of the modified and labeled systems with respect to the natural counterparts.

Fluorescent molecular rotors (FMRs) are discussed in chapter 6. They are an important class of environment sensitive dyes which have application in analytical, environmental, optical and biochemical areas. Their wide application in different areas is due to their ability to permeate cell membrane easily because of their smaller size and to sense environment dependent processes at intracellular level. All these features of FMRs make them a subject of extensive research. In the study reported here, MD simulations and florescence lifetime imaging microscopy (FLIM) were combined to study the application of 4-(diphenylamino) phthalonitrile (DPAP), a recently synthesized FMR, as a probe for detecting the local order within lipid bilayers. In this work, a force field development was tailored towards DPAP potential energy surface and corresponding gradient in the first excited state as evaluated from quantum mechanical calculations at time-dependent DFT level. The sampling of the first electronically excited state (EES) potential energy surface allowed us to effectively simulate excited state properties of DPAP embedded in several solvents (i.e., acetonitrile, cyclohexane and o-xylene) and lipid bilayers, and to finally model fluorescence wavelengths on hundreds of snapshots issuing from the computed classical MD trajectories at a reasonable computational cost. However, in this particular study the molecular rotor (DPAP) in its excited state inserted inside multiple environments demonstrated its ability to perfectly sense both viscosity and polarity of the local environments. This ability of DPAP is because of its propeller like geometry, which favors the barrier free flexible configurations inside those environments. The study highlights the structural and dynamical effects of the DPAP on the different environments and its interactions within those environments and also how suitable is this molecular rotor in using as a probe for detecting subtle changes in lipid membranes.

In chapter 7, a study on a prototype of cell penetrating peptides (CPPs) is reported. CPPs are an important class of peptides which helps in facilitating the cellular uptake/intake of various types of molecular cargos and their ability to penetrate the cells make them an effective drug delivery vector. Tat_{11} is an arginine rich peptide from HIV-1 Tat protein which is a prototype for cationic CPPs and it was utilized for the study outlined in this thesis. It has been widely accepted now that for CPPs translocation through cell, the concentration of the peptide plays a significant role. Within nanomolar to low micromolar range the CPP takes an endocytic pathway, whereas when the concentration of the peptide goes above 10 μm, it takes spontaneous transduction through the plasma membrane as a pathway to release the attached cargo into the cytoplasm of the cell. The hypothesis outlined in this study was that Tat_{11} peptide

self-aggregation could play a role in the membrane pore stabilization favoring the onset of the transduction process. The impact of tetramethylrhodamine-5-maleimide (TAMRA) was also assessed in assisting the CPP translocation. Present study shed some light on the research question, which could lead to tremendous implications for the development of new therapeutic approaches. Here, a state-of-the-art computational study on the role of Tat_{11} self-aggregation in membrane pore stabilization is presented. Kinetic analysis was performed on the peptide in both monomeric and dimeric forms in native and dye TAMRA labelled counterpart inside the purposely created membrane pore through MD simulations and experimental techniques. The main goal of the present study was to evaluate the capability of the peptide to stabilize a lipid membrane pore over a prolonged period of time. The main outcome of the current study was that self-aggregation plays a major role in membrane transduction and TAMRA plays an indirect but effective role in CPP translocation.

Results coming out of MD simulations and experimental techniques performed on a Kv ion channel are elaborated in chapter 8 and 9. Cell membranes being highly selective in transporting materials through them provide barrier to essential ingredients including ions Na+, K+, Ca2+ and Cl- and this is where ion channels come in to play their most significant role in making the lipid bilayers more permeable. This communication is extremely important to regulate the normal functioning of the cells. Potassium voltage gated ion channels (Kv) represents the most diverse and widespread class of the membrane proteins, playing their major role in regulation of the cell. For example, mutations occurring in the gene of Kv4.3 ion channel can lead to severe genetic disorders. To understand how hereditary and de-novo mutations can cause such channelopathies there is a need to study the molecular mechanism of these channels. Kv4.3 is an important ion channel for neuronal communication. Recently, hereditary and de novo pathologic mutant versions were identified with severe consequences. To understand how mutations cause such problems, we need to investigate the molecular mechanism altering the physiological function of these channels. The previous investigations on the hereditary mutations have shown that while some of the mutant channels could not reach to the cell membrane, others had an altered voltage dependency and/or gating. However, due to the lack of a suitable crystal structure, how the mutations affect the structure and how these changes alter the gating mechanism and ultimately the neuronal activity is unknown. The solution to the problem discussed above is to design a systematic study of the channel gating at the molecular level with an integrated approach using experimental and in silico methods.

The wild-type and two mutants of the channel were studied using the electrophysiology and molecular dynamics simulations to identify which stages of the gating is affected and what is the underlying molecular mechanism. In this study, M373I and M373E mutations were chosen to investigate the effects of these single point mutations at a molecular level. The approach taken to unravel such molecular details was to 1) express the channels heterologously in mammalian cell lines for experimental work and generate the full-atomistic model of the WT channel and the mutants for the in silico experiments and 2) study the voltage-dependence and kinetics of the channel gating to understand how M373E and M373I affect the channel activity, what is the structural basis of this, and what these mutations tells us about the channel (mal-)functioning. The model described here allowed us to explain the experimental findings and identify specific atomic interactions in the mutant channels, and propose a mechanism of malfunctioning of each mutant, which is not possible to identify by experimental tools only. In chapter nine, the objective of the study is to decipher the effect of the KChIP auxiliary subunits on the Kv4.3 channel, which was never performed before computationally. KChIPs modulate two important functions of Kv4.3 N-terminal domain: the remodeling of the current biophysical properties and the increase of the surface expression of Kv4.3 channel. Besides, KChIP also accelerates recovery of Kv4 from closed-state inactivation. The crystal structures of the N-terminal ICD of Kv4.3 channel in complex with KChIP1 auxiliary subunits are already available. For the investigation of KChIP1 subunits effect on the Kv4.3 channel, MD simulations of the full complex structure were performed.

Finally, all the results reported in this thesis are brought together as a summary in chapter 10 and also the future perspectives of this work are discussed in this chapter.

Chapter 2 Biological Background

2.1 Overview

Living organisms may be composed by trillions of cells which provide nutrients to body, help in converting the nutrients to energy and, most importantly, contribute to specialized physiological functions. Hence, there are several processes going on inside the cell for the normal functioning of the body. It is necessary for the cell to maintain its form and function, therefore all living cells have special protection around them, namely biological membranes made up mostly by lipid molecules. A biological membrane acts as a barrier and helps in regulating the transport in and out of the cell through specialized integral proteins, thus making possible the necessary transport of chemicals, nutrients and drugs to the cell. This chapter provides a quick and necessarily incomplete overview of biological membranes, briefly describes the functional role of some peptides and proteins relevant for biophysical and biochemical processes occurring at the level of the membranes, and reports on the use of molecular dyes and rotors for studying the physical and chemical properties of biological membranes and lipid membrane models.

2.2 Plasma Membranes: Models and Structural Composition

Plasma membranes are not just homogenous mixture of lipids and proteins but they also contain discrete domains comprising lipids and proteins clustered together to form structural and functional units. In the year 1972, Jonathan Singer and Garth Nicholson proposed the fluid mosaic model for the membranes,[1,2] which today is the basis of all the research on lipid bilayers. According to the fluid mosaic model shown in Figure 2.1, a cell membrane consists of amphiphilic lipids with proteins residing inside the lipid bilayer and diffusing along with the lipids in lateral directions. At that time, the fluid mosaic model helped to explain several poorly understood characteristics of the lipid bilayer, such as lipid asymmetry and how proteins are incorporated into the lipid bilayer, however it did not explain the variable lipid bilayer composition and structure.

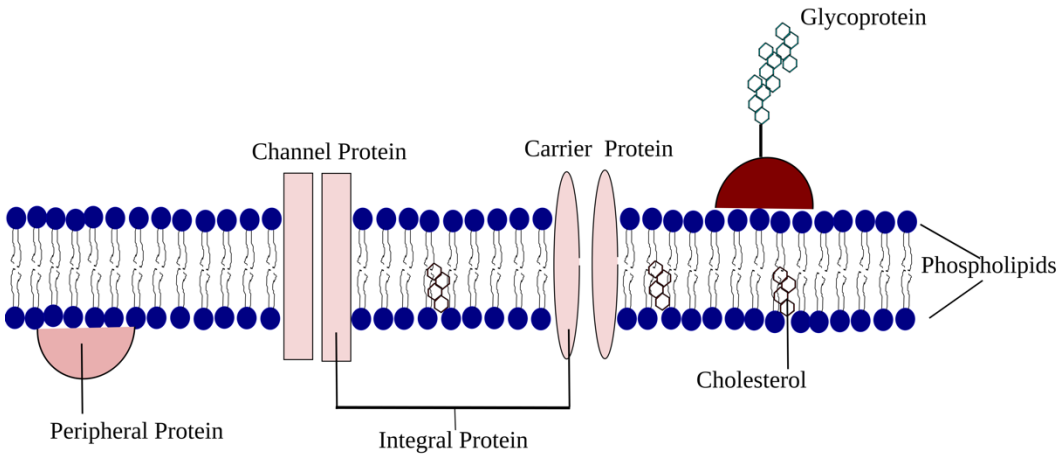

Figure 2.1: Fluid mosaic model proposed by Jonathan Singer and Garth Nicholson in the year 1972.

In 1984. Mouritsen and Bloom developed a mattress model according to which it was established that lipids and proteins in a bilayer can distribute themselves inhomogenously.[3] The idea that lipid membrane may be heterogeneous led to further development in the understanding of the structure of the plasma membrane. In 1997, Simmons and Ikonen came up with the revolutionizing concept of lipid rafts or domains residing inside the lipid bilayer.[4] These domains are rich in sphingolipids and cholesterol and are laterally segregated, and tend to float in a mixture of the lipid bilayer. Lipids rafts are small (i.e., 10-200 nm) highly dynamic and heterogeneous structures. Depending on their size they can be termed as micro or nanodomains.[4–8]

Lipid membrane is a complex structure, which not only compartmentalizes the cell but also has its own constituents in the form of lipids, membrane proteins and carbohydrates. Lipids which are the primary components of the membrane bilayer can be grouped into three major classes i) phosphoglycerides ii) sphingolipids and iii) sterols. Phospholipids containing phosphate groups categorize phosphoglycerides and sphingolipids. Phosphoglycerides have glycerol as a backbone whereas sphingolipids have sphingosine backbone, e.g. sphingomyelin which is the most common sphingolipid. Membrane glycerides are diglycerides in which two hydroxyl groups of the glycerol are esterified to the fatty acids, the third hydroxyl group is esterified to the phosphate group. Sterols commonly are cholesterol molecules embedded within the lipid molecules oriented in such a way that their hydrophilic hydroxyl group faced towards the membrane surface while its hydrophobic rings which are flat and rigid are embedded inside the

lipid bilayer which causes interference with the movements of the lipid tail fatty acids, in return this increases membrane fluidity. Cholesterol molecules are much shorter and less amphipathic than the lipids itself.[9–12]

Membrane phosphoglycerides have additional alcohol group linked to the phosphate, most commonly, which includes choline, ethanolamine, serine and inositol.[13] The esterification of the phosphatidic acid with these alcohol groups coupled with acyl chains are abbreviated as dioleoylphosphatidylcholine (DOPC), dipalmitoylphosphatidylcholine (DPPC), 1-palmitoyl-2-oleoyl-phosphatidylcholine (POPC) and many more. In this thesis, particular importance is given to work related to DOPC, POPC and DPPC lipid bilayers. The chemical structures of the DOPC, POPC and DPPC are shown in the Figure 2.2. All of these groups along with the negatively charged phosphate group make a highly water soluble (hydrophilic) head group. At physiological PH, the headgroups of the phosphatidylserine (PS) and phosphatidylinositol (PI) are negatively charged, whereas the headgroups containing choline and ethanolamine which forms phosphatidylcholine and phosphatidylethanolamine, respectively, possess a neutral electric charge. Lipids that contain carbohydrate group or sugars are known as glycolipids. A significant feature of phospholipids is that they are amphiphilic/amphipathic molecules having both hydrophilic heads and hydrophobic tails. These lipid heads and tails are arranged in a way that polar headgroups are faced towards the water surface and interact directly with water molecules, while non-polar lipid tails are located away from the water, within the membrane interior. This organization of head groups and hydrocarbon tails gives shape to the lipid membranes into two separate leaflets, which is the reason lipid membranes are often termed as lipid bilayers. The structural organization of head and tail groups of the lipid membranes are very crucial in determining the membrane function, while another important determining feature is the nature of the chemical group that is attached to the phosphate in the lipids. The general depiction of the lipid molecules and lipid bilayer shown in Figure 2.1. DOPC, POPC and DPPC lipid bilayers are used in the studies reported in this thesis because of their simple zwitterionic nature, making them less interacting with the type of charged molecular species, their relatively high phase-transition temperature, and the fact they represent, in general, a good model for the cell membrane.

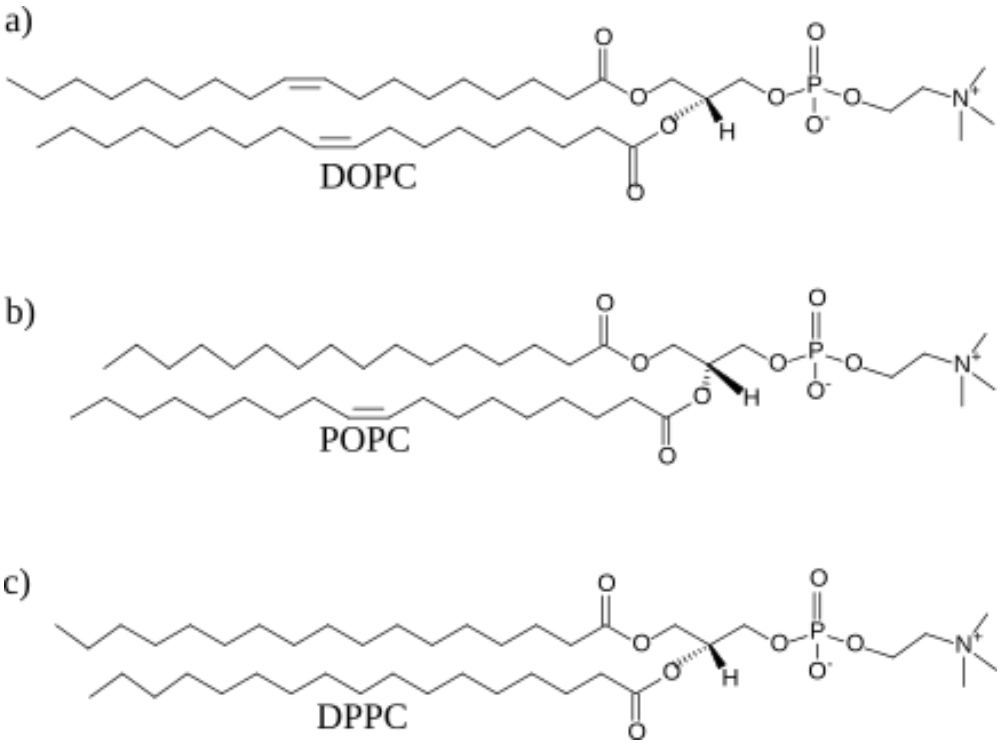

Figure 2.2: Structure of lipid molecules used in this thesis.

Another relevant feature of these phospholipid bilayers is that they are characterize as either solid or liquid phase. The liquid phase of the lipid bilayers is further divided in to two distinct phases i.e. **i) liquid disordered (L_d)** and **ii) liquid ordered (L_o)** phases. L_o phase contains generally a mixture of phospholipids and cholesterol due to which it has slightly larger degree of order, tight packing of lipid tails, increased bilayer thickness and slower dynamics in contrast to the more fluid L_d phase. On the other hand, solid phase is much more ordered, more tightly packed and has the lowest degree of dynamic flexibility compared to liquid phases. It is believed that biological membranes are primarily in the liquid/fluid phase. The transition temperature (Tm) between the two phases i.e. solid and liquid depends on the lipid chemical structure, length of the lipid tail chain and degree of unsaturation.[14–19]

2.3 Mode of transport in biomembranes and role of proteins in transportation

Membrane transport can be generally classified into i) passive transport and ii) active transport, passive transport can be further divided into **a) non-mediated transport** that occurs through simple diffusion process and **b) mediated transport** that requires facilitated diffusion in which a specific molecule flows from high concentration to low concentration and is dependent on the permeability nature of the cell membrane, i.e composition of the lipid membrane, and it does not require chemical energy unlike active transport. This type of transport is usually adopted by the polar or large substances and is mediated by membrane proteins called carriers, permeases, channels, and transporters, whereas in **active transport** a molecule is transported from low concentration to high concentration and the transport requires energy most commonly in the form of ATP. However, other energy sources also drive the active transport processes, including light energy and energy stored in the ion gradient. The illustrative schematic of different modes of transportation of membrane is shown in Figure 2.3. Active transport is divided further into **a) primary active transport** which uses energy directly to transport molecules across the membrane and **b) secondary active transport** in which molecules do not require direct coupling of ATP, instead the electrochemical potential difference by pumping ions out of the cell is required to carry out the transport process.[20] Most of these transport systems either operate as **symport** in which the ion and the transported molecule moves in one direction or either as **antiport** in which the ion and the transported molecule moves in the opposite direction shown in the Figure 2.3. Molecules which are too large to pass through the membrane require another type of active transport which can be generally called as vesicle transport and it includes **i) exocytosis and ii) endocytosis**. Usually, toxins are secreted through vesicles within the plasma membranes. In endocytosis, the particle is engulfed from outside the cell and is completely enclosed by the membrane, then a membrane-bound sac or vesicle pinches off and moves the substance into the cytosol, while during exocytosis the molecule is released outside of the cell within the vesicle. All of these transport mechanisms are taking place inside the cell to make the cell work in optimum environment keeping the temperature, ions, small molecules, pH and various other biological factors in control. In the last two

decades, there was a great effort to make possible efficient transport of drugs inside the cells, thus surpassing the first barrier outside the cell, i.e. the plasma membrane.

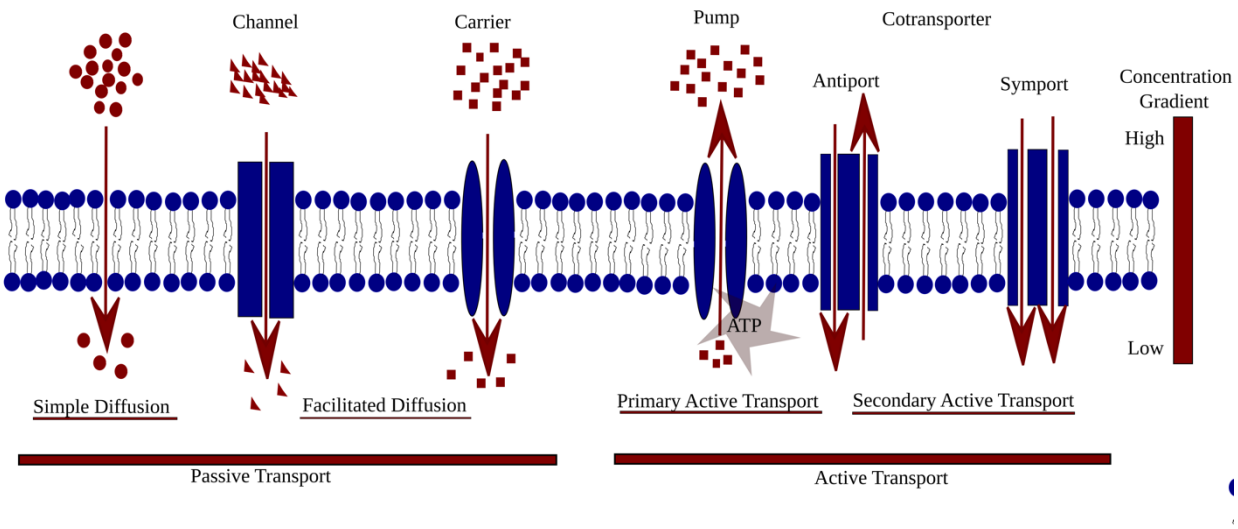

Figure 2.3: Schematic of different mode of transports mediated by channel, carrier and transport proteins.

2.4 Cell Penetrating Peptides

All of the transport mechanisms that membranes can undergo are important to make communication between inner and outer environment of the cell and to transport the therapeutics inside the cell. Some drugs are large hydrophilic molecules and show hindrance for the translocation through the cell membranes. The discovery of a new class of peptides called cell penetrating peptides (CPPs) in the late 1980s, which includes human immunodeficiency virus type 1 (HIV-1) encoded TAT peptide and amphiphilic Drosophila Antennapedia homeodomain derived 16 amino acid penteratin peptide (pAntp), paved the way for the transport of large molecules inside the cells with potentially useful clinical application.[21–26] Generally, CPPs are short sequences of amino acids, usually containing up to 30-35 residues, and are hydrophilic in nature with a net positive charge at physiological pH.[24,27] Since the discovery of CPPs, extensive research has been devoted to the investigation of the cellular uptake mechanism such peptides. It has been suggested that these peptides either take endocytosis or direct penetration (energy independent) routes to deliver covalently or either non-covalently attached cargo molecules, such as drugs with low toxicity and high efficiency.

[28,29] Endocytosis is one of the main routes acquired by the CPPs for internalization and is an energy-dependent process involving several pathways: i) macropinocytosis [23,30–32] ii) clathrin or caveolin-mediated endocytosis [33–35] and iii) phagocytosis.[36,37] Whereas direct translocation, which is an energy independent process, may include different mechanisms such as i) inverted micelle,[38] ii) toroidal and barrel stave pore,[39–41] iii) carpet like model,[1,2] and iv) membrane thinning model[43] shown in Figure 2.4. The first step in all these mechanisms is the interaction of the positively charged CPP with negatively charged sulfate groups, which is then characterized by the folding of the peptide on the lipid membrane by stable or transient destabilization of the membrane.

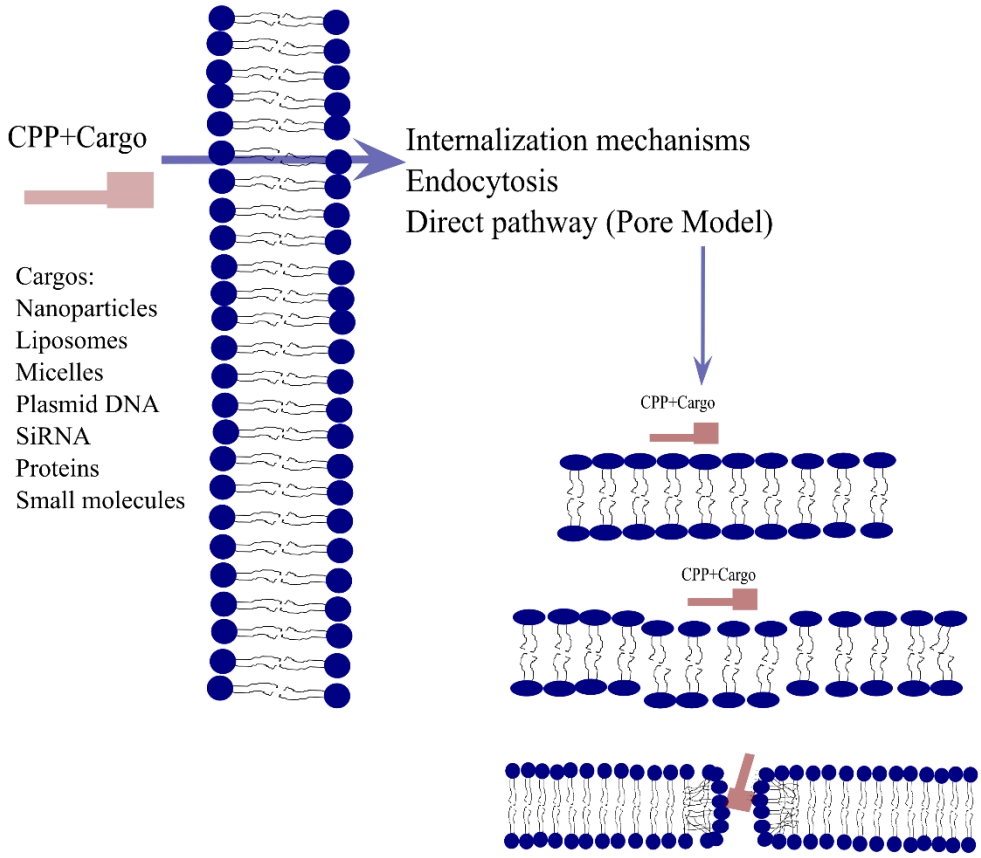

Figure 2.4: Cell penetrating peptide (CPP) along with cargo molecule can take direct penetration pathway to permeate through lipid bilayer, the toroidal pore model a direct penetration pathway is shown.

The mode of transport CPPs would take is mostly influenced by the concentration and positive electric charge of these short peptides inside the cell, type of the cargo attached, lipid membrane composition and the number of amino acid residues they contain, thus making internalization

and penetration a complex process.[4] Based on their origin, CPPs can be classified in to three main classes: i) protein derived CPPs (e.g., penetratin, TAT and pVEC) ii) chimeric CPPs, which are formed by the fusion of two natural sequences (e.g., transportan, MPG and Pep-1) and iii) synthetic CPPs, formed by rationally designed sequences usually based on structure activity studies. For example, some of the peptides in synthetic CPPs are polyarginines, MAP and R_6W_3. One important aspect of peptide translocation across the lipid bilayer is represented by the formation and stabilization of a pore within the membrane, a process not yet well understood. In chapter 4 of this thesis, a study is dedicated to the TAT peptide, aiming at understanding the kinetics of its translocation and the role of a fluorescent probe in its self-aggregation.

2.5 Voltage-gated potassium ion channels

Membrane proteins span the biological membranes and interact with, at least in part, the membranes in the form of i) integral membrane proteins or in the form of ii) peripheral membrane proteins, which unlike integral membrane proteins are temporarily bound to the lipid membranes. Membrane proteins account for more than 25% of the total proteome of an organism and also they constitute more than 50% of the current drug targets.[4–8] On the other hand, integral membrane proteins in the form of ion channels regulate the ion gradient inside the cell and help in sending neuronal signals for the proper functioning of the body. These ion channels are large proteins anchored on and across cell membranes consisting of multiple subunits and arranged in a cluster to form a small pore. Such pores or ion channels determine the permeation of specific ions through selectivity filters (SFs) and regulate the ion flow through the gating process, i.e., ion conduction is turned off or on in response to specific external stimuli.[9–12] On the contrary, the dysfunction of ion channels or membrane proteins interacting with lipid bilayers can cause diseases affecting tissues in muscles, bones, heart, brain and kidneys. Diseases due to genetic alterations or acquired structural modifications of ion channels are termed as channelopathies.

Ion channels involved in electrical signals generation can be widely classified in two major classes: i) ligand gated ion channels and ii) voltage-gated ion channels. Potassium voltage-gated ion channels (KV) represent the most diverse and widespread class of membrane proteins in the human genome and they are classified into 12 families ranging from Kv1 to Kv12. Kv

channels play important regulatory roles in the cell and mutations in the genes expressing Kv channels can lead to severe genetic disorders, which include epilepsy, deafness, cardiac rhythm disorders, multiple sclerosis and are also linked to proliferation to tumor.[13] All Kv channels have high level of similarity and, since the discovery of the Shaker channel, it has been recognized that a functional channel requires four α-subunits located in the transmembrane domain (TMD) of the Kv channel. Each α-subunit consists of six helices named S1-S6. These helices define two important structural and functional parts of the channel: i) the voltage sensing domain (VSD), which is made up of helices S1-S4 located on the channels periphery and is sensible to changes in the membrane potential and ii) helices S5-S6 located in the center of the channel, thus shaping the pore domain (PD). PD is therefore the potassium ion conducting domain. PD of the Kv channels consists of the channel gate and a selectivity filter (SF) allowing only K+ ions to pass through it. The gate is formed by crossing C-termini of S6 helices, whereas SF is formed with S5-S6 loop and a highly conserved fragment of the PD region. The VSD and PD are covalently bonded by the S4-S5 linker. The combination of VSD, PD and SF makes up the fully functional K+ ion permeation pathway.[48,49] There is still not an atomic resolution structure of Kv4.3 in its open conformation. Since Kv4.3 shares high sequence similarity with Kv1.2, the combined application of homology modeling, molecular modeling, computational and experimental techniques can shed some light on the structure and dynamics of Kv4.3 inserted into a lipid bilayer and is shown in Figure 2.5. In Chapter 8 and 9 of this dissertation thesis, we focus our interest on studying the effect of a specific novel point mutation on the Kv4.3 ion channel and on the interaction between Kv4.3 and one of its auxiliary subunit in some detail.

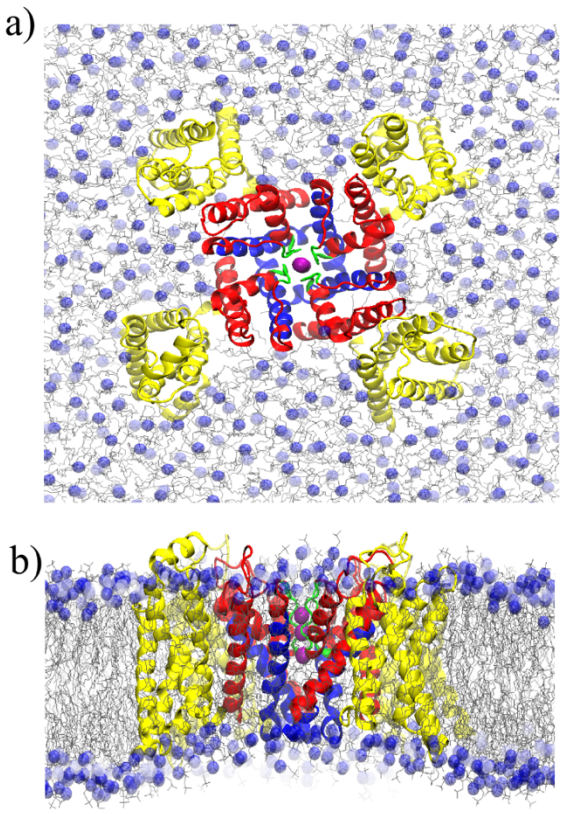

Figure 2.5: a) Top view of the KV gated ion channel embedded inside the POPC lipid bilayer b) Side view of the KV gated ion channel embedded inside the POPC lipid bilayer.

2.6 Molecular rotors as probes for membrane properties

Fluorescent molecular rotors have played a great role in the investigation of lipid membranes, as the latter are not intrinsically fluorescent; indeed, rotors have been used to elucidate different physical and dynamical properties of the lipid bilayers. However, the behavior of the probes when inserted inside the bilayer have been poorly understood and this makes it difficult to distinguish between the actual membrane properties and the perturbations arising from the choice of the probe.[14–19] To better understand the membrane dynamics, in the last two decades extensive research has led to the discovery and synthesis of many new molecular probes. Out of this large number of variety of probes, there is a need to assess carefully the effects of the optical probes, which depend also specifically on the type of membrane and physical and chemical property under investigation.

Generally, the fluorophores used in membrane biophysics can be divided into two classes i) natural fluorophores that include naturally occurring amino acids and green fluorescent proteins and ii) synthetic organic fluorophores, which are environment-sensitive probes.[52–54] In the past decade, much of the focus has been put on the organic fluorophores to study membrane properties, among which common probes are PYRENE, DPH, NBD BODIPY, PRODAN, fluorescein , Texas Red, etc. These fluorescent synthetic probes can either be attached covalently to the lipid head groups or lipid acyl chains, these kind of probes are termed as fluorescent lipids. There are some fluorophores, likes LAURDAN and PRODAN, which are mostly used to study the phase partitioning of the lipid membranes, whereas relatively new class of fluorophores, i.e. fluorescent molecular rotors, are used to study the microviscocity of the membrane bilayers.[20]

In this thesis, Rhodamine dyes (RHB and TAMRA) have been used as fluorescent dyes, the basic structure of both molecules are shown in Figure 2.6. Rhodamine belongs to the class of xanthene dyes and they possess excellent photostability and photophysical properties.[56,57] Texas red dye is another important and widely used probe in membrane biophysics studies and is also a derivative of the xanthene dye. On the other hand, DPAP[21–26] is used as a molecular rotor and LAURDAN[57,60] as a partitioning dye: both dyes are shown in Figure 2.6. In the present thesis (Figure 2.7), molecular dynamic simulations, along with fluorescent techniques, of molecular models of such probes have been utilized to analyze the location and dynamics of the probes and their effects arising from the perturbation of the lipid membranes.

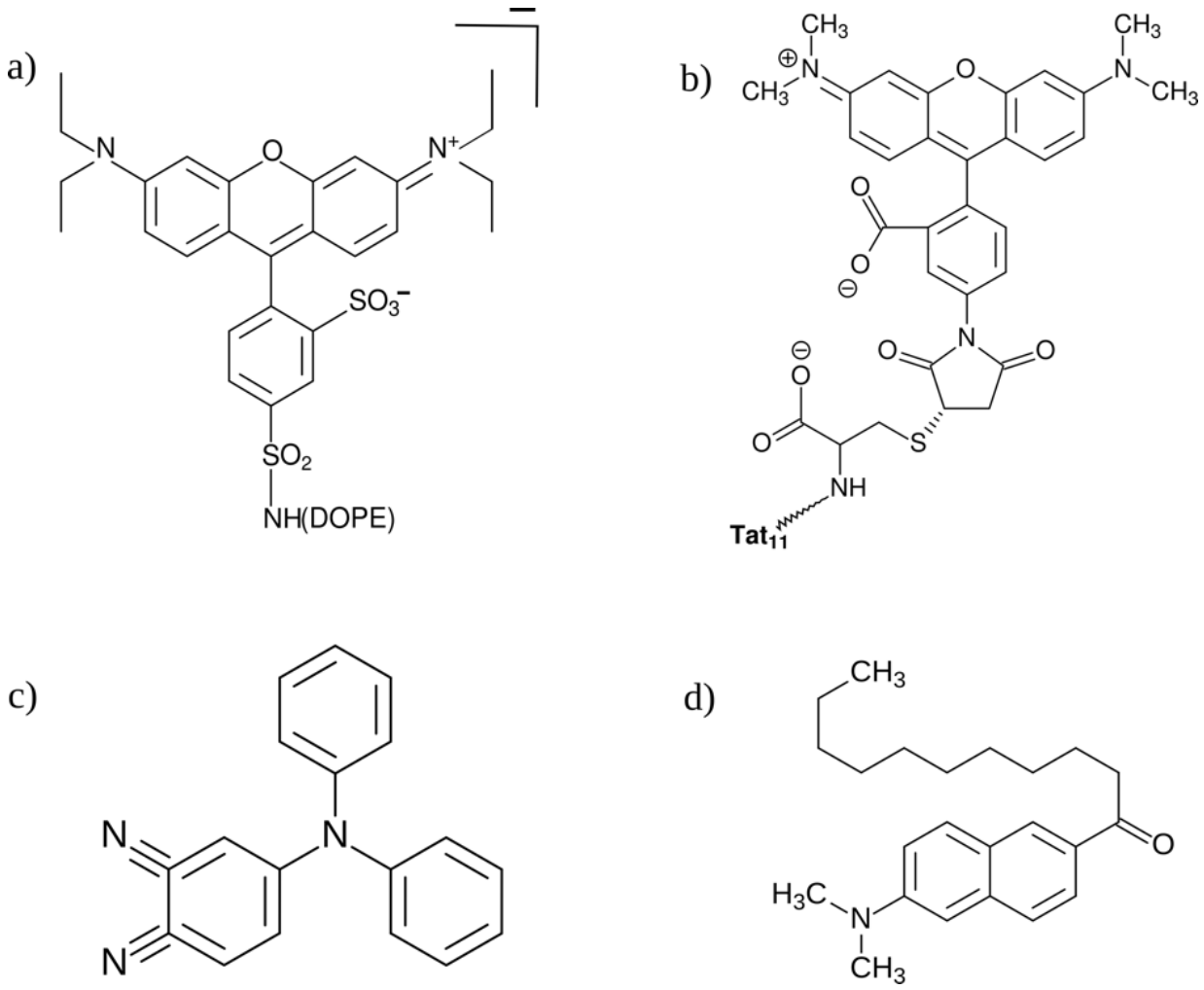

Figure 2.6: structures of probes used in experimental and computational studies mentioned in this thesis, a) Rhodamine B linked to 1,2-dioleoyl-sn-3-phosphatidylehanolamine (RHB) b) tetramethylrhodamine-5-

maleimide (TAMRA) dye c) 4-(diphenylamino)phthalonitrile (DPAP) d) 6-Dodecanoyl-N,N-dimethyl-2-naphthylamine (LAURDAN).

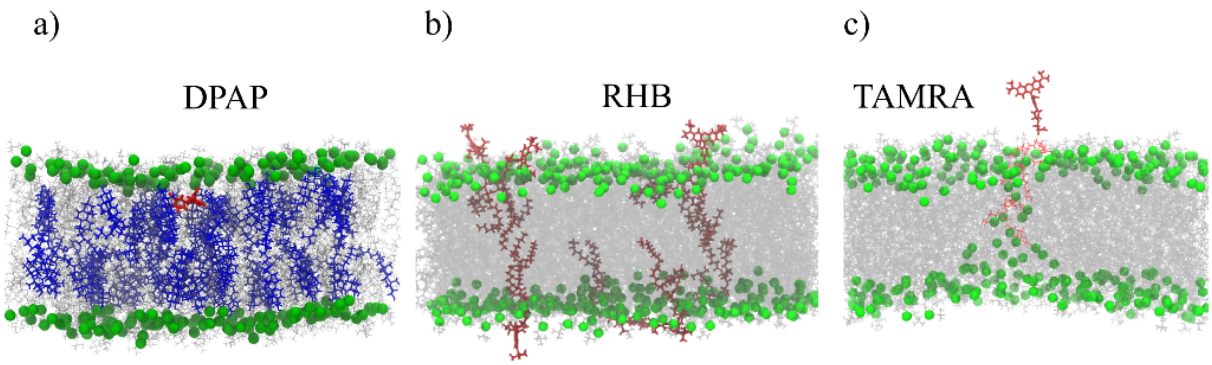

Figure 2.7: Snapshots from atomistic molecular dynamic simulations of different systems with the chromophores. a) DPAP embedded inside the DPPC bilayer containing cholesterol, b) RHB embedded inside DOPC bilayer and c) is TAMRA dye embedded inside the DOPC lipid bilayer.

Constant and speedy advancement in the MD simulations, fluorescent techniques, and the innovation in the development of novel chromophores are providing great help for the detailed understanding of lipid dynamics, in particular, and membrane biophysics, in general. MD simulations often come in handy whenever experiments fail to provide accurate quantification of observables[52] or could not access information at the molecular level. MD also provides an opportunity for membrane biologists to save both time and money otherwise spent on expensive experiments, which can be performed at a more affordable cost through computational approaches. Various experimental observables, e.g. area per lipid, membrane thickness, lipid lateral diffusion, lipid order parameter can be understood well with the help of MD simulations by verifying both probe free and probe related membrane systems.

This thesis is an effort towards understanding the dynamics of lipid membranes and the direct role of fluorescent dyes on the study of lipid membranes. Snapshots from the MD simulations of the dyes within the membrane environment, as used in this thesis work, are shown in Figure 2.7. Studies have been devised to elucidate the role played by the probes inside the lipid bilayer by introducing either structural or dynamical perturbations. In one study, a molecular rotor is

considered, which can sense both viscosity and polarity and can be proved very powerful in studying lipid dynamics in future applications.

Chapter 3 Theoretical and Computational Methods

3.1 Molecular Dynamics Simulations

Molecular dynamics (MD) is the technique through which interactions between molecules and atoms over a period are studied through computer simulations. Such a method is well suited for studying the time evolution of biological molecules while exhibiting the detailed information on the fluctuations and conformational changes of molecular systems like proteins and nucleic acids. Structural validation, dynamics and thermodynamics of complex biological systems are often interpreted by using MD simulations.[61] Alder and Wainwright, while studying the interactions of hard spheres in late 1950s, introduced the molecular dynamics methodology. Rahman and Stillinger in 1974 achieved the first MD simulation of liquid water, while in 1977 the first protein simulations were performed on bovine pancreatic trypsin inhibitor (BPTI).[62] Nowadays, following the improvements in computational power, the number of specialized simulation techniques is tremendously increased for addressing various particular problems. Biological molecules have different dynamical properties, local motions, rigid body motions and large-scale motions which correspond to biological processes occurring at different timescales. Local motions address the atomic fluctuations, side chain motions and loop motions between 10^{-15} s to 10^{-1} s with typical distances in the range 0.01 Å to 5 Å. Rigid body motions falls in the time range of 10^{-9} s to 1 s with the distance travelled between 1 Å to 10 Å, including helix motions, domain motions and subunit motions, whereas large scale motions require generally much longer timescale. For example, they are characterized by helix - coil transitional motions, folding and unfolding of proteins and dissociation or association of the molecules with time ranging between 10^{-7} s to 10^{4} s.[63] There are two main MD methods based on the model and the resulting mathematical formalism one is Molecular mechanics (MM) which deals with the motion of particles within the classical physics instead of quantum

physics and the atoms are dealt as balls and bonds as springs. Unlike quantum mechanics (QM), MM is also less computationally demanding and allows treating molecular systems containing tens of thousands of atoms.

3.2 Statistical Mechanics

Statistical mechanics are required to examine the microscopic level of information that includes atomic positions and velocities to macroscopic level of information that includes pressure, energy, heat capacity. Statistical mechanics is the fundamental step in molecular dynamics simulations studies to achieve these observable level of macroscipic information. Statistical mechanics provides the correlation between microscopic simulations and macroscopic properties [64.] The concept of phase space is often discussed with regards to simulation. Phase space denotes a 6N dimensional space in which there is an axis for every position and every conjugate momentum. A single microstate corresponds to a point in phase space. The time-evolution of a system can be described as a trajectory through phase space. For classical systems, the energy is conserved and the phase space trajectory adheres to a surface of constant energy. Ergodic hypothesis is fundamental to statistical mechanics, the hypothesis states that for a conserved classical system, a particle in some phase state or microstate is equally probable to exist in another phase or microstates. These microstates are collectively called as an ensemble. Therefore ensemble can be defined as the collection of all possible systems which have different microscopic states but have an identical macroscopic or thermodynamic state.

$$\boldsymbol{A_{(ensemble)}= A_{(Time)}} \qquad \textbf{(Eq. 3.1)}$$

There are four major types of ensmemles in statistical mechanics [65] as described below

- Cannonical Ensemble (NVT): the thermodynamic state of cannonical ensemble is characterized by fixed number of atoms N, fixed volume V and a fixed temperature T
- Microcanonical Ensemble (NVE): it is characterized by a fixed number of atoms N, fixed volume V and fixed energy E

- Isobaric-Isothermal Ensemble (NPT): this ensemble is characterized by fixed number of atoms N, fixed pressure P and a fixed temperature T.
- Grand Cannonical Ensemble (mVT): the thermodynamic state for this ensemble is characterized by a fixed chemical potential m, a fixed volume V and a fixed temperature T.

3.2.1 Classical Mechanics, Newton's Second Law of Motion

Classical mechanics is the set of laws of physics more appropriately newton's equation of motion, that describes the motion of bodies under the influence of the applied force. Newton's equation of motion F=ma, where F is the force exerted on the particle, m is its mass and a is the acceleration, is the foundation of the molecular dynamics simulation method. The trajectory produced through integration of equations of motion defines the position, velocities and accelerations of the particles as they vary with time. This information helps to predict the macroscopic state of the system [66–71]. Newton's equation of motion is;

$$F_i = m_i\, a_i \qquad \textbf{(Eq. 3.2)}$$

where F_i is the force exerted on particle i, m_i is the mass of particle i and a_i is the acceleration of particle i. As the acceleration is the second derivative of distance r with respect to time t it can be written as:

$$F_i = m_i \frac{d^2 r_i}{dt^2} \qquad \textbf{(Eq. 3.3)}$$

Change in potential energy V of mass m can be calculated as the distance covered by the application of force F and is given by the equation *(Eq.3.4)*.

$$F_i = -\frac{dV}{dr_i} \qquad \textbf{(Eq. 3.4)}$$

By Combining upper two equations *Eq. 3.3* and *Eq. 3.4* it yields;

$$-\frac{dV}{dr_i} = \frac{d^2 r_i}{dt^2} \quad \textbf{(Eq. 3.5)}$$

To determine the next set of possible coordinates at time t as a function of the acceleration a, using initial position x_0 , and the initial velocity, v_0. Taking the case where the acceleration is constant,

$$a = \frac{dV}{dt} \quad \textbf{(Eq. 3.6)}$$

Expression of velocity is

$$v = at + v_0 \quad \textbf{(Eq. 3.7)}$$

$$v = \frac{dx}{dt} \quad \textbf{(Eq. 3.8)}$$

$$x = v.t + x_0 \quad \textbf{(Eq. 3.9)}$$

Combining this equation with the expression for the velocity, yield

$$x = at^2 + v_0.t + x_0 \quad \textbf{(Eq. 3.10)}$$

3.2.2 Verlet Algorithm

The verlet time integration algorithm [72] is another numerical application of newton's equation of motion, verlet algorithm approximates the positions, velocities and accelerations by a taylor series of expansion.

$$r\,(t+\delta t) = r(t) + v(t)\delta t + \frac{1}{2}\,a(t)\delta t^2 + \cdots$$

$$v\,(t+\delta t) = v(t) + a(t)\delta t + \frac{1}{2}\,b(t)\delta t^2 + \cdots$$

$$a\,(t+\delta t) = a(t) + b(t)\delta t + \cdots \qquad \textbf{(Eq. 3.11)}$$

Where ***r*** is the position, ***v*** is the velocity (the first derivative with respect to time), ***a*** is the acceleration (the second derivative with respect to time), etc.
To derive the verlet algorithm:

$$r\,(t+\delta t) = r(t) + v(t)\delta t + \frac{1}{2}\,a(t)\delta t^2 \qquad \textbf{(Eq. 3.12)}$$

$$r\,(t-\delta t) = r(t) - v(t)\delta t + \frac{1}{2}\,a(t)\delta t^2 \qquad \textbf{(Eq. 3.13)}$$

Summing these two equations will give;

$$r\,(t+\delta t) = 2r(t) - r(t-\delta t) + \,a(t)\delta t^2 \qquad \textbf{(Eq. 3.14)}$$

The Verlet algorithm uses positions and accelerations at time *t* and the positions from time *t-dt* to calculate new positions at time *t+dt.* The Verlet algorithm uses no explicit velocities. The advantages of the Verlet algorithm are, *i)* it is straightforward, and *ii)* the storage requirements are modest. The disadvantage is that the algorithm is of moderate precision.

3.3 Molecular Mechanics

Molecular mechanics is the extension of classical mechanics. It is designed so that by using force fields the potential energy of all the systems are calculated, it can be used to study large biological systems. Force field is used to describe the non bonding electrostatic interactions and van der waals forces and it also determines the time evolution of bond angles, lengths and torsions. The general functional form of force field is:

$$E = E_{non-bonded} + E_{bonded} \quad \textbf{(Eq. 3.15)}$$

$$E = E_{bond} + E_{angle} + E_{dihedral} \quad \textbf{(Eq. 3.16)}$$

$$E_{non-bonded} = E_{electrostatic} + E_{van\ der\ waals} \quad \textbf{(Eq. 3.17)}$$

Bonded terms relate to atoms that are covalently bonded and non bonded specifies the electrostatic and vander waals forces.With the advancement in computational power andthe algorithms these time dependent molecular dynamics simulation techniques can be a great resource for achieving some of the cutting edge results in the field of medicine, and drug discovery by having an in depth and real time molecular simulations of the proteins involved in various neurological disorders, AIDs, Cancer and so many other life threatening diseases. This would elucidate the processes that occur to cause some disease and would provide more specific potential drug targets [73–81]. D.E. Shaw Research in New york has developed supercomputer Anton that is specially designed to achieve MD simulations of proteins and other macromolecules. Through this machine one can achieve the run of about milliseconds, it has vast number of application specific integrated circuits (ASICs). Super computers like anton will help us to achieve larger runs and predict more precise results and help us to study more precisely structure determination, drug designing, protein stability and folding, molecular binding, ion transport and conformational changes.

3.4 Trajectory Analysis

Average area per lipid was obtained by the ratio of the number of lipids in each leaflet to that of the membrane lateral dimension. Membrane thickness was obtained from average distance between the phosphates from upper and lower leaflets.

3.4.1 Radial Distribution Function

Radial distribution function (Rdf) was obtained considering the inter-phosphate coordination within upper and lower leaflets. Rdf characterize the average number of atoms radially packed around each other and is estimated as follows;

$$g(r) = n(r)/\rho\ 4\pi r^2\ \Delta r \qquad \textbf{(Eq. 3.18)}$$

where n(r) the mean number of atoms in the shell of distance r, Δr the width, ρ the mean atom density.

3.4.2 Mean Square Displacement

Diffusion coefficient for lateral lipid diffusion was obtained from mean square displacement of the phosphate atoms. Mean square displacement (MSD) is evaluated as;

$$MSD(t) = < [\, r(t + t') - r(t') \,]^2 >, i.e., < r^2 > \qquad \textbf{(Eq. 3.19)}$$

where < > represents the ensemble average over all the lipid molecules, *r(t)*. Diffusion coefficient was then obtained from the slope of MSD Vs time using the Einstein relation;

$$< r^2 > = 4Dt \qquad \textbf{(Eq. 3.20)}$$

3.4.3 Lipid Order Parameter

Lipid order parameter (SCD) was estimated by considering the average orientation of the methylene groups along the lipid hydrocarbon chain with respect to the membrane normal[82]. It is calculated as;

$$SCD = ½ (3 < cos^2 \Theta CD > -1) \quad \textbf{(Eq. 3.21)}$$

where ΘCD is the angle between each CH bond and the membrane normal (z-axis). Angular brackets < > denotes the ensemble average over time and number of lipid molecule.

3.4.4 Normalized Water Density

We have analyzed the local water density going from bulk solution to the center of the lipid bilayer, along a direction normal to the membrane surface. Local water density was evaluated considering the position of water oxygen atoms in a range of distance between +20 Å and −20 Å with respect to the layer surface (i.e., average P coordinates). In the case of the RHB aggregated system, we applied a further restriction by selecting only the water molecules (i.e., oxygen atoms) falling within a distance of 5 Å from the center of the RHB assembly in the XY plane parallel to the membrane surface, thus analyzing the local water distribution in proximity of the dye assembly.

3.4.5 Pulling Simulation and pulling force analysis

When proteins or drugs cross lipid bilayers, the free energy is obtained vs the distance between drug and bilayer center along membrane normal (z axis). In order to sample the states along this path in a reasonable computational time, the drug has to be forced to fully explore this path. The way is to use a pulling MD simulation also known as steered MD simulation (SMD) with constant velocity pulling, in which the protein is slowly forced by a applying a small constant velocity. The concept behind SMD simulations is that in this type of simulations SMD atom is attached to dummy atom through a virtual spring, the spring moves at constant velocity and the force between the SMD atom and virtual spring is measured using the following equations:

$$F = -\nabla U \quad \textbf{(Eq. 3.22)}$$

$$U = 1/2k[vt - (r - r_o).n]^2 \quad \textbf{(Eq. 3.23)}$$

Where *U* is potential energy, *k* is spring constant, *v* is pulling velocity, *t* is time, *r* is actual position of the SMD atom, r_o is initial position of the SMD atom and *n* is the direction of pulling. In this thesis SMD simulations were carried out on the peptide by gently pulling the center of mass of the peptide along the longitudinal axis i.e z-axis of the pore inside the lipid membrane at a constant velocity of 1 A"ns^{-1}. The pulling force was then averaged in the bins of 2 Å width along the Z-coordinate representing the distance from the center of the pore inside the lipid membrane and then averaged on all the performed SMD simulations of the same system to obtain the averaged pulling force required to break the kinetic energy barrier inside the pore w.r.t to the distance traveled by the peptide.

3.4.6 Average Pore Radius

The average pore radius in this work was measured with the HOLE program [83]. The Hole program requires three inputs 1) the coordinates of the protein of interest 2) an initial point z which can be anywhere in the pore 3) and a user specified vector L that is approximately along the direction of the pore. Hole reads the atoms from within the pdb and sets van der waals radius for each, then the program looks for maximum radius R(z) of a sphere centered at point z without overlapping with the van der waals surface of protein atoms:

$$R(z) = min\, Natom\, [|xi - z| - vdWi] \quad \textbf{(Eq. 3.24)}$$

Where *xi* is the position of the atom number *I , vdWi* is van der waals radius of the atom *I*, and *N* atom is the total number of atoms.

3.4.7 Permeation and Conductance

The number of permeation events were measured with a homemade script, which divided the simulation box in three different main regions, the first one was before the intracellular side of the lipid membrane, the second one was including the selectivity filter and the third one was after the extracellular side of the lipid membrane in the bulk. The first and last two regions were interspaced by buffer regions spanning the areas occupied by the cavity and the interface between the selectivity filter and the bulk solution, respectively. The conductance, C, of K^+ ions, with units in Siemens (S = 1A/1V) defined as the number of electron charges per nanosecond, was calculated by using the conversion factor of 160.217 x N e/ ns, corresponding to 1 pA, and the following equation: Conductance=160.217 x Number of permeation events/time of simulation in ns.

Chapter 4 Insights into the interplay between dye concentration, lipid lateral diffusion and membrane permeability in lipid bilayers

4.1 Introduction

Plasma membrane not only provides the necessary compartmentalization to protect the cell, but is directly involved in a variety of vital cellular processes such as signaling, transport of biomaterial, cell adhesion, etc... [84] To comply with such a variety of roles, the plasma membrane does require a high degree of structural plasticity. Dynamic lateral assembly of lipid/protein complexes combined with a regulated compositional patterning of lipids on both membrane leaflets provide cells with the opportunity to decorate this interface with specific molecules in an organized but dynamic manner. For such reasons, in recent years a great effort has been directed towards the understanding of lipid diffusion and self-organization at a molecular level. Among others, fluorescence-based optical microscopy methods have gradually emerged as versatile, quantitative tools to investigate the complex spatiotemporal organization of lipid membranes in both model bilayers and living cells: both localization-based (e.g. single-particle tracking, SPT) and statistical methods (e.g. fluorescence correlation spectroscopy, FCS), eventually combined with super-resolution approaches, greatly contributed to build the current knowledge on this topic (see, among many, refs. [85–89]).

Irrespective of the particular technique chosen, however, a common requisite for optical microscopy measurements is labelling the molecule of interest with a fluorescent tracer, or probe. In studies on lipids, in particular, optical probes are typically chosen as lipid analogs, [90] such as the dialkylcarbocyanines, or dye-labeled lipids, such as Bodipy, Rhodamine or Atto. [91] In the typical configuration of a comparative study, the measured dynamics of the labeled lipid will depend, and provide information, on several crucial aspects, such as the water content,[92]

the aqueous phase composition (ionic strength and other soluble species, like sugars), the specific lipid composition (i.e. mixture of lipids and/or sterol components) and other physical/mechanical conditions, such as temperature, pressure, membrane tension, etc. Moreover, these investigations will also provide information on the lipid phase, including the possible co-existence of liquid-disordered (L_d), liquid-ordered (L_o) or raft-like domains.

Still, in all these optical microscopy studies, the implicit assumption is made of ignoring the perturbing effect of the probe, based on the consideration that any spurious effect, if present, is irrelevant with respect to the physico-chemical properties under study. While this is perhaps a reasonable assumption to make, especially in comparative studies involving systems of variable chemical compositions, it is worth noting that optical probes have often shown a non-neutral role when tagged to biomolecules, as it was recently reported by some of us in the context of cell-penetrating peptides and their interaction with biomembranes.[93,94] Along the same line, previous studies in which different optical probes have been tested in the same lipid bilayer systems, have reported either different [95,96] or comparable[97] lipid diffusion properties, making the interpretation of the results not always straightforward. Besides, diffusion measurements based on dye-labeled lipids have been shown to depend on lipid bilayer compositions, but also on the dye concentration.[98]

Based on these considerations, it appears desirable to better assess the role of a tracer molecule when exploited for studying lipid diffusion in planar membranes. In this context, molecular dynamics (MD) simulations represent a valuable tool to gather structural and dynamic features of complex biosystems not easily accessible from experiments. [99–101] However, care has to be taken in order to fruitfully exploit MD techniques, since previous studies have highlighted unwanted artifacts due to the limited timescale and the typical finite size of the atomistic models. For example, local lipid diffusion was shown to be affected by the system size in small bilayer models [102–104] and displayed anomalous (non-Brownian) behavior when evaluated at short timescales (i.e., 1-10 ns). [105] Thus, here we propose a combination of FCS experiments and extended atomistic MD simulations to shed lights on some important features concerning lipid dynamics and lipid structural properties within a simple 1,2-dioleoyl-sn-glycero-3-phosphocholine (DOPC) bilayer.

Through such an integrated approach, our study attempts at better assessing the possible direct and indirect effects of a typical dye-labelled lipid, here Rhodamine B linked to 1,2-dioleoyl-sn-3-phosphatidylehanolamine (hereafter referred to as RHB, see scheme of the molecule in

Figure 4.1a), on the estimation of the lipid diffusion coefficient in a planar membrane. To this end, giant unilamellar vesicles (GUVs) of DOPC with increasing concentration of RHB (from 10-4 % to 10%) have been produced, since they are considered a more realistic membrane model than supported lipid bilayers (SLBs), and an in silico molecular model of up to 400 lipids has been considered in our complementary computational investigation, see Figure 4.1b,c. In particular, we evaluated the hydrodynamic effect of the Rhodamine B fluorophore and investigated the effects of RHB concentration on the structural and dynamic properties of the lipid bilayer. Results have shown a non-negligible role of the tracer molecule, which induced a decrease of about 20% in the observed lipid lateral diffusion with respect to the unlabeled species. Moreover, we have characterized the effect of the dye-driven RHB self-aggregation with concentration and the relevant impact that the formed dye-labeled lipid clusters (Figure 4.1d,e) have on both membrane structure and permeability.

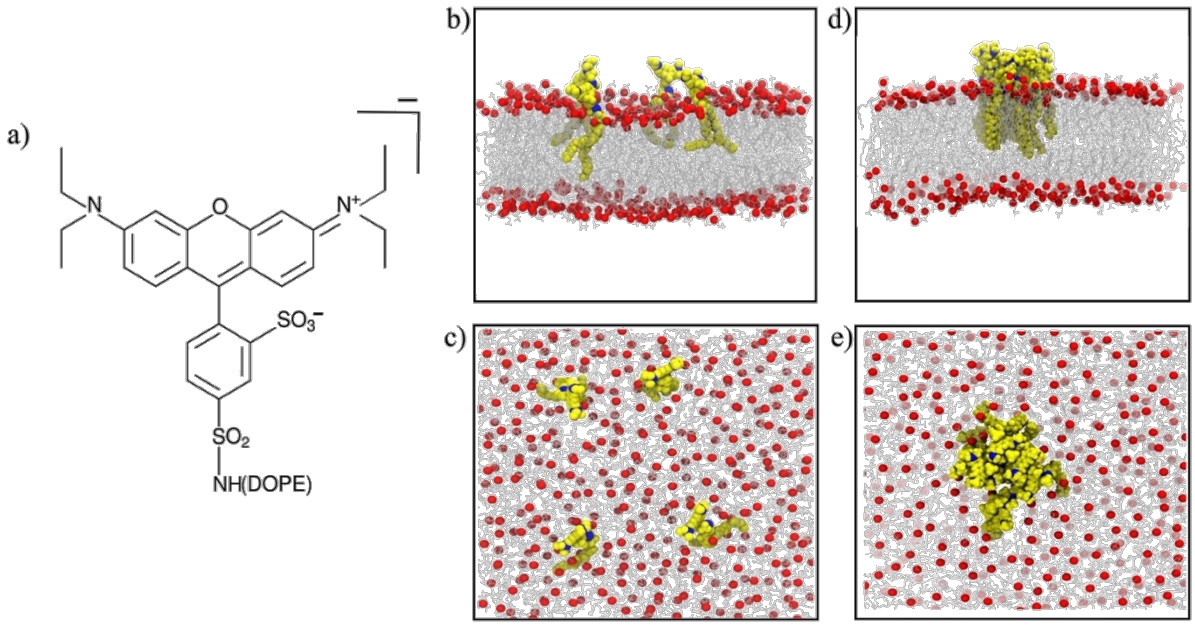

Figure 4.1: a) Scheme of the RHB lipid. b) Side and c) top view of a MD simulation snapshot of the RHB-DOPC lipid bilayer. d) Side and e) top view of a MD simulation snapshot of the RHB-DOPC bilayer displaying RHB self-aggregation. RHB lipids are shown in yellow, with nitrogen in blue, while DOPC lipids are in gray with corresponding phosphate atoms in red; water is omitted for clarity.

4.2 Computational Details

4.2.1 Molecular models of DOPC and dye-labelled lipid

Starting structure for pure DOPC membrane bilayer was obtained from a pre-equilibrated system, using CHARMM-GUI server. [106] The bilayer consisted of 400 lipids (200 per leaflet) and extended up to ~125 Å along its lateral dimensions (XY plane). The system was then solvated with TIP3P water up to 30 Å from the bilayer along the normal to the membrane surface (Z-axis). Rhodamine B structure was initially generated with the Chimera software.[107] The starting geometry was optimized by quantum mechanical calculations using the B3LYP/6-31+G(d,p) level of theory using Gaussian09 [108], while partial charges were derived from molecular electrostatic potential obtained using the HF/6-31G(d) level of theory in vacuum. The latter generally provides effectively "polarized" charges more suitable for modeling complex systems in the condensed phase without resorting on computationally demanding calculations of molecular polarization.[109] Note, also, that small deviations were observed when partial charges were computed using either B3LYP or including solvent effects through the Polarizable Continuum Model[110] (mean absolute error < 0.1). Besides, in the present work we have neglected the possible electronic rearrangement occurring in the excited state of the dye,[111] assuming that, once tagged to the lipid, its orientation within the bilayer and diffusive dynamics would not be particularly affected. Rhodamine B was then attached to the lipid according to Figure 4.1a in order to build a RHB molecular model. Note that the overall charge of the molecule is -1e, since the phosphate group of the lipid is not compensated by the Rhodamine B headgroup. Forcefield parameters for the so obtained dye-labeled lipid were adapted from CHARMM general force field (CGenFF) [112] for a small molecule (RHB force field details are provided in Table 4.1). On the other hand, RHB lipid tail parameters were borrowed from the corresponding standard DOPC CHARMM parameters, being the two structures chemically equivalent. Eight RHB lipid molecules (4 per leaflet) were then embedded into a well-equilibrated pure DOPC bilayer, previously created as described above, by replacing a corresponding number of DOPC lipids at random locations. The final structure had 196 DOPC and 4 RHB molecules in each membrane leaflet. Water molecules in close contact with the RHB headgroup were deleted and an additional water layer (extending up to ~20 Å) was added along the Z-dimension to build up the final system (box edges: 117x117x92

Å^3, water thickness: ~54 Å). Eight sodium ions were added to keep the system electrically neutral. The RHB-DOPC bilayer is depicted in Figure 4.1b,c. Four different replicas of the RHB-DOPC system were produced by regenerating the velocities in each system replica. In addition, one more RHB-DOPC system was created from one of the above replicas with a salt concentration of 0.5 M NaCl. In all cases, force field included NBFIX terms for sodium and chloride ions.[113]

Table 4.1: List of atoms of the RHB lipid model reporting atom types and atomic charges.

```
* ----------------------------------------------------------------------------- *
*       CGenFF: Topology for the Charmm General Force Field v. 2b7              *
*               for Small Molecule Drug Design                                  *
* ----------------------------------------------------------------------------- *
*
36  1
! ----------------------------------------------------------------------------- !


RESI RHB
GROUP

ATOM S1f        SG3O2        1.100
ATOM O1f        OG2P1       -0.570
ATOM O2f        OG2P1       -0.570
ATOM C1f        CG2R61      -0.150
ATOM C2f        CG2R61       0.020
ATOM H3f        HGR61        0.150
ATOM C3f        CG2R61      -0.290
ATOM H4f        HGR61        0.090
ATOM C4f        CG2R67       0.310
ATOM C5f        CG2R61      -0.140
ATOM C6f        CG2R61      -0.060
ATOM H5f        HGR61        0.150
ATOM S2f        SG3O1        1.100
ATOM O3f        OG2P1       -0.700
ATOM O4f        OG2P1       -0.700
ATOM O5f        OG2P1       -0.700
ATOM C7f        CG2R67       0.330
ATOM C8f        CG2R61      -0.300
ATOM C9f        CG2R61       0.610
ATOM O6f        OG3R60      -0.430
ATOM C10f       CG2R61       0.610
ATOM C11f       CG2R61      -0.300
ATOM C12f       CG2DC1       0.160
ATOM H6f        HGA4         0.08
ATOM C13f       CG2DC1      -0.460
ATOM H7f        HGA4         0.210
ATOM C14f       CG2DC2       0.640
ATOM C15f       CG2DC1      -0.640
ATOM H8f        HGA4         0.250
ATOM N2f        NG2P1       -0.50
ATOM C16f       CG324        0.23
ATOM H9f        HGA2         0.01
```

```
ATOM H10f        HGA2         0.01
ATOM C17f        CG331       -0.270
ATOM H11f        HGA3         0.090
ATOM H12f        HGA3         0.090
ATOM H13f        HGA3         0.090
ATOM C18f        CG324        0.23
ATOM H14f        HGA2         0.01
ATOM H15f        HGA2         0.01
ATOM C19f        CG331       -0.270
ATOM H16f        HGA3         0.090
ATOM H17f        HGA3         0.090
ATOM H18f        HGA3         0.090
ATOM C20f        CG2R61       0.160
ATOM H19f        HGR61        0.08
ATOM C21f        CG2R61      -0.460
ATOM H20f        HGR61        0.210
ATOM C22f        CG2R61       0.640
ATOM C23f        CG2R61      -0.640
ATOM H21f        HGR61        0.250
ATOM N3f         NG301       -0.50
ATOM C24f        CG321        0.23
ATOM H22f        HGA2         0.01
ATOM H23f        HGA2         0.01
ATOM C25f        CG331       -0.270
ATOM H24f        HGA3         0.090
ATOM H25f        HGA3         0.090
ATOM H26f        HGA3         0.090
ATOM C26f        CG321        0.23
ATOM H27f        HGA2         0.01
ATOM H28f        HGA2         0.01
ATOM C27f        CG331       -0.270
ATOM H29f        HGA3         0.090
ATOM H30f        HGA3         0.090
ATOM H31f        HGA3         0.090

! Polar Head and glycerol backbone
GROUP               !

ATOM N    NH3L  -0.670 !          HN2
!ATOM HN1  HCL    0.33 !           |
!ATOM HN2  HCL    0.33 !  (+) HN1---N---HN3
ATOM HN3  HCL    0.350 !           |
ATOM C12  CTL2   0.100 !           |
ATOM H12A HAL2   0.090 !     H12A--C12---H12B
ATOM H12B HAL2   0.090 !        |
GROUP               !           |     alpha5
ATOM C11  CTL2  -0.08 !           |
ATOM H11A HAL2   0.09 !     H11A--C11---H11B
ATOM H11B HAL2   0.09 !           |     alpha4
ATOM P    PL     1.50 !   (-) O13  O12
ATOM O13  O2L   -0.78 !        \ /      alpha3
ATOM O14  O2L   -0.78 !         P (+)
ATOM O11  OSLP  -0.57 !        / \      alpha2
ATOM O12  OSLP  -0.57 !   (-) O14  O11
ATOM C1   CTL2  -0.08 !           |     alpha1
ATOM HA   HAL2   0.09 !       HA---C1---HB
ATOM HB   HAL2   0.09 !           |     theta1
```

```
GROUP              !                    |
ATOM C2   CTL1   0.17 !      HS---C2- - - - - - -
ATOM HS   HAL1   0.09 !          | beta1       |
ATOM O21  OSL   -0.49 !      O22  O21         theta3
ATOM C21  CL     0.90 !       \\ /  beta2       |
ATOM O22  OBL   -0.63 !         C21
ATOM C22  CTL2  -0.22 !         |   beta3       |
ATOM H2R  HAL2   0.09 !   H2R---C22---H2S
ATOM H2S  HAL2   0.09 !         |              |
GROUP              !            beta4
ATOM C3   CTL2   0.08 !         |              |
ATOM HX   HAL2   0.09 !                  HX---C3---HY
ATOM HY   HAL2   0.09 !         |              |   gamma1
ATOM O31  OSL   -0.49 !                  O32  O31
ATOM C31  CL     0.90 !         |          \\ /    gamma2
ATOM O32  OBL   -0.63 !                     C31
ATOM C32  CTL2  -0.22 !         |           |    gamma3
ATOM H2X  HAL2   0.09 !                  H2X---C32---H2Y
ATOM H2Y  HAL2   0.09 !         |           |
GROUP              !                        gamma4
ATOM C23  CTL2  -0.18 !         |           |
ATOM H3R  HAL2   0.09 !   H3R ---C23---H3S     |
ATOM H3S  HAL2   0.09 !         |           |
GROUP              !         |           |
ATOM C24  CTL2  -0.18 !         |           |
ATOM H4R  HAL2   0.09 !   H4R ---C24---H4S     |
ATOM H4S  HAL2   0.09 !         |           |
GROUP              !         |           |
ATOM C25  CTL2  -0.18 !         |           |
ATOM H5R  HAL2   0.09 !   H5R ---C25---H5S     |
ATOM H5S  HAL2   0.09 !         |           |
GROUP              !         |           |
ATOM C26  CTL2  -0.18 !         |           |
ATOM H6R  HAL2   0.09 !   H6R ---C26---H6S     |
ATOM H6S  HAL2   0.09 !         |           |
GROUP              !         |           |
ATOM C27  CTL2  -0.18 !         |           |
ATOM H7R  HAL2   0.09 !   H7R ---C27---H7S     |
ATOM H7S  HAL2   0.09 !         |           |
GROUP              !         |           |
ATOM C28  CTL2  -0.18 !         |           |
ATOM H8R  HAL2   0.09 !   H8R ---C28---H8S     |
ATOM H8S  HAL2   0.09 !         |           |
GROUP              !         |           |
ATOM C29  CEL1  -0.15 !         |           |
ATOM H9R  HEL1   0.15 !   H9R ---C29          |
GROUP              !         || (CIS)      |
ATOM C210 CEL1  -0.15 !         ||          |
ATOM H10R HEL1   0.15 !   H10R---C210         |
GROUP              !         |           |
ATOM C211 CTL2  -0.18 !         |           |
ATOM H11R HAL2   0.09 !   H11R---C211--H11S    |
ATOM H11S HAL2   0.09 !         |           |
GROUP              !         |           |
ATOM C212 CTL2  -0.18 !         |           |
ATOM H12R HAL2   0.09 !   H12R---C212--H12S    |
ATOM H12S HAL2   0.09 !         |           |
```

```
GROUP              !        |           |
ATOM C213 CTL2  -0.18 !        |           |
ATOM H13R HAL2   0.09 !   H13R---C213--H13S    |
ATOM H13S HAL2   0.09 !        |           |
GROUP              !        |           |
ATOM C214 CTL2  -0.18 !        |           |
ATOM H14R HAL2   0.09 !   H14R---C214--H14S    |
ATOM H14S HAL2   0.09 !        |           |
GROUP              !        |           |
ATOM C215 CTL2  -0.18 !        |           |
ATOM H15R HAL2   0.09 !   H15R---C215--H15S    |
ATOM H15S HAL2   0.09 !        |           |
GROUP              !        |           |
ATOM C216 CTL2  -0.18 !        |           |
ATOM H16R HAL2   0.09 !   H16R---C216--H16S    |
ATOM H16S HAL2   0.09 !        |           |
GROUP              !        |           |
ATOM C217 CTL2  -0.18 !        |           |
ATOM H17R HAL2   0.09 !   H17R---C217--H17S    |
ATOM H17S HAL2   0.09 !        |           |
GROUP              !        |           |
ATOM C218 CTL3  -0.27 !        |           |
ATOM H18R HAL3   0.09 !   H18R---C218--H18S    |
ATOM H18S HAL3   0.09 !        |           |
ATOM H18T HAL3   0.09 !       H18T          |
GROUP              !                    |
ATOM C33  CTL2  -0.18 !                        |
ATOM H3X  HAL2   0.09 !              H3X ---C33---H3Y
ATOM H3Y  HAL2   0.09 !                        |
GROUP              !                    |
ATOM C34  CTL2  -0.18 !                        |
ATOM H4X  HAL2   0.09 !              H4X ---C34---H4Y
ATOM H4Y  HAL2   0.09 !                        |
GROUP              !                    |
ATOM C35  CTL2  -0.18 !                        |
ATOM H5X  HAL2   0.09 !              H5X ---C35---H5Y
ATOM H5Y  HAL2   0.09 !                        |
GROUP              !                    |
ATOM C36  CTL2  -0.18 !                        |
ATOM H6X  HAL2   0.09 !              H6X ---C36---H6Y
ATOM H6Y  HAL2   0.09 !                        |
GROUP              !                    |
ATOM C37  CTL2  -0.18 !                        |
ATOM H7X  HAL2   0.09 !              H7X ---C37---H7Y
ATOM H7Y  HAL2   0.09 !                        |
GROUP              !                    |
ATOM C38  CTL2  -0.18 !                        |
ATOM H8X  HAL2   0.09 !              H8X ---C38---H8Y
ATOM H8Y  HAL2   0.09 !                        |
GROUP              !                    |
ATOM C39  CEL1  -0.15 !                        |
ATOM H9X  HEL1   0.15 !              H9X ---C39
GROUP              !                    ||
ATOM C310 CEL1  -0.15 !                         ||
ATOM H10X HEL1   0.15 !               H10X---C310
GROUP              !                    |
ATOM C311 CTL2  -0.18 !                        |
```

```
ATOM H11X HAL2   0.09 !              H11X---C311--H11Y
ATOM H11Y HAL2   0.09 !                   |
GROUP            !                  |
ATOM C312 CTL2  -0.18 !                 |
ATOM H12X HAL2   0.09 !              H12X---C312--H12Y
ATOM H12Y HAL2   0.09 !                   |
GROUP            !                  |
ATOM C313 CTL2  -0.18 !                 |
ATOM H13X HAL2   0.09 !              H13X---C313--H13Y
ATOM H13Y HAL2   0.09 !                   |
GROUP            !                  |
ATOM C314 CTL2  -0.18 !                 |
ATOM H14X HAL2   0.09 !              H14X---C314--H14Y
ATOM H14Y HAL2   0.09 !                   |
GROUP            !                  |
ATOM C315 CTL2  -0.18 !                 |
ATOM H15X HAL2   0.09 !              H15X---C315--H15Y
ATOM H15Y HAL2   0.09 !                   |
GROUP            !                  |
ATOM C316 CTL2  -0.18 !                 |
ATOM H16X HAL2   0.09 !              H16X---C316--H16Y
ATOM H16Y HAL2   0.09 !                   |
GROUP            !                  |
ATOM C317 CTL2  -0.18 !                 |
ATOM H17X HAL2   0.09 !              H17X---C317--H17Y
ATOM H17Y HAL2   0.09 !                   |
GROUP            !                  |
ATOM C318 CTL3  -0.27 !                 |
ATOM H18X HAL3   0.09 !              H18X---C318--H18Y
ATOM H18Y HAL3   0.09 !                   |
ATOM H18Z HAL3   0.09 !                  H18Z

! Bond order

BOND S1f    O1f    S1f    O2f    S1f    C1f
BOND C1f    C2f    C1f    C6f
BOND C2f  H3f
BOND C2f  C3f
BOND C3f  H4f
BOND C3f  C4f
BOND C4f  C5f
BOND C4f  C7f
BOND C5f  C6f
BOND C5f  S2f
BOND C6f  H5f
BOND S2f  O3f
BOND S2f  O4f
BOND S2f  O5f
BOND C7f  C8f
BOND C7f  C11f
BOND C8f  C9f
BOND C8f  C12f
BOND C9f  O6f
BOND C9f  C15f
BOND O6f  C10f
BOND C10f C11f
BOND C10f C23f
```

```
BOND C11f C20f
BOND C12f H6f
BOND C12f C13f
BOND C13f H7f
BOND C13f C14f
BOND C14f C15f
BOND C14f N2f
BOND C15f H8f
BOND N2f  C16f
BOND N2f  C18f
BOND C16f H9f
BOND C16f H10f
BOND C16f C17f
BOND C17f H11f
BOND C17f H12f
BOND C17f H13f
BOND C18f H14f
BOND C18f H15f
BOND C18f C19f
BOND C19f H16f
BOND C19f H17f
BOND C19f H18f
BOND C20f H19f
BOND C20f C21f
BOND C21f H20f
BOND C21f C22f
BOND C22f C23f
BOND C22f N3f
BOND C23f H21f
BOND N3f  C24f
BOND N3f  C26f
BOND C24f H22f
BOND C24f H23f
BOND C24f C25f
BOND C25f H24f
BOND C25f H25f
BOND C25f H26f
BOND C26f H27f
BOND C26f H28f
BOND C26f C27f
BOND C27f H29f
BOND C27f H30f
BOND C27f H31f


! CONNECT FLUOROPHORE TO DOPE

BOND S1f   N

! Polar headgroup

BOND  N     HN3       N    C12
BOND  C12  H12A      C12  H12B      C12  C11
BOND  C11  H11A      C11  H11B      C11  O12
BOND  O12  P         P    O11       P    O13       P    O14

! Glycerol backbone
```

```
BOND  C1   HA      C1   HB     C1   C2      C1   O11
BOND  C2   HS      C2   C3     C2   O21
BOND  C3   HX      C3   HY     C3   O31

! Chain from C2

BOND  O21  C21
BOND  C21  C22
DOUBLE  C21  O22
BOND  C22  H2R     C22  H2S     C22  C23
BOND  C23  H3R     C23  H3S     C23  C24
BOND  C24  H4R     C24  H4S     C24  C25
BOND  C25  H5R     C25  H5S     C25  C26
BOND  C26  H6R     C26  H6S     C26  C27
BOND  C27  H7R     C27  H7S     C27  C28
BOND  C28  H8R     C28  H8S     C28  C29
BOND  C29  H9R
DOUBLE  C29 C210
BOND  C210 H10R    C210 C211
BOND  C211 H11R    C211 H11S    C211 C212
BOND  C212 H12R    C212 H12S    C212 C213
BOND  C213 H13R    C213 H13S    C213 C214
BOND  C214 H14R    C214 H14S    C214 C215
BOND  C215 H15R    C215 H15S    C215 C216
BOND  C216 H16R    C216 H16S    C216 C217
BOND  C217 H17R    C217 H17S    C217 C218
BOND  C218 H18R    C218 H18S    C218 H18T

! Chain from C3

BOND  O31  C31
BOND  C31  C32
DOUBLE  C31  O32
BOND  C32  H2X     C32  H2Y     C32  C33
BOND  C33  H3X     C33  H3Y     C33  C34
BOND  C34  H4X     C34  H4Y     C34  C35
BOND  C35  H5X     C35  H5Y     C35  C36
BOND  C36  H6X     C36  H6Y     C36  C37
BOND  C37  H7X     C37  H7Y     C37  C38
BOND  C38  H8X     C38  H8Y     C38  C39
BOND  C39  H9X
DOUBLE C39 C310
BOND  C310 H10X    C310 C311
BOND  C311 H11X    C311 H11Y    C311 C312
BOND  C312 H12X    C312 H12Y    C312 C313
BOND  C313 H13X    C313 H13Y    C313 C314
BOND  C314 H14X    C314 H14Y    C314 C315
BOND  C315 H15X    C315 H15Y    C315 C316
BOND  C316 H16X    C316 H16Y    C316 C317
BOND  C317 H17X    C317 H17Y    C317 C318
BOND  C318 H18X    C318 H18Y    C318 H18Z

IMPR C14f  C13f  C15f  N2f
IMPR C21 O21 C22 O22  C31 O31 C32 O32

END
```

4.2.2 Molecular model of an aggregated cluster of dye-labeled lipids

Moreover, we generated a molecular model of an aggregated cluster of RHB lipids within a DOPC bilayer (i.e., RHB^{Agg}-DOPC). Initially, a well-equilibrated RHB-DOPC configuration was taken, and at the center of one leaflet (i.e., upper leaflet) eight RHB lipids were introduced in a stacked configuration, while keeping four RHB lipids in the other (lower) leaflet at random locations. DOPC lipids showing clash contacts with any RHB molecules were removed. The overall RHB aggregated system had: 8 RHB (forming a cluster) and 182 DOPC molecules in the upper layer, 4 RHB (randomly distributed) and 186 DOPC molecules in the lower layer. Counterions were also added to neutralize the overall electric charge of the system. The initial system configuration was then relaxed following the simulation protocol described below. A molecular representation of the system is shown in Figure 4.1d,e.

4.2.3 Molecular dynamic simulation parameters

All simulations were performed in NAMD 2.10 [114] using CHARMM36 [115] force field for lipids under periodic boundary condition. Bonds involving hydrogens were restrained using SHAKE,[116] which permitted the usage of a 2 fs time step for numerical integration. Long-range electrostatic interactions were calculated using the Particle Mesh Ewald (PME) algorithm[117], while dispersion interactions were calculated with a cutoff of 12 Å, applying a smoothing functions beyond 10 Å. All production MD simulations were performed in a NPT ensemble with a constant pressure of 1 atm and a temperature of 303 K, using a langevin thermostat and barostat for pressure and temperature coupling, respectively[118]**.** All simulations were performed with a cell box constant-ratio constraint, which allows to keep the ratio of the unit cell constant in X and Y axis while allows fluctuation along all three dimensions. Prior to production phase, all systems were subject to a short round of energy minimization and system density equilibration (1000 steps of steepest-descent minimization and about 50 ns of MD equilibration). After equilibration, all MD simulations were carried out for about 200 ns, except the four RHB-DOPC replica system, for which we collected about 100 ns each. For the aggregated RHB system, an initial NpT simulation was performed while applying harmonic

position restraints on the headgroups of the RHB lipids for about 30 ns. In order to speed up the aggregation process and create a RHB cluster not biased towards a specific configuration, we applied a harmonic restraint to the radius of gyration (Rg) of the eight Rhodamine B headgroups in the upper layer, using the collective variable module of NAMD (force constant 1 kcal/mol $Å^{-1}$, Rg 1.0 nm), thus obtaining an equilibrated RHB cluster as shown in Figure 4.1d,e.

4.2.4 Data analysis

FCS and spectra measurements were carried out on an Olympus FluoView FV-1000 inverted confocal microscope with a 60x water immersion objective (NA: 1.20). LAURDAN was imaged at 780 nm with two-photon excitation using a Titanium-Sapphire laser (Chameleon; Coherent, USA). The emission signal was collected in the 410-510 nm range. RHB was excited using a laser at 543 nm and the emission signal was collected in the range 550-650 nm. The emission spectrum of RHB was collected from 550 to 640 nm with a detection bandwidth of 2 nm and number of steps 42. The photomultipliers were set in the photon-counting detection mode. The Generalized Polarization (GP) measurement was performed on a Zeiss LSM 800 inverted confocal microscope equipped with two GaAsP detectors using a 63x oil immersion objective (NA 1.40). LAURDAN was excited at 405 nm. Then its emission was split by a dichroic mirror (with cutoff at 470 nm) into two detectors set to collect fluorescence in the 400-470 nm and 470-540 nm range, respectively. The emission spectrum of LAURDAN partially overlaps with the adsorption spectrum of Rhodamine B and Fluorescence Resonance Energy Transfer (FRET) may occur. In order to suppress FRET contribution to the measured GP, the acceptor Rhodamine B was photobleached before LAURDAN measurements. FCS measurements were analyzed with simFCS software (www.lfd.uci.edu, University of California Irvine). GP was calculated from the emission of the two channels using the following equation[119] :

$$GP = \frac{I_{440} - I_{490}}{I_{440} + I_{490}} \qquad \textbf{(Eq. 4.1)}$$

Dynamics of the pure (DOPC) and modified (RHB) lipid bilayers have been characterized via a number of properties such as i) area per lipid (ApL), ii) membrane thickness, iii) radial

distribution function (RDF), iv) diffusion coefficient (D), and v) lipid order parameters (S_{CD}), using in-house developed codes based on the MDAnalysis library[120] or available analysis tools in Gromacs[121] and Amber[121,122] software. Average area per lipid (ApL) was obtained from the average area of the membrane surface (i.e., XY plane) divided by the total number of lipids in each layer. Membrane thickness was obtained from the average distance between the phosphate groups belonging to the upper and lower leaflets. Radial distribution functions (RDF) were evaluated by considering the interatomic distances of the P atoms belonging to the phosphate groups of either DOPC or RHB, performing distinct analyses on each leaflet and then averaging the results. Diffusion coefficient for lateral lipid diffusion was obtained from the mean square displacement (MSD) of the phosphate atoms, removing the effect of the center of mass motion of the entire system, using the Einstein relation:

$$MSD(t) = 4Dt \qquad \textbf{(Eq. 4.2)}$$

$\mathrm{MSD}(t) = 4Dt$

and performing a linear fitting of the MSD data on the time interval between 11 and 50 ns. Deuterium order parameter (S_{CD}) was evaluated by considering the average orientation of the methylene groups along the lipid hydrocarbon chains with respect to the membrane normal [82], and computed as:

$$SCD = ½\,(3 < cos^2\Theta CD > -1) \qquad \textbf{(Eq. 4.3)}$$

where ΘCD is the angle between each CH bond and the normal to the membrane (Z-axis), and angular brackets denote an average over all lipids and ensemble configurations. Uncertainties in the estimates of the above properties were evaluated as standard errors from multiple partitions (i.e., 8) of the simulated trajectories. In case of RHB-DOPC simulations, standard errors were computed by considering separately the upper and lower leaflets in all replica simulations.

4.3 Results

4.3.1 Structural properties of the RHB-DOPC bilayer

Structural properties of the DOPC membrane upon insertion of a dye-labelled lipid were investigated using atomistic MD simulations. A membrane with concentration of 2% RHB (corresponding to 8 lipids over a total of 400 lipids, 4 in each leaflet) was generated as described in the Methods. First, we evaluated the membrane thickness and the average area per lipid as compared to the pristine DOPC membrane. Bilayer thickness was defined as the average distance between phosphate head groups of both leaflets. Average thickness of the pure DOPC system was found to be 38.6 Å (Table 4.2), in well agreement with previous experiments (36.7-38.5 Å [105,123,124]), and displaying no significant difference with respect to the Rhodamine B-labeled bilayer: all RHB-DOPC systems have shown a membrane thickness of about 38 Å. Average area per lipid (ApL) is the most common determining feature in the packing of the lipid bilayer and structure. Pure DOPC system provided ApL of 68.2 $Å^2$, close to recent experimental data and well within previously reported measurements at similar temperature (67.4 – 72.5 $Å^2$ [123–125]). On the other hand, RHB-DOPC systems have shown a slight increase in ApL (about 69 $Å^2$). Area per lipid and membrane thickness for all systems are reported in Table 4.2.

Table 4.2: Structural and dynamical properties of the DOPC and RHB-DOPC bilayer systems as issuing from corresponding MD simulations.

System	ApL (Å^2)	Thickness (Å)	D^{DOPC} ($\mu m^2 s^{-1}$)	D^{RHB} ($\mu m^2 s^{-1}$)
DOPC	68.2 ± 0.8	38.6 ± 0.4	8.4 ± 0.4	-
RHB-DOPC (Average over 4 replica)	69.2 ± 0.8	38.2 ± 0.4	7.8 ± 0.4	6.7 ± 0.7
RHB-DOPC (NaCl 0.5M)	67.7 ± 0.8	38.5 ± 0.4	7.7 ± 0.7	6.0 ± 2.1
RHB^{Agg}-DOPC (RHB self-aggregation)	68.7 ± 0.8	37.9 ± 0.4	8.7 ± 1.0	4.0 ± 1.2

Moreover, radial distribution functions (RDFs) of both native DOPC and Rhodamine B-labelled lipid were evaluated considering the common phosphate group (i.e. P atom). Results are reported in Figure 4.2a,b. RDFs show two main peaks and a less pronounced third peak corresponding to successive lipid shells, where the first shell extends from 6.0 to 7.5 Å and the second one from 8.2 to 10 Å. Positions of the first two RDF peaks, which determine the probability of finding phosphate groups in the neighboring shells, are consistent throughout all lipid membrane simulations, although peak height is somewhat different in the two simulations as a result of local lipid rearrangements upon RHB insertion: in terms of P-P RDF, the lipid bilayer appears less structured around RHB lipids. Note, however, that RHB-DOPC results are

affected by larger noise with respect to DOPC ones, owing to poorer statistics (i.e., RHB lipids are two orders of magnitude less than DOPC lipids).

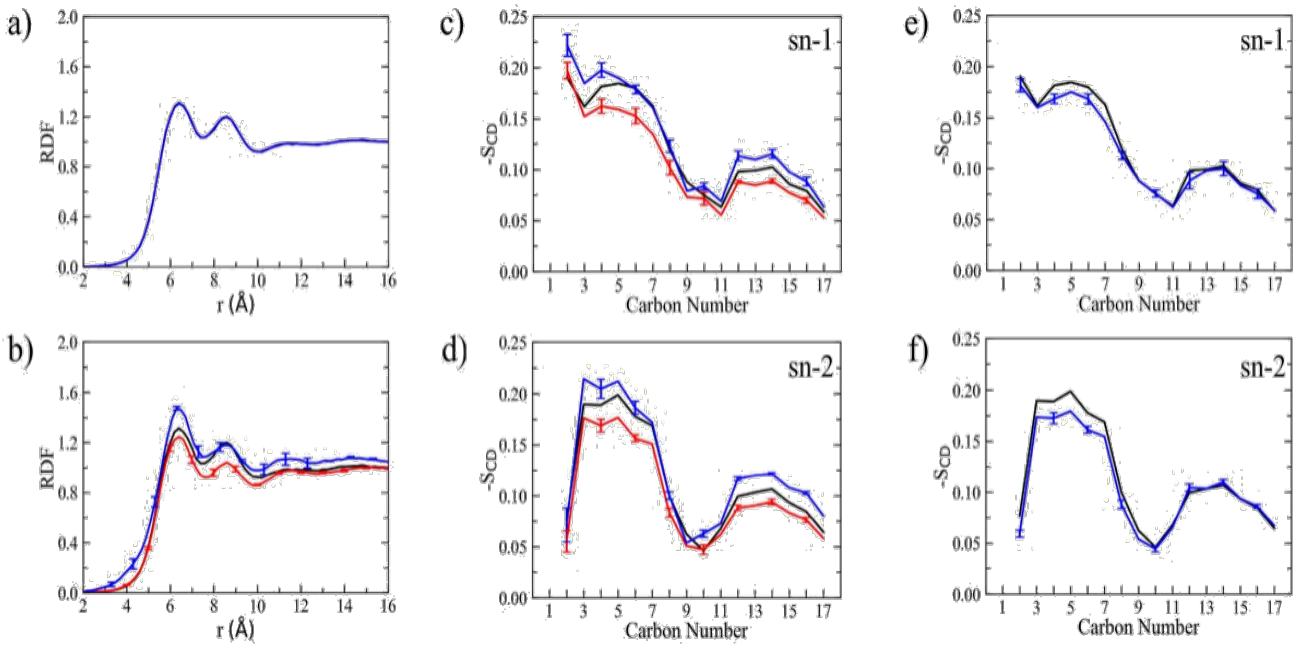

Figure 4.2: a) P-P radial distribution functions (RDFs) obtained considering only DOPC-DOPC pairs as issuing from MD simulations of DOPC (black), RHB-DOPC (red) and RHBAgg-DOPC (blue, RHB self-aggregation) lipid bilayers. b) P-P RDFs obtained from DOPC (black, DOPC-DOPC pairs), RHB-DOPC (red, RHB-DOPC pairs) and RHBAgg-DOPC (blue, RHBAgg-DOPC pairs) bilayer simulations. c,d) Deuterium order parameters (SCD) evaluated for lipid acyl chains (i.e., sn-1 and sn-2) as issuing from MD simulations of DOPC (black, DOPC lipids), RHB-DOPC (red, RHB lipids) and RHBAgg-DOPC (blue, RHBAgg lipids) lipid bilayers. e,f) Deuterium order parameters (SCD) from MD simulations of DOPC (black, DOPC lipids) and RHBAgg-DOPC (blue, only DOPC lipids within 5 Å from any RHBAgg lipid) lipid bilayers. In all diagrams, error bars correspond to standard errors.

Furthermore, we calculated the deuterium order parameters, *S*CD, for both hydrocarbon chains (i.e., sn-1 and sn-2 chains) of the lipid tails in DOPC and RHB. Note that the chemical structure of the acyl chains is exactly the same in both lipids, with a double bond between carbon 9 and 10. The *S*CD values can vary between 0 to 0.5, where smaller values indicate more flexible/disordered regions while higher values correspond to relatively more rigid/ordered regions. [105,126] The computed *S*CD, as depicted in Figure 4.2c,d, show that the degree of flexibility of the lipid tails does increase when going towards the terminal parts, since the mobility is rather unrestricted in the middle of the bilayer, with the exception of the typical sharp dip caused by the presence of the double bond (i.e. C=C at 9-10) and the unusual small

value of C2 in the second tail (i.e., sn-2). Overall, *S*CD of DOPC matches well reported order parameters from previous computational[127] and experimental[128] studies. Concerning RHB, *S*CD is observed to be rather similar to the unlabeled counterpart, as expected giving the identical chemical nature of the tail, although *S*CD values do appear as consistently lower than DOPC (Figure 4.2c,d). Hence, the present result suggests that RHB lipids are somewhat less ordered in comparison to DOPC. Nevertheless, the above structural analyses (i.e. thickness, ApL, RDF and *S*CD) have shown, overall, no large effects caused by the introduction of RHB in the DOPC bilayer.

4.3.2 Lipid lateral dynamics: DOPC vs RHB-DOPC

Lipid lateral dynamics for DOPC and RHB-DOPC membranes was analyzed in terms of mean square displacements (MSD) and diffusion coefficient as issuing from the corresponding MD simulations (see Methods for details). To increase the statistics, reported results represent the average over all four RHB simulations. MSD results are depicted in Figure 4.3a,b. In the initial 10 ns, an anomalous non-linear increase of the MSD versus time was observed: this is due to a "cage effect" in the short timescale motions of the lipids, as previously reported.[129] Beyond 10 ns, the lipid dynamics becomes fully Brownian and it corresponds to the dynamical regime usually detected in fluorescence experiments at longer timescale (i.e., > microsecond). In each system, diffusion coefficient was then calculated by fitting the MSD data according to (Eq. 4.2), skipping the first 10 ns of each trajectory. The obtained diffusion coefficients are reported in Table 4.2. The evaluated diffusion coefficient of DOPC, D = 8.4 $\mu m^2\ s^{-1}$, is in line with previous experimental and computational studies reporting a diffusion constant in the range 5-14 $\mu m^2\ s^{-1}$, depending on temperature, relative water content and the nature of the planar membrane (e.g., GUVs vs SLBs).[92] Besides, DOPC mobility was analyzed as issuing from the RHB-DOPC simulations and a very similar diffusion coefficient was obtained (7.8 $\mu m^2\ s^{-1}$). On the other hand, RHB displayed some noticeable slower dynamics ($6.7 \pm 0.7\ \mu m^2\ s^{-1}$) with respect to the unlabeled lipid, thus reflecting, in our view, the larger hydrodynamic drag due to the bulky Rhodamine B headgroup. Moreover, we tested the effects of ion concentration on the lateral dynamics of the dye-labelled lipid considering the addition of 0.5M NaCl. Results have shown a slight difference with salt concentration, within the estimated noise error, providing a diffusion coefficient of $6.0 \pm 2.1\ \mu m^2\ s^{-1}$ and a decrease in ApL (67.7 $Å^2$). Both

effects have been noticed in previous FCS and MD simulations studies:[130,131] upon NaCl salt addition, sodium ions penetrate into the headgroup region of the membrane, thus perturbing slightly the lipid structure and, in turn, altering the lipid dynamical properties. Note, however, that no sodium ion over binding versus lipid phosphate groups was observed when comparing DOPC and RHB (see P-Na RDFs depicted in Figure 4.4; average number of sodium ions around each RHB or DOPC phosphate group within a radius of 0.6 nm was found to be 0.28, a result in well agreement with previous findings[131]).

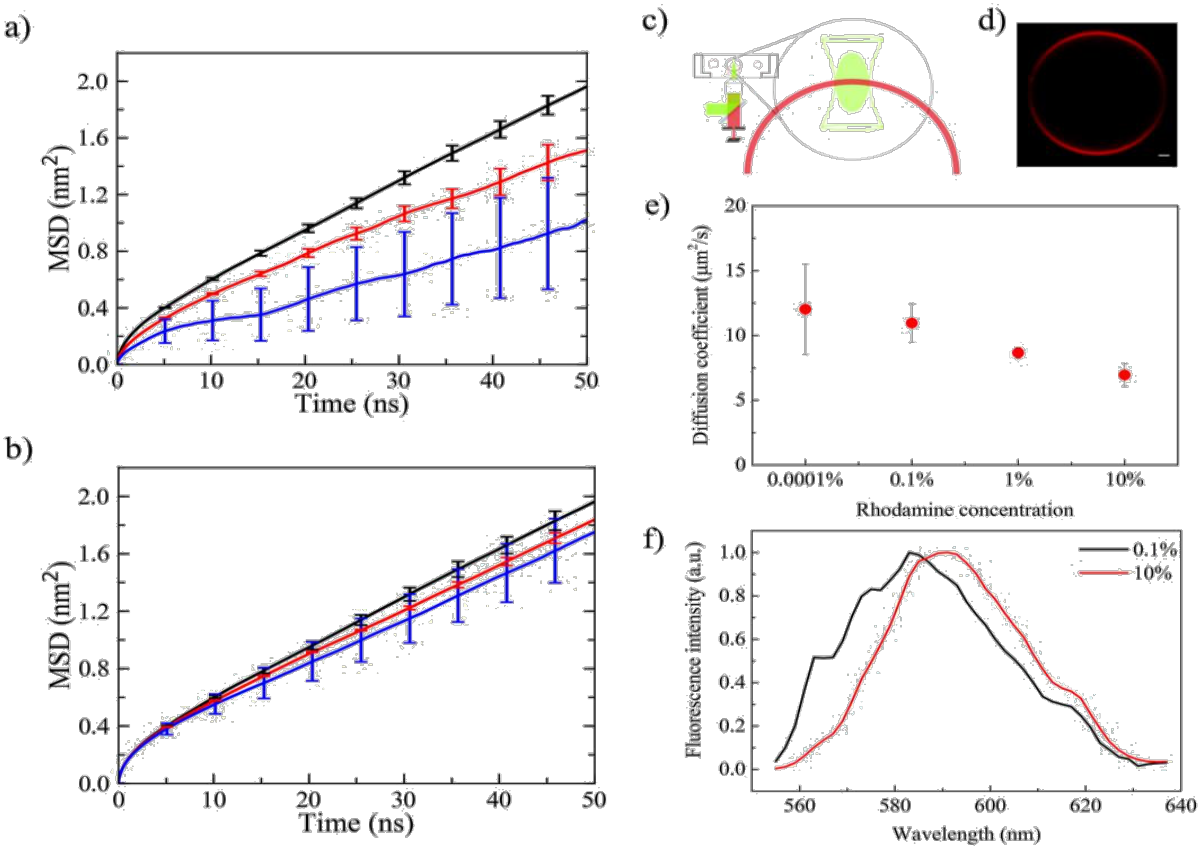

Figure 4.3: a) Mean square displacement (MSD) evaluated as a function of time from MD simulations of DOPC (black, DOPC lipids), RHB-DOPC (red, RHB lipids) and RHBAgg-DOPC (blue, RHBAgg lipids) lipid bilayers. Error bars correspond to standard errors. b) Mean square displacement (MSD) evaluated as a function of time from MD simulations of DOPC (black, DOPC lipids), RHB-DOPC (red, DOPC lipids) and RHBAgg-DOPC (blue, DOPC lipids) lipid bilayers. Error bars correspond to standard errors. c) Schematic representation of a FCS measurement. d) Confocal microscopy image of a GUV DOPC - 0.1% RHB, scale bar 1 micron. e) Effect of fluorophore concentration on the diffusion of RHB lipids in GUVs. f) Emission spectra of Rhodamine B at different concentration (0.1% and 10%) in GUVs, the aggregation of Rhodamine B induces an emission spectra red shift of 8 nm, from 583 to 591 nm.

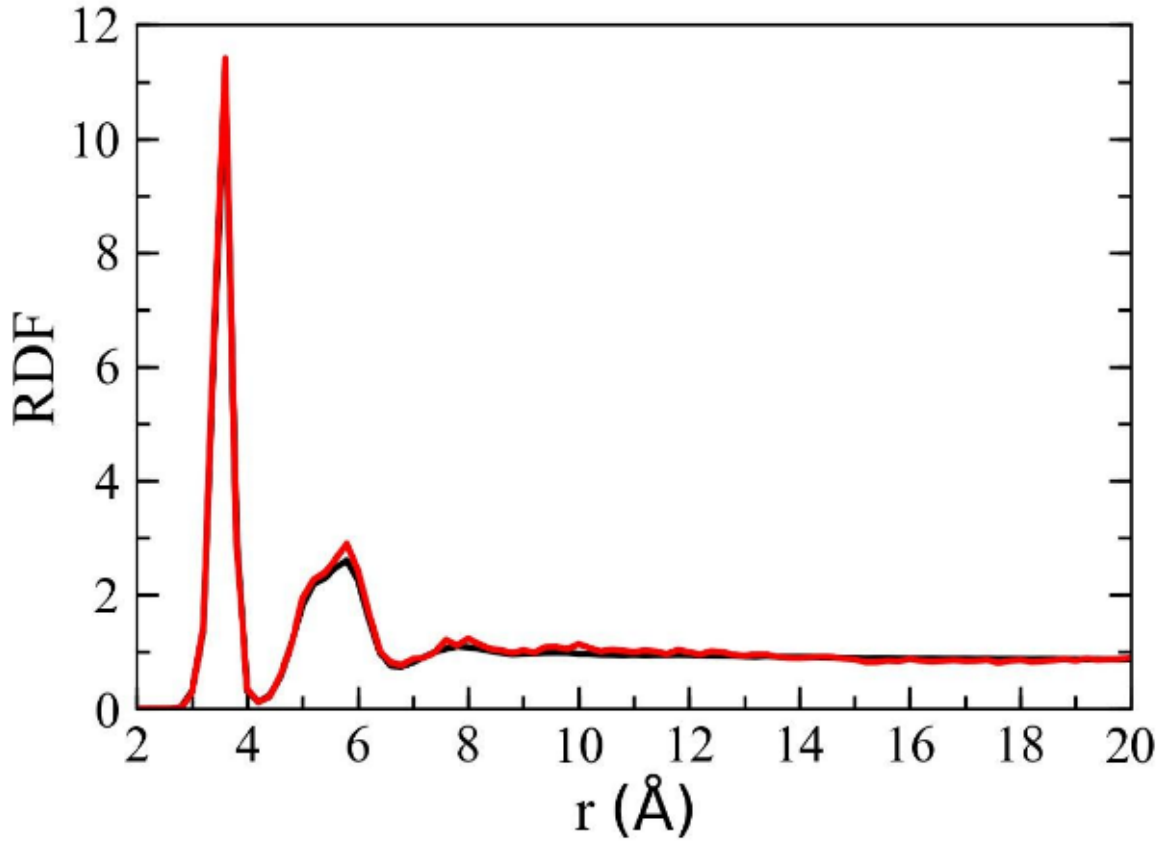

Figure 4.4: P - Na^+ radial distribution functions (RDFs) obtained considering DOPC (black line) and RHB (red line) lipids as issuing from the RHB-DOPC MD simulation with 0.5M NaCl. Sodium ions are observed to penetrate the phosphate region of the lipid bilayer in a similar way with respect to both RHB and DOPC lipids.

4.3.3 FCS measurements of lipid lateral diffusion effects of RHB concentration

The lateral diffusion of RHB lipids at different concentrations was investigated in a parallel experimental setup. GUVs of RHB-DOPC in a ratio ranging from 10^{-4} % to 10% have been prepared. Immobilization of GUVs in agarose gel allowed performing FCS measurements on vesicle membranes (Figure 4.3c,d). FCS was used to measure the diffusion of the dye-labelled lipid, RHB, across the membrane bilayer. Fluorophore concentration was high in vesicles and for this reason photobleach of Rhodamine B has been necessary. The measured diffusion coefficient of RHB lipid has shown a stark decrease with concentration as depicted in Figure

4.3e at very low concentration (10^{-4} %), RHB diffusion is about 12 $\mu m^2 s^{-1}$, and it becomes as low as 7.0 $\mu m^2 s^{-1}$ at high concentration (10%) (Table 4.3).

Table 4.3: FCS measurements of RHB and LAURDAN, diffusion coefficients (D) and G0

Dye		DOPC	0.0001%	0.1%	1%	10%
RHB	D (μm^2/s)	N.A.	12 ± 3.5	10.9 ± 1.5	8.7 ± 2.4	6.9 ± 0.9
	G_0	N.A.	0.12 ± 0.06	N.A.*	N.A.*	N.A.*
LAURDAN	D (μm^2/s)	12.2 ± 3.6	N.D.	10.1 ± 2.2	17.3 ± 5.1	24.8 ± 3.5
	G_0	$3.3\ 10^{-3}$ ± $1.9\ 10^{-3}$	N.D.	$0.94\ 10^{-3}$ ± $0.5\ 10^{-3}$	$3.7\ 10^{-3}$ ± $0.9\ 10^{-3}$	$2.3\ 10^{-3}$ ± $0.5\ 10^{-3}$

* Data not available due to bleaching of Rhodamine B

4.3.4 High RHB concentration aggregation and membrane permeability change

One of the possible effects of the anomalous decrease in the mobility of the dye-labelled lipid with concentration is self-aggregation, since Rhodamine is capable to form stable pi-stacking self-interactions owing to its extended aromatic moiety. Indeed, Rhodamine was reported to form oligomers of growing size with concentration, [132,133] when dissolved in solution. We set out to demonstrate whether RHB aggregation occurred in the lipid membrane by recording the fluorescence spectra of RHB-DOPC GUVs at different concentration of the dye-labelled lipid, i.e. 0.1% and 10%. Figure 4.3f reports the fluorescence spectra. The observed red-shift (about 8 nm) in the emission spectrum of the sample at higher RHB concentration (10%) was interpreted as a fingerprint of the occurring aggregation of the fluorophore, also following previous detailed analyses. [132,133] On the other hand, no significant change in emission was observed at low concentration (<0.1%). Based on this observation, we decided to further investigate the properties of the mixed RHB-DOPC membrane with a second molecular probe, i.e. LAURDAN. LAURDAN is a membrane fluorescent dye which is known to integrate easily within the lipid bilayer owing to its highly hydrophobic tail. Due to its peculiarities, this optical probe is especially well suited to report on lipid structural changes or rearrangements. Moreover, LAURDAN is sensitive to the polarity of its micro-environment and displays a

typical red shift in its emission spectrum upon change in dipolar relaxation caused by the increase of water content in the membrane.[134,135] First, we performed FCS measurements of LAURDAN diffusion coefficient when the probe was introduced in the same RHB-DOPC GUVs described above. In contrast with RHB, the diffusion coefficient of LAURDAN was observed to increase at higher RHB:DOPC concentration ratio (Table 4.3,Figure 4.5a), reaching a maximum at 10% RHB in the considered concentration range. Then, in order to quantify any change in the spectral behavior of LAURDAN, the GP ratio of its emission spectrum was evaluated from GUV images according to (Eq. 4.1) In the polarity maps depicted in Figure 4.5b different colors represent different GP values, according to the reported color scale. Indeed, low GP values indicated an enhanced water permeation into the membrane. As shown in Figure 4.5c, LAURDAN GP values decreased with RHB increase, thus supporting a higher water permeability of the RHB-DOPC lipid bilayer under such conditions.

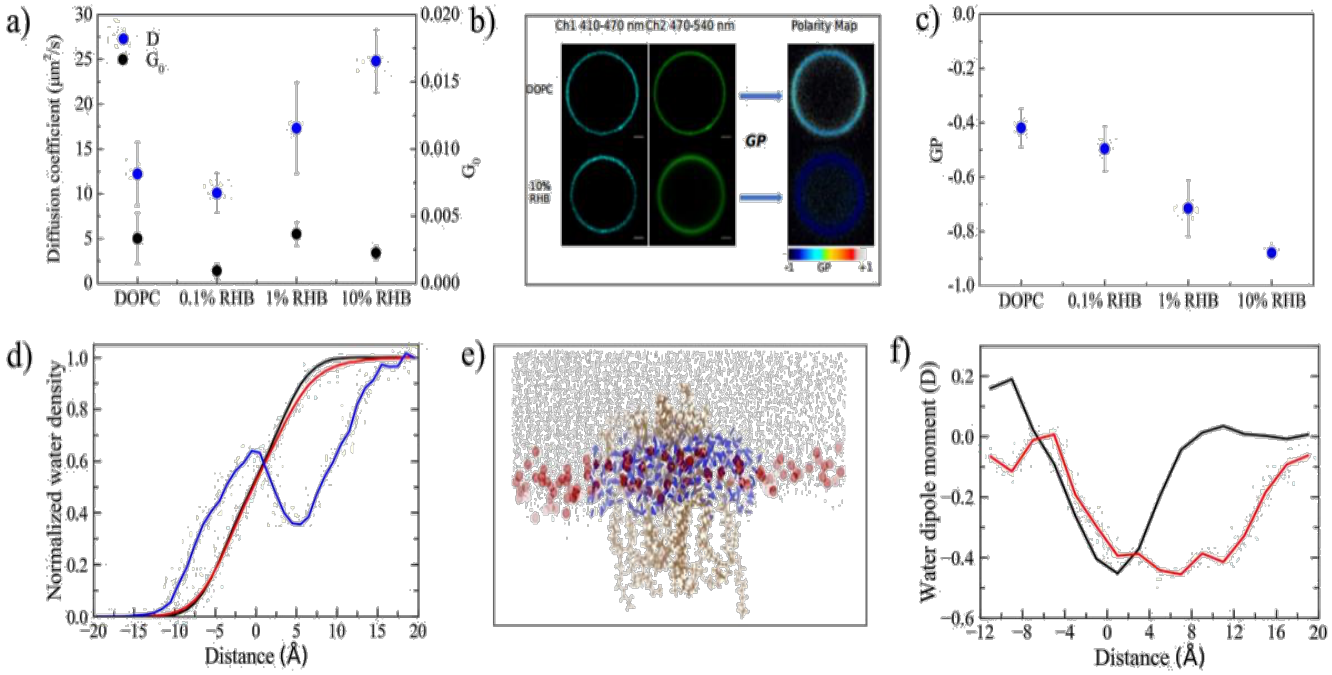

Figure 4.5: a) Diffusion coefficient of LAURDAN increases with increasing concentration of RHB (blue dots), G0 remains constant (black dots). b) Confocal microscopy images of GUVs labelled with LAURDAN, the emission signal was split in two channels and polarity maps were obtained from these images using GP equation. c) GP values obtained in GUVs at different concentration of RHB. d) Water density distribution evaluated along a direction normal to the membrane surface as issuing from MD simulations of DOPC (black), RHB-DOPC (red) and RHBAgg-DOPC (blue, water within 5 Å in XY plane from the center of the RHB cluster) lipid bilayers. Origin was set to the average position of P atoms in one leaflet, negative values correspond to the inner bilayer region, positive values to the outer region and bulk solution. Water density

was normalized with respect to bulk density. e) MD snapshot of the RHB cluster: RHB lipids are shown in orange, DOPC phosphate groups in red, water molecules within 5 Å from the RHB aggregate are in blue, while remaining water molecules at the membrane-water interface are in gray. f) Average water dipole moment evaluated along a direction normal to the membrane surface as issuing from MD simulations of DOPC (black) and RHBAgg-DOPC (red, water within 5 Å in XY plane from the center of the RHB cluster) lipid bilayers.

4.3.5 Modelling RHB aggregation structural effects and lipid diffusion

A model of RHB lipid aggregation (i.e., RHB^{Agg}-DOPC), consisting of 8 RHB molecules in the same layer of a DOPC membrane, was generated according to the computational protocol described in the Methods, see a molecular representation of the system in Figure 4.1d,e. First, we analyzed some structural properties of the aggregated system. The P-P RDF of the RHB^{Agg}-DOPC system has shown some deviations with respect to non-aggregated RHB-DOPC and pure DOPC systems (Figure 4.2b): the structural perturbations caused by RHB lipids in the aggregated form, in the membrane upper layer, has clearly displayed a more structured profile than both the other systems. This is also a manifestation of the stability of the RHB assembly, which is maintained throughout the simulation with minor changes in the overall structure. In terms of deuterium order parameters, *S*CD, RHB lipids in the RHB^{Agg}-DOPC system have shown a slightly higher ordered structure in comparison to the non-aggregated systems (Figure 4.2c,d). Moreover, to investigate possible structural changes of DOPC lipids in close proximity to the RHB assembly, *S*CD was evaluated by considering only a selected region of DOPC lipids within 5 Å of any RHB molecule in the upper layer. Results have shown a slightly less ordered structure of DOPC in this region as compared to all other remaining DOPC molecules of the same RHB^{Agg}-DOPC system (data not shown) and also to the pure DOPC system (Figure 4.2e,f). Note that by extending the selection of DOPC lipids to a distance of 7.5 Å, i.e. including the whole first lipid shell around the RHB assembly, very similar results were obtained (see Figure 4.6). In the case of the aggregated system, the diffusion coefficient of the clustered RHB molecules was significantly lower, 4.0 $\mu m^2\ s^{-1}$, in comparison to the non-aggregated RHB systems, while surrounding DOPC lipids showed same mobility as in pure DOPC system, 8.7 $\pm$ 1.0 $\mu m^2\ s^{-1}$ (Table 4.2). The relative slower diffusion of RHB in the upper layer of the

aggregated system was the consequence of the prolonged retention of the RHB molecules within the cluster throughout the simulation.

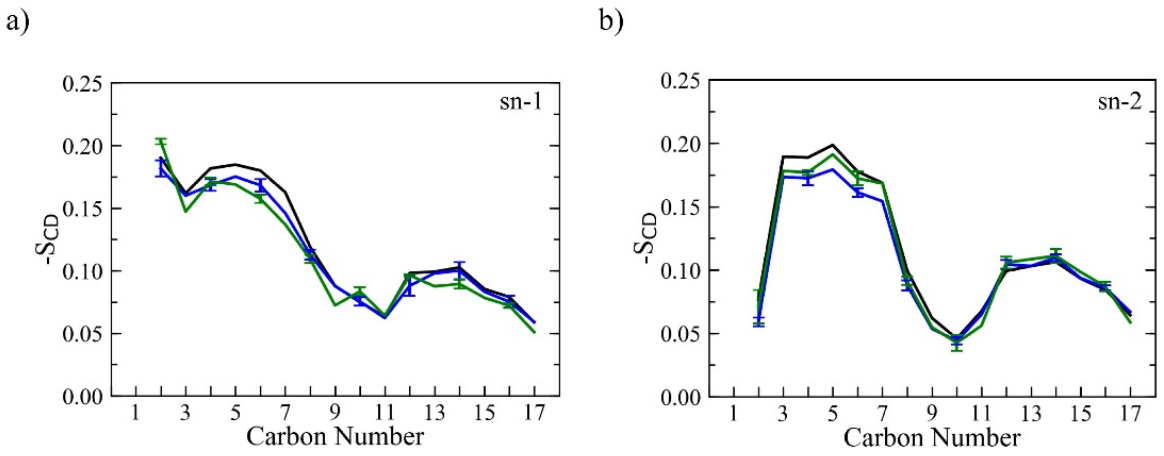

Figure 4.6: a,b) Deuterium order parameters (S_{CD}) evaluated for lipid acyl chains (i.e., sn-1 and sn-2) as issuing from MD simulations of DOPC (black, DOPC lipids), RHB^{Agg}-DOPC (blue, only DOPC lipids within 5 Å from any RHB lipid) and RHB^{Agg}-DOPC (green, only DOPC lipids within 7.5 Å from any RHB lipid) lipid bilayers. Small differences in DOPC order parameters appeared as caused by the local interaction with RHB lipids. In all diagrams, error bars correspond to one standard errors. Error bars of pure DOPC system (black lines) are negligible and then omitted for clarity in all plots.

4.3.6 Modelling RHB aggregation water permeation into the membrane

We have analyzed the local water density going from bulk solution to the center of the lipid bilayer, along a direction normal to the membrane surface. Local water density was evaluated considering the position of water oxygen atoms in a range of distance between +20 Å and -20 Å with respect to the layer surface (i.e., average P coordinates). In the case of the RHB aggregated system, we applied a further restriction by selecting only the water molecules (i.e., oxygen atoms) falling within a distance of 5 Å from the center of the RHB assembly in the XY plane parallel to the membrane surface, thus analyzing the local water distribution in proximity of the dye assembly. Finally, water density was normalized with respect to bulk density, as depicted in Figure 4.5d. In pure DOPC, the observed water density has shown a smooth drop while going from bulk (i.e., positive distance) towards the bilayer center (i.e., negative distance). A very similar density profile was observed in all RHB-DOPC systems considered. On the other hand, water density displayed a peculiar non-monotonic trend when evaluated in the surrounding of the RHB aggregate from the MD simulation of the RHB^{Agg}-DOPC bilayer, showing a marked increase (>25%) in water content inside the lipid bilayer in the region

between 0 and -10 Å (as depicted in Figure 4.5e). A peak in water density was observed around the phosphate groups of the RHB lipids. This results clearly supported an increased water permeability of the lipid membrane in correspondence of the aggregate. The effects of the latter contributed also to a change in the mean dipole moment of water across the membrane surface as compared to the unlabeled lipid bilayer, as shown in Figure 4.5f. Water dipole orientation is more pronounced in the headgroup region of the RHB aggregated system, possibly as a result of an enhanced local electric field due to the net electric charge on the RHB lipid and a decreased capability to screen effectively electrostatic interactions by the Rhodamine B moiety. Such an interfacial region was further investigated in both DOPC and RHB aggregated systems by evaluating the local electrostatic potential. Figure 4.7a-d report the 2D electrostatic potential maps evaluated on a lateral plane of the lipid bilayer and the corresponding electric potential along a normal to the membrane surface. Figure 4.7d highlights the asymmetric electrostatic potential in correspondence of the RHB cluster (i.e., peak around Z = 30 Å). We expect the qualitative picture emerging from Figure 4.7d not to change significantly with cluster size since it refers to a local property (center of the cluster), at least for an extended concentration range not leading to lipid phase changes or other drastic phenomena.

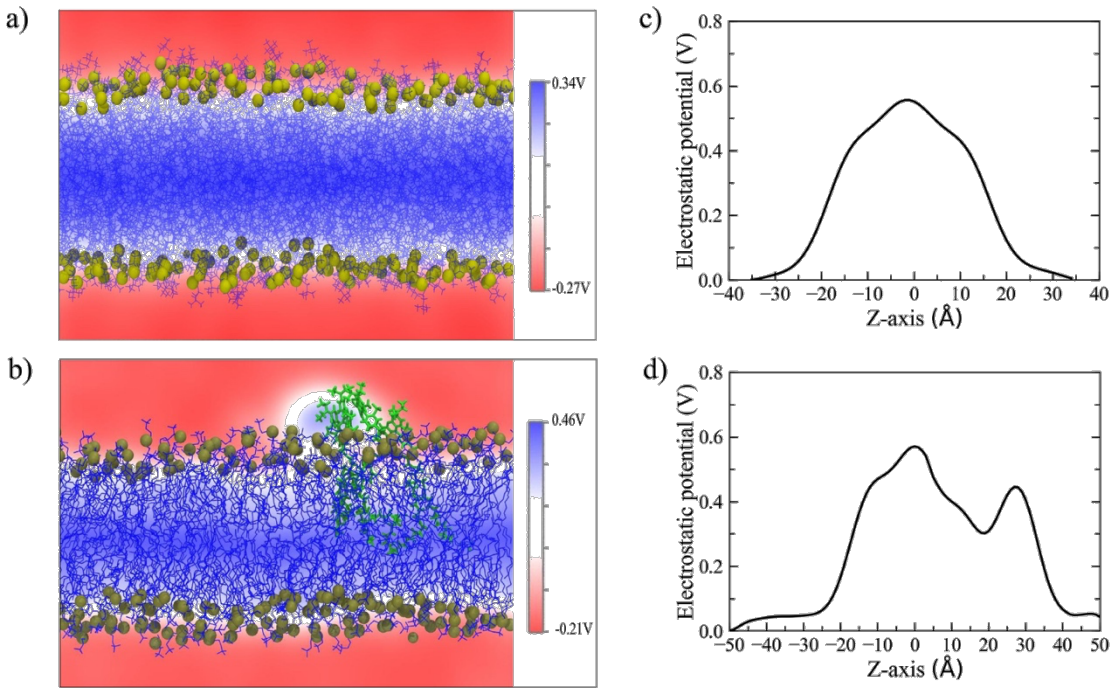

Figure 4.7: 2D electrostatic potential maps as issuing from MD simulations of a) DOPC and b) RHBAgg-DOPC lipid bilayers evaluated on a lateral plane (i.e, XZ) of the simulation cell. Electrostatic potential evaluated along a direction normal to the membrane surface as issuing from MD simulations of c) DOPC and d) RHBAgg-DOPC lipid bilayers. In the latter case, the normal was selected to pass through the center of the RHB cluster. Origin was set to the center of the bilayer in both cases. Overall, the electrostatic potential can change by up to 0.6 V across the lipid bilayer, but RHBAgg-DOPC system shows a high degree of asymmetry with a peak at about 30 Å in correspondence to the RHB aggregate.

4.4 Discussion

In this work, we studied the structural, dynamic and self-aggregation properties of a dye-labeled lipid embedded into a simple DOPC planar membrane as a function of its concentration. Our combined MD-FCS approach provided new insights into the subtle interplay between dye concentration, lipid lateral diffusion and membrane permeability. On one hand, our study better assessed the role and the effects of a typical optical probe, here a Rhodamine B dye, if used to gather information on lipid dynamics from time-resolved measurements. In particular, we observed both a direct, concentration-independent, and an indirect, concentration-dependent, effect of the dye. Once tagged to a phospholipid, the tracer molecule induced a noticeable decrease (about 20%) in lipid lateral diffusion with respect to

the unlabeled lipid, as estimated by our MD simulations (i.e., DOPC: $D = 8.4 \pm 0.4$ $\mu m^2 s^{-1}$; RHB: $D = 6.7 \pm 0.7$ $\mu m^2 s^{-1}$). This is a direct manifestation of the higher hydrodynamic drag due to the bulky Rhodamine headgroup. Moreover, the diffusion coefficient obtained from FCS measurements on GUVs made up by a similar RHB-DOPC composition (i.e., 1%) with respect to our model displayed a somewhat higher but comparable value, 8.7 ± 2.4 $\mu m^2 s^{-1}$. This is a notable result considering the approximations affecting the model (e.g., forcefield parameters, periodic boundary conditions, planar lipid bilayer, etc.). Conversely, FCS experiments at very dilute concentrations (10^{-4}%) provided a diffusion coefficient of about 12 $\mu m^2 s^{-1}$. Since optical experiments can only probe the dynamics of dye-labeled lipids and assuming a dye hydrodynamic effect of 20%, our best estimate for lipid diffusion in pure DOPC membrane under normal conditions would be about 14 $\mu m^2 s^{-1}$. This result is within the range of previous studies on similar phospholipids (5-14 $\mu m^2 s^{-1}$),[89,92] and it is close to the upper limit. Owing to the paramount importance of lipid mobility for setting the dynamics of complex biophysical and biochemical processes occurring at cell membranes, we believe that an accurate assessment of lipid lateral diffusion could be beneficial for a quantitative understanding of such phenomena. Besides, an accurate diffusion coefficient can serve as a useful benchmark for testing and developing new forcefields on which MD simulations of lipid bilayer rely upon. In this regard, we note that in our simulations DOPC diffusion (8.4 ± 0.4 $\mu m^2 s^{-1}$) seems a little underestimated with respect to the above "corrected" measure, a result possibly reflecting inaccuracies of the present model parameters. Moreover, the Saffman-Delbrück theory for periodic bilayers[102,103] predicts our computed diffusion constant to be underestimated owing to the limited system size, while the accurate theoretical estimate can be recovered, in principle, at infinite size limit (for the present DOPC simulation, the predicted D^{∞} is ~22 $\mu m^2 s^{-1}$). Nevertheless, the above considerations on the hydrodynamic effect of the dye are reasonably not affected by the choice of periodic boundary conditions as they stem from a comparative study of same-size molecular systems.

Furthermore, our study reported a sensible slowdown of the diffusion mobility of the dye-labeled lipid in the concentration range going from 10^{-4}% to 10%. Lipid lateral diffusion decreased from about 12 $\mu m^2 s^{-1}$ to 7 $\mu m^2 s^{-1}$, thus suggesting again a non-neutral role of the dye. Observed fluorescence spectra of GUVs recorded at low and high RHB concentration confirmed the occurrence of self-aggregation among dye-labeled lipids. This result was not surprising owing to the well-known capability of Rhodamine derivatives to undergo self-

assembly in solution.[132,133] Nevertheless, our study clearly highlighted the impact of such transient lipid clusters on the resulting diffusive dynamics of the same dye-labeled lipids. Indeed, the increased inertial mass and hydrodynamic drag of such aggregates have a non-negligible effect on the observed lipid dynamics. While the extent of such an effect may depend on the peculiar chemical nature of the chosen tracer molecule, a similar behavior is expected to be shared by a large number of organic fluorophores typically employed as tracking probes in bioimaging studies. Note that self-aggregation could be perhaps one of the causes for the observed variability in lipid diffusion measurements recently reported by Guo et al.[98] in lipid bilayers with different dye-labeled lipid content.

To proceed further, the observed self-aggregation was further investigated to highlight possible structural rearrangements of the membrane bilayer. The concomitant use of a second probe, LAURDAN, unraveled a pronounced change in membrane fluidity and water permeability upon formation of RHB aggregates (Figure 4.5a-c). More insights emerged from our complementary modeling study of the RHB lipid self-assembly: the structural lipid-lipid rearrangements displayed by the computed P-P RDF (Figure 4.2b) and the substantial change in the local electrostatic potential at the water-membrane interface (Figure 4.7a-d) had the combined effect of enhancing water permeation into the interior of the membrane lipid bilayer, in stark contrast to the low concentration RHB-DOPC systems (Figure 4.5d). Furthermore, the depletion in the water density in correspondence to the Rhodamine B headgroups (around 5 Å, Figure 4.5d) reflects the hydrophobicity of the dye, an effect that may help to retain water molecules once inside the lipid bilayer. It is worth noting that no significant changes in lipid membrane structure was observed in our MD simulations of RHB-DOPC systems in absence of dye-labeled lipid cluster formation (Table 4.2 **and** Figure 4.2). Hence, we think that pronounced structural changes in the present two-component dye-labeled/unlabeled lipid system can be mainly ascribed to the formation of such self-aggregates, and to a minor extent to the concentration ratio per se. Following self-aggregation, membrane structural changes are further boosted by the increase in water permeability. The increase in LAURDAN diffusivity with RHB concentration and the change in its photophysical response seem to agree nicely with the present interpretation.

Once more, our study confirms that lipid lateral diffusion is not only one of the most important dynamical parameters, but it is also intimately related to the membrane structure. Overall, the analyses carried out in the present study showed a non-neutral role of the tracer molecule in

determining the lateral dynamics of the dye-labeled lipid as compared to the unlabeled parent lipid. The effect of the tagged dye becomes even more dramatic by increasing its concentration (>1%), since it enables the formation of self-aggregates and, in turn, a significant change in the local electric and structural properties of the membrane, also enhancing water permeability and fluidity at the same time.

While the main goal of this work was to develop an effective integrated approach based on FCS and MD analyses to investigate the qualitative and quantitative effects of the use of optical probes for tracking lipid lateral dynamics, our results pave the route to systematic studies on additional tracer/lipid systems under variable experimental conditions. We predict that a similar approach could be further extended to study multi-component lipid bilayers or protein mobility in membranes. A key point in our successful strategy is represented by the use of two optical probes to report concomitantly on the structural and dynamic properties of the lipid bilayer, respectively. While the use of multiple probes in fluorescence applications is, in general, a very attractive and fruitful approach, we would like to point out that extreme care has to be taken in the present context. First, one has to assess the specific choice of the fluorophores to avoid possible interferences in the optical signal, such as FRET. Then, as our study has clearly shown, one has to assess carefully whether unwanted effects are introduced by the probe itself with respect to the biophysical property under scrutiny. We believe that experimental results may inevitably suffer from the effect of lipid/protein labeling, to some extent. Further advances are expected by new generation of functional probes that report on membrane dynamical changes, and ultimately on the organizational hierarchy of cellular membranes, with negligible effects on the host systems.

4.5 Conclusions

Lipid lateral diffusion in membrane bilayers is a fundamental process exploited by cells to enable complex protein structural and dynamical reorganizations. For its importance, lipid mobility in both cellular and model bilayers has been extensively investigated in recent years, especially through the application of time-resolved, fluorescence-based, optical microscopy techniques. However, one caveat of fluorescence techniques is the need to use dye-labeled variants of the lipid of interest, thus potentially perturbing the structural and dynamical properties of the native species. Generally, the effect of the dye/tracer molecule is implicitly

assumed to be negligible. Nevertheless, in view of the widespread use of optically-modified lipids for studying lipid bilayer dynamics, it is highly desirable to well assess this point. Here, fluorescence correlation spectroscopy (FCS) and molecular dynamics (MD) simulations have been combined together to uncover subtle structural and dynamic effects in DOPC planar membranes enriched with a standard Rhodamine-labeled lipid.

The structural analysis of pure DOPC and RHB-DOPC lipid systems have shown no significant change by the introduction of the fluorophore itself, as the statistics obtained from the basic structural analysis like thickness, area per lipid and order parameter were well within the observed previous experimental values of such lipid systems. Though there was a noticeable change in the dynamics of the RHB labelled lipids in comparison to its unlabeled counterpart. The bulky Rhodamine head groups and related hydrodynamic drag because of these bulky headgroups leads to slower dynamics of RHB. Another important finding of this study is the ability of the Rhodamine- B to self-aggregate with the increasing concentration, which was proved with our experimental and computational protocol and lead us to conclude that with increasing concentration of RHB lipids has showed stark decrease in lateral movement. Not only the diffusion coefficient was decreased for the Rhodamine aggregates but we have also observed increased water permeability surrounding the aggregates in the lipid system. This was further proved when the water density profile shows non monotic behavior around the aggregates of RHB and also the change in the mean dipole moment was observed for the labelled lipids with respect to the unlabeled lipid system. Our findings support a non-neutral role of the dye-labeled lipids in diffusion experiments, quantitatively estimating a decrease in lipid mobility of up to 20% with respect to the unlabeled species. Moreover, results highlight the existing interplay between dye concentration, lipid lateral diffusion and membrane permeability, thus suggesting possible implications for future optical-microscopy studies of basic membrane biophysical processes.

Chapter 5 Temperature dependence of the structure and dynamics of a dye-labeled lipid in a planar phospholipid bilayer, a computational study

5.1 Introduction

Plasma membranes, which constitute a protective barrier for living cells, are involved in many biologically relevant processes such as signal transduction, endocytosis, cell motility, etc... [136]. Due to its heterogeneous lipid composition, the plasma membrane is characterized by the coexistence of liquid ordered (L_o) and liquid disordered (L_d) domains. The different lateral organization of lipids translates into a preferential packing of sphingolipids and cholesterol with saturated lipids in L_d domains, forming lipid rafts onto which specific transmembrane proteins can be found [137]. This dynamic lateral assembly of lipids and proteins arises from an asymmetric distribution of lipids over exoplasmic and cytoplasmic leaflets of the plasma membrane. Recently, the organization of lipids in both model and cell membranes at a molecular level has been investigated using fluorescent labeled lipids [138,139]. In particular, fluorescence-based optical microscopy methods are versatile quantitative tools to monitor the complex spatiotemporal organization of lipid membranes in both model lipid bilayers and living cells: both localization-based (e.g. single-particle tracking, SPT) and statistical methods (e.g. fluorescence correlation spectroscopy, FCS), eventually combined with super-resolution approaches, have greatly contributed to build the current knowledge on this topic [85–89,140].
However, independently of the chosen technique, a common prerequisite for optical microscopy measurements is labelling the molecule of interest with a fluorescent probe. Biological membranes are routinely investigated, both experimentally and computationally, by using various fluorescent probes, including molecular rotors [141–143]. In order to study the structure and dynamics of lipids, optical probes are usually attached to lipid molecules, as in dialkylcarbocyanines [90] and dye-labeled lipids, such as Bodipy, Rhodamine, Atto or Nitrobenzoxadiazole (NBD) [144–146]. The dynamics of a labeled lipid can depend, and provide

information, on several crucial aspects, such as the water content [147], the aqueous phase composition (ionic strength and other soluble species, like sugars), the specific lipid composition (i.e. mixture of lipids and/or sterol components) and other physical/mechanical conditions, such as temperature, pressure, membrane tension, etc. Moreover, these investigations can also provide information on the lipid phase, including the possible co-existence of L_d and L_o domains, using a variety of fluorescent molecular probes that can partition specifically either to L_d or L_o phase [138,139,148,149].

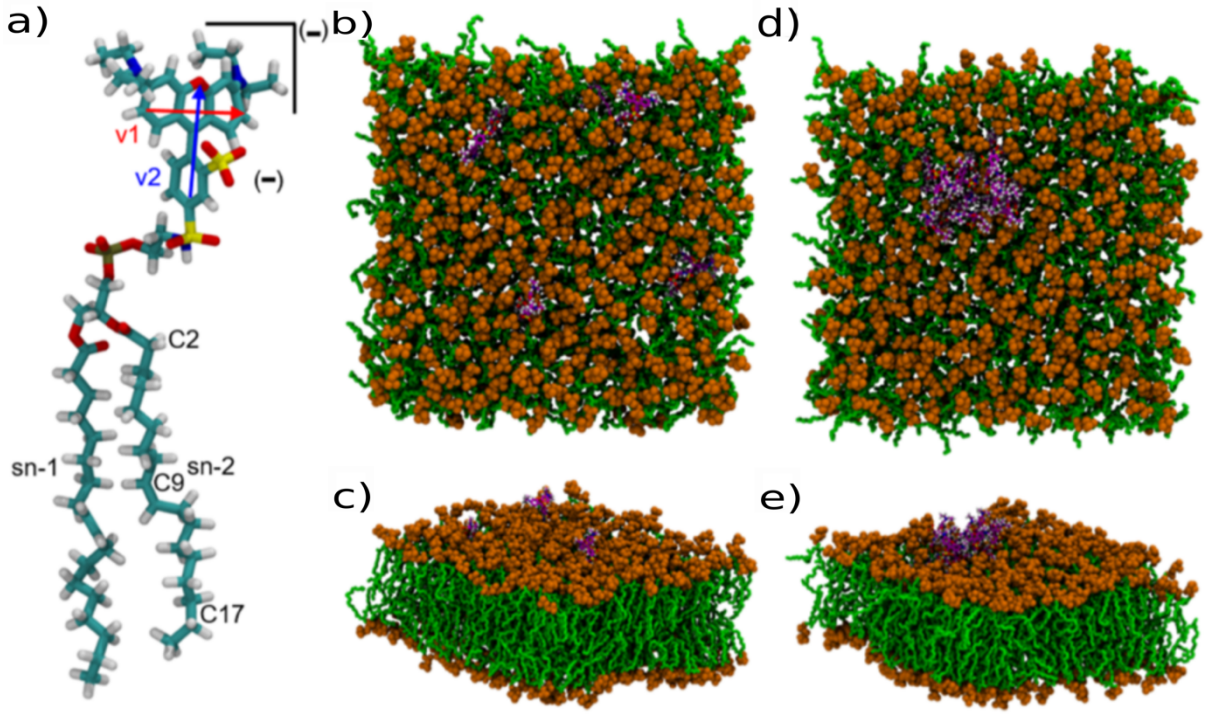

Figure 5.1: a) Molecular structure of the RHB lipid with the definition of vertical (v1) and horizontal (v2) molecular axes of the fluorescent polar headgroup. RHB sn-1 and sn-2 acyl chains are labeled together with significant carbon atoms of hydrophobic lipid tails on the sn-2 chain. Carbon, hydrogen, sulphur, phosphorus, oxygen and nitrogen atoms are shown in cyan, white, yellow, tan, red and blue, respectively. b) Side and c) top view of a MD simulation snapshot of the RHB-DOPC lipid bilayer with a 0.02 mol% RHB concentration. d) Side and e) top view of a 155 ns MD simulation snapshot of the RHB-DOPC lipid bilayer displaying RHB self-aggregation. Carbon atoms of RHB lipids inserted into the DOPC lipid bilayer are shown in magenta, with the other atoms having the same color code of panel a, while DOPC lipids glycerol backbone and hydrophobic acyl chains are in green with corresponding polar headgroups in orange. For clarity, water and ions are not displayed.

In optical microscopy studies, it is generally assumed to ignore the perturbing effect of the probe, based on the consideration that the eventual presence of any spurious effects are

irrelevant with respect to the physico-chemical properties under study. This assumption is especially reasonable in comparative studies involving systems of variable chemical compositions. However, it is worth noting that optical probes have also shown a non-neutral role when tagged to biomolecules, as it was reported in our recent works on cell-penetrating peptides and their interaction with biomembranes [93,94,150]. In recent studies different optical probes inserted into lipid bilayers have shown either different [95,96] or similar [97] lipid diffusion properties, making the interpretation of these results not always straightforward. Moreover, the lateral mobility of lipids investigated using different dye-labeled lipids is also affected not only by lipid bilayer compositions, but also by the dye concentration [98], the temperature and the ionic strength [151].

Under the light of the above findings, it is gaining increasing interest the understanding of the role of fluorescent labeled molecules employed for the investigation of the structure and dynamics in lipid planar membranes. Atomistic molecular dynamics (MD) simulations have become a valuable tool to collect structural and dynamical information on complex biological systems not easily accessible from experiments [99–101]. To our knowledge, apart from our recently published work [150], there is only another atomistic MD simulation study of a DPPC lipid bilayer containing Rhodamine B-labeled 1,2-dioleoyl-sn-3-phosphatidylehanolamine (DOPE) lipids (hereafter RHB) [152]. The limited timescale and the typical finite size of atomistic models, as reported in previous studies, can give rise to undesired artifacts, which have to be taken into account in order to extract meaningful results from MD simulations. In particular, the system size in small bilayer models has been shown to affect the lipid diffusion [102–104], which can also display a non-Brownian behavior when evaluated at short timescales (i.e., 1-10 ns) [105]. More recently, coarse grained (CG) MD simulations have also been employed to investigate the interactions of methylene blue (MB) with DOPC lipid bilayers [153] and the orientation of NBD labeled lipids in POPC membranes [154].

In our recent study [150], we have combined FCS experiments and extended atomistic MD simulations to shed light on some important features concerning lipid dynamics and structural properties within a 1,2-dioleoyl-sn-glycero-3-phosphocholine (DOPC) bilayer. This integrated approach has allowed us to study the possible direct and indirect effects of RHB lipids (Fig. 1a) on the estimation of the lipid diffusion coefficient in a DOPC membrane. In particular, our results have shown a non-negligible role of the fluorescent labeled lipid molecule, which induced a decrease of about 20% in the observed lipid lateral diffusion with respect to the

unlabeled species, and they have characterized the effect of the dye-driven RHB self-aggregation with concentration and the relevant impact that the formed dye-labeled lipid clusters Figure 5.1d,e have on both membrane structure and local hydration at the membrane surface. In this study, we have investigated the effect of the temperature on different structural and dynamic parameters of DOPC lipid bilayers in the absence and in the presence of RHB labeled lipids, whose concentration did not lead to the formation of aggregates during the timescale of MD simulations. In addition, we have closely analyzed the structural effect of the dye in terms of local lipid order and its positioning and orientation within the lipid bilayer. Results have highlighted the role of temperature in modulating lipid lateral diffusion, local hydration of lipid headgroups and dye orientation in fluorescent labeled lipids, thus suggesting possible implications for optical microscopy studies of cell and lipid membranes.

5.2 Computational Details

5.2.1 Molecular models of DOPC and dye-labeled lipid

Starting structure for pure DOPC membrane bilayer was obtained from a pre-equilibrated system, using CHARMM-GUI server [106]. The bilayer consisted of 400 lipids (200 per leaflet) and extended up to ~125 Å along its lateral dimensions (XY plane). The system was then solvated with TIP3P water up to 30 Å from the bilayer along the normal to the membrane surface (Z-axis). Rhodamine B structure was initially generated with the Chimera software [107]. The starting geometry was optimized by quantum mechanical calculations using the B3LYP/6-31+G(d,p) level of theory using Gaussian09 [108], while partial charges were derived from molecular electrostatic potential obtained using the HF/6-31G(d) level of theory in vacuum. The latter generally provides effectively "polarized" charges more suitable for modeling complex systems in the condensed phase without resorting on computationally demanding calculations of molecular polarization [109]. Note, also, that small deviations were observed when partial charges were computed using either B3LYP or including solvent effects through the Polarizable Continuum Model [110] (mean absolute error < 0.1). Besides, in the present work we have neglected the possible electronic rearrangement occurring in the excited state of the dye [111], assuming that, once tagged to the lipid, its orientation within the bilayer and diffusive dynamics would not be particularly affected. Rhodamine B was then attached to the lipid

according to Figure 5.1a in order to build a RHB molecular model. Overall electric charge of the dye-labeled lipid is -1e, since the phosphate group of the lipid is not compensated by the Rhodamine B headgroup. Forcefield parameters for the so obtained dye-labeled lipid were adapted from CHARMM general force field (CGenFF) [112] for a small molecule (RHB force field details are provided in the Supplementary Information of our recently published article [150]). On the other hand, RHB lipid acyl chains parameters were borrowed from the corresponding standard DOPC CHARMM parameters, being the two structures chemically equivalent. Eight RHB lipid molecules (4 per leaflet) were then embedded in a well-equilibrated pure DOPC bilayer, previously created as described above, by replacing a corresponding number of DOPC lipids at random locations. RHB lipids were inserted into the DOPC lipid bilayer in order to minimize self-interactions and the formation of aggregates. The final structure had 196 DOPC and 4 RHB molecules in each membrane leaflet. Water molecules in close contact with the RHB headgroup were deleted and an additional water layer (extending up to ~20 Å) was added along the Z-dimension to build up the final system (box edges: 117x117x92 $Å^3$, water thickness: ~54 Å). Eight sodium ions were added to keep the system electrically neutral. The RHB-DOPC bilayer is depicted in Figure 5.1b,c. Four different replicas of the RHB-DOPC system were produced by regenerating the velocities in each system replica. In all cases, force field included NBFIX terms for sodium in interaction with chloride ions and carboxylate groups [113,155].

5.2.2 Molecular dynamic simulation parameters

All simulations were performed with the NAMD v2.10 software package [114] using CHARMM36 [115] force field for lipids under periodic boundary conditions. Bonds involving hydrogens were restrained using SHAKE [116], which permitted the use of a 2 fs timestep for numerical integration. Long-range electrostatic interactions were calculated using the Particle Mesh Ewald (PME) algorithm [117], while dispersion interactions were evaluated with a cutoff of 12 Å, applying a smoothing functions beyond 10 Å. All production MD simulations were performed in a NpT ensemble with a constant pressure of 1 atm and at three different temperatures (i.e., 293 K, 303 K and 320 K), above the gel or solid ordered (S_o) to liquid crystalline (L_α) or liquid disordered (L_d) phase transition temperature of DOPC (T_m = 256 K) [156]. Langevin thermostat and barostat were employed for pressure and temperature coupling,

respectively [118]. All simulations were performed with a cell box constant-ratio constraint, which allows to keep the ratio of the unit cell constant in X and Y axis while allowing fluctuation along all three dimensions. Prior to production phase, all systems were subject to a short round of energy minimization and system density equilibration (1000 steps of steepest-descent minimization and about 50 ns of MD equilibration). After equilibration, all MD simulations were carried out for about 200 ns, except the four RHB-DOPC replica systems, for which we collected about 100 ns each.

5.2.3 Data analysis

The structure and dynamics of the pure (DOPC) and two-component (RHB-DOPC) lipid bilayers have been characterized via a number of properties, such as i) area per lipid (A_L), ii) membrane thickness, iii) radial distribution function (RDF), iv) diffusion coefficient (D), v) lipid order parameters (S_{CD}), vi) partial density and vii) water density, using in-house developed codes based on the MDAnalysis library [120] or available analysis tools from the Gromacs and Amber [121,122,157] MD software packages. Average area per lipid (A_L) was obtained from the average area of the membrane surface (i.e., XY plane) divided by the total number of lipids in each layer. Membrane thickness was obtained from the average distance between the phosphate groups belonging to the upper and lower leaflets. Radial distribution functions (RDF) were evaluated by considering the interatomic distances of the P atoms belonging to the phosphate groups of either DOPC or RHB, performing distinct analyses on each leaflet and then averaging the results. Diffusion coefficients for lateral lipid dynamics was obtained from the mean square displacement (MSD) of the phosphate groups, removing the effect of the center of mass motion of the entire system, using the Einstein relation mentioned in (Eq. 4.2) and performing a linear fitting of the MSD data on the time interval between 11 and 50 ns, thus skipping the initial ballistic regime usually spanning a few nanoseconds. While diffusion coefficients are generally obtained from MD simulations performed in a microcanonical ensemble, this is rather unfeasible in the case of lipid bilayer systems owing to unwanted temperature fluctuations and drifts occurring in the nanosecond timescale. Since our aim is mainly to provide a fair comparative study upon the relative effects of temperature on the same molecular system, we kept a thermal coupling similarly to many other studies on lipid membranes [99,101,158]. Deuterium order parameter (S_{CD}) was evaluated by considering the

average orientation of the methylene groups along the lipid hydrocarbon chains with respect to the membrane normal [82], and evaluated as shown in (Eq. 4.3), where Θ_{CD} is the angle between each CH bond and the normal to the membrane (Z-axis), and angular brackets denote an average over all lipids and ensemble configurations. Partial density profiles of different moieties of DOPC and RHB molecules were calculated using the standard analytical tool gmx density of Gromacs v5.1.1 [157]. The orientation of the RHB headgroups was described through the definition of a horizontal (v1) and a vertical (v2) axis consistent with the dye moiety, connecting atom pairs C13f-C21f and C1f-O6f, respectively (Figure 5.1a and Figure 5.2). Hence, we evaluated the tilting angle of both v1 (i.e., α angle) and v2 (i.e., β angle) axes with respect to the outwardly directed bilayer normal (i.e., Z-axis), considering the upper and lower leaflets separately (Figure 5.2). Angle distributions and averages were estimated using the gangle analytical tool from the Gromacs v5.1.1 software suite [157].

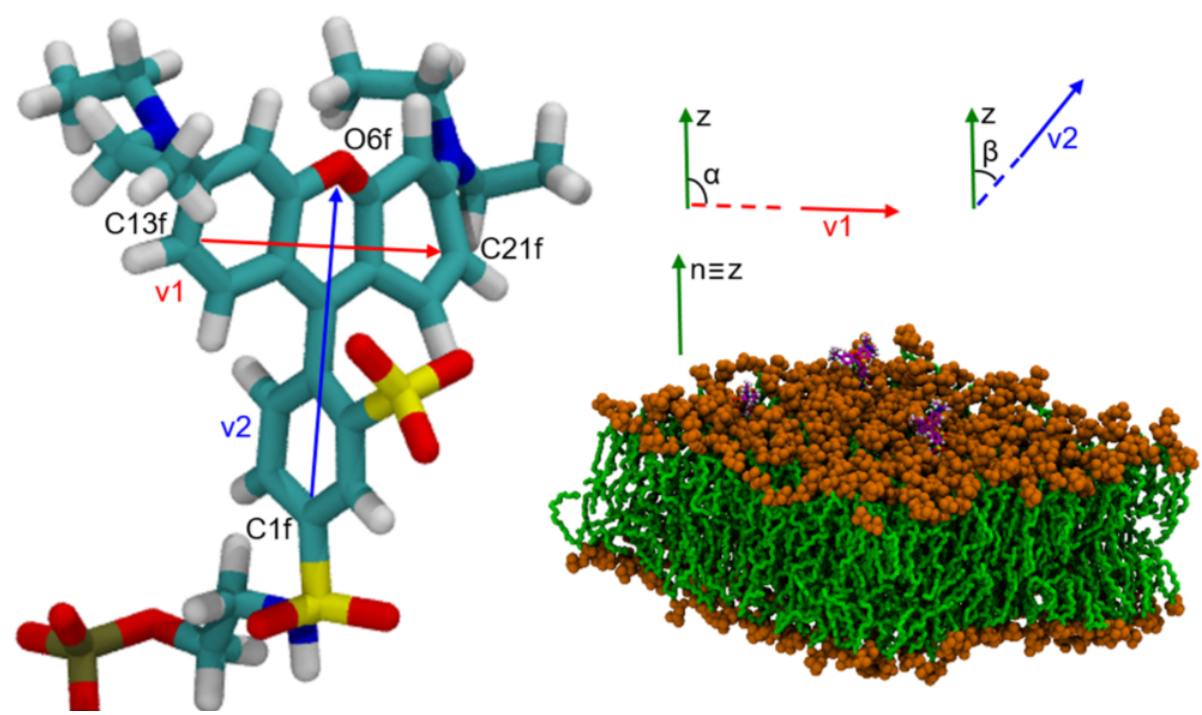

Figure 5.2: Atoms selected to define horizontal (v1, red) and vertical (v2, blue) axes of the RHB fluorescent polar headgroup. Horizontal and vertical axes of the RHB polar fluorescent headgroup form angles α and β, respectively, with the lipid bilayer normal n, which is assumed to be coincident with the z-axis. A side view of a MD simulation snapshot of the RHB-DOPC lipid bilayer with a 2 mol% RHB concentration is shown in the right panel of the figure. The same color code of Fig. 1 is used for DOPC and RHB molecules.

Uncertainties in the estimates of MSD values were evaluated as standard errors from multiple partitions (i.e., 8) of the simulated trajectories. In the case of S_{CD}, RDFs, and RHB headgroup tilt angles, standard deviations were evaluated by considering separately the upper and lower leaflets in all replica simulations. The average number of water molecules within 0.28 nm of any atom of the RHB fluorescent headgroup was evaluated using an in-house VMD Tcl script over the last 50 ns of each simulation at each temperature. Errors on the average number of water molecules were estimated as one standard deviation.

5.3 Results

5.3.1 Temperature effects on the structural properties of the RHB-DOPC bilayer

Structural properties of a DOPC lipid membrane in the absence and in the presence of a concentration of 2 mol% Rhodamine B-labeled lipid (corresponding to 8 lipids over a total of 400 lipids, 4 in each leaflet) were investigated using atomistic MD simulations over a range of about 30 K (i.e., 293 K, 303 and 320 K). It is worth noting that one of the effects of the presence of an organic moiety in dye-tagged lipids in model membranes is the propensity to undergo self-aggregation at moderate to high concentrations (Figure 5.1d) [150]. In this work, we focused on the modeling and simulation of low concentration conditions and, as a result, we have not observed the formation of any RHB aggregate throughout our simulations (Figure 5.3). First, we evaluated the membrane thickness and the average area per lipid (A_L) of pure DOPC and RHB-DOPC membranes as a function of temperature. Results for both systems at different temperatures are reported in Table 5.1. Bilayer thickness is defined as the average distance between phosphorus atoms in phosphate headgroups of both leaflets. At 293 K, the average membrane thickness of the pure DOPC system was found to be 37.9 Å (Table 1), which is in good agreement with previous computational and experimental values of 36.7 Å and 37.6 Å, respectively [127]. Also, the presence of RHB molecules did not affect the lipid bilayer thickness. When the temperature was raised to 303 K, the average thickness of the pure DOPC system was found to be 38.6 Å (Table 5.1) [150], again in good agreement with previous computational studies and experiments (36.7-38.5 Å [105,124,159,160]), and it displayed no significant difference with respect to the Rhodamine B-labeled lipid bilayer: all RHB-DOPC systems have shown a

membrane thickness of about 38 Å. The further increase of the temperature to 320 K caused a reduction of the lipid bilayer thickness to 37.5 Å and 37.7 Å for pure DOPC and RHB-DOPC membranes, respectively (Table 5.1). It is worth noting that even at the highest temperature the membrane thickness, which was somewhat overestimating the experimental value of 36.1 Å at 318 K [161], was not influenced by the presence of RHB molecules. The average area per lipid (A_L) is the most common determining feature in the packing of the lipid bilayer and structure, being a useful indicator of phase transitions. It is affected by the hydration of lipids [158,162], the temperature [127], the type of cation [163] and the type of force field [158,164]. An increase of the average DOPC A_L in both pure DOPC and RHB-DOPC bilayers was observed when the temperature was increased from 293 K to 320 K, which is in agreement with previous results for DOPC lipid membranes [127] . In particular, at 293 K the average A_L in a pure DOPC membrane was 67.4 $Å^2$, which nicely matches the value of 67.3 $Å^2$ reported by Jämbeck et al. in 2012 [127]. At 303 K, the pure DOPC bilayer had an average A_L of 68.2 $Å^2$, which is close to recent experimental data and well within previously reported measurements at the same temperature (67.4 – 72.5 $Å^2$ [124,160,165]). When the temperature is raised to 320 K, we observed an average A_L of 69.8 $Å^2$ in the pure DOPC membrane, which is similar to previous computational (i.e., 70.3 $Å^2$ at 323 K) and experimental results [127]. Interestingly, RHB-DOPC systems have shown a slight increase in A_L as compared to the pure DOPC bilayer at all temperatures, which becomes more evident at the highest temperature considered (Table 5.1). This behavior is in contrast with the slight condensation effect induced by 1,2-dioleoyl-sn-glycero-3-phospho-L-serine-N-(NBD) (NBD-PS), which is structurally similar to the DOPC lipid labeled with Rhodamine B (RHB) except for the less bulkier fluorescent polar headgroup, in DOPC lipid bilayers without and with cholesterol at 293 K [166]. A similar result has also been reported for phosphatidylethanolamines fluorescently labeled in the headgroup region with NBD inserted into POPC lipid bilayers [167]. However, our result is in line with the observed increase of the A_L in a DPPC system containing RHB molecules, interpreted by Kyrychenko et al. as a consequence of the interaction of the bulky sulforhodamine fluorophore of RHB with the polar membrane interface, which induces a “softening” of the lipid bilayer structure [152,168]. These recent findings suggest that the extent of the steric hindrance and the interaction of the fluorescently labeled hydrophilic headgroup of a lipid with the polar membrane interface can play a role in the observed slight decrease or increase in A_L.

Table 5.1: Structural and dynamical properties of DOPC and RHB-DOPC lipid bilayers from AA MD simulations at three different temperatures.

System	Temperature (K)	A_L (Å^2)	Thickness (Å)	D^{DOPC} (μm^2 s^{-1})	D^{RHB} (μm^2 s^{-1})
DOPC	293	67.4 ± 0.6	37.9 ± 0.3	7.0 ± 0.4	-
	303	68.2 ± 0.8	38.6 ± 0.4	8.4 ± 0.4	-
	320	69.8 ± 0.7	37.5 ± 0.3	13.4 ± 0.1	-
RHB-DOPC (Average over 4 replicas)	293	68.8 ± 0.4	38.2 ± 0.2	5.2 ± 0.3	3.7 ± 0.5
	303	69.2 ± 0.8	38.2 ± 0.4	7.8 ± 0.4	6.7 ± 0.7
	320	71.4 ± 0.4	37.7 ± 0.2	14.0 ± 0.6	11.2 ± 1.0

Errors in A_L and lipid bilayer thickness correspond to one standard deviation. Diffusion coefficients and corresponding uncertainties were evaluated according to the procedure described in the Methods section.

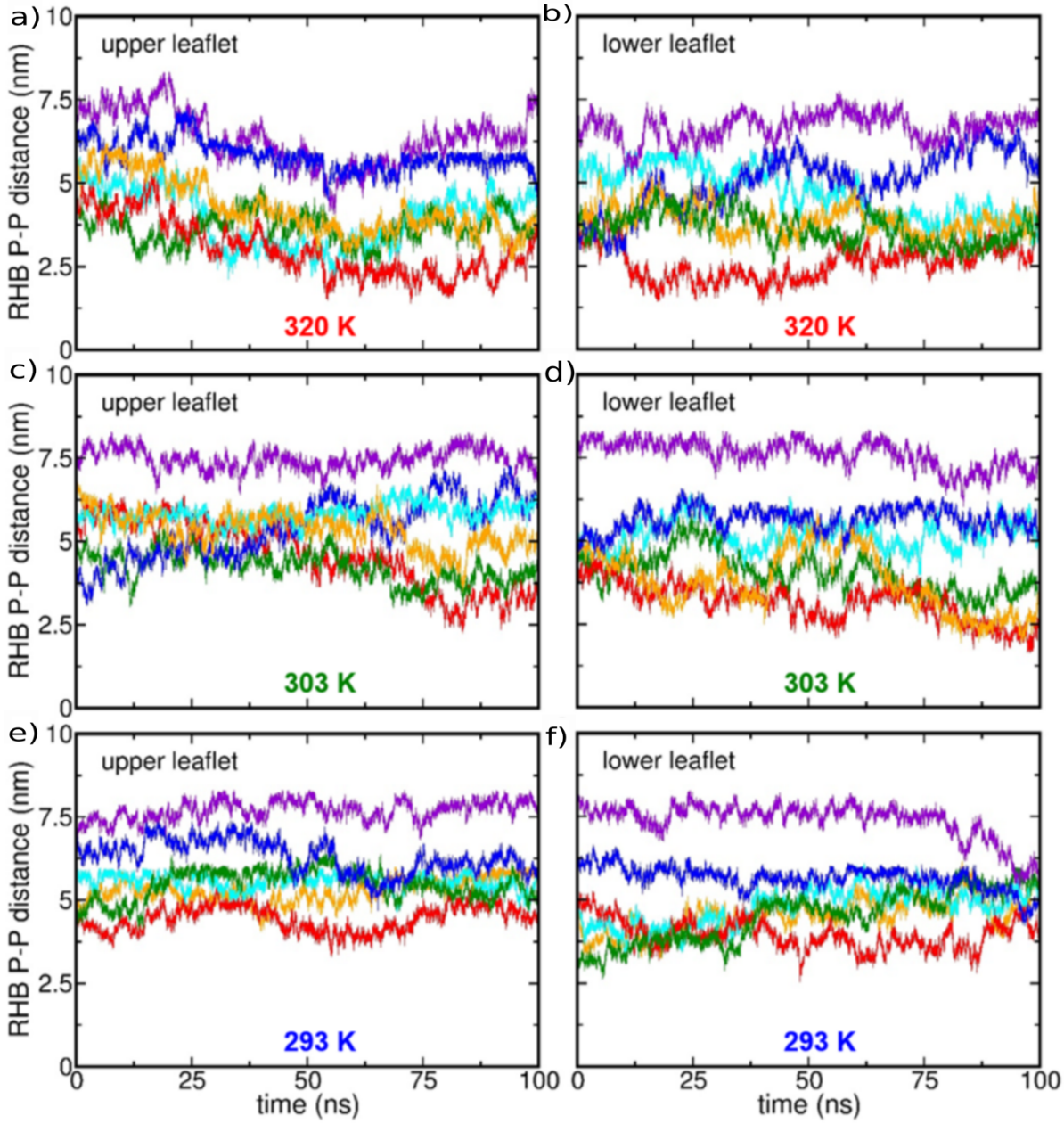

Figure 5.3: RHB P-P distances from AA MD simulations of RHB-DOPC lipid bilayers with a 2 mol% RHB concentration performed at a), b) 320 K, c), d) 303 K and e), f) 293 K. Different colors are used for different P-P distances between all possible pairs of RHB molecules in upper and lower leaflets of the RHB-DOPC lipid bilayer. The formation of RHB aggregates is not observed at any temperature (RHB P-P distance > 2 nm).

Moreover, radial distribution functions (RDFs) of intermolecular P-P pairs for both DOPC and RHB lipids were evaluated at every temperature (Figure 5.4a,b). RDFs show two main peaks and a more broadened third peak corresponding to successive lipid shells, where the first shell

extends from 0.6 to 0.75 nm, the second one from 0.8 to 1 nm and the third one from 1.05 to 1.25 nm. RDFs of DOPC-DOPC pairs were marginally influenced by temperature, showing no significant deviations on the height and the peak positions as the temperature is raised from 293 K to 320 K (Figure 5.4a).

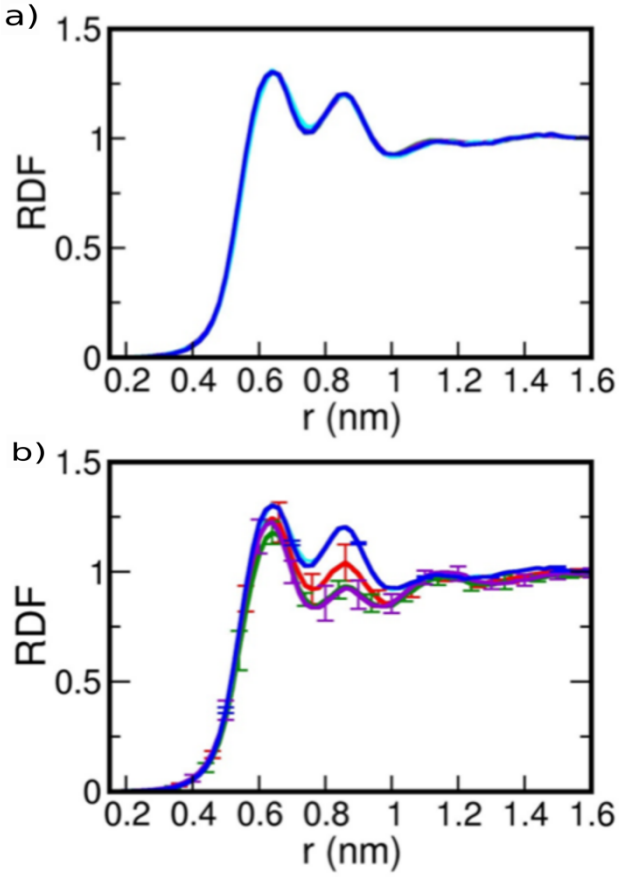

Figure 5.4: P-P radial distribution functions (RDFs) of DOPC-DOPC and RHB-DOPC pairs from MD simulations of DOPC and RHB-DOPC lipid bilayers at three different temperatures. a) P-P RDFs of DOPC-DOPC pairs from MD simulations of DOPC (blue: 293 K, turquoise: 303 K and cyan: 320 K) and RHB-DOPC (violet: 293 K, magenta: 303 K and purple: 320 K) lipid bilayers. Note that the six lines appear as superimposed on one another. b) P-P RDFs of DOPC-DOPC (blue: 293 K, turquoise: 303 K and cyan: 320 K) and RHB-DOPC pairs (purple: 293 K, red: 303 K and green: 320 K) from DOPC and RHB-DOPC lipid bilayer simulations. Error bars of P-P RDFs DOPC-DOPC pairs in pure DOPC and RHB-DOPC systems are negligible and omitted for clarity in panel a. In all diagrams of panel b error bars correspond to standard deviations.

The positions of the three RDF peaks of RHB-DOPC pairs, which determine the probability of finding phosphate groups in the neighboring shells, are consistent throughout all lipid membrane simulations at different temperatures, while the peak heights are somewhat different as a result of local lipid rearrangements upon RHB insertion: in terms of P-P RDF, the lipid bilayer appears less structured around RHB lipids, with a slight and a more pronounced decrease of the peak height at 0.64 and 0.86 nm, respectively, with respect to pure DOPC. In turn, this perturbation affects the local DOPC structure in both second and third lipid shells. This result could be a consequence of the interaction of the fluorescent-labeled lipid headgroup with the surrounding lipid bilayer surface at the water-membrane interface (*vide infra*). Note, however, that since RHB lipids are two orders of magnitude less than DOPC lipids, RHB-DOPC results are affected by a larger noise with respect to DOPC ones (Figure 5.4b).

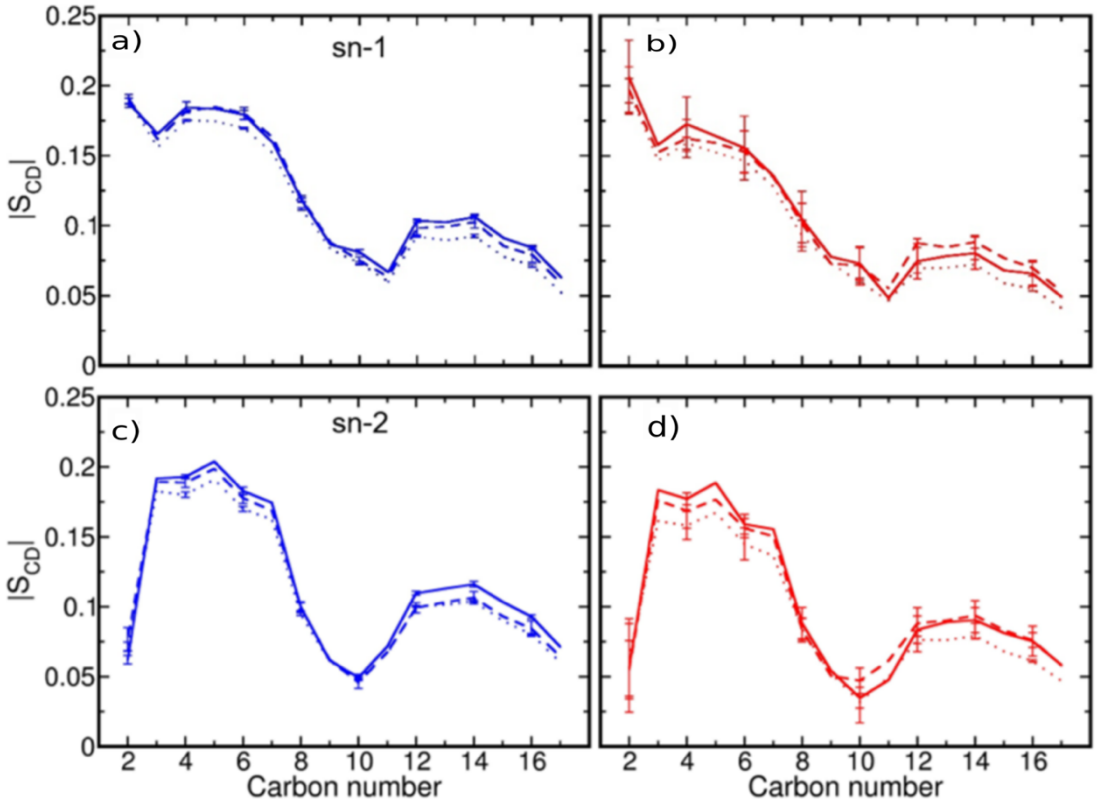

Figure 5.5: Deuterium order parameters (SCD) evaluated for sn-1 and sn-2 lipid acyl chains from MD simulations of DOPC and RHB-DOPC lipid bilayers at three different temperatures (solid, dashed and dotted lines: 293 K, 303 and 320 K, respectively). SCD of a), b) sn-1 and c), d) sn-2 acyl chains of DOPC and RHB molecules, respectively, from MD simulations of DOPC (blue, DOPC lipids) and RHB-DOPC (red, RHB lipids) lipid bilayers. Errors were estimated as standard deviations.

Furthermore, we evaluated the deuterium order parameters, S_{CD}, for both the hydrocarbon acyl chains (i.e., sn-1 and sn-2 chains) of DOPC and RHB lipids, which share the same chemical structure with a double bond between carbon 9 and 10 (Figure 5.1a). The S_{CD} values can vary between 0 to 0.5, where smaller values indicate more flexible/disordered regions while higher values correspond to relatively more rigid/ordered regions [105,126]. The computed S_{CD} for DOPC molecules in a pure lipid bilayer, as depicted in Figure 5.5a and c, shows that the degree of flexibility of the lipid tails does increase when going towards the terminal ends, since the mobility is rather unrestricted in the middle of the bilayer, with the exception of the typical sharp dip caused by the presence of the double bond (i.e., C=C at carbon number 9 and 10) and the unusual small value of C2 in the second acyl chain (i.e., sn-2). Overall, S_{CD} of DOPC matches well reported order parameters from previous computational [127,169] and experimental [128] studies at different temperatures. Concerning RHB, S_{CD} is observed to be rather similar to the unlabeled counterpart, as expected giving the identical chemical nature of hydrophobic acyl chains, although S_{CD} values do appear as consistently lower than DOPC (Figure 5.5b,d). Hence, the present result suggests that RHB lipids are somewhat less ordered in comparison to DOPC. Both DOPC and RHB S_{CD} are observed to decrease when the temperature is increased (Figure 5.5a-d). In RHB-DOPC bilayers, DOPC displays order parameters similar to pure DOPC membranes (Figure 5.6). The softening induced by the bulky fluorescent headgroups of RHB molecules, as shown by the increased A_L, has essentially a negligible effect on the order parameters of DOPC molecules in RHB-DOPC membranes, in contrast with the reduction observed in DPPC lipid bilayers containing RHB-DPPE lipids [152,170]. This result is most probably due to the more fluid nature of unsaturated DOPC lipids with respect to saturated DPPC lipids. Overall, the above structural analyses (i.e., lipid bilayer thickness, A_L, RDF and S_{CD}) have shown no large effects caused by the introduction of RHB in the DOPC bilayer, and expected changes upon temperature increase.

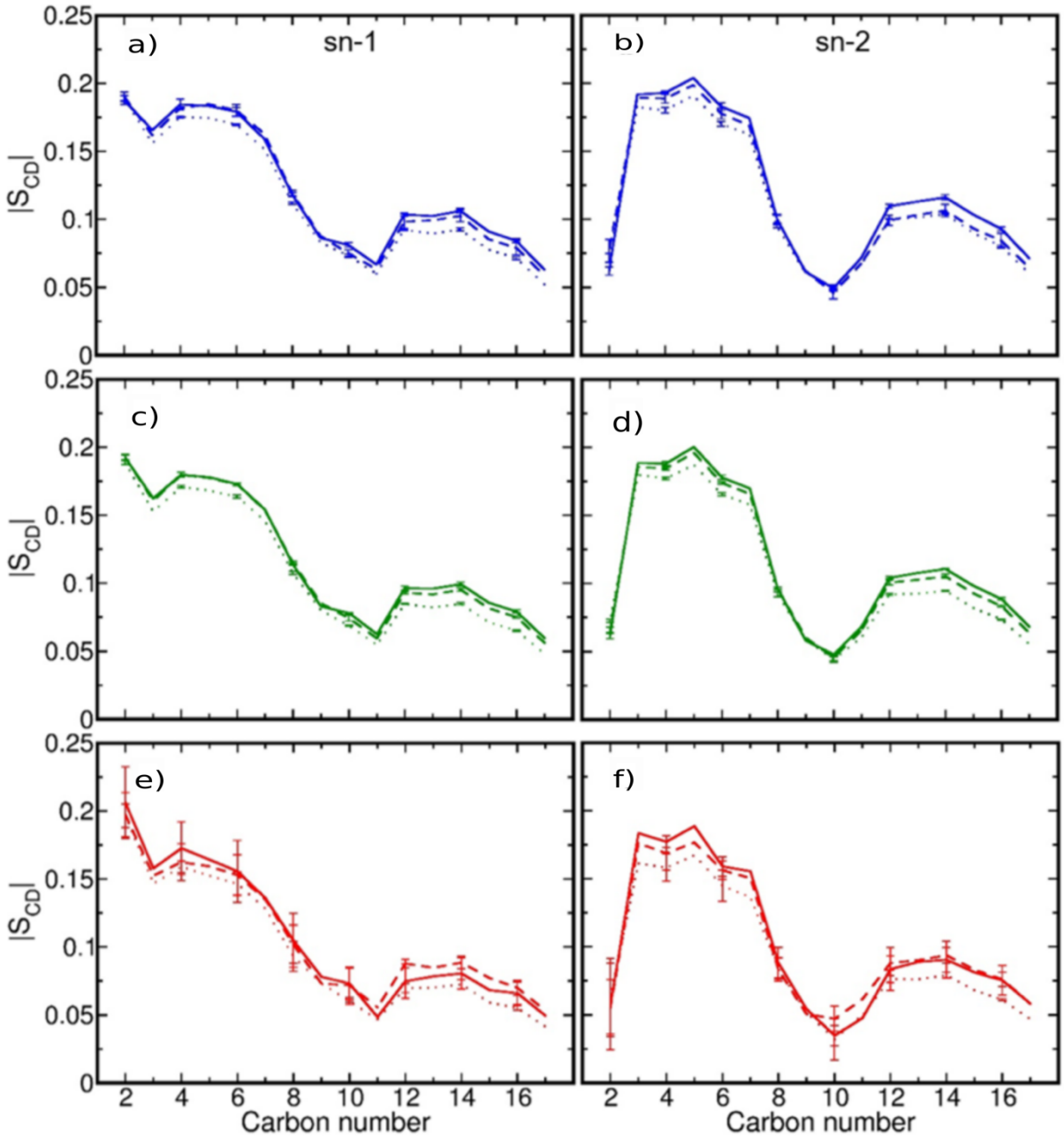

Figure 5.6: Deuterium order parameters (S_{CD}) evaluated for sn-1 and sn-2 lipid acyl chains from MD simulations of DOPC and RHB-DOPC lipid bilayers at three different temperatures (solid, dashed and dotted lines correspond to 293 K, 303 and 320 K, respectively). S_{CD} of a), c), e) sn-1 and b), d), f) sn-2 acyl chains of DOPC and RHB molecules, respectively, from MD simulations of pure DOPC (blue) and RHB-DOPC (DOPC and RHB order parameters are shown in green and red, respectively) lipid bilayers. Errors were estimated as one standard deviation.

5.3.2 Lipid lateral diffusion in pure DOPC and RHB-DOPC membranes

Mean square displacements (MSD) and diffusion coefficients of lipids in DOPC and RHB-DOPC membranes were estimated from corresponding MD simulations, as described in the Methods, to provide information about the lipid lateral dynamics (Figure 5.7a,b). The MSD exhibits an anomalous non-linear increase in the initial 10 ns, which is due to the so-called "cage effect" occurring in short timescale motions of the lipids [129]. The lipid dynamics becomes fully Brownian at longer timescales (i.e., > microsecond), corresponding to the diffusive regime usually detected in fluorescence experiments. Because of the "cage effect", the first 10 ns of each trajectory were not included in the analysis of diffusion coefficients, which were calculated by fitting the MSD as reported in the Methods. The obtained diffusion coefficients at three different temperatures are reported in Table 5.1. At 293 K the diffusion coefficient of DOPC is 7.0 $\pm$ 0.4 $\mu m^2 s^{-1}$, which is in good agreement with previous experimental and computational studies [127]. Upon temperature increase to 303 K, the DOPC diffusion coefficient also increases to 8.4 $\pm$ 0.4 $\mu m^2 s^{-1}$, which is in line with previous experimental and computational studies reporting a diffusion constant in the range 5-14 $\mu m^2 s^{-1}$, depending on temperature, relative water content and the nature of the planar membrane (e.g., GUVs vs SLBs) [127,147]. At the highest temperature (320 K), the lateral mobility of DOPC molecules corresponds to a diffusion coefficient of 13.4 $\pm$ 0.1 $\mu m^2 s^{-1}$, which is still within the range of experimental and computational values reported in the literature. Moreover, DOPC mobility was also analyzed from MD simulations of the RHB-DOPC bilayer at different temperatures, providing very similar diffusion coefficients as seen above (Table 5.1). On the other hand, RHB molecules displayed some noticeable slower dynamics with respect to unlabeled lipids at all temperatures, reflecting the larger hydrodynamic drag due to the bulky Rhodamine B headgroup. In particular, RHB diffusion coefficients underwent reductions of about 47%, 20% and 16% at 293 K, 303 K and 320 K, respectively, as compared to pure DOPC diffusion coefficients (Figure 5.7b and Table 5.1). The increase of temperature affects similarly the diffusion coefficient of both DOPC and RHB molecules in pure DOPC and RHB-DOPC lipid bilayers, causing an expected increase in the lateral mobility of both lipids. In our previous study, the lateral diffusion of RHB lipids at different concentrations was also investigated experimentally in GUVs of RHB-DOPC with FCS measurements [150]. The measured diffusion coefficient of the RHB lipid at a concentration comparable with that of the simulated systems

(i.e., 1 %) is 8.7 $\pm$ 2.4 $\mu m^2 s^{-1}$, which is close to the computed diffusion coefficient at 303 K (Table 5.1).

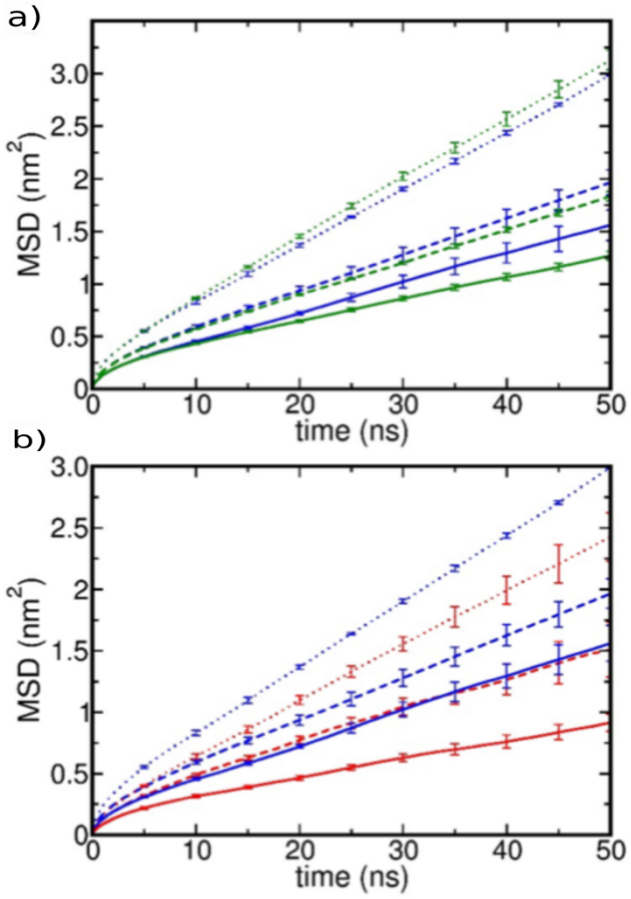

Figure 5.7: a) Mean square displacement (MSD) of DOPC lipids evaluated as a function of time from MD simulations of DOPC (blue) and RHB-DOPC (green) lipid bilayers at three different temperatures (solid, dashed and dotted lines: 293 K, 303 and 320 K, respectively). b) MSD evaluated as a function of time from MD simulations of DOPC (DOPC lipids MSDs are shown in blue) and RHB-DOPC (RHB lipids MSDs are shown in red) lipid bilayers at three different temperatures (solid, dashed and dotted lines: 293 K, 303 and 320 K, respectively). Error bars correspond to standard errors. Differences in error bars reflects mainly the different number of systems (i.e., 400 DOPC lipids and 8 free RHB lipids).

5.3.3 Partitioning of RHB lipids into the membrane

Partial density profiles of different chemical groups of DOPC and RHB molecules from MD simulations of RHB-DOPC (Figure 5.8) bilayers show the effect of temperature on the partitioning of RHB polar headgroups into the lipid membrane (Figure 5.8b,d). In particular, partial density profiles of different moieties of the DOPC molecule are affected by the

temperature in a similar way for both pure DOPC and RHB-DOPC bilayers (data not shown). As the temperature is increased, the density of DOPC phosphate groups decreases and it undergoes an inward shift in the position of its peaks (Figure 5.8a). This result is consistent with the decrease of membrane thickness in going from 293 K to 320 K (Table 5.1). A similar behavior is also observed for other DOPC chemical groups (Figure 5.9,Figure 5.10,Figure 5.11). It is worth noting that RHB sulfonate groups mainly partition in the region of DOPC phosphate groups at every temperature (Figure 5.8b). However, RHB sulfonate groups display also a relevant partition in the water phase as evidenced by the shoulders around ~2.7 nm in the partial density profiles at 293 K and 303 K. Interestingly, RHB polar headgroups mainly partition at the level of DOPC glycerol backbone, slightly above the region of DOPC carbonyl groups (Figure 5.8c,d and Figure 5.9), as shown by the pronounced peak of the partial density profile around 1.5 nm from the bilayer center at every temperature (Figure 5.8d). Moreover, partial density profiles of RHB fluorescent headgroups show even more pronounced shoulders around ~2.7 nm at 293 K and 303 K, indicating their favorable interaction with bulk water as observed for sulfonate groups (Figure 5.8b,d). Due to the low statistics (only 8 RHB molecules in each simulated system), we should stress that the presence of these shoulders in the density profiles of RHB fluorescent headgroups does not allow us to quantitatively describe this interaction at the water-membrane interphase. However, these results clearly highlight the amphiphilic nature of the sulforhodamine (SRB) moiety of the RHB molecule, as supported by a recent study reporting the penetration of SRB molecules in sodium dodecyl sulfate (SDS) micelles [171].

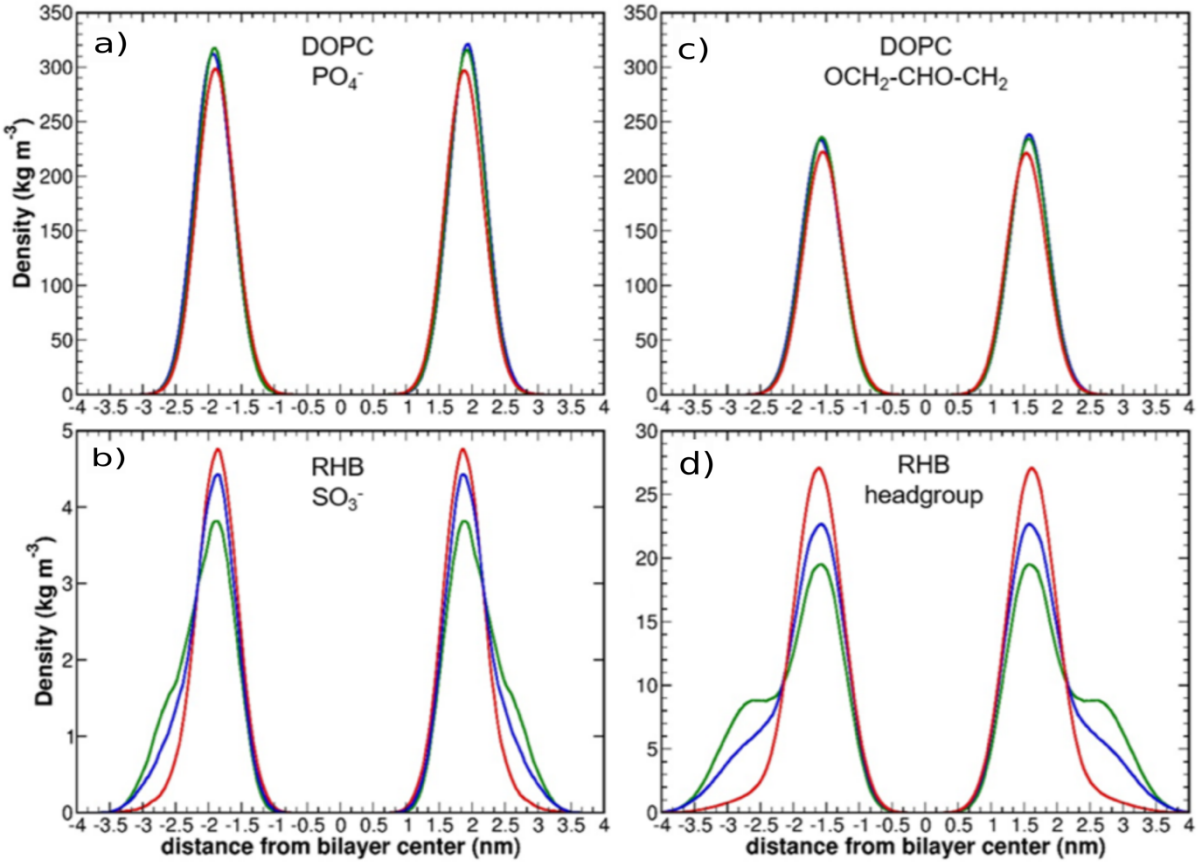

Figure 5.8: Partial density profiles across the lipid bilayer for different lipid components of DOPC and RHB lipids from MD simulations of RHB-DOPC lipid membranes at three different temperatures. Blue, green and red lines correspond to 293 K, 303 and 320 K, respectively, for a) DOPC phosphate (PO_4^-), b) RHB sulfonate (SO_3^-), c) DOPC glycerol (OCH2-CHO-CH2) and d) RHB headgroup (NH-sulforhodamine B) groups. The partial density of each lipid moiety was initially averaged over the last 50 ns of the simulation and, then, the final average was performed over the four replicas at each temperature.

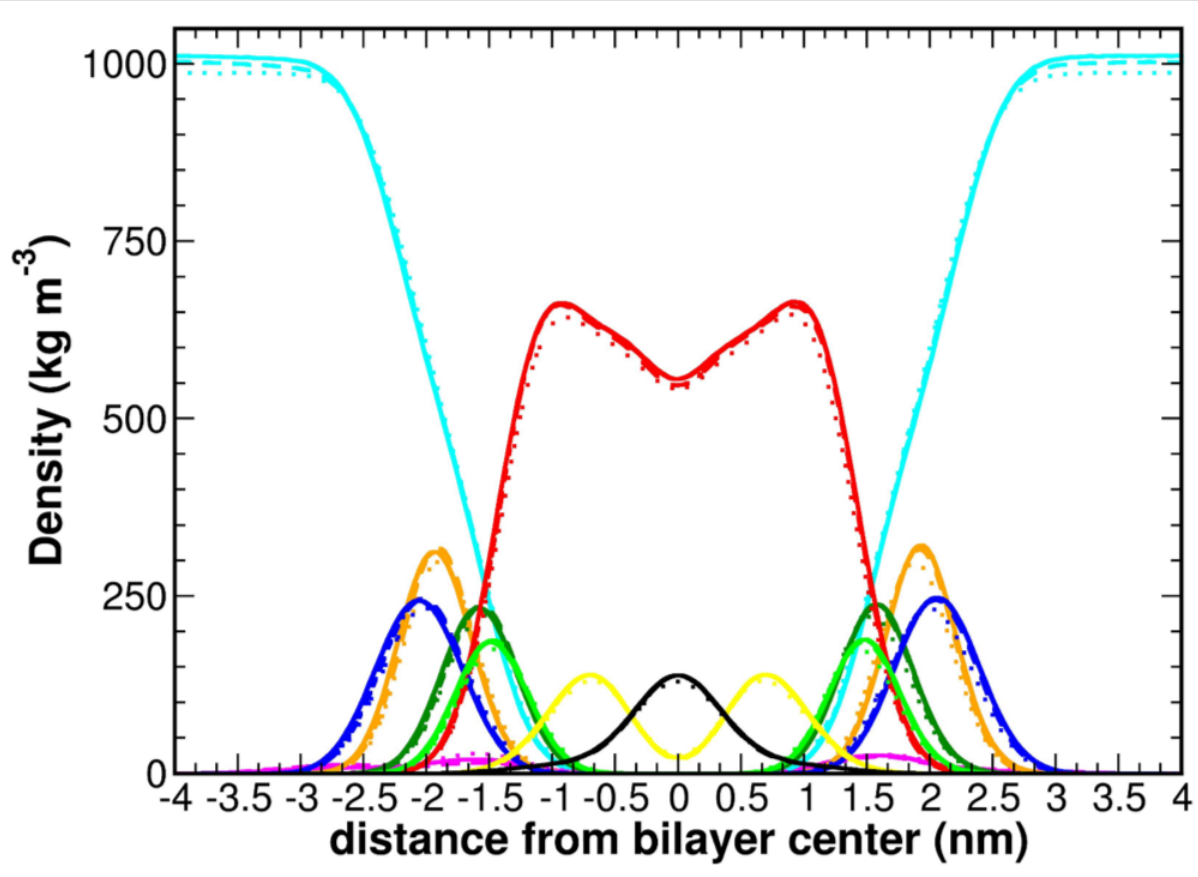

Figure 5.9: Partial density profiles across the lipid bilayer for different lipid components of DOPC and RHB lipids from MD simulations of RHB-DOPC lipid membranes at three different temperatures. Solid, dashed and dotted lines correspond to 293 K, 303 and 320 K, respectively. DOPC choline (CH_2-CH_2-N-$(CH_3)_3^+$), phosphate (PO_4^-), carbonyl (C=O), glycerol (OCH_2-CHO-CH_2), methylene (CH_2), double bond (C=C) and methyl (CH_3) groups are shown with blue, orange, light green, green, red, yellow and black lines. RHB fluorescent polar headgroups (NH-sulforhodamine B) are shown with magenta lines. The partial density of each lipid moiety was initially averaged over the last 50 ns of the simulation and, then, the final average was performed over the four replicas at each temperature.

Moreover, the observed mass distribution of the Rhodamine B moiety of the RHB molecule is in good agreement with a recent computational investigation [152]. It is also worth noting that the partial density profiles of RHB chemical groups in common with DOPC molecules exhibit the same peak positions as in unlabeled lipids and a similar behavior when temperature is raised from 293 K to 320 K (Figure 5.12 and Figure 5.13). Another interesting aspect of RHB fluorescent headgroups is the interaction with water molecules as a function of temperature.

The average number of water molecules within one hydration layer (using a cut-off radius of 0.28 nm) of each RHB headgroup is 19 ± 2, 23 ± 2 and 15 ± 2 at 293 K, 303 K and 320 K, respectively (Figure 5.14). Hence, the observed higher hydration level of RHB fluorescent headgroups at temperatures below 320 K does reflect the shoulders in partial density profiles described above.

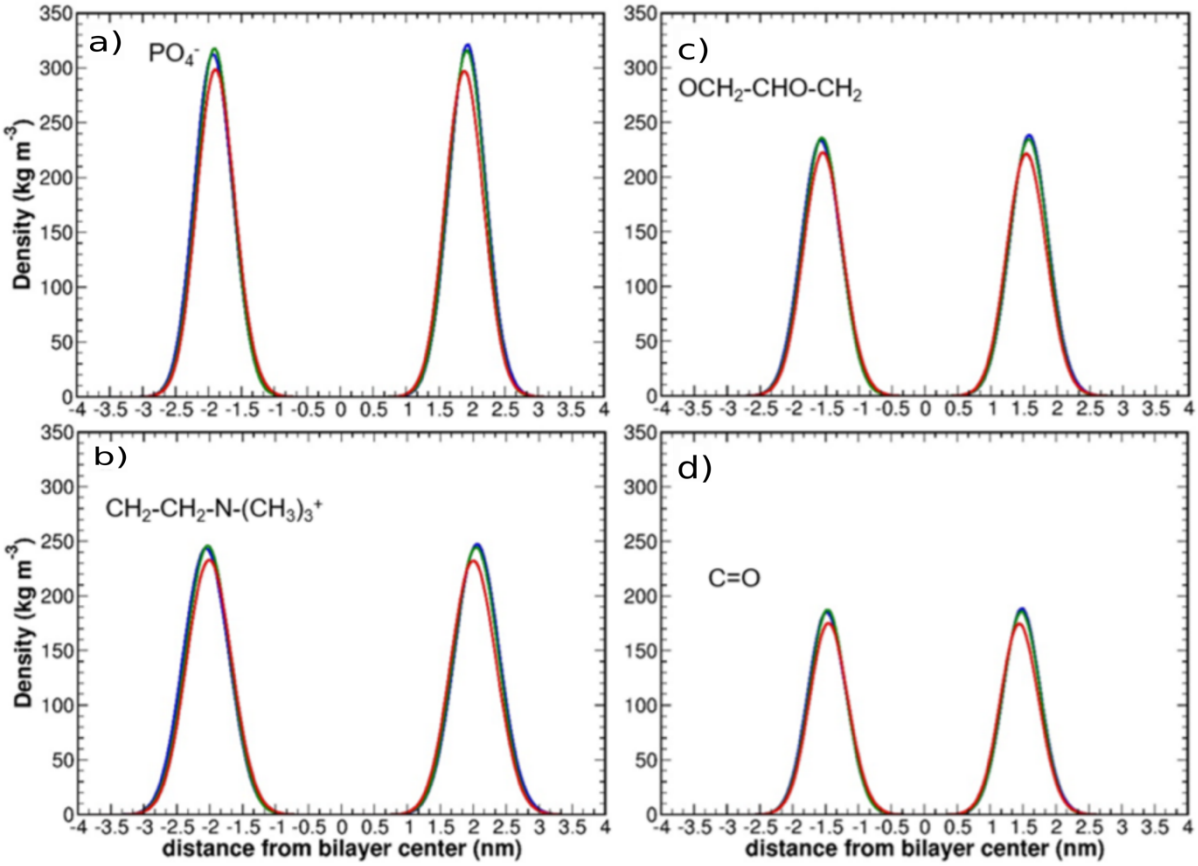

Figure 5.10: Partial density profiles across the lipid bilayer for different lipid components of DOPC lipids from MD simulations of RHB-DOPC lipid membranes at three different temperatures. Blue, green and red lines correspond to 293 K, 303 and 320 K, respectively, for DOPC a) phosphate (PO_4^-), b) choline (CH_2-CH_2-N-$(CH_3)_3^+$), c) glycerol (OCH_2-CHO-CH_2) and d) carbonyl (C=O) groups. The partial density of each lipid moiety was initially averaged over the last 50 ns of the simulation and, then, the final average was performed over the four replicas at each temperature.

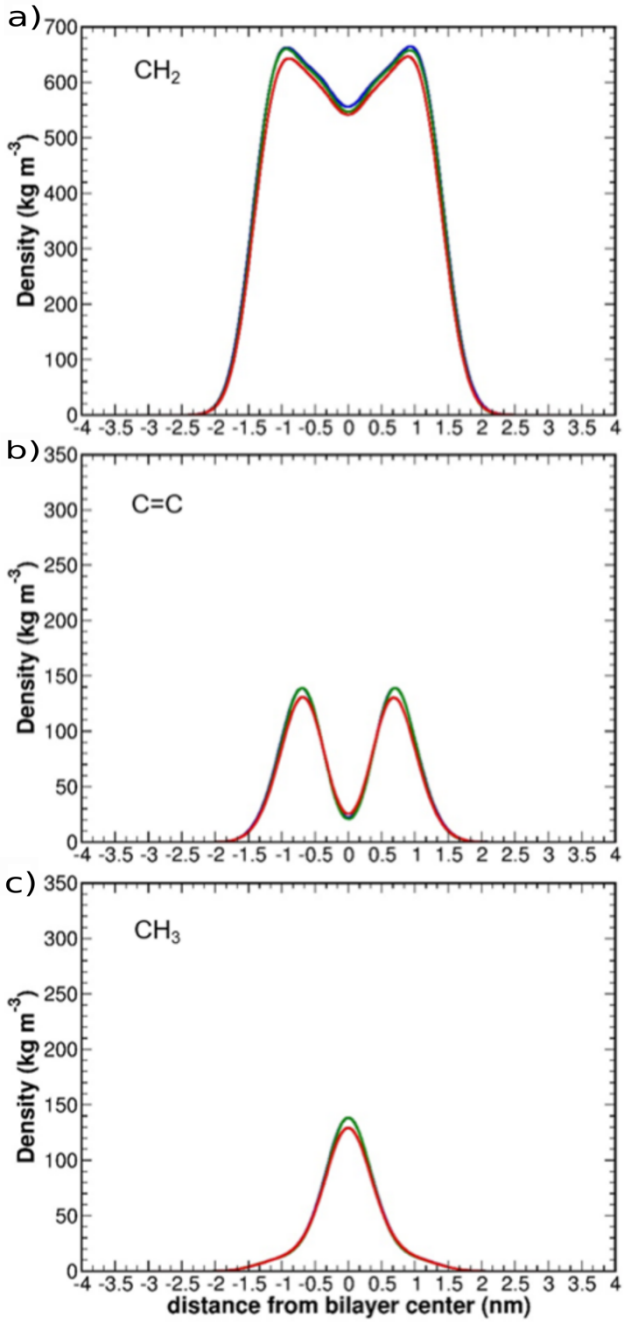

Figure 5.11: Partial density profiles across the lipid bilayer for different lipid components of DOPC lipids from MD simulations of RHB-DOPC lipid membranes at three different temperatures. Blue, green and red lines correspond to 293 K, 303 and 320 K, respectively, for DOPC a) methylene (CH_2), b) double bond (C=C) and c) methyl (CH_3) groups. The partial density of each lipid moiety was initially averaged over the last 50 ns of the simulation and, then, the final average was performed over the four replicas at each temperature.

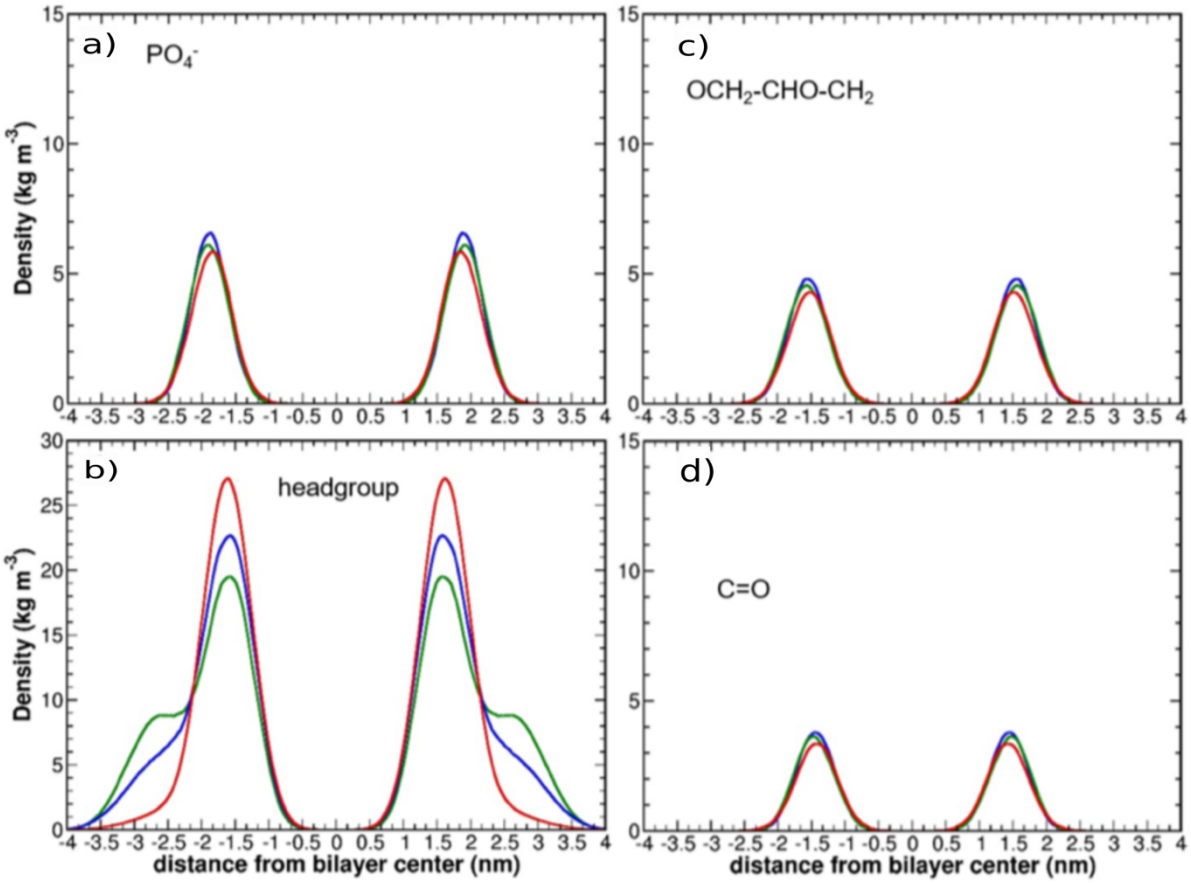

Figure 5.12: Partial density profiles across the lipid bilayer for different lipid components of RHB lipids from MD simulations of RHB-DOPC lipid membranes at three different temperatures. Blue, green and red lines correspond to 293 K, 303 and 320 K, respectively, for RHB a) phosphate (PO_4^-), b) fluorescent polar head (NH-sulforhodamine B), c) glycerol (OCH_2-CHO-CH_2) and d) carbonyl (C=O) groups. The partial density of each lipid moiety was initially averaged over the last 50 ns of the simulation and, then, the final average was performed over the four replicas at each temperature.

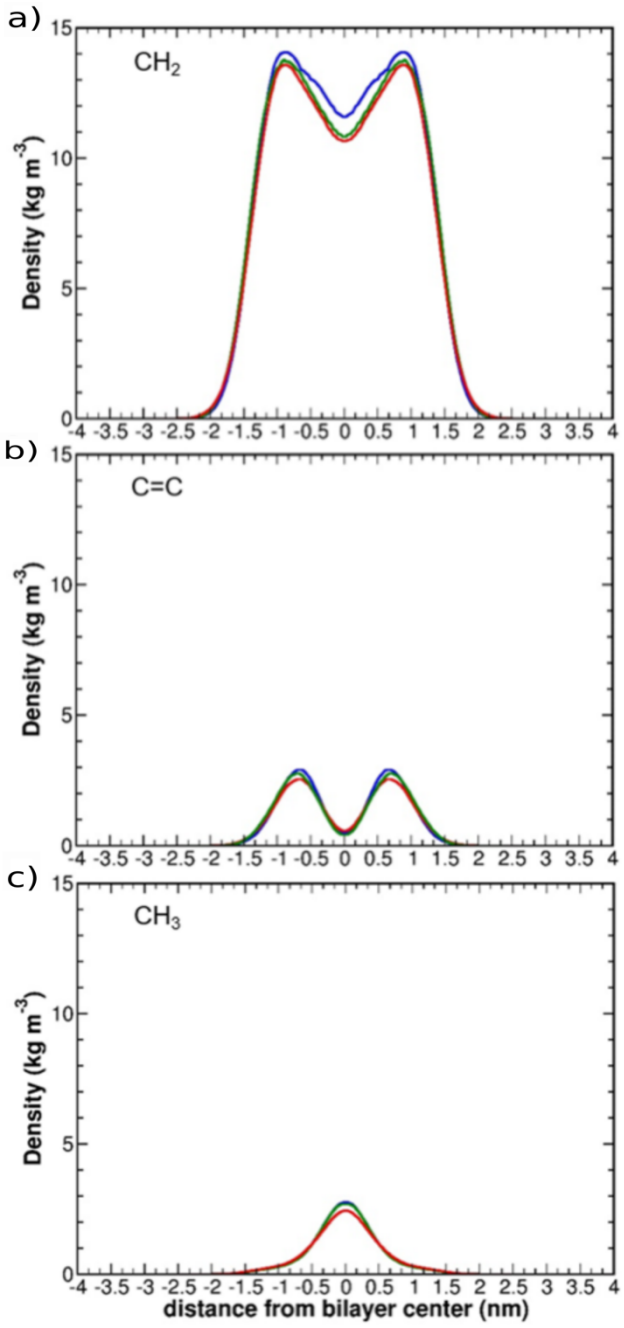

Figure 5.13: Partial density profiles across the lipid bilayer for different lipid components of RHB lipids from MD simulations of RHB-DOPC lipid membranes at three different temperatures. Blue, green and red lines correspond to 293 K, 303 and 320 K, respectively, for RHB a) methylene (CH_2), b) double bond (C=C) and c) methyl (CH_3) groups. The partial density of each lipid moiety was initially averaged over the last 50 ns of the simulation and, then, the final average was performed over the four replicas at each temperature.

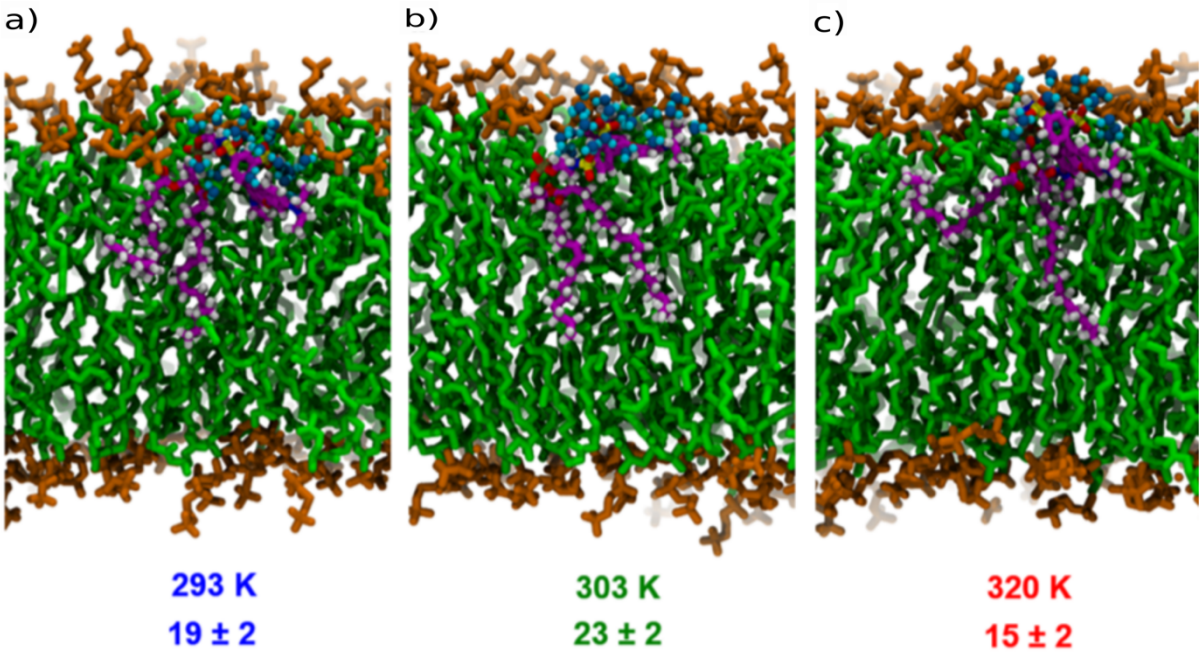

Figure 5.14: Snapshots of a single RHB molecule at a) 293 K, b) 303 and c) 320 K show the effect of temperature on the hydration of the RHB fluorescent headgroup. The lower panel of the figure reports the temperature and the average number of water molecules within one hydration layer (0.28 nm) of any atom of the RHB fluorescent headgroup from MD simulations of RHB-DOPC lipid membranes at three different temperatures. The number of water molecules was averaged over the last 50 ns of each simulation at each temperature. The errors are standard deviations. The same color code of Fig. 1 is used for DOPC and RHB molecules. Oxygen and hydrogen atoms of water molecules are shown in skyblue and cyan, respectively.

5.3.4 Local hydration at the RHB-DOPC membrane surface

We have also analyzed the water partial density profile for pure DOPC and RHB-DOPC bilayers going from the bulk solution to the center of each lipid bilayer along a direction normal to the membrane surface at every simulated temperature (Figure 5.15a). In pure DOPC, the observed water partial density displays a smooth drop while going from bulk (i.e., distances more than ~2.5 nm) towards the bilayer center, in agreement with previous results reported in the literature. In these water density profiles: (i) negative and positive values until ~2.5 nm correspond to lower and upper leaflet regions including water-membrane interfaces; (ii) negative and positive values above ~2.5 nm refer to bulk solution. It is worth noting that the

presence of RHB lipids induced a slight increase of water density in the region defined by DOPC carbonyl and glycerol backbone groups (i.e., -1.5 nm; 1.5 nm) at every simulated temperature (Figure 5.16). This result, which becomes more evident at the highest temperature (Figure 5.15b,c), indicates that the RHB-DOPC membrane has a higher local hydration at the level of the glycerol backbone than that observed in pure DOPC (note that the membrane thickness is basically the same in both systems).

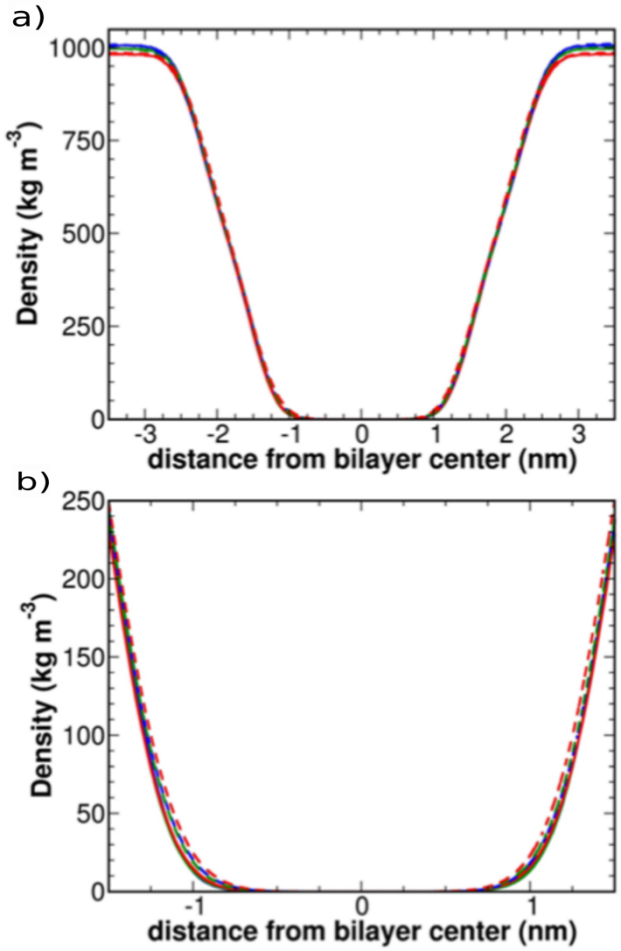

Figure 5.15: Water density distribution evaluated along a direction normal to the membrane surface from MD simulations of DOPC (solid lines) and RHB-DOPC (dashed lines) lipid bilayers at three different temperatures. a) Blue, green and red lines correspond to 293 K, 303 and 320 K, respectively. The origin was set to the average position of P atoms in both leaflets. Negative and positive values until ~2.5 nm correspond to lower and upper leaflets bilayer regions including water-membrane interfaces, respectively. Negative and positive values above ~2.5 nm refer to the bulk solution. b) A zoomed view in the region defined by the highest peak intensity of partial density profiles of DOPC glycerol and carbonyl groups (1.5 nm) show a higher water density in RHB-DOPC (dashed lines) lipid bilayers as compared to DOPC membranes (solid lines) at every temperature.

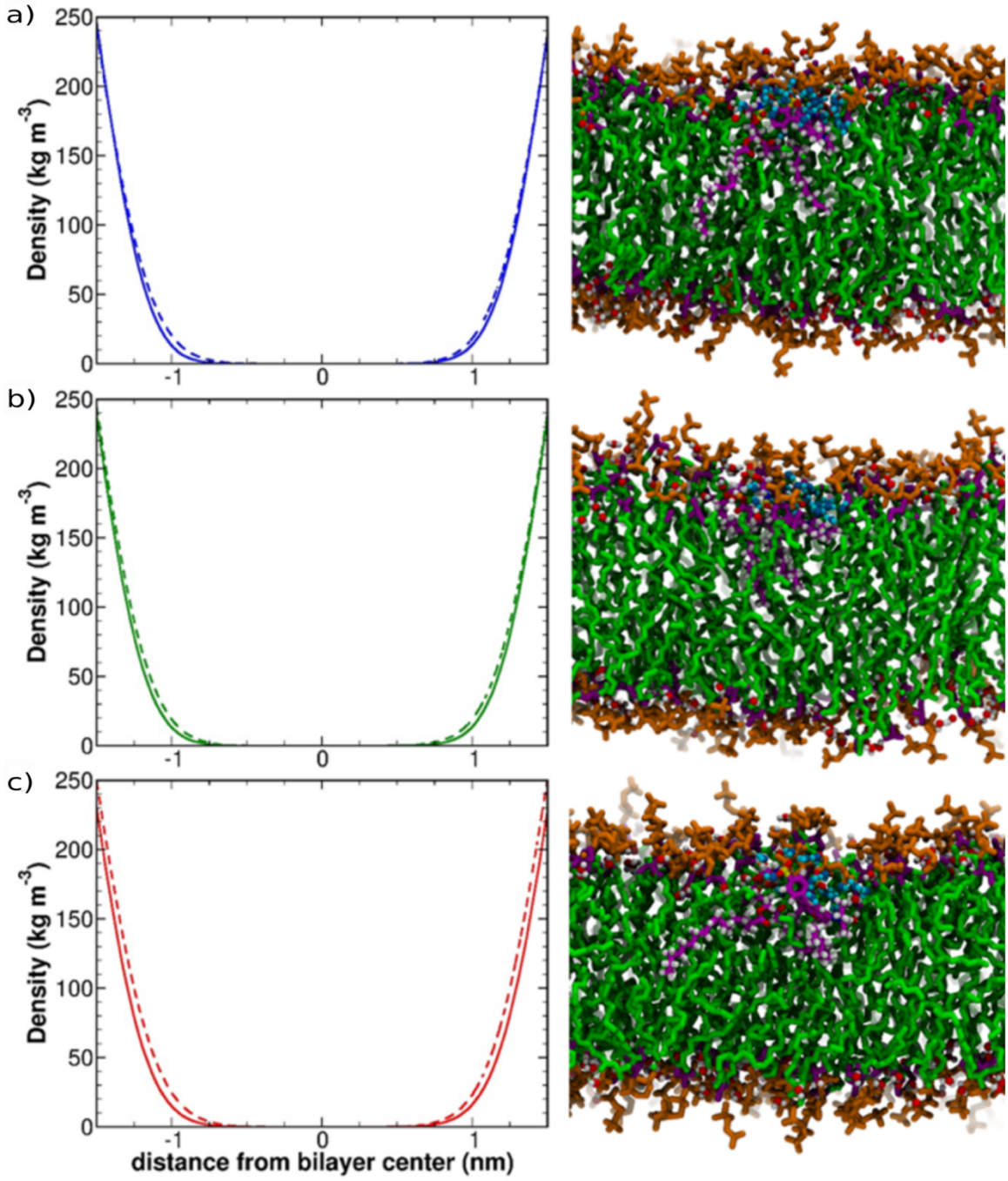

Figure 5.16: Water partial density profiles in the region defined by the highest peak intensity of partial density profiles of DOPC glycerol and carbonyl groups (1.5 nm) from MD simulations of DOPC (solid lines) and RHB-DOPC (dashed lines) lipid bilayers at a) 293 K (blue lines), b) 303 K (green lines) and c) 320 K (red lines). Snapshots of single RHB molecules at different temperatures show the increase in the hydration around RHB fluorescent headgroups below the DOPC glycerol backbone region. The same color code of Fig. 6 is used for DOPC, RHB and different types of water molecules.

5.3.5 Orientation of the RHB fluorescent headgroups

The orientation of RHB headgroups with respect to the bilayer normal has been analyzed as a function of temperature through the angle distributions of horizontal (v1) and vertical (v2) molecular axes, as defined in Figure 5.1a and Figure 5.2(see the Methods section) (Figure 5.17). In particular, v1 has a unimodal distribution (α angle) centered at about 90°: the polar headgroups on average remain parallel to the membrane surface at every simulated temperature (Figure 5.17a and Table 5.2). The v2 molecular axis is almost parallel to the amino-oxygen (O6f) vector (see Fig. 1a) and its pronounced tilting suggests either the insertion into the membrane or the accessibility to bulk water (an angle of ~180°, 90° and 0° denotes a RHB headgroup pointing towards the bilayer center, parallel to the bilayer plane, and outwardly directed, respectively). Indeed, v2 has a bimodal distribution, suggesting that it can adopt two different orientations with an average tilt angle (β) of about 50° and 120° with respect to the bilayer normal, especially at 293 K and 303 K (Figure 5.17b). However, the population of RHB polar headgroups with an average β angle of ~120° is larger than that displaying an angle of ~50° (Table 5.2). Interestingly, this behavior is more evident when the bimodal distribution becomes almost completely unimodal at 320 K (Figure 5.17b), which is also reflected by the shift of the average tilt angle towards 120° (i.e., 114°, see Table 5.2). These results are also in line with the computed density profiles of the RHB fluorescent headgroups at different temperatures (Figure 5.8b) and they show the existence of two populations of RHB headgroups having two different orientations relative to the lipid bilayer normal, in which the RHB headgroup can be either more exposed to water (β = ~50°) or incorporated into the membrane (β = ~120°). Moreover, it is also worth noting that RHB fluorescent headgroups exhibit an increased insertion into the membrane as the temperature is raised from 293 K to 320 K. This behavior supports the capability of fluorescent polar moieties to act as amphiphilic groups even in DOPC bilayers [171]. Furthermore, we observed that the pendant group of the SRB moiety of RHB, which is formed by a charged sulfonate atomic group and a sulfobenzene group and mainly resides in the water-membrane interface (Figure 5.8b), is basically perpendicular to the one containing the xanthene group, 90° ± 10° [171], since the sulfonate group contributes to stabilize this relative orientation between the pendant and the xanthene moiety.

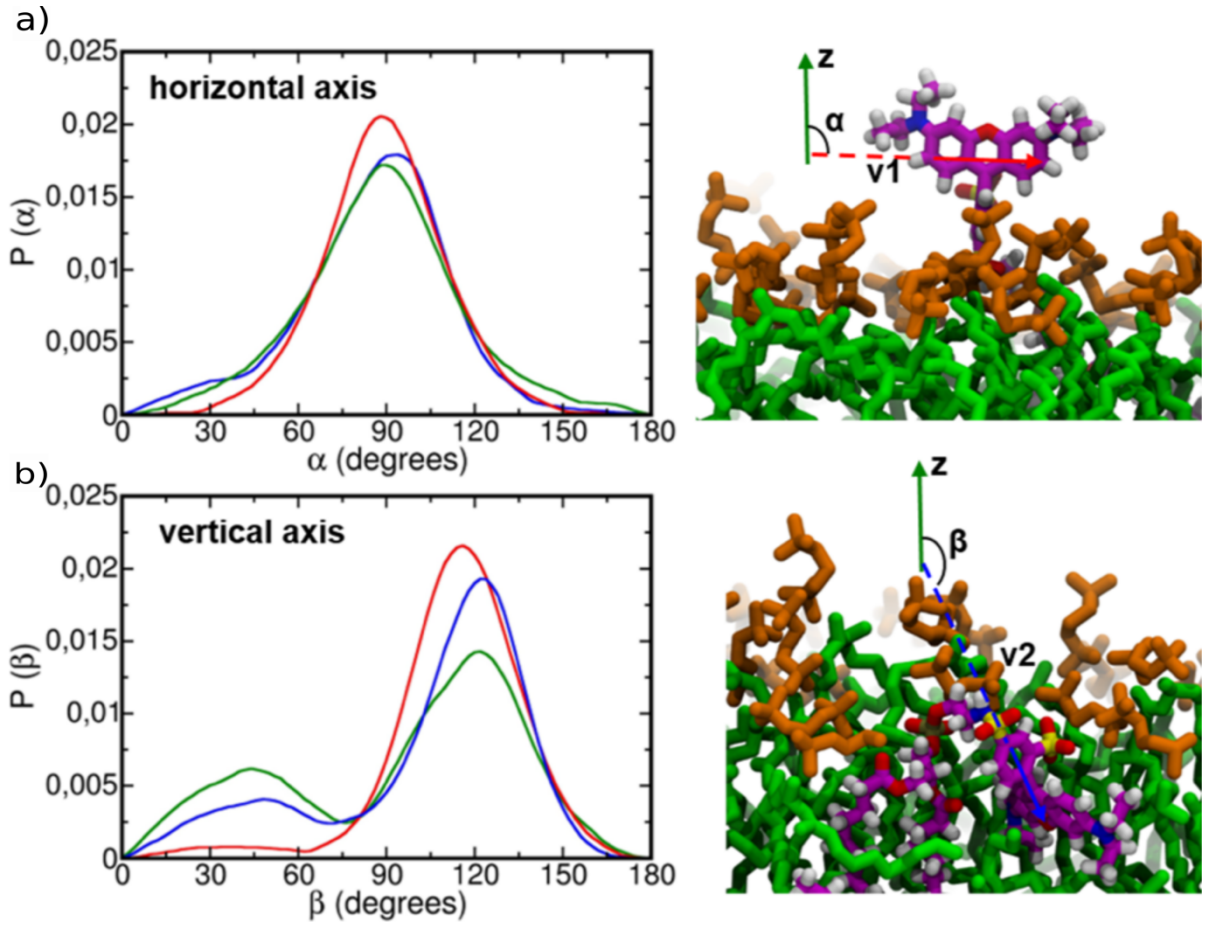

Figure 5.17: Angle distributions of a) horizontal (v1) and b) vertical (v2) axes of RHB fluorescent polar headgroups at three different temperatures. Blue, green and red lines correspond to angle distributions at 293 K, 303 and 320 K, respectively. Horizontal and vertical axes of the RHB polar fluorescent headgroup forming angles α and β, respectively, with the lipid bilayer normal, which is assumed to be the z-axis, are also shown in the molecular representations of specific RHB molecules in right panels of the figure. The same color code of Fig. 1 is used for DOPC and RHB molecules.

Table 5.2: Average tilt angles of horizontal and vertical axes of RHB fluorescent polar headgroups from AA MD simulations of RHB-DOPC lipid bilayers at three different temperatures.

Temperature (K)	α (°)	β (°)
293	85 ± 14	104 ± 16
303	88 ± 13	96 ± 18
320	89 ± 11	114 ± 10

Errors in tilt angles correspond to one standard deviation.

5.4 Discussion

In this work, we have studied the structural and dynamic properties of a Rhodamine B-labeled lipid inserted into a DOPC membrane as a function of temperature. The introduction of RHB in a DOPC bilayer has a negligible effect on the area per lipid and the bilayer thickness at every simulated temperature (Table 5.1). The presence of RHB molecules did not affect the order parameters of DOPC molecules, which showed a similar temperature dependence with respect to the pure DOPC system (Figure 5.5 and Figure 5.6). Also, RHB molecules display a tiny reduction in their order parameters as compared to DOPC lipids (Figure 5.5). On the other hand, RHB lipids showed a marked decrease in lipid lateral diffusion compared to the unlabeled lipid (Figure 5.7), as measured from our MD simulations (i.e., DOPC: $D = 7.0 \pm 0.4$ $\mu m^2\ s^{-1}$; RHB: $D = 3.7 \pm 0.5$ $\mu m^2\ s^{-1}$ at 293 K, see Table 5.1 for more values at other temperatures). As reported in our previous work [150], this behavior is a consequence of the higher hydrodynamic drag due to the bulky Rhodamine B fluorescent polar headgroup, therefore it is mostly due to the chemical nature of this lipid and it is observed at every temperature. Given that optical analytical methods commonly probe the dynamics of dye-labeled lipids and assuming a non-negligible hydrodynamic effect of the dye, our findings have important consequences on the experimental estimate of lipid mobility. Indeed, lipid diffusion coefficients obtained from fluorescence microscopy applications could be significantly underestimated, hence care must be taken in assessing these measurements. Moreover, the Saffman-Delbrück theory for periodic bilayers [102,103] predicts our computed diffusion constant to be underestimated owing to the limited system size, while the accurate theoretical estimate can be recovered, in principle, at infinite size limit (for the present DOPC simulation, the predicted D^{∞} is ~22 $\mu m^2\ s^{-1}$). Nevertheless, the above considerations on the hydrodynamic effect of the dye are reasonably not affected by the choice of periodic boundary conditions as they stem from a comparative study of same-size molecular systems.

It is worth noting that no significant changes in lipid membrane structure were observed in our MD simulations of RHB-DOPC systems in the absence of dye-labeled lipid aggregates at different temperatures (Table 5.1 and Figure 5.4). More insights emerged from our previous modeling study of the RHB lipid self-assembly, which showed that the structural lipid-lipid rearrangements displayed by the computed P-P RDF had the combined effect of enhancing water insertion into the interior of the membrane lipid bilayer, in stark contrast to the low

concentration RHB-DOPC systems. However, the observed increase in the water partial density profile in correspondence of the region occupied by Rhodamine B headgroups (between 0.5 nm and 1.5 nm, Figure 5.8 and Figure 5.15b) can be associated to the hydrophobicity of the fluorescent dye, which contributes to retain water molecules once inside the lipid bilayer. More pronounced structural changes in the present two-component dye-labeled/unlabeled lipid system are expected to take place at high RHB concentration due to the formation of RHB self-aggregates, which promote a more dramatic increase of the local hydration at the membrane surface. Furthermore, the analysis of the orientation of the RHB headgroups, as observed in this work, shows that the horizontal axis of the RHB fluorescent heads remains essentially parallel to the lipid membrane surface at every temperature. On the contrary, the vertical axis of the RHB headgroups is characterized, on average, by two distinct tilting angles associated to different populations of RHB at low temperatures, while the same analysis provides an almost unimodal distribution at 320 K, thus indicating that amphiphilic RHB heads are less exposed to the water phase and more inserted into the lipid membrane.

Our study confirms that the lipid lateral diffusion, which is the most important dynamic parameter in lipid bilayers, and the bilayer structure are intimately correlated and both reflect the interaction of the RHB headgroups with the surrounding unlabeled DOPC lipids. Overall, our results show evidence of a non-neutral role of the tracer molecule in determining the dynamics, and to less extent the structure, of dye-labeled lipids as compared to unlabeled ones, therefore suggesting a careful use of tagged lipids in the biophysical studies of cell and model membranes.

5.5 Conclusions

Fluorescent probes are widely employed to label lipids for the investigation of structural and dynamic properties of model and cell membranes through optical microscopy techniques. Although the effect of tagging a lipid with an organic dye is generally assumed to be negligible, optically modified lipids can nonetheless affect the local lipid structure and, in turn, the lipid lateral mobility. To better assess this potential issue, all-atom (MD) molecular dynamics simulations have been performed to study structural and dynamic effects in a model DOPC membrane in the presence of a standard Rhodamine B-labeled DOPE lipid (RHB) as a function

of temperature, i.e. 293 K, 303 K and 320 K. As the temperature is increased, we observe similar changes in the structural properties of both pure DOPC and RHB-DOPC lipid bilayers: an increase of the area per lipid, a reduction of the membrane thickness and a decrease of lipid order parameters. The partial density profile of the RHB headgroups and their orientation within the lipid bilayer confirm the amphiphilic nature of the RHB fluorescent moiety, which mainly partitions in the DOPC glycerol backbone region at each temperature. Moreover, at all temperatures, our results on lipid lateral diffusion support a non-neutral role of the dye with respect to the unlabeled lipid mobility, thus suggesting important implications for optical microscopy studies of lipid membranes.

Chapter 6 Probing liquid-ordered and disordered phases in lipid membranes, a combined theoretical and spectroscopic study of a fluorescent molecular rotor

6.1 Introduction

Fluorescent molecular rotors (FMRs) are a class of chemical species capable of modulating their structural and optical properties in response to changes in the viscosity and polarity of the local environment, a feature that make them particularly suitable for sensing and imaging applications.[172–175] Such a peculiar capability mainly arises from the intrinsic structural flexibility of the FMRs: typically, this is ascribed to an unrestrained and environmentally sensitive dihedral angle, whose internal dynamics largely affects the FMR emission intensity and lifetime upon photo-excitation.[176] Thanks to these interesting properties, FMRs can act as viscosity sensors in different environments,[177] and they have been considered in recent years in order to report on local properties of various biophysical systems.[178–180] Among others, a very interesting application field concerns the investigation of lipid membrane structures. Indeed, the composition and organization of biological membranes is one of the most relevant topics in molecular biophysics. The modern view identifies a spatially interlaced combination of liquid ordered (L_o) and liquid disordered (L_d) phases, enriched respectively in saturated and unsaturated lipids, together with different amounts of cholesterol.[181–183] This nano-structured dynamic assembly of L_d and L_o phases does not entail definite boundaries but is organized around the cytoskeletal network. Moreover, such a dynamical membrane organization was

proposed to be relevant for most membrane processes, such as the formation of protein clusters, signal transduction, endocytosis, and cell polarization and motility. [4,182–185] In this context, it is not surprising that FMRs have been employed to detect the different phases of cell membranes[186–189] and to probe the transition from the gel-like to the liquid-crystal phase or, in general, to gain information on the microviscosity of the phospholipid bilayers.[190] In these studies, it was assumed that more viscous environments may slow down the FMR intramolecular motions,[191] thus leading to stronger intensities in the corresponding emission spectra and increased fluorescence lifetimes. An effective relation between solvent viscosity and fluorescence quantum yield is represented by the Forster-Hoffmann model,[192] which has been experimentally proved to hold over a wide range of viscosity and polarity scales [193,194]. It is worth noting that, in turn, lipid membrane viscosity can influence crucial membrane-associated functions, including, for example, passive permeability of hydrophobic molecules, active solute transport and protein-protein interactions.[195]

Despite the success of these applications, many features of the complex dynamical organization of the cell membranes still remain elusive. One fruitful approach towards a better understanding of membrane biophysics is to combine fluorescence microscopy and molecular modeling techniques. Molecular Dynamics (MD), in particular, is commonly adopted for an effective understanding at the atomic level of the dynamics that governs macromolecular functions[196,197] as well as for investigating basic properties of lipid bilayer models, thus potentially uncovering the subtle interplay between membrane structural rearrangements and lipid dynamics.[198] Several types of FMRs have been reported to date: some of them show a more pronounced dependency on the dielectric properties of the surrounding medium, while others are mainly affected by the molecular free volume of the solvent residues.[199–201] An optimal combination of strong solvatochromism and viscosity sensitivity was recently shown by the 4-(diphenylamino)phthalonitrile (DPAP, see structure in

Figure 6.1a), whose peculiar *modus operandi* is based upon a barrier-free flexible rotation of its phenyl rings.[59,202]

Here, we combined MD simulations and fluorescence lifetime imaging microscopy (FLIM) to study the application of DPAP as a probe in detecting local order within lipid bilayers representing simple models for both L_o and L_d phases. To this end, two different phospholipidic systems have been considered, one consisting of pure 1,2-dioleoyl-sn-glycero-3-phosphocholine (DOPC) and another one of dipalmitoylphosphatidylcholine (DPPC) enriched with cholesterol

(DPPC:CHOL 70:30): cholesterol is, in fact, known to increase plasma membrane (PM) viscosity by promoting lipids organization in cellular membranes. In particular, we adopted a computational strategy that included the development of a reliable force field (FF) for the molecular probe and its validation through molecular dynamics simulations and spectroscopic calculations in various environments. Note that the development of a proper molecular model for this investigation was strictly required since anomalous dye geometries can lead to artifacts in the spectroscopic calculations, and DPAP excitation energies was found to be rather sensitive to its intramolecular configuration.[58,59] In this work, FF development was tailored towards DPAP potential energy surface and corresponding gradient in the first excited state as evaluated from quantum mechanical calculations at time-dependent DFT level. The sampling of the first electronically excited state (EES) potential energy surface allowed us to effectively simulate excited state properties of DPAP embedded in several solvents (i.e., acetonitrile, cyclohexane and *o*-xylene) and lipid bilayers, and to finally model fluorescence wavelengths on hundreds of snapshots issuing from the computed classical MD trajectories at a reasonable computational cost. Using MD simulations, it is shown that DPAP rotational dynamics is significantly retarded in more structured (i.e., with high concentrations of cholesterol) lipid bilayers. The obtained results, coming from both computational and experimental investigations, consistently support the use of DPAP as a feasible and useful tool in the investigation of biological membranes.

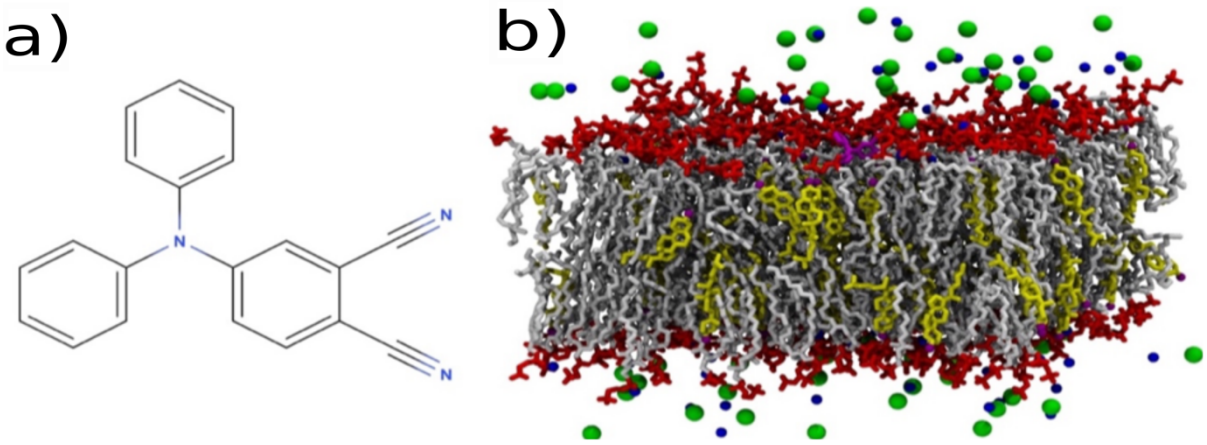

Figure 6.1: 4-(diphenylamino)phthalonitrile (DPAP) 2D molecular structure a) and a con- figuration of the DPAP rotor (in magenta) in the DPPC:CHOL system b) highlighting in yellow the cholesterol molecules, in red and gray the polar head and non-polar tails, respectively.

6.2 Computational details

6.2.1 Force field parameterization and QM calculations

Classical force field (intermolecular and intramolecular terms) used in this work adopt the following energy expression:

$$E = \sum_{\mu \in bonds} \frac{1}{2} k_\mu^2 \left(b_\mu - b_\mu^{eq}\right)^2 + \sum_{\mu \in angles} \frac{1}{2} k_\mu^\theta \left(\theta_\mu - \theta_\mu^{eq}\right)^2 + \sum_{\mu \in Rtors} \frac{1}{2} k_\mu^\phi \left(\phi_\mu - \phi_\mu^{eq}\right)^2 + \sum_{\mu \in Ftors} \sum_{j}^{N_{cos}^\mu} k_{j\mu}^\delta \left(1 + cos\left(n_j^\mu \delta_\mu - \gamma_j^\mu\right)\right) + \sum_i \sum_{j \neq i} 4\epsilon_{ij} \left[\left(\frac{\sigma_{ij}}{r_{ij}}\right)^{12} - \left(\frac{\sigma_{ij}}{r_{ij}}\right)^{6}\right] + \sum_i \sum_{j \neq i} \frac{q_i q_j}{4\pi\epsilon_0 r_{ij}} \quad \textbf{(Eq. 6.1)}$$

Where *i, j* run over atoms and μ runs over the internal coordinates. R_{tors} and F_{tors} indicate stiff and flexible torsions, respectively. Deviations from bonds, angles and rigid dihedral angles equilibrium values (b_μ^{eq}, θ_μ^{eq} and ϕ_μ^{eq} respectively) are associated with energy penalties which depend on the corresponding force constants ($k_\mu^b, k_\mu^\theta \; and \; k_\mu^\phi$). Flexible dihedrals are described by a sum of cosine functions, with $k_{j\mu}^\delta$, n_j^μ and γ_j^μ being the force constant, the multiplicity and the phase factor of the *j*-th cosine. Non-bonded interactions are modeled by using the standard Lennard-Jones and Coulomb potentials. Force field force constants are analytically computed through the minimization of the Joyce objective function. [203]

$$I^{intra} = \sum_{g=0}^{N_{geom}} \left[W_g \left[U_g - E_g^{intra} \right]^2 \right] + \sum_{k}^{3N-6} W' \left[G_K - \left(\frac{\partial E^{intra}}{\partial Q_K} \right) \right]_{g=0}^2 + \sum_{K \leq L}^{3N-6} \frac{2W''_{KL}}{(3N-6)(3N-5)} \left[H_{KL} - \left(\frac{\partial^2 E^{intra}}{\partial Q_K \partial Q_L} \right) \right]_{g=0}^2 \quad \textbf{(Eq. 6.2)}$$

Here, *K, L* run over the normal coordinates, N_{geom} is the number of sampled conformations; U_g is the energy difference between the energy of the g-th conformation and the one computed on the global minimum ($g = 0$). G_K is the energy gradient with respect to the normal coordinate *K*, while H_{KL} is the Hessian matrix with respect to *K* and *L*. Both G_K and H_{KL} are evaluated at $g = 0$. The constants W, $W'$and W'' weight the several terms at each geometry and can be chosen in order to drive the results depending on the circumstances. The energy, gradient and Hessian terms, calculated on the obtained equilibrium geometry, are normalized in order to account for the different number of terms and to make the weights independent from the number of atoms in the molecule. The first term of (Eq. 6.2) is evaluated only if flexible dihedral angles are intended to be parametrized: in this case, N_{geom} corresponds to the number of scanned geometries submitted to partial QM optimization. Such process is evaluated under the Frozen Internal Rotation Approximation (FIRA), which assumes that no relevant geometry rearrangements are experienced by the molecule during the scan, except for the scanned dihedral itself. Equilibrium values of (Eq. 6.1) are simply measured on the minimum geometry. Atomic charges have been computed on the minimum of the reference molecule using the Charge Model 5,[204] while Lennard-Jones parameters have been taken from the OPLS-AA[205] force field. Minimum geometry has been located with the time dependent extension of the Density Functional Theory (TD-DFT), using the CAM-B3LYP functional and the SNSD basis set.[206,207] Environment effects have been included in the geometry optimization procedure by means of the Conductor-like Polarizable Continuum Model (C-PCM),[208] using the butanoic acid (dielectric constant ε of 2.9931) as solvent in order to reproduce the specific low dielectric medium of the phospholipidic membranes. Acetonitrile also has been considered in some cases (*vide infra*) to verify the influence of a more dielectric environment in the computation of

chemical properties of interest. Different configurations along the flexible torsions have been generated to accurately parametrize soft dihedral angles, modifying each torsional angle in steps of 25°. Vertical electronic transitions have been computed at the CAM-B3LYP/SNSD level using state-specific PCM approaches[209] to model fluorescence properties. Computations have been performed on 200 molecular configurations extracted from the classical MD trajectories. Single values have been then averaged to obtain the final fluorescence wavelength. All the QM calculations were performed with the Gaussian suite of program (G16).[108]

6.2.2 Molecular dynamic simulation parameters

The classical MD simulations for DPAP in acetonitrile, cyclohexane, *o*-xylene and DOPC bilayer were performed using GROMACS 4.6.5, [210] adopting the protocol already done in our previous work.[34] The OPLS-AA force field[37] was chosen for modeling the *o*-xylene and acetonitrile solvents. In the case of cyclohexane instead, the General Amber Force Field (GAFF)[211] was used, because of its better reproduction of the cyclohexane density experimental value respect to OPLS-AA. The DOPC bilayer was hydrated with TIP3P[212] water molecules and modeled by means of CHARMM force field.[213]

To simulate DPAP in DPPC-Cholesterol bilayer an all-atom DPPC:CHOL lipid bilayer was taken from a previously well equilibrated DPPC:CHOL system,[214] which contained 1200 lipids with CHOL in a molar concentration of 30%. The system was Coarse Grained (CG) for 40 μs at 298 K and 1 atm using the CG MARTINI force field for lipids.[215] The 1200 lipids CG system was further scaled down to 600 lipids with 23.7% molar concentration of cholesterol to perform all-atom MD simulation. This well equilibrated system was further reduced in the current study to perform all atoms MD simulation with CHARMM36 force field. [216] The final system comprised 240 DPPC and 75 cholesterol molecules, evenly distributed between the upper and lower layer, and 1 DPAP molecule inserted into one layer using VMD.[217] A 0.15 M NaCl salt concentration was added and the whole system solvated with TIP3P 45 water molecules, with approximately 38 water molecules per lipid.

The initial systems were minimized by using the steepest descent algorithm implemented in GROMACS using an energy threshold of 10 kJ mol^{-1}. Equilibration runs were performed in the isothermal-isobaric ensemble: the systems were heated to 300 K using the velocity rescale method[218] and the Berendsen barostat[219] (using coupling constants of 0.1 and 1 ps,

respectively) for 500 ps with a timestep of 0.2 fs. Production runs were performed in the NVT ensemble: starting from the last configurations of the previous equilibration run, the integration step was increased to 2 fs and the total simulation time was set to 130 ns. LINCS[220] was introduced to fix fastest degrees of freedom at their equilibrium values. In the case of cyclohexane and DPPC:CHOL lipid, only bonds with hydrogen atoms were kept rigid. Non-bonded interactions were truncated at 1.4 nm. Long-range electrostatic interactions were modeled by means of the Particle mesh Ewald (PME) technique[221] with a spline interpolation of order 4. System coordinates were stored every 500 steps. For DPPC:CHOL lipid the final box side length are 8.5, 8.4 and 8.6 nm.

Autocorrelation functions ($C_p(t)$) have been calculated as

$$Cp(t) = < P_2(p(t_0) \cdot (t_0 + t)) > \qquad \textbf{(Eq. 6.3)}$$

where P_2 is the second order Legendre polynomial, and p is the vector defined as the cross product of the ij and jk vectors (being i, j and k three different atoms of the considered molecular structure).

6.3 Results

6.3.1 Structure analysis and FF development

The optimized excited state structure of the DPAP molecular rotor (shown in Figure 6.2 with labeling of atoms) adopts a propeller like shape in order to minimize steric hindrance among the three phenyl rings, with the central moiety defined by the three ipso carbons and the amminic nitrogen adopting a nearly planar conformation.

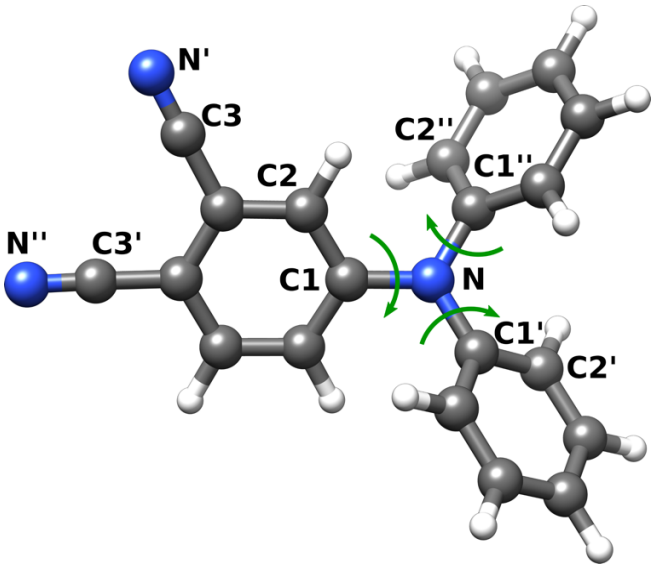

Figure 6.2: DPAP propeller-like conformation as optimized in butanoic acid (solvent effect modeled by the PCM). Flexible dihedral are indicated with green vectors. The ipso (C1, C1' and C"), the ortho (C2, C2' and C2") carbon atoms are labeled in black together with the nitrogen (N' and N") and the carbon (C3 and C3') atoms of the two cyano groups.

As a preliminary investigation, we performed a comparison between the internal coordinates values which significantly change as we go from the GS to the EES structure (see Table 6.1). This kind of analysis is important, since the differences between the GS and EES geometries are generally associated with the stokes shifts values in the UV-Vis spectrum.[222] Significant structural rearrangements are observed for the chemical bonds involving the cyano groups. From the analysis of the DPAP HOMO and LUMO (graphically shown in Figure 6.3), it can be assumed that these alterations can be ascribed to the migration of the electronic density from the unsubstituted phenyl rings to the dicyano substituted moiety, taking place upon the excitation process. It is worth noting also the change in the *ipso* region geometry, with an increase of $C1'\widehat{NC}1''$ and a decrease of $C1\widehat{NC}1'$ and $C1''\widehat{NC}1$ angles amplitudes in the EES geometry with respect to the GS one.

Table 6.1: Comparison between ground state (GS) and electronically excited state (EES) DPAP geometry optimized. Atom labeling in Figure 6.2.

Geometric Parameters	GS	EES
C3′-N′′(Å)	1.156	1.165
C3-N′ (Å)	1.155	1.164
N-C1 (Å)	1.382	1.406
N-C1′′(Å)	1.430	1.406
N-C1′ (Å)	1.430	1.396
$\boldsymbol{C1\widehat{NC}1'}$ **(degree)**	121.16	118.96
$\boldsymbol{C1'\widehat{NC}1''}$ **(degree)**	117.55	121.52
$\boldsymbol{C1''\widehat{NC}1}$ **(degree)**	121.30	119.51

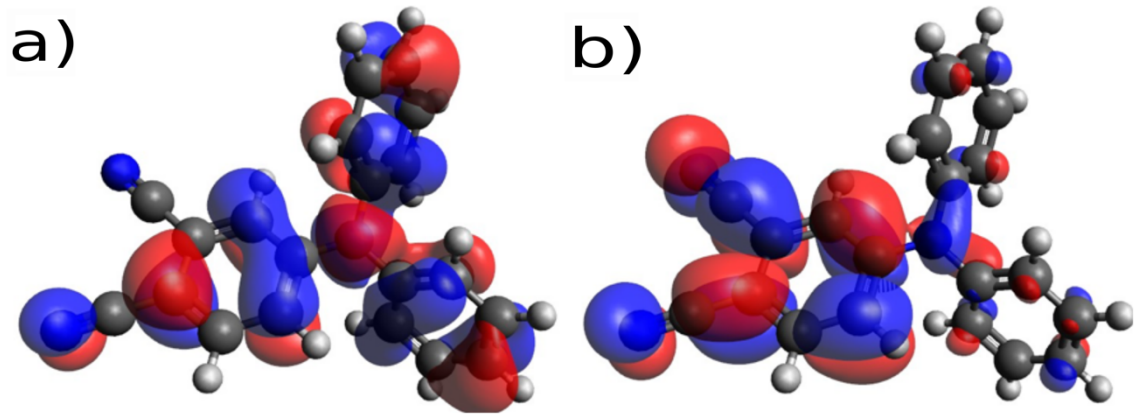

Figure 6.3: Frontier molecular orbitals of DPAP: HOMO a) and LUMO b). An isosurface value of 0.02 a.u. has been used.

As mentioned in section 6.2, the FF atomic point charges have been computed on the minimum of the reference molecule using the Charge Model 5. To verify the influence operated by the chosen solvent in the estimation of the atomic charges, the same population analysis has been conducted also using acetonitrile (ε=35.688) as solvent. Negligible differences on the estimated charges were found, with the computed largest deviation being about 0.023 e. This small differences in

the atomic charges slightly affect the dipole moment value, going from 21.19 D in butanoic acid to 23.14 D in acetonitrile. Overall, the observed insensibility of the estimated atomic charges values to the surrounding medium allows for the employment of the same set of charges (the one computed in butanoic acid, in this case) for all the investigated environments in the following MD simulations.

A comparison between the GS and EES atomic charges computed in acetonitrile is shown in Table 6.5. The choice of acetonitrile for this analysis allows for an effective comparison with the GS force field, which was developed by considering this environment during the previous parametrization[58]. Main differences have been observed for the cyano nitrogen atoms (N' and N", according to Figure 6.2) which became more negative after the electronic excitation, and for N and C1 atoms ($7.15x10^{-2}$ and $4.71x10^{-2}$ *e* respectively). In this case, the lower atomic charge values confirm a more pronounced electrons density in the EES, as already indicated by the interpretation of the geometric parameters alteration. The high degree of intramolecular charge transfer is reflected also by the important difference between the GS and the EES dipole moments in acetonitrile, the calculated dipole moment is 12.79 D for the GS and 23.14 D in the EES.

The bonded terms of the molecular force field have been derived according to the protocol described in Section 6.2.1. A fundamental step in this procedure is represented by the parametrization of the flexible dihedral angles. The DPAP conformation is mainly affected by three dihedral angles, which define the rings torsions with respect to the central amine group: dihedral **1** (C2C1NC1", see Figure 6.2 for labeling), dihedral **2** (C1"NC1'C2') and dihedral **3** (C2"C1"NC1'). The last two dihedral angles (**2** and **3**) are equivalent. The related DFT potential energy curves (PEC) have been used to derive the FF torsions potential terms of the DPAP excited state FF. The result of the fitting procedure is shown in Figure 6.4, where the dihedral angle **1** (Figure 6.4a) and **2**/**3** (Figure 6.4b) energy potentials are compared with the corresponding DFT reference data.

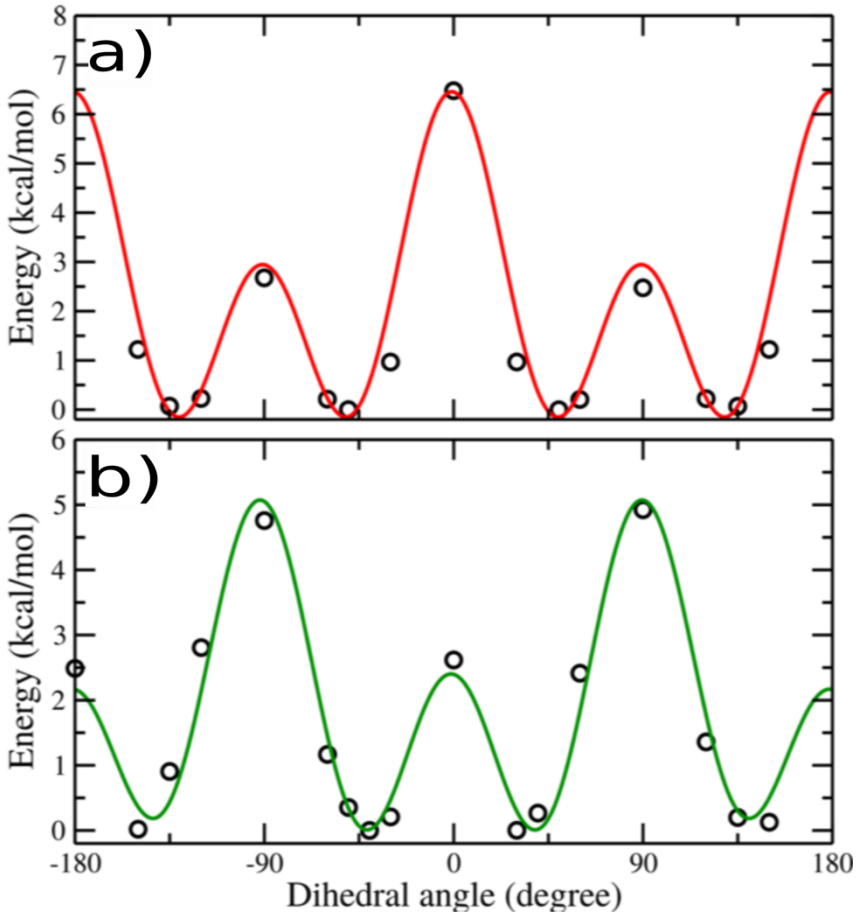

Figure 6.4: Potential energy curve of dihedral angle 1 (panel a)) and 2/3 (panel b)). QM data, black points; MM data, continuous lines.

Dihedral angle **1** shows four symmetry related energy minima at ±130° and ±50°. Two energy barriers hinder the inter-conversion among these minimum energy conformations, corresponding to the planar and orthogonal geometry of the considered ring with respect to the central amine moiety; the related energy height values are ≈7 kcal/mol and ≈3 kcal/mol respectively. For dihedral angles **2**/**3** instead the situation is reversed, with orthogonal configuration being the one energetically more disfavored. In such case the four energy minimum configurations are located at about ±45° and ±135°. Moreover, in both the energy panels in Figure 6.4a,b satisfactory agreement between the optimized classical FF and the DFT reference data can be observed, thus allowing a reliable sampling of the first EES potential energy surface of the DPAP molecular rotor by means of the new FF. The whole parameter set is available in the (Table 6.6 to Table 6.11).

As a further analysis, the potential energy curves of the scanned flexible torsions can be compared with the corresponding ones obtained for the ground state case.[58] The energy barriers values are higher for the EES for both the investigated torsions, and the highest energy configurations are exchanged: in the GS, the highest energy barrier for dihedral 1 corresponds to the orthogonal configuration and to the planar configuration in the EES. A reverse situation is observed for dihedral **2/3**. This interesting appreciation is due to the important electron delocalization which involves the two unsubstituted rings in the EES, thus leading to an extra stabilization energy when dihedral **2/3** is nearly planar.

6.3.2 Model validation in organic solvents

The FF developed in the previous section has been tested and validated by means of MD simulations of the DPAP in acetonitrile, o-xylene and cyclohexane. The different solvation shells experienced by the analyzed FMR at its first excited state have been described by means of the radial distribution function (rdf) computed between the dye and the solvent molecules center of mass (COM). The obtained profiles, shown in Figure 6.5, pointed out well defined first solvation shells for cyclohexane and *o*-xylene. In the former cited solvent, a first peak of height 1.75 takes place at 6 ˚A of COM distance, while a considerable second peak of height 1.25 has been located at 9 ˚A. As regarding o-xylene, the first peak takes a height of ≈ 1.5 at 5 ˚A; the second peak is not well resolved and it covers a large area from 8 to 12 ˚A. Only few molecules of acetonitrile instead are able to closely approach the solute, since the height of the rdf first peak is significantly lower if compared to the previous ones. On the contrary, the second solvation shell is easy to detect from the distribution profile, being located at approximately 8 ˚A with a peak of roughly 1.1.

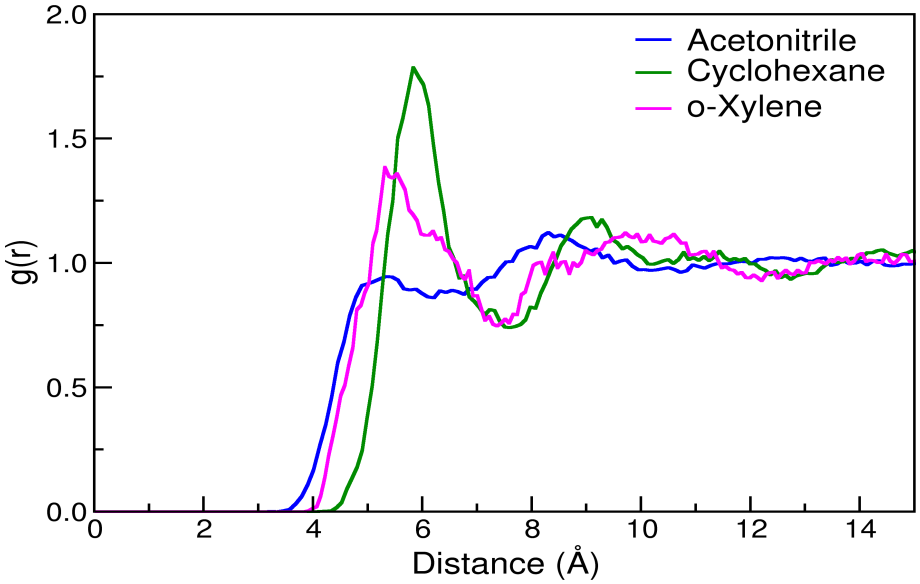

Figure 6.5: Radial distribution functions between DPAP and acetonitrile (blue), cyclohexane (green) and o-xylene (magenta) center of mass.

The distributions of the three flexible dihedral angles, evaluated in all the performed MD simulations, confirm the reliability of the first excited state FF for the DPAP molecule. Indeed, as it is shown in Figure 6.6 for the case of acetonitrile, each dihedral angle selectively populates the four corresponding energy minima. High energy configurations are avoided, according to the DFT energy profile depicted in Figure 6.4 on which the FF in use was parameterized. Each flexible torsion undergoes complete rotations, thus to being able to properly populate the four energy minima predicted by the QM calculations.

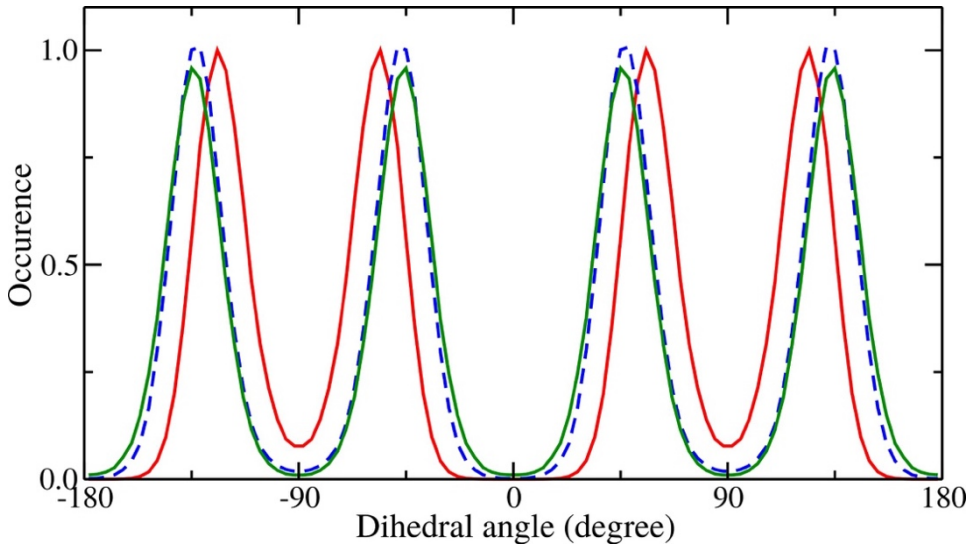

Figure 6.6: Dihedral distribution function of the three dihedral angles in acetonitrile: in solid red line dihedral angle 1, in blue dashed line dihedral angle 2 and in solid green line dihedral angle 3.

The time required to a dihedral angle for a complete rotation, however, strictly depends on the features of the surroundings. The viscosity of the solvent in particular is well known to affect solute dynamics, and more viscous media decelerate dihedral angles rotation which involves large chemical portions. Regarding our system, a qualitative picture can be easily gained by monitoring the dihedral angles evolution along the sampled simulation time. As emerging from inspection of Figure 6.7a, 1 ns in acetonitrile (the less viscous solvent here considered) is enough to observe an oscillation of the considered dihedral (dihedral angle **1**, in the present case) from 120° to 60° and vice versa. After 5 ns instead no clear oscillations were detected in the more viscous liquids cyclohexane and *o*-xylene (Figure 6.7b,c), for which similar viscosity values are reported in the literature.[223,224]

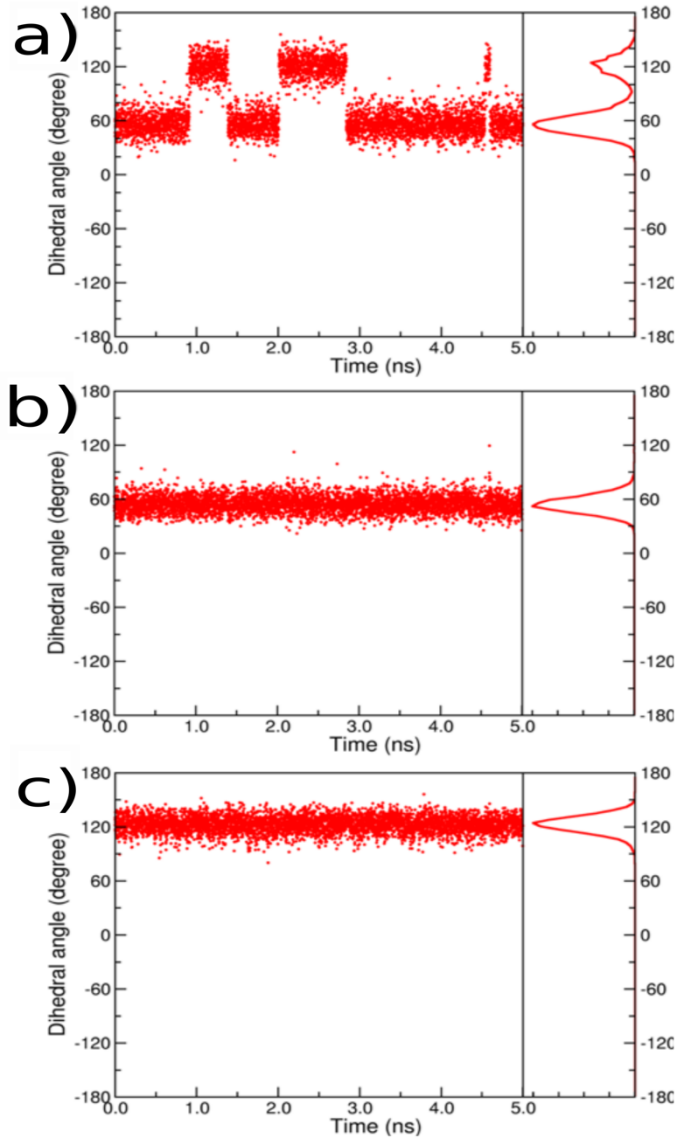

Figure 6.7: Time dependent dihedral distribution function for dihedral angle 1 for the first 5 ns of simulation in acetonitrile (ACN) a), cyclohexane b), o-xylene c).

Focusing on the acetonitrile (ACN) case, where a higher flexibility to the rotor internal dynamics is allowed, we noted that the torsional angles rotate simultaneously in order to diminish steric hindrance between the aromatic rings, meaning that the three torsions are highly coupled. This phenomenon was already pointed out in the previous work on DPAP ground state and can be better realized by looking at Figure 6.8 the first rotation takes place after almost 1 ns of simulation, and the following at roughly 1.4 ns and 2 ns. It is interesting to note that in the time lapse (5 ns) considered in this figure only small oscillations are allowed for dihedral **1**, involving the overcome of a low energy barrier of ≈ 3 kcal/mol. The first 5 ns of simulated

time are therefore not enough to dihedral angle **1** for exceeding the higher energy barrier of 7 kcal/mol. As regarding dihedral **2/3** instead, whose minima are separated by energy barriers of 2.5 and 5 kcal/mol, all the corresponding energy equilibrium structures are populated. From a quantitative point of view, we further confirmed the observed trend among the three considered solvents by computing along the entire MD trajectories the time autocorrelation function (ACF) of the rotation of both ring 1 torsional angle (τ_{rot}^{dih}) and of the whole molecule (τ_{rot}). In the latter case, the axis perpendicular to the plane defined by the three *ipso* carbon **C1**, **C1'** and **C1"** was considered as vector.

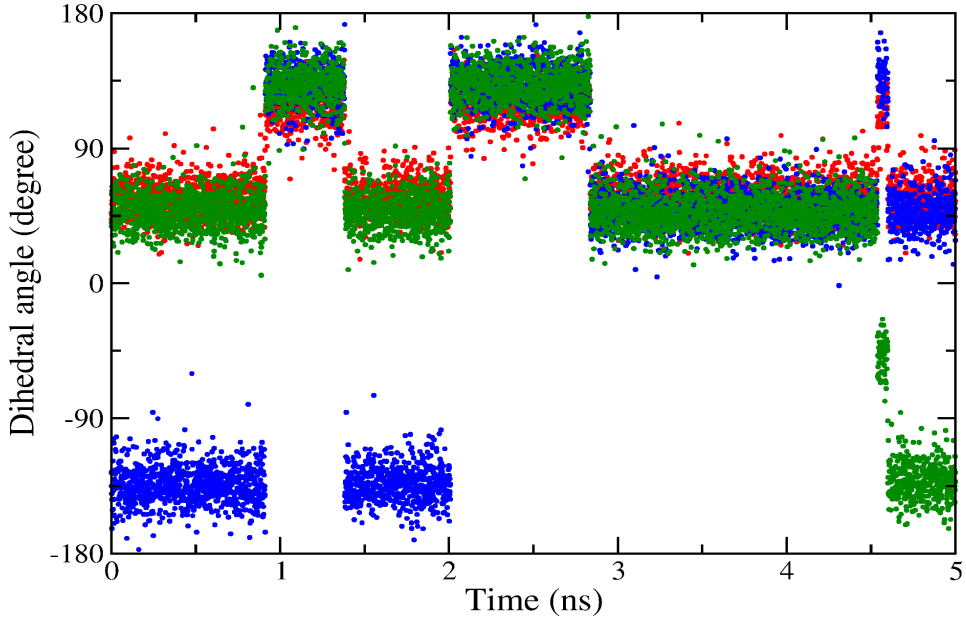

Figure 6.8: Time dependent dihedral angle distribution function in acetonitrile (in red results for dihedral angle 1, in blue for dihedral angle 2 and in green for dihedral angle 3). The first 5 ns of simulation are reported.

Table 6.2: Dynamic properties of DPAP in solvents.

Solvent	τ_{rot} (ps)	τ_{rot}^{dih}(ps)	τ_{fl} (ns)
Acetonitrile	8.17± 0.02	7.98± 0.02	2.61
Cyclohexane	89±3	94±5	9.16
o-Xylene	117±16	126±13	12.5

The calculated quantities, stored in Table 6.2, indicate ACN as the liquid where DPAP detects a higher internal and external flexibility, followed by cyclohexane and *o*-xylene.This outcome is

in line with the different solvation shells sampled during the MD simulations, already seen in Figure 6.5 respect to the cyclohexane case, when in o-xylene solution the solvent molecules are closer to the solute center of mass, thus obstructing to a greater extent the DPAP internal and global movements. Moreover, from inspection of Table 6.2, an apparent correlation between τ_{rot} (or τ_{rot}^{dih}) and the experimental fluorescence lifetime τ_{fl} emerges. According to our procedure (explained in Section 6.2.1), TD-DFT calculations were performed on dye configuration frames extracted each 250ps of simulations, for a total of 200 fluorescence energy calculations for each of the considered environment. It has to be recalled that the considered structures correspond to S1 configurations, so that the computed emissions occur from the first excited state S1. The frontier molecular orbitals have been already shown in Figure 6.3. During the aforementioned computations, solvent coordinates were not considered, and environment effects have been modeled through the PCM scheme. The CAM-B3LYP functional has been chosen because of its reliability with chemical systems involving charge transfer upon excitation. Furthermore, the experimental and theoretical calculations for maximum emission peak wavelength and stoke shift of DPAP in different environments are summarized in Table 6.3. It is clear from our theoretical calculations that polarity solvent effects are significant, since the change in polarity is highly reflected in the outcome of the spectroscopic prediction: higher the value of the *s* value of the medium, higher is the emission energy.

Table 6.3: Experimental and theoretical maximum emission peak wavelength (nm) and Stokes shift of DPAP in different environments. In parenthesis the dielectric constant of the solvent. Stoke shift values are computed by considering the absorption peak wavelength determined in our previous work. [58] For DOPC bilayer no experimental counterpart is available.

	ACN (35.688)	**Cyclohexane (2.016)**	**o-Xylene (2.545)**	**DOPC (2.993)**
		Fluorescence		
Exp.(nm)	552	431	471	**-**
Calc.(nm)	682(±127)	442 (±29)	470 (±34)	**496 (±31)**
		Stokes shift		
Exp.(nm)	231	107	144	**-**
Calc.(nm)	**353(±147)**	**115(±44)**	**145(±51)**	**173(±43)**

In the lower polar solvent cyclohexane the theoretical prediction of the DPAP emission wavelength is at 442 nm, similar to the corresponding experimental quantity (431 nm). Considering the results of our previous work (where an absorption peak at 325 nm was found) we can also estimate the Stoke shift provided by the CAM-B3LYP/SNSD/PCM model, leading to a value of 114 nm, in acceptable agreement with the experimental one (107 nm). In the case of *o*-xylene, the fluorescence energy experimental value is reproduced with high accuracy, with an underestimation of only 1 nm. As a consequence of the pre computed absorption, the estimated Stoke Shift value (144 nm) differs from the experiment of only 1 nm.

Finally, the emission wavelength computed for acetonitrile (the highest polar solvent) is located at 682 nm, with an overestimation of the experimental value of more than 100 nm. Also the Stoke shift is overestimated, suggesting that the polarity effect in this case is amplified. However, besides that, it is worth noting that the polarity-sensitivity of DPAP is correctly described by the CAM-B3LYP/SNSD/PCM protocol here adopted, proving that the same model is able to reproduce the experimental trend. This statement can be easy confirmed even if the related statistical errors reported in Table 6.3 are taken into account.

The errors themselves are interesting to be analyzed by inspecting the corresponding values, it is possible to note that they are significantly higher in ACN. This can be easily explained by looking back to the rdf profiles mentioned previously and can be graphically realized looking at the distribution of the computed emission wavelengths for each liquid, shown in Figure 6.9. Moreover, looking at the acetonitrile case, an apparent effect of the conformational changes on the predicted optical property arises from inspection of Figure 6.10, where the value of dihedral angle 1 is related to the corresponding emission wavelength. Higher values in the emission energy are associated with the considered torsional angle within the interval 70°-120° (Figure 6.10b) while lower values arise from torsional angle values close to the corresponding energy minima (as indicated by the panel (a) in Figure 6.10 where the potential energy curve is shown). In Figure 6.10c the dihedral 1 distribution of the 200 conformations extracted from MD trajectory used for the fluorescence wavelength calculation is shown: as expected, the dihedral angle 1 correctly populates the related energy minima.

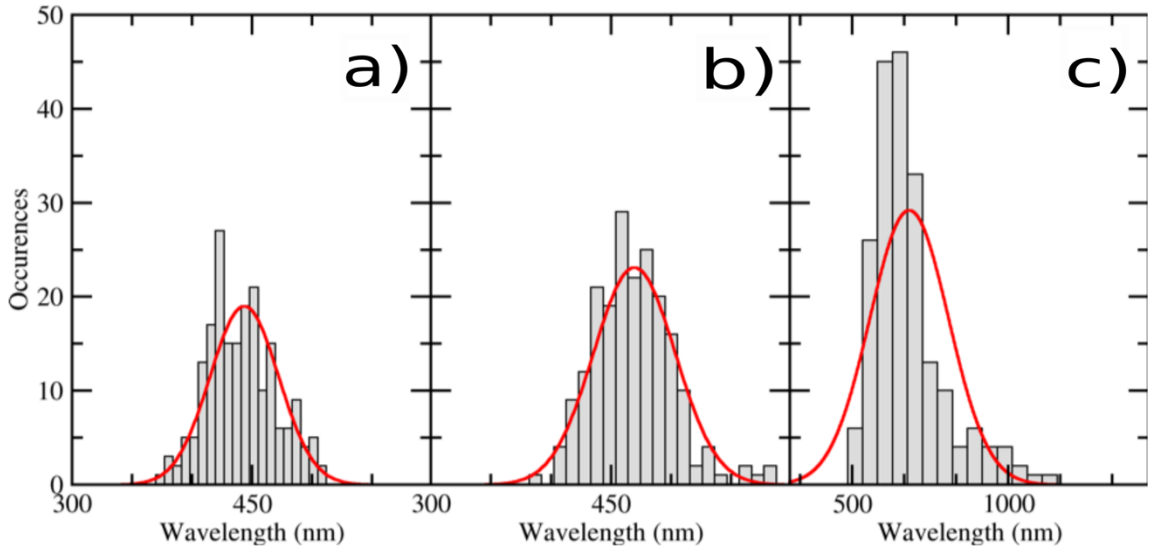

Figure 6.9: Distribution of the emission wavelengths computed for 200 DPAP geometries extracted from the MD trajectories in cyclohexane a), o-xylene b) and acetonitrile c). The solid lines represent the fitting to a Gaussian curve. For sake of clarity a different number of bins have been used in the three panels.

6.3.3 Probing lipid phase in model bilayers through DPAP fluorescence lifetime

The sensitivity of DPAP photophysics for local viscosity, as observed in previous studies, prompted us to test such a FMR for probing lipid membrane structure. To this end, we set up two liposome solutions of pure DOPC and DPPC-Cholesterol (70:30), as described in the Methods section, which are known to provide convenient L_d and L_o membrane phase models, respectively. In particular, in order to probe the nature of lipid phase through DPAP emission lifetime, we adopted the phasor approach [224] to confocal fluorescence lifetime imaging microscopy (ph-FLIM) as a convenient means to spatially map the phase composition in lipid bilayers. Besides, this is a propedeutic step towards probing local order in living cells. The phasor analysis represents in a polar 2D plot (phasor plot [225]) the cosine ($g_{i,j}$) and sine ($s_{i,j}$) Fourier transforms of the normalized emission decay collected in each pixel i, j of an image. For monoexponential decays, the phasor ($g_{i,j}$, $s_{i,j}$) lies on a semicircle (universal circle) of radius 1/2 and center (1/2,0); for multi-exponential decays the phasor lies inside the semicircle.

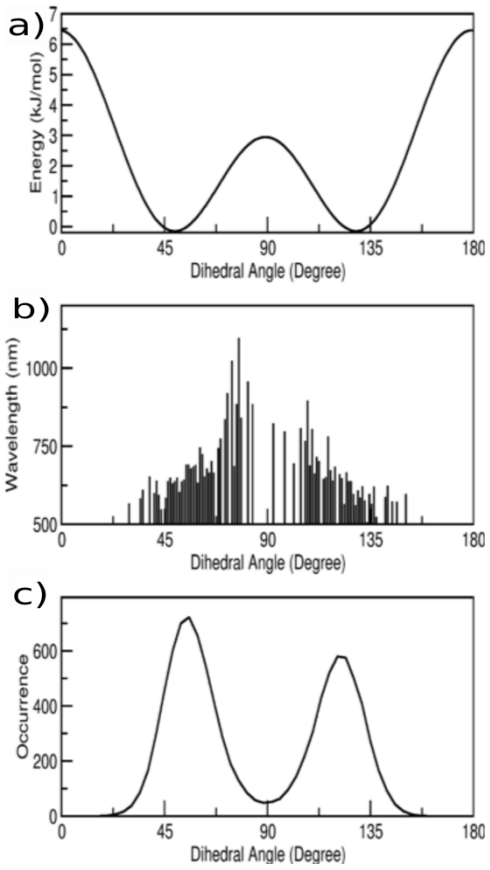

Figure 6.10: Conformational dependence of the fluorescence wavelength computed in acetoni- trile. a) Energy profile of dihedral angle 1. b) Relation between DPAP emission energy and dihedral angle 1 amplitude. c) Dihedral 1 distribution for the selected conformations taken from the MD trajectory and used for fluorescence wavelength calculation.

Experimentally, we applied confocal ph-FLIM to DPAP embedded on multilamellar vesicles characterized by homogeneous L_d or L_o phases. Notably, L_d or L_o phases were found to be characterized by well-distinguishable phasors localized in the phasor plot (Figure 6.11). The dispersed nature of the phasor cloud owes to the finite precision of our measurements and the vesicle heterogeneity. As expected for its longer lifetime (τfl = 6.75 ns), the phasor cloud of the more rigid L_o phase mapped closer to the (0,0) point as compared to the L_d phase (τfl = 1.93 ns). On the phasor plot the combinations of distinguishable photophysical states, such as those determined by L_d and L_o phases, follow a vectorial addition rule, regardless of the number of exponentials.[226] Therefore, we may hypothesize that interleaved L_d and L_o phases, such as those expected in the plasma membrane of the cell, would fall along the segment that connects the two reference phasors. Accordingly, h-FLIM applied to DPAP could, in principle, help in

determining the composition of the membrane with the sub-micrometer resolution typical of confocal microscopy.

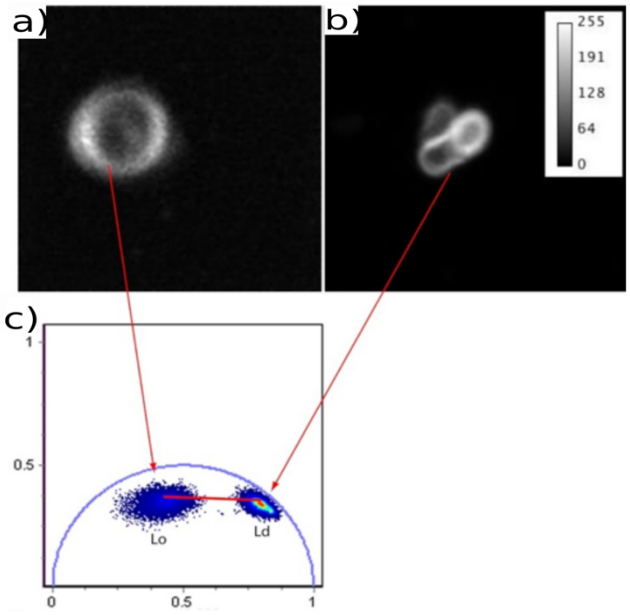

Figure 6.11: ph-FLIM of multilamellar vesicles characterized by homogeneous lipid phases. a) Fluorescence image of a multilamellar vesicle characterized by homogeneous Lo phase. b) Fluorescence image of a multilamellar vesicle characterized by homogeneous Ld phase. c) Phasor plot relevant to vesicles a) and b): the segment connecting the averages of the two reference phasor clouds is depicted in red.

6.3.4 DPAP molecular dynamics in different lipid phases

The influence of lipid membrane viscosity on DPAP dynamics was further investigated by means of molecular dynamics simulations. A DPAP molecule was embedded in pre-equilibrated planar DOPC and DPPC:CHOL model bilayers, thus reproducing the experimental setup, and MD simulations of both systems were carried out for about 150 ns after equilibration. In Table 6.4, the ACF of the rotation of both ring 1 torsional angle τ_{rot}^{dih} and of the whole molecule (τ_{rot}) in DOPC and DPPC:CHOL bilayer are reported. In DPPC:CHOL bilayer both motions are retarded, due to the increase of the viscosity induced by the presence of cholesterol. Looking at the two motions under exam, the ring rotation is less likely to occur with respect to the global rotation (expressed by the τ_{rot} parameter) in the DPPC:CHOL system; an opposite trend happens in the DOPC bilayer, where the whole spin of DPAP is blocked to

a greater extent. However, in general, the motions recorded in the membrane systems are more retarded if compared to the ones measured in the solvents.

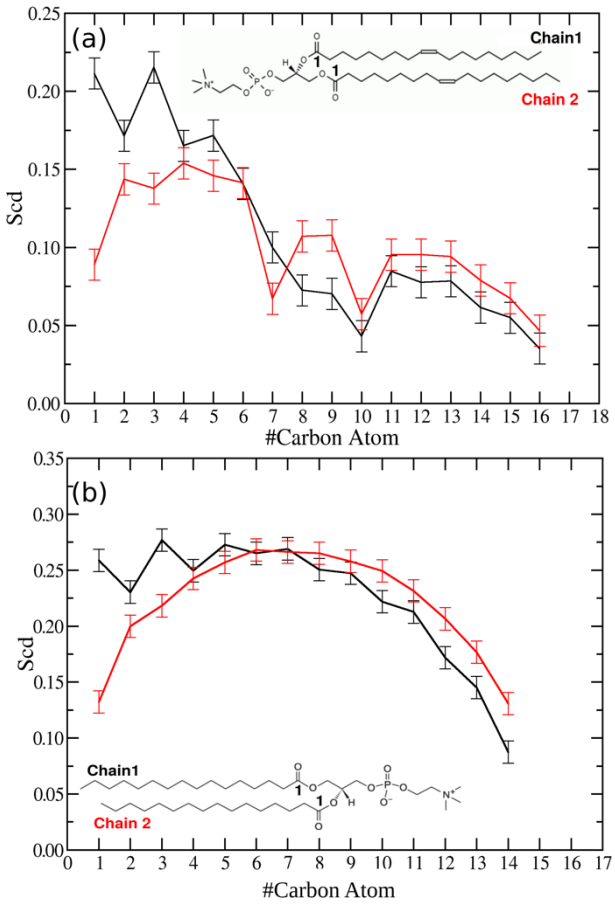

Figure 6.12: Deuterium order parameter for a) DOPC and b) DPPC lipid, the lipid nomenclature is indicated inside the inset of the graph. The first order parameter corresponds to the first CH_2 group of the acyl chain (position 2).

In addition the structural effect due to the presence of DPAP in the DPPC:CHOL membrane can be evaluated considering the order parameter for the first shell of lipids around DPAP or those not in close contact with the dye. The results are reported in Figure 6.12, where the deuterium order parameter for each of the two DPPC hydrophobic chains has been evaluated. The deuterium order parameter is a measure of the structural anisotropy of a particular C−D bond and yields its time-averaged orientation during the MD simulation, thus providing some information about the structural orientation and flexibility of lipid chains in a bilayer. From the inspection of Figure 6.12, the structural effect caused by the introduction of the FMR within the membrane which especially acts on chain 2 and on lipids close to DPAP is apparent.

Table 6.4: Dynamic properties of DPAP in DOPC and DPPC:CHOL bilayers. Errors are in brackets.

Environment	τ_{rot}(ns)	τ_{rot}^{dih} (ns)	τ_{fl} (ns)
DOPC	19 ()	20 ()	**1.93**
DPPC:CHOL (b)	78 (19)	32 (23)	**6.75**
DPPC:CHOL (c)	**11 (8)**	**12 (9)**	**6.75**

DPAP fluorescence has been investigated also in the DOPC and DPPC:CHOL bilayers. As done in Ref. Macchiagodena et al.[58] the butanoic acid (ε= 2.9931) was considered as the model environment for the plasmatic membrane within the PCM calculations. The maximum emission peak wavelength of DPAP in DOPC and DPPC:CHOL were located at 496(±30) and 503(±38) nm, respectively.

6.4 Discussion

The use of molecular probes in various biological membrane studies has become very common now for a long time but the choice of molecular probe for predicting correct structural and dynamical properties of a lipid system is still debatable. To predict correct dynamics of such systems and to use any molecular probe embedded inside the lipid bilayer one has to validate the molecular probe through molecular dynamic simulations and various spectroscopic calculations. DPAP as described earlier in the results section in its EES state has proved to be feasible to be useful as a tool to investigate the complex structural and dynamical properties of the lipid bilayers. The alterations observed in the cyano group and ipso region of the DPAP molecule moving from its GS to EES can be due to the higher electronic delocalization which takes place in the EES, owing to the inductive and resonance effects on the unsubstituted phenyl rings due to the dicyano aromatic moiety.[227,228] The distributions of the three flexible dihedral angles, evaluated in all the performed MD simulations, confirm the reliability of the first-excited state FF for the DPAP molecule. Each flexible torsion undergoes complete rotations, thus to being able to properly populate the four energy minima predicted by the QM calculations. The time required to a dihedral angle for a complete rotation, however, strictly depends on the features of the surroundings. The viscosity of the solvent in particular is well known to affect solute dynamics, and more viscous media decelerate dihedral angles rotation

which involves large chemical portions. Regarding our system, a qualitative picture can be easily gained by monitoring the dihedral angles evolution along the sampled simulation time. Focusing on the acetonitrile (ACN) case, where a higher flexibility to the rotor internal dynamics is allowed, we noted that the torsional angles rotate simultaneously in order to diminish steric hindrance between the aromatic rings, meaning that the three torsions are highly coupled. This phenomenon was already pointed out in the previous work on DPAP ground state [58]. Statistics emerging from the correlation between τ_{rot} and the experimental fluorescence lifetime τ_{fl} reported in Table 6.2 are corroborating the fact that more viscous and hindering environments promote radiative processes, as a consequence of the obstruction to the rotation of the dye subgroup adopting the TICT state. This interesting finding (graphically shown in Figure 6.13), which relates an experimental quantity with a computational prediction, could lead to interesting implications, considering that FMRs are often used within highly viscous media such as silica-based nanoparticles, in order to increase fluorescence lifetimes and to be fruitfully used for imaging applications.[225] DPAP emission spectra have been experimentally determined in recent years,[59] proving that the fluorescence (in contrast to the absorption, which is insensitive to the environment) is highly solvatochromic since it shows a red-shift of up to 120 nm going from the less polar cyclohexane (having a ε of 2.016) to the most polar solvent acetonitrile.

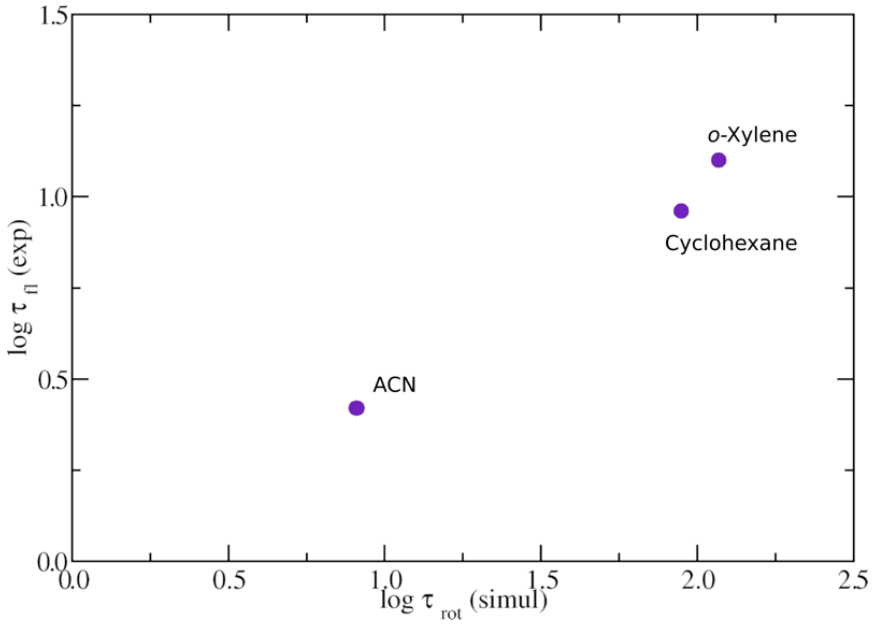

Figure 6.13: Correlation between DPAP rotational correlation time (ps) and experimental fluorescence lifetimes (ns) in the considered environments.

Experimental and theoretical maximum emission peak wavelength (nm) and Stokes shift of DPAP in different environments as described in Table 6.3 are significantly higher for ACN which is due to fact that they lack a defined solvation shell which in turn allows for a greater internal flexibility, thus increasing the conformational variability on which the spectroscopic investigations have been conducted. On the contrary, in cyclohexane and o-xylene the structured surrounding solvation shells prevent DPAP from large amplitude motions, which can turn in larger deviations from the fluorescence energy mean value. Once provided to the liposome solutions, DPAP was readily embedded in the lipid membranes, owing to its highly hydrophobic character that makes it highly insoluble in aqueous solution. As usual in FMR imaging applications, we focused specifically on the fluorescence lifetime of the dye, since other optical features such as emission intensities and wavelengths are strongly dependent on local concentration or less sensitive to the microviscosity of the environment. DPAP fluorescence was investigated in the DOPC and DPPC:CHOL environments Note that in the DPPC:CHOL case the Stoke shift cannot be determined, since the corresponding MD simulation with DPAP at its fundamental state is missing. The predicted emission wavelength is similar for the two phospholipidic bilayers, the small discrepancy being ascribed to the different DPAP configurations sampled during the classical MD simulations. The Stoke shift

computed in DOPC (173 nm) is in line with the previous assumption that higher solvent polarity tends to increase the difference between the positions of the band maxima of the absorption and emission spectra. Moreover, the obtained emission values fall into the wavelength ranges considered for the evaluation of the fluorescence lifetime, thus confirming from an experimental point of view the reliability of this study.

6.5 Conclusions

In this work, we analyzed the developed FMR DPAP as a molecular probe for detecting ordered and disordered phases in plasmatic membranes. Both experimental and computational techniques have been integrated together, giving rise to a methodology that can be easily extended to investigate at the atomistic level the complex phenomena occurring upon interaction between lipids and probe molecules. The first part of this work has been devoted to model development and validation. A tailor-made classical force field for modeling the rotor at its first excited state has been developed, by using first-principle quantities (energy, first and second derivatives) as reference data during the parametrization procedure. Liquid solution such as acetonitrile, cyclohexane and o-xylene have been considered to validate the force field. MD simulations have allowed for the investigation of the rotor excited-state properties upon dissolution, showing how the rotor internal and global dynamics are strictly affected by the viscosity of the surrounding environment. The corresponding fluorescence wavelength values has been then modeled by means of TD-DFT calculations on hundreds of uncorrelated snapshots extracted from the trajectories. The theoretical optical computations reproduced the solvatochromic trend of the emission signals and estimating with fair agreement the Stock shift values. In the second part, DPAP has been studied when dissolved within two different lipid membranes, one of pure DOPC and one of DPPC with cholesterol. Using confocal fluorescence lifetime imaging microscopy (ph-FLIM), different signals have been measured when going from a liposome solution to the other one, owing to the different membrane phases experienced by the probe. MD simulations in the two membrane systems revealed that both flexible dihedral angles and global rotations are significantly retarded in the presence of cholesterol, thus further confirming the high sensitivity of DPAP to its local environment as well as its capability in detecting different structures and level of plasmatic membranes organization.

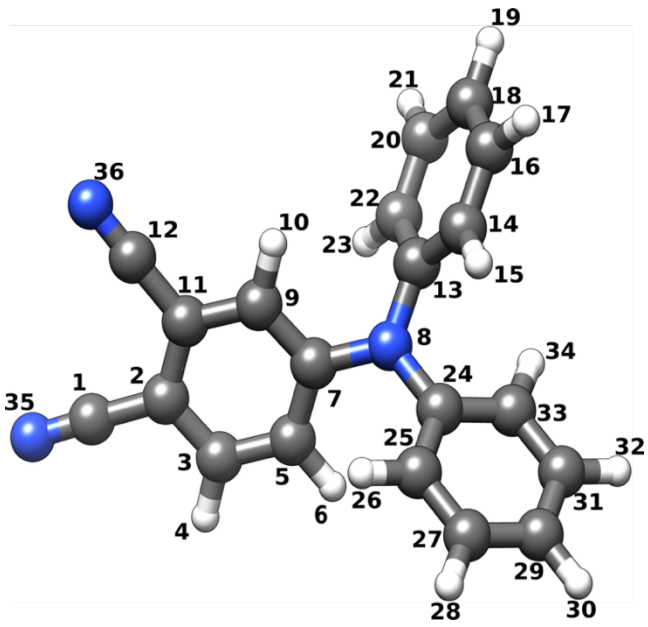

Figure 6.14: DPAP atom labelling.

Table 6.5: Comparison between GS and EES atom charges (e) of DPAP in acetonitrile. For atom labeling see Figure 6.14

Atom	GS	EES
1 C	0.194079	**0.164758**
2 C	0.001146	**-0.027896**
3 C	-0.063950	**-0.083191**
4 H	0.129524	**0.121794**
5 C	-0.082391	**-0.121011**
6 H	0.120872	**0.109216**
7 C	0.137370	**0.090235**
8 N	-0.295163	**-0.223643**
9 C	-0.074139	**-0.066829**
10 H	0.123468	**0.127786**
11 C	0.022105	**-0.032730**
12 C	0.207369	**0.163206**
13 C	0.099989	**0.117867**
14 C	-0.093409	**-0.077099**
15 H	0.115333	**0.125068**

16 C	-0.095904	**-0.085173**
17 H	0.111804	**0.122825**
18 C	-0.101147	**-0.074777**
19 H	0.109806	**0.122366**
20 C	-0.096474	**-0.086623**
21 H	0.111513	**0.122566**
22 C	-0.094721	**-0.073565**
23 H	0.113578	**0.125177**
24 C	0.099678	**0.121806**
25 C	-0.093336	**-0.075309**
26 H	0.115508	**0.121248**
27 C	-0.095608	**-0.086700**
28 H	0.111993	**0.122849**
29 C	-0.100695	**-0.071814**
30 H	0.110007	**0.123147**
31 C	-0.096134	**-0.085702**
32 H	0.111669	**0.123073**
33 C	-0.094409	**-0.074080**
34 H	0.113786	**0.125302**
35 N	-0.400313	**-0.449702**
36 N	**-0.382804**	**-0.454445**

Table 6.6: DPAP force field non-bonded parameters for atom labelling see Figure 6.14

Non-bonded Parameters			
atom	σ (nm)	s (kJ/mol)	**charge**
1	3.65000e-01	6.27600e-01	**0.186654**
2	3.55000e-01	2.92880e-01	**0.019087**
3	3.55000e-01	2.92880e-01	**-0.059224**
4	2.42000e-01	1.25520e-01	**0.125066**
5	3.55000e-01	2.92880e-01	**-0.062729**
6	2.42000e-01	1.25520e-01	**0.126168**
7	3.55000e-01	2.92880e-01	**0.124887**
8	3.30000e-01	7.11280e-01	**-0.282292**
9	3.55000e-01	2.92880e-01	**-0.062916**
10	2.42000e-01	1.25520e-01	**0.127709**
11	3.55000e-01	2.92880e-01	**0.031833**
12	3.65000e-01	6.27600e-01	**0.192961**
13	3.55000e-01	2.92880e-01	**0.099550**
14	3.55000e-01	2.92880e-01	**-0.097983**
15	2.42000e-01	1.25520e-01	**0.106604**
16	3.55000e-01	2.92880e-01	**-0.092697**
17	2.42000e-01	1.25520e-01	**0.104930**
18	3.55000e-01	2.92880e-01	**-0.104520**
19	2.42000e-01	1.25520e-01	**0.100278**
20	3.55000e-01	2.92880e-01	**-0.093007**
21	2.42000e-01	1.25520e-01	**0.105063**
22	3.55000e-01	2.92880e-01	**-0.102183**
23	2.42000e-01	1.25520e-01	**0.104397**
24	3.55000e-01	2.92880e-01	**0.102670**
25	3.55000e-01	2.92880e-01	**-0.107760**
26	2.42000e-01	1.25520e-01	**0.102222**
27	3.55000e-01	2.92880e-01	**-0.095023**
28	2.42000e-01	1.25520e-01	**0.104000**
29	3.55000e-01	2.92880e-01	**-0.110641**
30	2.42000e-01	1.25520e-01	**0.097695**
31	3.55000e-01	2.92880e-01	**-0.094128**
32	2.42000e-01	1.25520e-01	**0.104120**
33	3.55000e-01	2.92880e-01	**-0.103733**
34	2.42000e-01	1.25520e-01	**0.104017**
35	3.20000e-01	7.11280e-01	**-0.356519**
36	**3.20000e-01**	**7.11280e-01**	**-0.344556**

Table 6.7: DPAP force field stretching parameters for atom labeling see Figure 6.14

Bonds			
ai	aj	r_{eq}(nm)	**k^s (kJ/mol nm^2)**
1	2	0.1413	**331022.256**
2	3	0.1398	**267669.331**
3	4	0.1085	**341351.000**
3	5	0.1379	**333590.929**
5	6	0.1082	**341351.000**
5	7	0.1439	**288139.658**
7	8	0.1416	**259638.001**
7	9	0.1378	**288139.658**
9	10	0.1085	**341351.000**
2	11	0.1453	**217365.339**
9	11	0.1400	**267669.331**
11	12	0.1409	**331022.256**
8	13	0.1404	**259638.001**
13	14	0.1403	**288139.658**
14	15	0.1084	**341351.000**
14	16	0.1384	**333590.929**
16	17	0.1085	**341351.000**
16	18	0.1392	**333590.929**
18	19	0.1085	**341351.000**
18	20	0.1394	**333590.929**
20	21	0.1085	**341351.000**
13	22	0.1403	**288139.658**
20	22	0.1382	**333590.929**
22	23	0.1084	**341351.000**
8	24	0.1391	**259638.001**
24	25	0.1408	**288139.658**
25	26	0.1083	**341351.000**
25	27	0.1385	**333590.929**
27	28	0.1085	**341351.000**
27	29	0.1390	**333590.929**
29	30	0.1085	**341351.000**
29	31	0.1399	**333590.929**
31	32	0.1085	**341351.000**
24	33	0.1409	**288139.658**
31	33	0.1378	**333590.929**
33	34	0.1083	**341351.000**
1	35	0.1162	**1101330.351**
12	**36**	**0.1163**	**1101330.351**

Table 6.8: DPAP force field bending parameters.

Angles				
ai	aj	ak	θ_{eq}(degr)	**k^{θ}(kJ/mol rad^2)**
1	2	3	119.35	**632.2333**
1	2	11	121.16	**515.7457**
2	1	35	180.00	**668.0000**
2	3	4	118.34	**310.1840**
2	3	5	122.15	**650.9733**
3	2	11	119.49	**162.0124**
4	3	5	119.51	**329.1979**
3	5	6	121.62	**329.1979**
3	5	7	117.76	**658.7915**
6	5	7	120.47	**297.0103**
5	7	8	118.15	**668.5092**
5	7	9	121.50	**274.2746**
8	7	9	120.31	**668.5092**
7	8	13	119.19	**240.7903**
7	8	24	118.73	**240.7903**
7	9	10	119.76	**297.0103**
7	9	11	120.94	**751.4922**
10	9	11	119.30	**310.1840**
2	11	9	118.13	**162.0124**
2	11	12	122.29	**515.7457**
9	11	12	119.59	**632.2333**
11	12	36	180.00	**668.0000**
8	13	14	120.33	**668.5092**
8	13	22	119.53	**668.5092**

13	8	24	122.07	**240.7903**
13	14	15	119.80	**297.0103**
13	14	16	119.56	**658.7915**
14	13	22	120.10	**274.2746**
15	14	16	120.60	**329.1979**
14	16	17	119.52	**329.1979**
14	16	18	120.36	**648.2884**
17	16	18	120.12	**329.1979**
16	18	19	119.98	**329.1979**
16	18	20	120.03	**648.2884**
19	18	20	119.99	**329.1979**
18	20	21	120.14	**329.1979**
18	20	22	120.34	**648.2884**
21	20	22	119.52	**329.1979**
13	22	20	119.60	**658.7915**
13	22	23	119.56	**297.0103**
20	22	23	120.82	**329.1979**
8	24	25	119.20	**668.5092**
8	24	33	120.92	**668.5092**
24	25	26	119.50	**297.0103**
24	25	27	119.58	**658.7915**
25	24	33	119.82	**274.2746**
26	25	27	120.87	**329.1979**
25	27	28	119.45	**329.1979**
25	27	29	120.41	**648.2884**
28	27	29	120.14	**329.1979**
27	29	30	120.04	**329.1979**

27	29	31	120.08	**648.2884**
30	29	31	119.87	**329.1979**
29	31	32	120.02	**329.1979**
29	31	33	120.39	**648.2884**
32	31	33	119.58	**329.1979**
24	33	31	119.70	**658.7915**
24	33	34	119.76	**297.0103**
31	**33**	**34**	**120.50**	**329.1979**

Table 6.9: DPAP force field stiff torsional parameters.

Stiff Dihedrals					
ai	aj	ak	al	ξeq	**k^{ξ}(kJ/mol)**
11	2	3	4	178.3	**75.979**
11	2	3	5	-1.4	**120.114**
35	1	2	3	0.1	**0.007**
1	2	11	9	179.9	**85.688**
2	3	5	6	177.2	**46.509**
3	2	11	12	-179.3	**85.688**
4	3	5	7	-178.0	**65.990**
3	5	7	9	-1.2	**61.628**
6	5	7	9	-176.8	**47.552**
5	7	9	10	-179.3	**47.552**
8	7	9	11	-177.5	**159.749**
7	9	11	2	-0.2	**32.329**
10	9	11	2	179.7	**75.979**
9	11	12	36	23.3	**0.007**
8	13	14	16	178.5	**195.234**
8	13	22	20	-179.2	**195.234**
13	14	16	17	-178.6	**65.990**
22	13	14	16	0.7	**61.628**
14	13	22	23	-179.9	**47.552**
15	14	16	18	177.9	**78.198**
14	16	18	20	-0.5	**49.866**
17	16	18	19	-1.0	**25.381**
16	18	20	21	179.8	**78.198**
19	18	20	22	179.2	**78.198**
18	20	22	13	1.1	**42.113**
21	20	22	23	-0.3	**25.381**

33	24	25	26	-179.0	**47.552**
8	24	33	31	178.3	**195.234**
24	25	27	28	-178.9	**65.990**
8	24	25	27	-178.7	**195.234**
25	24	33	31	1.1	**61.628**
26	25	27	29	178.3	**78.198**
25	27	29	30	179.6	**78.198**
28	27	29	31	179.9	**78.198**
27	29	31	33	-0.5	**49.866**
30	29	31	32	-1.1	**25.381**
29	31	33	34	177.6	**78.198**
32	**31**	**33**	**24**	**-179.1**	**65.990**

Table 6.10: DPAP force field improper dihedral angles parameters.

Improper Dihedrals					
ai	aj	ak	al	ξeq	**k^{ξ}(kJ/mol)**
2	1	3	11	0.4	**310.779**
5	2	4	3	-0.2	**282.979**
7	3	6	5	-2.8	**92.399**
9	5	8	7	-1.1	**471.574**
8	7	13	24	0.1	**28.016**
11	7	10	9	0.1	**301.297**
11	2	9	12	0.1	**310.779**
13	8	14	22	-1.3	**471.574**
16	13	15	14	1.4	**273.029**
18	14	17	16	0.6	**284.824**
20	16	19	18	0.4	**284.824**
22	18	21	20	-0.0	**284.824**
23	13	20	22	-0.8	**413.250**
24	8	25	33	1.6	**471.574**
27	24	26	25	1.5	**273.029**
29	25	28	27	0.2	**284.824**
31	27	30	29	-0.3	**284.824**
33	29	32	31	-0.6	**284.824**
34	**24**	**31**	**33**	**-1.2**	**413.250**

Table 6.11: DPAP force field flexible torsional parameters.

Flexible Dihedrals						
ai	aj	ak	al	γ	k^{φ}(kJ/mol)	**n**
9	7	8	24	0.00	3.674	**2**
9	7	8	24	0.00	4.913	**4**
5	7	8	13	0.00	3.674	**2**
5	7	8	13	0.00	4.913	**4**
13	8	24	25	0.00	-0.059	**1**
13	8	24	25	0.00	-2.916	**2**
13	8	24	25	0.00	0.304	**3**
13	8	24	25	0.00	3.612	**4**
7	8	24	33	0.00	-0.059	**1**
7	8	24	33	0.00	-2.916	**2**
7	8	24	33	0.00	0.304	**3**
7	8	24	33	0.00	3.612	**4**
24	8	13	22	0.00	-0.059	**1**
24	8	13	22	0.00	-2.916	**2**
24	8	13	22	0.00	0.304	**3**
24	8	13	22	0.00	3.612	**4**
7	8	13	14	0.00	-0.059	**1**
7	8	13	14	0.00	-2.916	**2**
7	8	13	14	0.00	0.304	**3**
7	**8**	**13**	**14**	**0.00**	**3.612**	**4**

Chapter 7 The role of Tat peptide self-aggregation in membrane pore stabilization

7.1 Introduction

In the last three decades, intense research has been devoted to the investigation of the cellular uptake mechanism of Cell Penetrating Peptides (CPPs), as they represent a promising platform for engineering safe and efficient drug delivery vectors (for more details, see exhaustive reviews refs.[229–232]). It is now widely accepted that, among many factors, peptide concentration plays a key role in defining the specific route taken by the CPP to enter cells.[233] More in detail, at relatively low CPPs concentrations, i.e. in the nanomolar to low-micromolar range, endocytosis is the dominant mechanism.[234–240] It has been shown that CPPs exploit distinct endocytic routes, such as macropinocytosis,[4] clathrin-mediated endocytosis,[241] and caveolae/lipid-raft-mediated endocytosis,[242] depending on the exact peptide sequence tested, the nature of the attached cargo, the specific cell line used, etc. On the other hand, at higher CPPs concentrations, i.e. above 10-μM, spontaneous massive transduction across the plasma membrane becomes evident for most of the sequences studied so far. This uptake process leads to a rapid release of the peptide in the cell cytoplasm by maintaining the full integrity of the plasma membrane.[230] It is well known that CPPs transduction occurs across spatially confined regions of the plasma membrane, also known as Nucleation Zones (NZs) [2] (an experiment reproduced also here and reported in Figure 7.1).

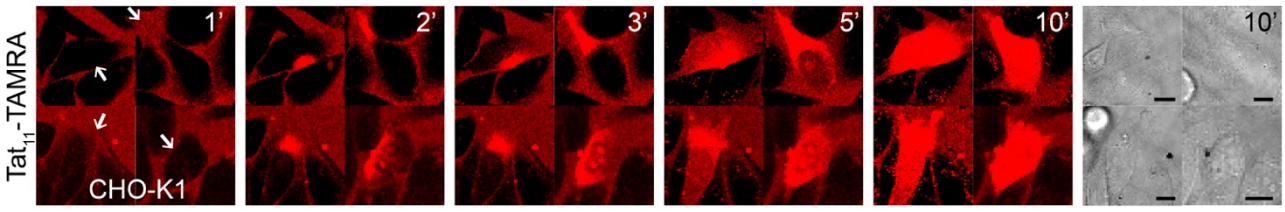

Figure 7.1: Transduction of Tat_{11} peptide, originating from spatially restricted zones (NZs) on the plasma membrane (white arrows). Time-lapse confocal microscopy at room temperature (with frames recorded every 30 seconds) for a free serum growth medium 15 μM solution of Tat_{11}-TAMRA administered to CHO-

K1 cells. Five frames recorded at 1, 2, 3, 5 and 10 min are shown; transmitted-light channel recorded at 10 min is shown in the last frame. Scale bars: 10 μm.

The exact nature of NZs has been extensively researched. It was shown, for instance, that cell-surface Heparan Sulphates (HS) on the plasma membrane are necessary for cytosolic transduction through NZs.[233] Also, it was proposed that CPPs effective transduction involves peptide-driven activation of intracellular acid sphingomyelinase (ASMase), followed by ceramide accumulation on the plasma membrane, local perturbation of membrane organization, and subsequent occurrence of peptide transduction at the border between ceramide-enriched regions and more fluid membrane domains.[241,242] At the same time, experimental evidence of CPPs transduction across artificial membrane models, i.e. Giant Unilamellar Vesicles (GUVs) and Large Unilamellar Vesicles (LUVs),[243–245] suggested that this process can happen also in absence of the complex cellular environment (see, e.g., ref.[246]). Of particular note, some of us recently proposed that an additional level of regulation, not directly related to the membrane, might be imparted by the peptide aggregation state.[247] Briefly, it was shown that the Tat_{11} arginine-rich peptide from HIV-1 Tat protein (sequence: **YGRKKRRQRRR**), which is the prototype of cationic CPPs, is able to self-aggregate in both its fluorescently labeled and unlabeled variants, exactly within the concentration range at which the shift in uptake mechanism (from endocytosis to transduction) is observed. Based on UV-Vis spectroscopy, NMR analysis and molecular dynamics (MD) simulations, Tat_{11} dimerization was proposed as the dominant aggregation process, with an associated equilibrium constant increasing ten-folds by labeling with the standard TAMRA dye. Overall, these findings suggest that Tat_{11} dimerization could play a role in facilitating transduction across the plasma membrane. This, in turn, is in keeping with several experimental observations using rationally engineered dimers/aggregates of Tat_{11}[248–253] or related CPPs[254–256] (obtained by covalent bonding or Lysine linkage at the C-termini) showing enhanced cellular activity. Yet, the possible mechanistic relationship between Tat_{11} self-dimerization and enhanced membrane transduction remains greatly elusive. However, the observation of NZs at high CPPs concentration may suggest the formation of local transitory structure in the plasma membrane. A plausible hypothesis could be that Tat_{11} self-assembly does stabilize membrane pores, thus favoring the onset of a sustained membrane transduction process. A further issue concerns the assessment of the role of organic fluorescent dyes tethered to the CPPs. Fluorescent dyes are commonly used in imaging and molecular detection studies, for their capability to track molecules and to report

on local polarity[257] or viscosity[258] in various environments.[259–261] However, recent experimental evidence highlighted a possible non-neutral role for dye labeling in assisting CPP translocation.[247,262] In an effort to shed some light on these issues, which has tremendous implications for the development of new therapeutic approaches, we present a computational study on the role of Tat_{11} self-aggregation in membrane pore stabilization. In view of the experiment results mentioned above, we have taken into consideration both the native and the TAMRA-labeled Tat_{11} peptide and we have carried out a kinetic analysis of the peptide in its monomeric and dimeric forms inside a purposely-created membrane pore, through extensive MD simulations. Therefore, the main goal of the present study is to evaluate the capability of the peptide to stabilize a lipid membrane pore over a prolonged period of time. In particular, we have extended the CHARMM force field for the treatment of the covalently linked TAMRA dye and performed both standard and steered MD simulations to characterize peptide escape-route kinetics. Results nicely support experimental evidence and further corroborate the view of a special role played by CPP self-aggregation in membrane transduction. Besides, our study suggests an effective, though indirect, action of the TAMRA dye in favoring CPP translocation.

7.2 Computational Details

7.2.1 Model system generation

Tat_{11} peptide is coupled with tetramethylrhodamine-5-maleimide (TAMRA, scheme depicted in Figure 7.2) by addition of a Cysteine residue at the C-terminal end. Both Tat_{11} and dye-labeled Tat_{11} (hereafter, referred to as Tat_{11}-TAMRA) were modeled according to the CHARMM36[115] force field, which is an additive, all-atom model that fixes some flaws in previous CHARMM27 and CHARMM27r force field resulting in greater accuracy. Topology of the TAMRA moiety was prepared using the model builder tools available in VMD[263] software. Bonded and non-bonded parameters were assigned by analogy to preexisting models of organic functional groups in the standard CHARMM force field. Atomic charges were obtained from a previous model[247] and are reported in Table 7.1. Initially, equilibrated configurations for Tat_{11} and Tat_{11}-TAMRA peptide and for Tat_{11}-TAMRA dimer were obtained from a previous computational study[247]. A pre-equilibrated hydrated bilayer made up of 400 1,2-dioleoyl-sn-glycero-3-phosphocholine (DOPC) lipids was used to generate the

initial membrane pore system following the procedure described in Sec. 3.1. However, to speed up calculations, after pore formation and equilibration the lipid system was reduced to 320 DOPC molecules, without affecting the overall membrane stability. In this case, the CHARMM36[115] force field for lipids was used to model the membrane

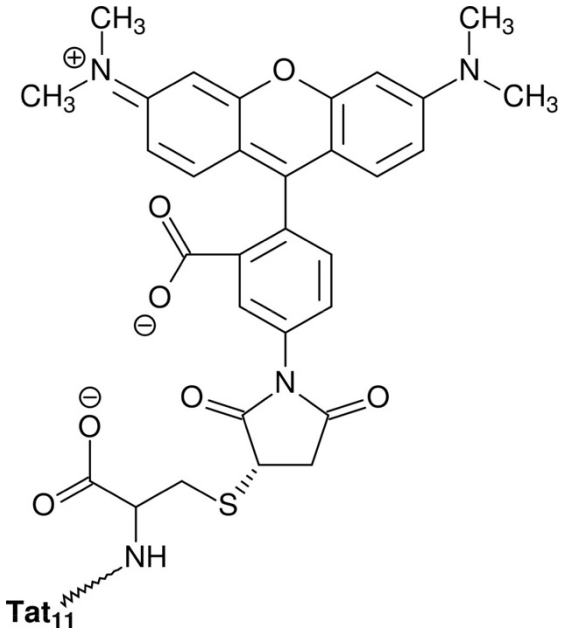

Figure 7.2: Chemical structure of TAMRA dye covalently linked to the Tat_{11} peptide.

bilayer. The obtained membrane pore system was then used for all peptide translocation simulations reported in the study, by preliminarily introducing the peptide within the pore in a parallel configuration to the orthogonal axis of the lipid bilayer, as depicted in Figure 7.3a,b. Chloride ions were added to ensure electric charge neutrality. All the systems were set up to run spontaneous, unconstrained MD simulations. Details on all simulated systems are collected in Table 7.2.

Table 7.1: List of atoms of TAMRA model reporting atom type and atomic charge (i.e., standard CHARMM format is adopted).

```
*>>>>>> CHARMM topology file generated by Molefacture <<<<<<
27 1

DEFA LAST NONE
AUTO ANGLES DIHE

RESI  TMR    -1.00
GROUP
ATOM   OO    O   -0.79810
ATOM   CC    C    0.74970
ATOM  OXT    O   -0.79810
ATOM   CA  CT1   -0.16350
ATOM    N  NH1   -0.38210
ATOM   HN    H    0.26810
ATOM   HA   HB    0.13960
ATOM   CB  CT2   -0.11960
ATOM  HB2   HA    0.14370
ATOM  HB3   HA    0.14370
ATOM    S    S   -0.30340
ATOM  CS4  CP1    0.04000
ATOM  CS3  CP2    0.04000
ATOM  CS2    C    0.45000
ATOM  OS2    O   -0.52700
ATOM  HS4   HA    0.01400
ATOM  H31   HA    0.01400
ATOM  H32   HA    0.01400
ATOM  CS1    C    0.45000
ATOM  OS3    O   -0.52700
ATOM   NS  NH1   -0.02900
ATOM   C1 CG2R61 -0.26300
ATOM   C6 CG2R61 -0.21100
ATOM   C5 CG2R61  0.27100
ATOM   C7    C    0.43600
ATOM   O2    O   -0.63400
ATOM   O3    O   -0.63400
ATOM   H6 HGR61   0.08400
ATOM   C2 CG2R61  0.00700
ATOM   H2 HGR61   0.11300
ATOM   C3 CG2R61 -0.23200
ATOM   H3 HGR61   0.10100
ATOM   C4 CG2R67 -0.00100
ATOM  C22 CG2R67  0.27000
ATOM   C8 CG2R61  0.03900
ATOM  C15 CG2DC1 -0.14100
ATOM   H8 HGA4    0.13300
ATOM  C14 CG2DC1 -0.18100
ATOM   H9 HGA4    0.14900
ATOM  C13 CG2DC2  0.10000
ATOM   N1  NH1    0.05100
ATOM  C20  CT3   -0.16600
ATOM  H16   HA    0.09300
ATOM  H17   HA    0.09300
ATOM  H18   HA    0.09300
ATOM  C23  CT3   -0.16600
ATOM  H13   HA    0.09300
ATOM  H14   HA    0.09300
ATOM  H15   HA    0.09300
ATOM  C12 CG2DC1 -0.23000
ATOM   H4 HGA4    0.14300
ATOM   C9 CG2R61  0.25700
```

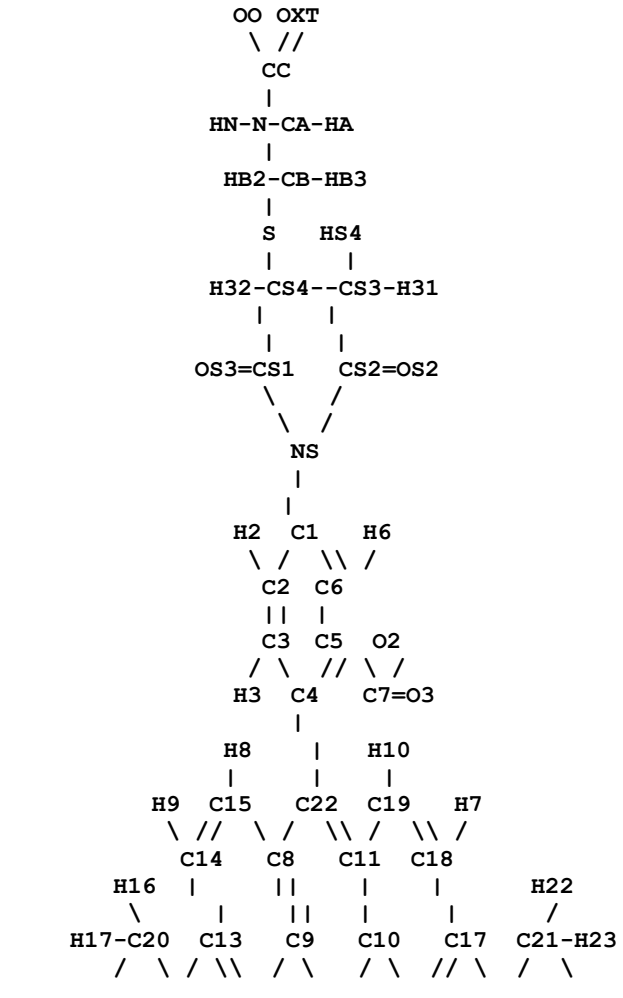

```
ATOM   O1 OG3R60 -0.21800
ATOM  C10 CG2R61  0.25700
ATOM  C16 CG2R61 -0.23000
ATOM   H5 HGR61   0.14300
ATOM  C17 CG2R61  0.10000
ATOM   N2  NH1    0.05100
ATOM  C21  CT3   -0.16600
ATOM  H22   HA    0.09300
ATOM  H23   HA    0.09300
ATOM  H24   HA    0.09300
ATOM  C24  CT3   -0.16600
ATOM  H25   HA    0.09300
ATOM  H26   HA    0.09300
ATOM  H27   HA    0.09300
ATOM  C18 CG2R61 -0.18100
ATOM   H7 HGR61   0.14900
ATOM  C19 CG2R61 -0.14100
ATOM  H10 HGR61   0.13300
ATOM  C11 CG2R61  0.03900

BOND OO CC  CC OXT  CC CA
BOND CA HA  CA CB  CA N  N HN
BOND CB HB3  CB S  CB HB2  S CS4
BOND CS4 H32  CS4 CS1  CS4 CS3  CS3 HS4
BOND CS3 H31  CS3 CS2  CS2 NS  CS2 OS2
BOND CS1 OS3  CS1 NS  NS C1  C1 C6
BOND C1 C2  C6 H6  C6 C5  C5 C4
BOND C5 C7  C7 O2  C7 O3  C2 H2
BOND C2 C3  C3 H3  C3 C4  C4 C22
BOND C22 C11  C22 C8  C8 C15  C8 C9
BOND C15 H8  C15 C14  C14 H9  C14 C13
BOND C13 N1  C13 C12  N1 C23  N1 C20
BOND C20 H18  C20 H17  C20 H16  C23 H13
BOND C23 H15  C23 H14  C12 H4  C12 C9
BOND C9 O1  O1 C10  C10 C11  C10 C16
BOND C16 C17  C16 H5  C17 N2  C17 C18
BOND N2 C24  N2 C21  C21 H22  C21 H23
BOND C21 H24  C24 H26  C24 H25  C24 H27
BOND C18 H7  C18 C19  C19 H10  C19 C11

IMPR C7 C5 O3 O2
IMPR C17 C18 C16 N2
IMPR C13 C14 C12 N1
IMPR CC OXT OO CA
IMPR CS1 CS4 NS OS3
IMPR CS2 CS3 NS OS2

IMPR N  -C  CA  HN
DONOR HN N

END
```

```
H18   N1  C12   O1    C16    N2    H24
     /     |      |     \
H12-C23    H4     H5     C24-H25
   /  \                  /  \
  H13  H14              H26  H27
```

Table 7.2: Molecular dynamics simulation details.

System	# lipids	# water mols	# ions	Replica / Length
DOPC lipid bilayer	400	33126	-	Unconstrained MD: 1; 100 ns
Tat_{11} monomer	320	19062	8 Cl^-	Unconstrained MD: 3; 400 ns
Tat_{11}-TAMRA monomer	320	19062	8 Cl^-	Unconstrained MD: 3; 600 ns Steered MD: 4; 40 ns
Tat_{11}-TAMRA dimer	320	19062	16 Cl^-	Unconstrained MD: 3; 0.6-1.0μs Steered MD: 4; 40 ns

Initial box size 105 x 95 x 95 $Å^3$.

7.2.2 Molecular dynamic simulation parameters

All MD simulations were performed under periodic boundary conditions using NAMD v2.10 software package.[114] The SHAKE algorithm[116] was adopted to keep all bonds containing hydrogen atoms rigid, with a time step of 2 fs. Long-range electrostatic interactions were computed using the Particle Mesh Ewald (PME)[117] method, while nonbonded interactions were evaluated with a cutoff radius of 12 Å, with a smoothing function applied at 10 Å. Constant pressure of 1 atm was enforced by using the Noose-Hover Langevin piston[118,264] and Langevin dynamics was employed to keep the temperature constant at 303.15 K (30 °C) which is above the main phase transition temperature (-20 °C) for DOPC.[265,266] In particular, a semi-isotropic NpT algorithm was imposed to allow the area of the lipid membrane (i.e., X-Y plane) to change independently from its orthogonal axis (i.e., Z-coordinate). All systems underwent a preliminary energy minimization and a short room-temperature MD equilibration. In particular, both monomer and dimer systems, once introduced into the lipid bilayer by aligning the peptide along the pore axis, were equilibrated for a few (about 5ns) nanoseconds to slowly move the center of mass of the peptide to the bilayer center (i.e., center of mass of phosphate groups). For each system, multiple production runs were carried out according to the NpT ensemble for some hundreds of nanoseconds (from 500ns to 1 μs). In the literature, it was reported that complete translocation of CPPs across plasma membrane could take up to 1

ms.[267,268] In our study, it was not possible to see the spontaneous translocation of the Tat_{11}-TAMRA dimer within the simulated time interval during unconstrained MD simulations. In this case, a convenient computational approach consists to rely on steered MD (SMD) simulations to induce translocation of molecules through pores and channels.[269] Hence, we also performed SMD simulations in order to pull the Tat_{11}-TAMRA monomer and dimer systems, while recording the pulling force required to drag the peptide across the membrane out into the bulk solution. Multiple SMD simulations allowed obtaining an average pulling force profile for peptide translocation. Center of mass of peptide and its aggregated form were pulled along the orthogonal axis (i.e., Z-coordinate) of the bilayer according to a constant velocity (1 Å/ns) algorithm. Four replica simulations with same pulling velocity were performed for both Tat_{11}-TAMRA monomer and dimer systems as reported in Table 7.2. Besides, energetic and hydrogen bonding analyses of the systems considered here were performed with the VMD software (in this case, one MD trajectory for each system was analyzed), while other structural analysis was performed with in-house codes.

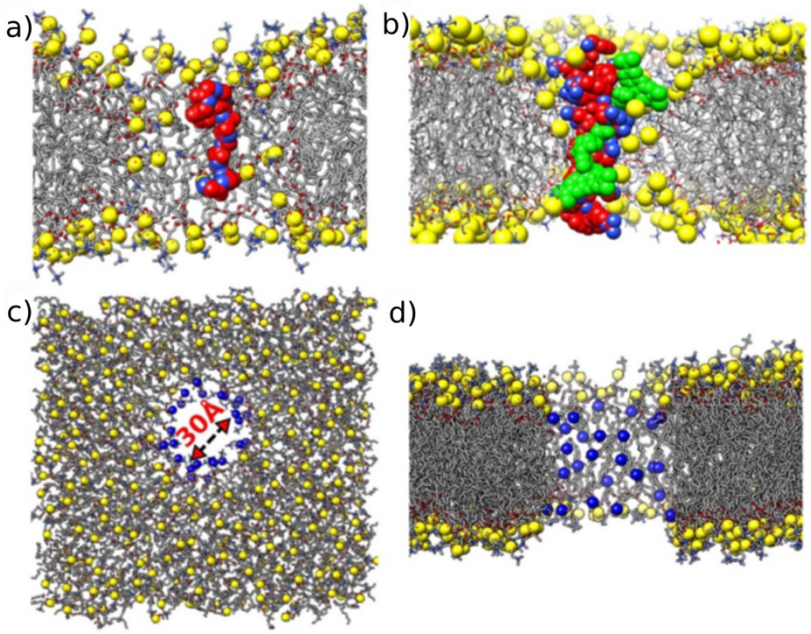

Figure 7.3: Representative initial configurations of a) Tat_{11} and b) Tat_{11}-TAMRA dimer peptides as embedded into a DOPC membrane pore. Peptide backbone is depicted in vdW representation, O atoms in red and N atoms in blue. Lipid chains are depicted in gray, phosphate groups in yellow. c) Top and d) side views of an equilibrated molecular configuration of the membrane pore. Lipid chains are depicted in gray, phosphate groups in yellow and lipid head groups shaping the pore in blue.

7.3 Results

7.3.1 Membrane pore formation and stabilization

Despite many experimental and theoretical studies have investigated pore formation in membranes, this process remains still not fully understood, especially in live cells. Whether CPPs have a promoting effect towards the appearance of pores in cellular and model lipid membranes it is still unclear. Different studies based on confocal microscopy and dye translocation seem to indicate that transient pore structures may determine the observed inward flux in NZs at high CPP concentration. Besides, from a computational point of view, it is highly unlikely the observation of spontaneous pore formation and translocation events on the typical timescales accessible to MD simulations.[270,271] For the reasons sketched above and in analogy with previous studies,[271,272] in this work we decided to artificially create a pore into a previously equilibrated DOPC lipid bilayer, then introducing a peptide monomer or dimer to carefully investigate its exit pathway dynamics. Starting from a pre-equilibrated 400 DOPC lipid bilayer, we sequentially applied an increasing surface tension from 40 to 90 dyn/cm in an isothermal-isobaric ensemble, over a simulation time interval of about 70 ns, in order to induce membrane rupture. During the simulation, a further water layer of about 24 Å was added owing to the excessive thinning of the membrane/water system. Once membrane rupture occurred, a number of pores formed rapidly and became well solvated, owing to the acquired bilayer instability. As a result, a pore of more than 20 Å of radius was obtained. Then, the lipid membrane was relaxed without any tension applied to restore its overall structure at normal conditions (i.e., area per lipids and thickness). During this simulation step, spanning about 60 ns, the large pore previously observed was stabilized by applying positional restraints to the water molecules located into a cylindrical region of 15 Å radius lined up across the lipid bilayer and with the axis center taken approximately in the middle of the pore. Under such conditions, a well-formed membrane pore was equilibrated within the lipid bilayer (Figure 7.3c-d), hence preventing its closure (i.e., final equilibrated pore was 30 Å width and about 40 Å long). Overall, structural parameters of the membrane, such as lipid density (area per lipid: 69.4±0.6 Å2) and thickness (39.0±0.6 Å), evaluated by excluding the pore region, nicely reproduced those of the native lipid bilayer (area per lipid: 68.2±0.6 Å2; membrane thickness: 38.5±0.4 Å).

7.3.2 Tat_{11} and Tat_{11}-TAMRA peptide translocation

As a first step in our kinetics study, we have located a Tat_{11} and Tat_{11}-TAMRA peptide inside the pre-formed membrane defect (i.e. pore). A short equilibration run was carried out to bring the center of mass of the peptide to the center of mass of the lipid membrane and to equilibrate the peptide within this confinement. Hence, unconstrained MD simulations of both peptide monomers have been carried out for several hundreds of nanoseconds in a NpT ensemble. To gain more statistics, we carried out multiple simulations for each peptide, for a total of six extended MD simulations (see details in Table 7.2). The interaction energy between the Tat_{11} peptide (and its labeled variant) and lipids was computed from the simulated trajectories by selecting an initial time interval of about 100ns displaying the peptide buried inside the lipid bilayer (Table 7.3). To better characterize such an interaction and to evaluate possible differences due to the presence of the dye, the interaction energy was decomposed in Coulomb and van der Waals terms. In addition, the distinct contribution of TAMRA and arginine residues was also considered. As shown in Table 7.3, the interaction between the Tat_{11} peptide with the phospholipids inside the pore is dominated by electrostatics owing to the electrically charged peptide residues (i.e., Arg), with other interaction terms having a minor role.

Table 7.3: Interaction energy and H-bond analysis of Tat_{11} and Tat_{11}-TAMRA peptides with DOPC

Int. energy	Tat_{11}/lipid	Tat_{11}-T/lipid	$(Tat_{11}\text{-}T)_2$/lip.	Arg/lip. head	Lys/lip. head	T/lip. head
Coulomb	-1120	-1035	-1913	-1309	-610	31
vdW	-87	-103	-191	-4	-8	-8
Total	-1207 $\pm$ 130	-1138 $\pm$ 130	-2104 $\pm$ 230	-1313 $\pm$ 160	-618$\pm$ 152	23 $\pm$ 20
H-bonds	6.2	6.4	10.7	4.6	1.3	0

Tat_{11}: Tat_{11} monomer; Tat_{11}-T: Tat_{11}-TAMRA monomer; $(Tat_{11}\text{-}T)2$: Tat_{11}-TAMRA dimer; T: TAMRA; Arg: arginine. Units are in kcal/mol. Interaction energy and H-bond analyses were performed on an initial time interval of the MD trajectories (100ns).

Indeed, the contribution of arginine residues interacting with the phospholipid head groups basically account for the interaction of Tat_{11}. Moreover, no significant energy difference exists between the labeled and unlabeled peptide taking into account statistical noise, TAMRA dye adding negligible effects on overall interaction. Similarity between Tat_{11} and Tat_{11}-TAMRA extends also to the hydrogen bonding pattern, both peptides displaying about six hydrogen bonds with surrounding lipids, on average.

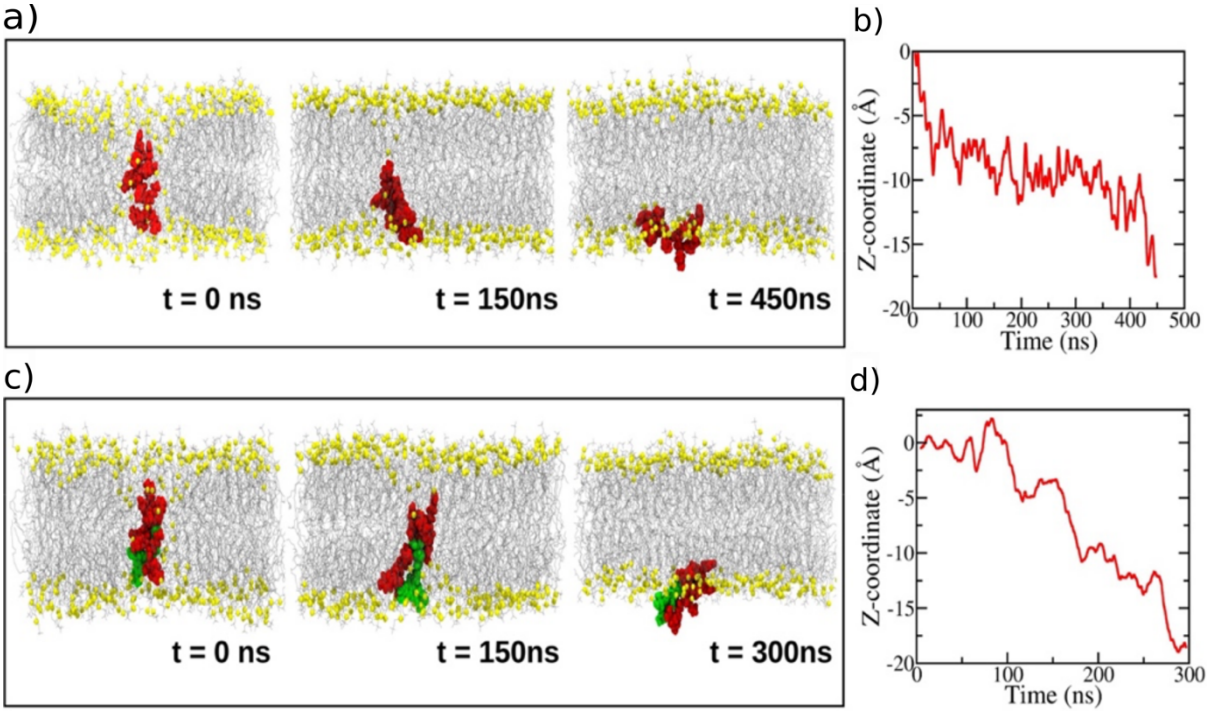

Figure 7.4: Snapshot configurations issuing from a) Tat_{11} and c) Tat_{11}-TAMRA MD simulations taken at different time intervals. Peptides are depicted in red with TAMRA dye in green. (b-d) Corresponding translocation distance of monomer center of mass along the longitudinal pore axis (i.e., Z-coordinate).

To proceed further, we have inspected Tat_{11} peptide dynamics in all systems under study. In one notable case, Tat_{11} monomer underwent full translocation out from the lipid membrane in about 450 ns, as shown in Figure 7.4a,b. In other two parallel simulations carried out for up to 400 ns, the same peptide has shown significant movements towards bulk solution though not completely out of the pore (Figure 7.5). Similarly, Tat11-TAMRA was able to move out of the pore in two simulations after about 300 ns and 550 ns (Figure 7.4c,d and Figure 7.6), whereas in a third case a complete translocation could not be observed, as shown in Figure 7.6.

Overall, our results show that, once inserted into a lipid pore membrane, Tat_{11} peptide has a translocation time in the sub- to 1-microsecond timescale, even if the poor statistics does not allow us to estimate it exactly. This timescale also reflects into the lifetime of the membrane defect before sealing back, which is substantially extended in this case (i.e., about one order of magnitude) with respect to the observed pore re-closure, as revealed by a test simulation in the absence of any peptide (i.e., about 30ns). These findings are well in line with previous studies[271,272] reporting, for example, a comparable kinetics for the Arg_8 homopeptide, whereas the Lys_8 homopeptide apparently showed a fast translocation due to significantly weaker interactions with the lipids.

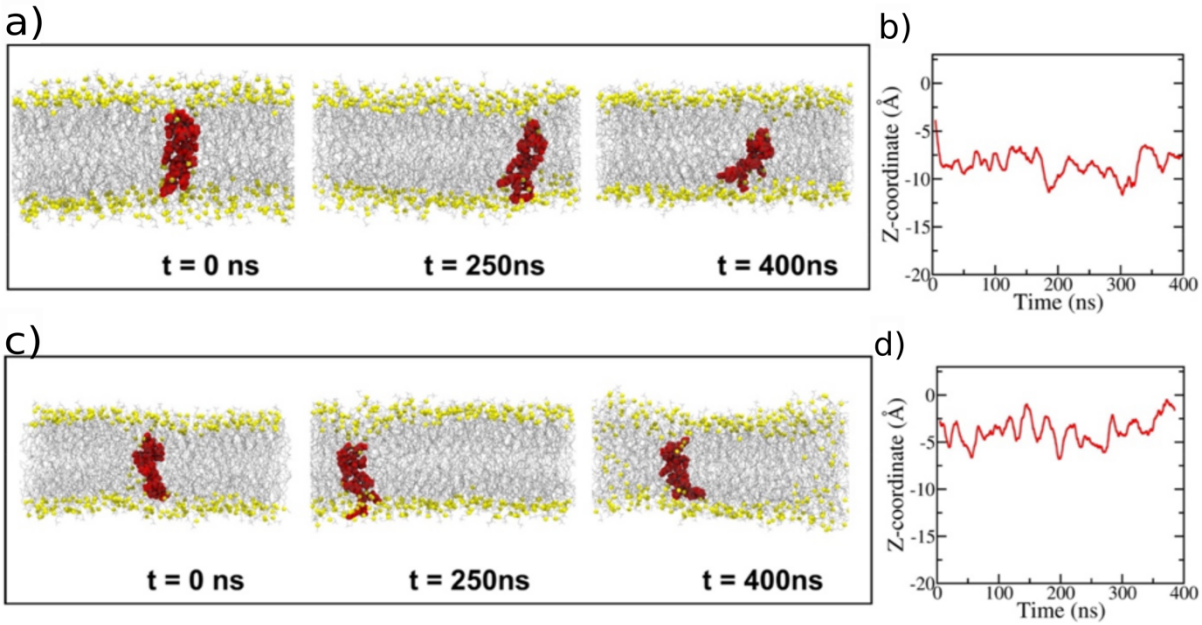

Figure 7.5: (a,c) Snapshot configurations issuing from Tat_{11} replica simulations taken at different time intervals. Peptides are depicted in red. (b,d) Corresponding translocation distance of monomer center of mass along the longitudinal pore axis (i.e., Z-coordinate).

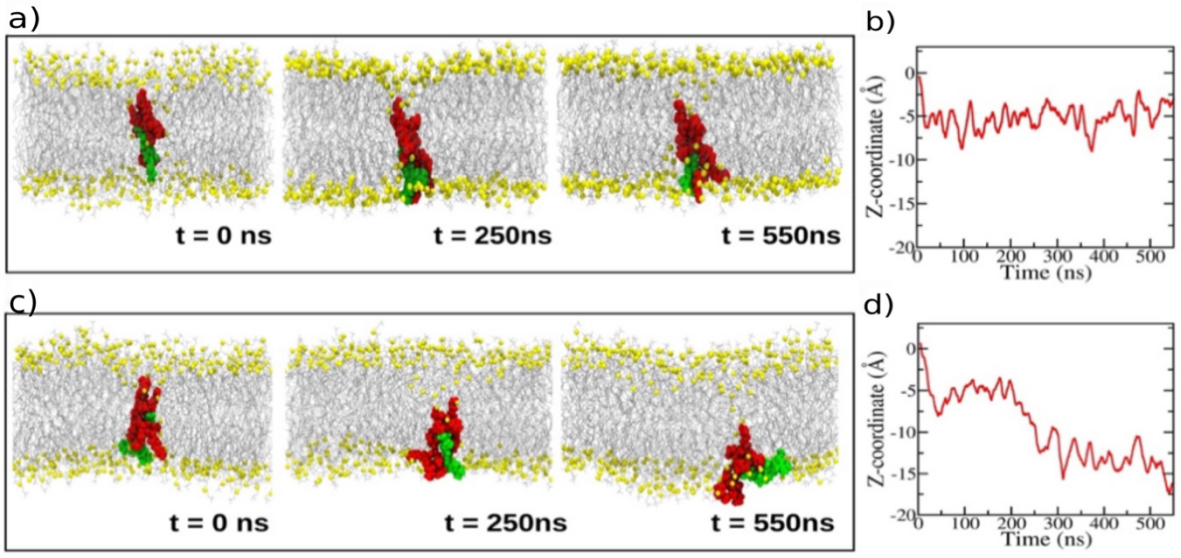

Figure 7.6: (a,c) Snapshot configurations issuing from Tat_{11}-TAMRA replica simulations taken at different time intervals. Peptides are depicted in red with TAMRA dye in green. (b,d) Corresponding translocation distance of monomer center of mass along the longitudinal pore axis (i.e., Z-coordinate).

7.3.3 Tat_{11}-TAMRA monomer versus dimer translocation

By a combination of cell uptake, NMR, UV-Vis and MD study,[247] some of the authors have already shown that Tat_{11} and Tat_{11}-TAMRA do form dimeric structures in solution at high concentration (i.e. micro- to millimolar). In particular, Tat_{11}-TAMRA does form prevalently dimers above the 5-10 μM threshold, whereas the unlabeled peptide shows self-aggregation at much higher concentration (>150 μM). Interestingly, above their corresponding threshold, both Tat_{11} peptides show a marked change of cell uptake mechanism, from energy-dependent endocytosis to diffusive peptide transduction. Here, we set out to probe the capability of Tat_{11}-TAMRA, in its dimeric form, to kinetically stabilize the membrane defect with respect to the corresponding monomeric unit. To this end, following the same protocol described above, the equilibrated structure of a transient Tat_{11}-TAMRA dimer was introduced into the pore of the lipid bilayer and initially equilibrated by restraining its longitudinal motions along the pore axis (i.e., an harmonic potential was applied to the dimer center of mass). Afterwards, all restraints were released, the system was replicated two times with initial velocities randomly regenerated and three fully unconstrained MD simulations were carried out. All Tat_{11}-TAMRA

dimer systems showed significant resistant to move along the pore and, as a consequence, no one exited from the pore despite simulation was extended up to 1 microsecond, as shown in Figure 7.7 and Figure 7.8. Besides, no noticeable peptide conformational changes were observed. Therefore, Tat_{11} peptide in its aggregated form, with twice the number of arginine residues (i.e., 12 Arg), has shown a translocation kinetics in stark contrast to its monomeric counterpart: the physical origin of the slower kinetics is ascribed to both the higher inertial mass and the stronger interaction of Tat_{11}-TAMRA dimer with the lipids lining the pore. To further confirm, we evaluated the interaction energy of the dimer with the surrounding lipids and compared results to the ones for the individual peptide. Results are reported in Table 7.3 highlighting the enhanced interaction (about twice the interaction energy and the number of hydrogen bonds) of the self-assembled peptide with respect to the monomer, with a predominant contribution from electrostatics. Indeed, strong binding between the peptide and the lipids lining the pore is the reason that prevents lipid reorganization and pore sealing.[270,271]

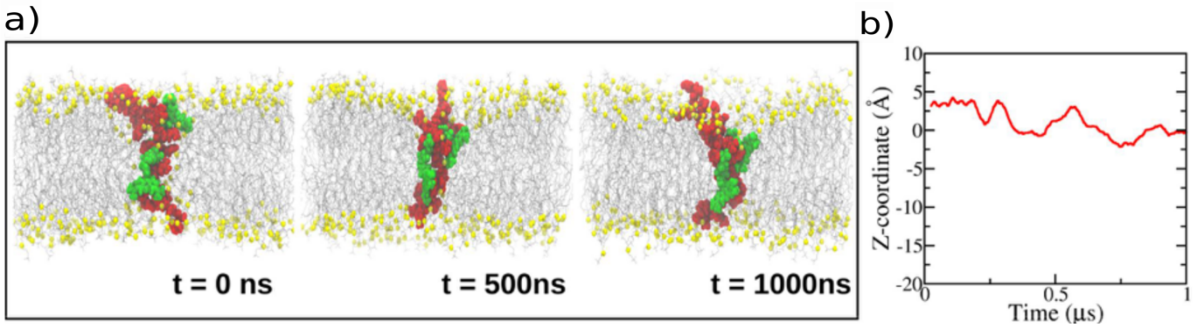

Figure 7.7: a) Snapshot configurations issuing from Tat_{11}-TAMRA dimer MD simulation taken at different time intervals. Peptides are depicted in red with TAMRA dye in green. b) Corresponding translocation distance of dimer center of mass along the longitudinal pore axis (i.e., Z-coordinate).

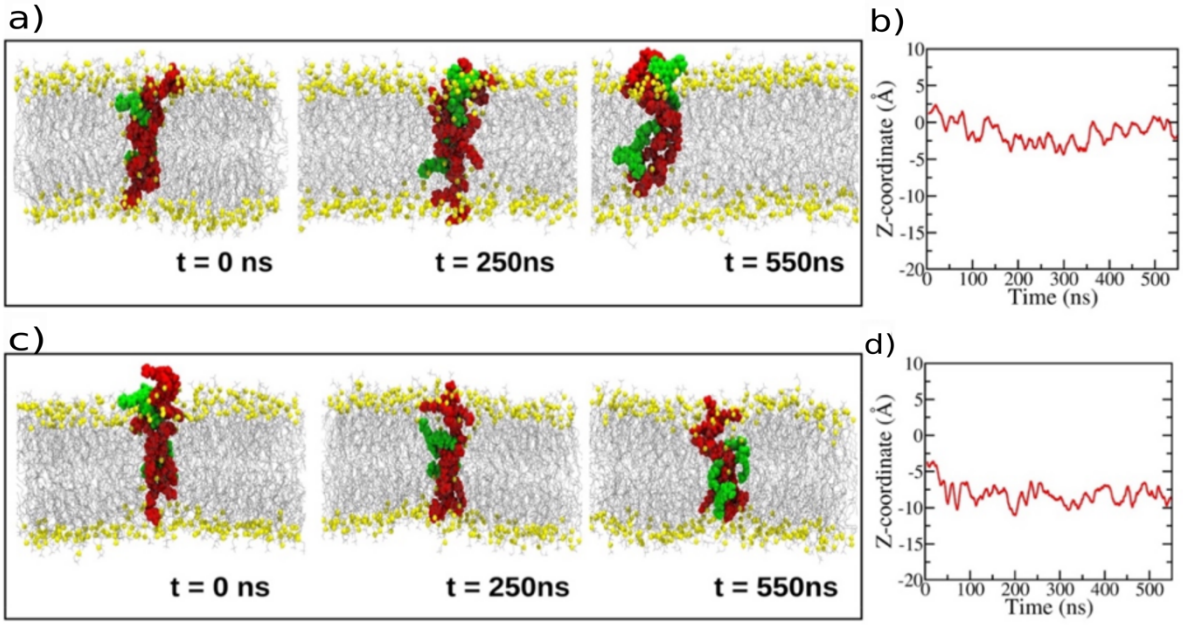

Figure 7.8: (a,c) Snapshot configurations issuing from Tat_{11}-TAMRA dimer replica simulations taken at different time intervals. Peptides are depicted in red with TAMRA dye in green. (b,d) Corresponding translocation distance of dimer center of mass along the longitudinal pore axis (i.e., Z-coordinate).

Furthermore, due to the limits of the timescales typically accessible to atomistic simulations, we relied upon steered molecular dynamics (SMD) to make a more direct comparison between the Tat_{11}-TAMRA monomer and dimer system. To this purpose, multiple SMD simulations were carried out by gently pulling the center of mass of each peptide system initially centered within the lipid bilayer, along the longitudinal axis (i.e., Z-coordinate) of the pore and at constant velocity (i.e., 1 Å/ns) towards bulk solution (Figure 7.9).

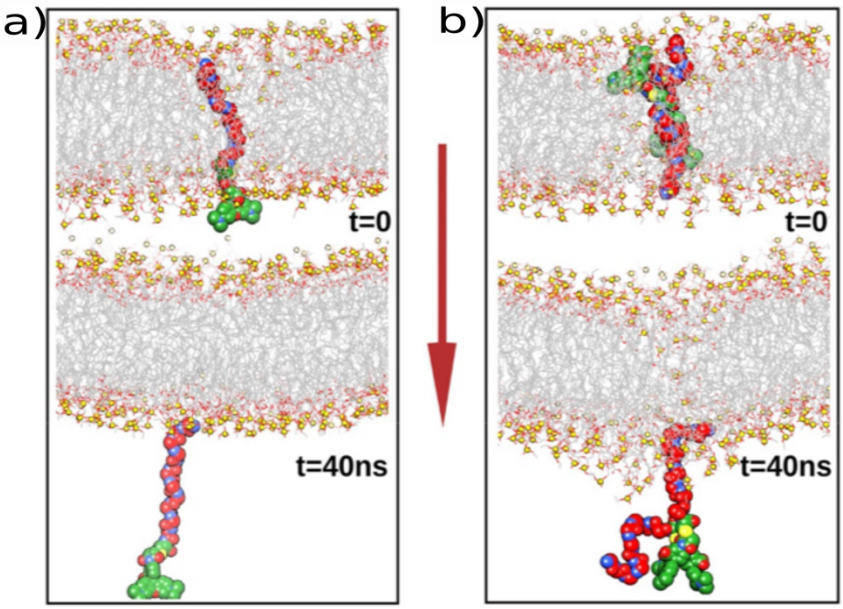

Figure 7.9: Initial (top) and final (after 40 ns, bottom) configurations issuing from Tat_{11}-TAMRA a) monomer and b) dimer SMD simulations. Peptide are depicted in red with TAMRA dye in green. Red arrow shows the direction of applied pulling force along the longitudinal pore axis (i.e., Z-coordinate).

All simulations were carried out for about 40 ns, recording the pulling force required to drive the peptide out every 1 ps. The pulling forces were then averaged in bins of 2 Å width along the Z-coordinate representing the distance from the center of the pore and then averaged over all four simulated trajectories (see details in Table 7.2). The resulting pulling force as a function of distance for both dye-labeled Tat_{11} monomer and dimer are depicted in Figure 7.10. At the beginning, it can be clearly observed that the force to pull the two peptide systems out of the pore is gradually increasing in a similar fashion, up to about 15 Å. At this point, however, a stark divergent profile becomes apparent with the force for dragging the dimeric form notably higher than the one needed for the monomer. Maximum value of pulling force reached about 150 pN, in the case of the monomer, and well above 220 pN, in the case of the dimer (max. difference between the two systems was >100 pN). At longer distances, the two force profiles declined and then converged again toward the end, at about 35 Å. Overall, Tat_{11}-TAMRA dimer required a larger pulling force to be completely extracted from within the lipid bilayer, thus supporting a higher kinetic energy barrier than its monomeric counterpart. This finding is in good agreement with our previous unconstrained MD simulations and energy analysis.

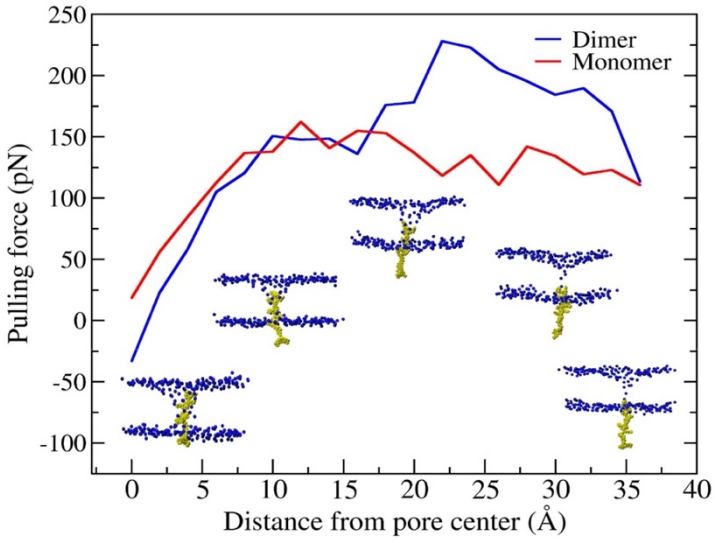

Figure 7.10: Average pulling force applied to gently move the Tat_{11}-TAMRA peptide (both monomeric and dimeric forms) out of the membrane pore as a function of distance from the lipid bilayer center. The resulting force profile is evaluated as the average of four SMD simulations for each system under consideration. Peptide (yellow) at various distances from pore center is depicted in the insets, with lipid head groups in blue. Standard error is 25 pN.

7.4 Discussion

We may argue that the ability to inhibit pore closure can be crucial in the stabilization of membrane defects by Tat_{11} when used at high concentrations, independently on the exact origin of the membrane defect. Of note, similar evidences were so far reported on selected variants of Tat_{11} peptide. First, some of us recently showed by MD simulations that a pore-like membrane defect can be similarly stabilized by Tat_{11} fused to CM_{18},[273] an antimicrobial peptide capable of enhancing Tat_{11} membrane disruption capabilities through carpet-like detergent effects.[274–276] Also, the higher pore-stabilization capability of the Tat_{11} dimer observed here agrees well with previous experimental reports showing that membrane transduction is greatly favored by the rational engineering of Tat_{11} dimers. In particular, it was reported that Tat_{11} dimers obtained by covalent bonds or Lysine linkage at the C-termini show enhanced cellular activity in terms of uptake efficacy and membrane destabilization[248–253]. Of particular note is the work by Erazo-Oliveras et al.[249] reporting on an engineered tetramethylrhodamine-labeled Tat dimer, closely resembles the self-assembled dimer investigated in our study, which is able to mediate efficient

endosomal leakage and deliver exogenous proteins into cultured cells after a simple co-incubation procedure.[249] Moreover, we note that arginine has the ability to make bidentate hydrogen bonds with multiple phosphate moieties on the lipid head groups, thus favoring peptide adsorption on the membrane surface, pore stabilization and, ultimately, peptide transduction.[277] The number of arginine residues present in a peptide chain could be the determining factor in the process of direct transduction, with the optimum number leading to more efficient translocation between 6 to 12 Arg, while more than 16 arginine residues in a peptide showed little or no transduction capabilities.[278,279] This is consistent with our results from spontaneous and SMD simulations as Tat_{11} dimer has twice the number of arginine residues and, as a consequence, the overall energy required to break the bonds between arginine and neighboring phosphates is higher in aggregated Tat_{11}. Most of the literature reporting on CPP cell-entry mechanisms entails the use of organic fluorophores for real-time tracing of peptide localization and activity, often without questioning on the possible effects brought about by such dyes. In this view, any gain of knowledge on the role of dye labeling on peptide uptake by cells or vesicles can help to rationalize previous observations and possibly guide new strategies of peptide engineering. Worthy of note, in our study we have observed no significant effect of the standard TAMRA dye both on the interaction energy of Tat_{11} monomer with membrane lipids and on the peptide residence time within the pore. This may suggest for TAMRA dye the role of a neutral watcher during Tat_{11}-pore interaction. On the other hand, however, we know from previous MD, NMR and UV-Vis analyses that TAMRA dye plays instead an active role in mediating monomer-monomer interactions, thus greatly favoring peptide aggregation as compare to unlabeled species.[247] Moreover, previous experimental studies, here fully confirmed by our *in silico* investigation, have suggested the special role of CPP dimers in penetrating plasma membranes and stabilizing membrane defects, then leading to the possible formation of NZs. Combined together, these results draw a final picture in which the TAMRA dye can be seen as a critical actor in the process of Tat_{11} membrane transduction: it promotes peptide dimerization and, by doing this, it remarkably slows down the translocation kinetics, thus enhancing, at the same time, the lifetime of the defect.

7.5 Conclusions

In this *in silico* study, we provided some further insights on a very complex and challenging cellular process, namely CPPs direct transduction through plasma membranes, whose action mechanism and efficacy have far-reaching consequences for understanding cell biophysics and for therapeutic developments. Remarkable differences have been uncovered between Tat_{11} peptide in its monomeric and dimeric forms. For the purposes of the study, a lipid bilayer pore was preliminarily created to investigate specifically the translocation kinetics of the CPP once inserted into the pore and the interactions with the surrounding lipids at molecular level. The much slower kinetics of the Tat_{11} aggregated form with respect to the monomeric counterpart, as observed in our simulations, was rationalized in terms of the higher interaction energy and hydrogen bondings between the peptide and the lipids shaping the translocation pore, in addition to the larger inertial mass. Tat_{11} dimer, which has double the number of arginine residues than the monomer, was able to stabilize the membrane pore over a prolonged period of time (>1 μs). Such an enhanced pore stabilization effect by the Tat_{11} dimer is attributed to the strong Coulomb interactions between arginine residues and surrounding lipid head groups. It was also proved further with the help of our SMD simulations that the force required to pull the dimer out of the pore by breaking up such electrostatic interactions was significantly larger (i.e., x2) than in the case of the monomer. Such interactions then interrupt the process of lipid diffusion required by the pore to close back and significantly extend the membrane defect lifetime (we may predict the difference to be a few orders of magnitude). Notably, results on the Tat_{11}-TAMRA peptide have also helped to assess the role of dye labeling in the translocation process of CPPs. In this case, our findings, coupled with previous experimental evidence, allow us to propose for TAMRA a "supporting actor" role towards peptide transduction, the dye being able to promote effectively self-aggregation at micromolar concentration, though not adding any relevant contribution to lipid interaction. Whether the present conclusions could be also extended to other dyes of widespread use in CPP translocation studies is a question that calls for further verifications. It is worth noting that in our comparative study lipid composition, which is an important factor possibly influencing peptide transduction, was not taken into examination. However, since our focus was on the effects of self-aggregation and dye tethering, the overall picture emerging from our results is expected to remain substantially unaltered for a number of lipids and lipid mixtures. We believe

our work may provide supportive ideas to peptide design and engineering in a large number of targeted applications aiming at improving CPP-mediated delivery inside the cells.

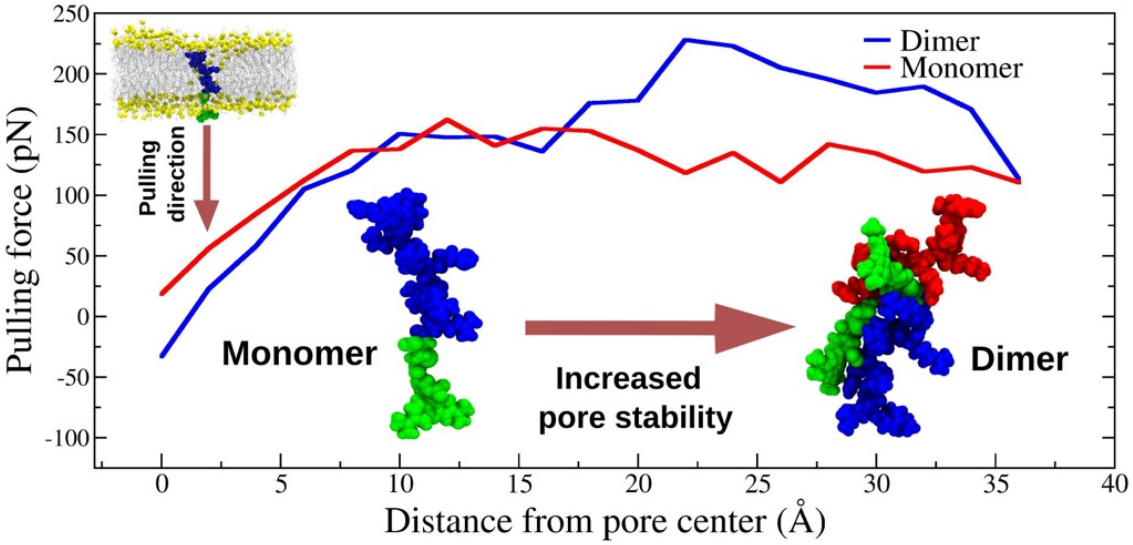

Figure 7.11: Role of Tat peptide self-aggregation to direct transduction in cells is highlighted in a computational study of dimer versus monomer.

Chapter 8 Tuning the ion conductance in a voltage-gated potassium channel through a single mutation

8.1 Introduction

Cell membranes provide barrier to essential ingredients including Na^+, K^+, Ca^{2+} and Cl^- ions and this is where ion channels come in to play their most significant role in making the lipid bilayers more permeable, which in turn efficiently provides the necessary communication between inner and outer environment of the cell. This communication between internal and external environment is necessary to regulate the normal biological functioning of the cell. The ion channels are characterized by three specific properties: i), ion conduction is a rapid process, ii), they are highly selective and specific to let the ions flow through them, and iii), they work in response to external stimuli to promote ion conduction through a process known as gating [46,280,281]. To maintain the normal cellular homeostasis there are high concentrations of K^+ ions inside the cell and of Na^+ ions outside the cell. Because of this ionic charge separation a voltage difference across the membrane is established, translating into a membrane potential on the order of -100 mV[46,47]. Na^+ and K^+ ions pass through unique protein pores inside the cell membranes maintaining their concentrations. Na^+ ions concentration increase inside the cell generates a depolarization of the membrane, establishing a more positive membrane potential and consequently leading to an outward current of K^+ ions outside the cell (this ionic current repolarizes the membrane)[282]. Protein pores or ion channels determine the permeation of specific ions through selectivity filters (SFs) and regulate ions flow through the gating process, i.e., ion conduction is turned off or on in response to specific external stimuli[46–49]. On the contrary, the dysfunction of ion channels or membrane proteins interacting with lipid bilayers can cause diseases affecting tissues in muscles, bones, heart, brain and kidneys. These diseases due to genetic alteration or acquired structural modification of ion channels are termed as channelopathies.

Ion channels involved in electrical signals generation can be widely classified in two major classes: i), ligand gated ion channels and ii), voltage-gated ion channels. Potassium voltage-

gated ion channels (K_V) represent the most diverse and widespread class of membrane proteins in the human genome and they are classified in to 12 families ranging from Kv1 to Kv12. Kv channels play important regulatory roles in the cell and mutations in the genes-expressing these Kv channels can lead to severe genetic disorders, which include epilepsy, deafness, cardiac rhythm disorders, multiple sclerosis and are also linked to proliferation to tumor[49,50]. All Kv channels have high level of similarity and, since the discovery of the Shaker channel, it has been recognized that a functional channel requires four α subunits located in the transmembrane domain (TMD) of the Kv channel. Each α subunit consists of six helices named S1-S6. These helices define two important structural and functional parts of the channel: i), the voltage sensing domain (VSD) is made up of helices S1-S4 located on the channels periphery and it is sensible to changes in the membrane potential, and ii), helices S5-S6 located in the center of the channel make a pore domain (PD), PD is the potassium ion conducting domain. The PD of the Kv channel consists of the channel gate and a selectivity filter (SF) allowing only K^+ ions to pass through it. The gate is formed by crossing C-termini of S6 helices, whereas SF is formed with S5-S6 loop and a highly conserved fragment of the PD region. The VSD and PD are covalently bonded by the S4-S5 linker. The combination of VSD, PD and SF makes up the fully functional K^+ ion permeation pathway[48,49]. The structure of Kv ion channel is shown in (Figure 8.1).

In the recent past, much of the work has been done on mutating different residues at different locations of the channels to study the effect of specific mutations on the functions of Kv channels. Recently, Lee et al. have identified Kv4.3 inherited mutations, such as ΔF227, V338E, G345V and T377M, as the cause of spinocerebellar ataxia type 19/22 (SCA19/22)[283]. All these mutations are responsible for the lack of A-type K^+ channel conductance. In particular, the deletion of F227 in the S2 helix affects the omega pathway, which is formed by S1-S3 helices and the S4 movement in response to membrane voltage changes leading to a current of ions through the VSD, and it causes a complete loss of channel function by interfering with proper plasma membrane targeting and incorporation into a functional tetrameric channel complex. More recently, Smets et al. have investigated the dramatic effects of a de novo KCND3 mutation (dup293-295) (the gene KCND3 encodes the Kv4.3 channel) duplicating the RVF motif of the S4 helix[284]. The addition of an extra positive charge to the VSD of Kv4.3 does not alter the α-helical nature of S4, causes a severe shift of the voltage-dependence gating to more depolarized voltages and leads to an early onset spinocerebellar

ataxia, which is complicated by intellectual disability, epilepsy, attention deficit hyperactivity disorder, strabismus, oral apraxia and joint hyperlaxity. Duarri et al. have studied thoroughly the effects of T352P, M373I and S390N mutations on the activity of Kv4.3 channel[285,286]. Although all these mutations cause spinocerebellar ataxia 19/22, they show a different reduction of the channel activity in the presence of the interacting protein KChIP2b: no activity for T352P mutant, extremely reduced activity for S390N and a reduction up to 75% for M373I mutants.

Although different X-ray crystal structures of the Shaker-type Kv1.2 channel in the open state conformation have been reported in the literature[287–290], only two crystal structures of the intracellular T1 domain of the Shal-type Kv4.3 channel complexed with the channel interacting protein KChIP1 have been deposited in the Research Collaboratory for Structural Bioinformatics (RCSB) Protein Data Bank (PDB)[291,292]. There is still not an atomic resolution structure of Kv4.3 in its open conformation. Since Kv4.3 shares high sequence similarity with Kv1.2, the combined application of homology modeling, molecular modeling, computational and experimental techniques can shed some light on the structure and dynamics of Kv4.3 inserted into a lipid bilayer. In one of our recent publication related to S390N mutation inside the Kv4.3 ion channel[293], and also in this work, we focus our interest on studying the effect of specific point mutation on the Kv4.3 ion channel. The mutations inside the Kv ion channels are responsible for different neuronal diseases. In the current study, we use all atom molecular dynamics (MD) simulations to investigate at a molecular level the effects of selected mutations (M373I and M373E) on the structural stability and conduction properties of the wild-type (WT) Kv4.3 TMD embedded in a POPC lipid bilayer using an ionic strength of 500 mM KCl and applied voltage 1 V.

In this work, from a careful inspection of a molecular model of the Kv4.3 channel, we further considered a single substitution of the same residue to aspartate (M373E) in order to obtain an opposite effect on single-channel conductance. Preliminary results from molecular dynamics simulations suggested a significant increase in Kv4.3 conductance, as initially predicted. Then, single-channel electrophysiology fully confirmed our prediction showing a sharp three-fold increase in ion conductance under the same physiological conditions. Together with previous observations, our findings strongly point towards a special role played by the local environment at the external side of the filter for the fine modulation of ion flux in K^+ channel and, at the same time, suggest a practical way to tune the electric properties of K^+ channels.

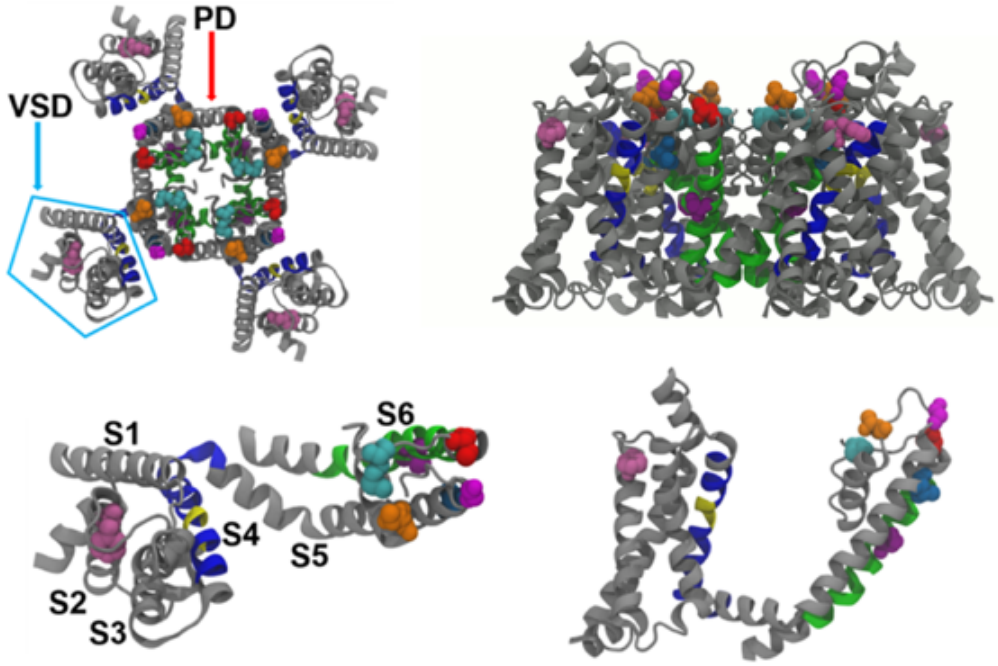

Figure 8.1: Top and side views of the open conformation of the transmembrane domain of wild-type Kv4.3 in its tetrameric (*top panels*) and monomeric (*bottom panels*) forms. The location of VSDs (residues 182-307), PD (residues 321-402) and SF (residues 367-372) are indicated by arrows. The sites of the single point mutation in residue M373 skyblue licorice representations, respectively. S4, S4-S5 linker, S5 and S6 helices are shown in red, blue and green, respectively. Crystallographic K^+ ions are shown in magenta space filling representation. All remaining residues are shown in white.

8.2 Computational Details

8.2.1 Kv4.3 Shal K+ channel system set up in the open state

A model of the full-length WT Kv4.3 Shal K^+ channel open state was built using a combination of homology modeling and molecular modeling. There is a ~47 % sequence identity in the transmembrane domain (TMD: helices S1-S6) between the Kv4.3 Shal K^+ channel and the high resolution X-ray crystal structure of the Kv2.1 paddle-Kv1.2 chimera channel (PDB ID 2R9R) [287], the structural model of Kv4.3 TMD was generated using as a template for this structure.

The homology modeling of a single monomer of the Kv4.3 TMD was performed with the SWISS-MODEL server and Swiss-PdbViewer[294–298]. Then, a full length tetrameric form of the WT Kv4.3 channel in its open state was also built with the monomeric form of the homology model of the Kv4.3 TMD[291,292] using the Membrane Proteins Tutorial of the VMD 1.9.3 software package[263]. Moreover, the model of Kv4.3 TMD was validated with the Memoir server[299,300] and the homology modeling algorithm designed for membrane proteins MEDELLER[301] by using the Kv4.3 TMD as a target sequence and the Kv2.1 paddle-Kv1.2 chimera channel TMD as a template. The structural alignments of Kv4.3 TMDs generated with two different methods gave Cα atoms RMSDs of the order of 0.2 Å. Initially, the structure of WT Kv4.3 TMD (residues 165-411) was embedded in a slightly asymmetric POPC lipid bilayer containing 443 lipids (225 and 218 POPC molecules were in upper and lower leaflets, respectively) in excess of 150 mM KCl using the CHARMM-GUI Membrane Builder tool[302–304] and the VMD 1.9.3 software package. Four crystallographic K+ ions were placed in the selectivity filter (SF: residues 367-372) using as a reference the position of the ions in the X-ray crystal structure reported by Long et al. in 2007[287]. The psfgen mutate command of VMD was employed on this starting system to generate M373I and M373E (in the pore domain (PD) next to the SF)) mutated Kv4.3 TMD systems. The total number of atoms of each Kv4.3 TMD system, including water and ions, was about 157,000.

8.2.2 Molecular dynamic simulation parameters

All simulations were performed with the NAMD 2.12 molecular dynamics software package[305]. The CHARMM36 force fields were used for the protein and lipids[115,306], and the TIP3P model was used for water[307]. The smooth Particle Mesh Ewald (PME) method was used to calculate electrostatic interactions [308,309]. Short-range real-space interactions were cut off at 12 Å using a switching function. A reversible multiple time-step algorithm was used to integrate the equations of motion with a time step of 4 fs for electrostatic forces, 2 fs for short-range non-bonded forces, and 1 fs for bonded forces [310]. All bond lengths involving hydrogen atoms were held fixed using the SHAKE algorithm[311]. Each system was subjected to the following protocol: (i) 5000 steps of energy minimization with the position of all protein atoms, crystallographic ions, POPC polar headgroups, water and ions fixed with a force constant of 1 Kcal/mol·Å^2; (ii) 25 ps and 100 ps NpT simulations with 0.5 fs and 1.0 fs timesteps,

respectively, with the position of all protein atoms, crystallographic ions, POPC polar headgroups, water and ions fixed using a force constant of 1 Kcal/mol·Å^2; (iii) 5000 steps of energy minimization followed by 75 ps and 100 ps NpT simulations with 1.5 fs and 2.0 fs timesteps, respectively, with the position of all protein atoms and crystallographic ions fixed using a force constant of 1 Kcal/mol·Å^2; (iv) 5000 steps of energy minimization followed by a 10 ns NpT simulation with a 2.0 fs timestep and all protein atoms and crystallographic ions with harmonic positional restraints using a force constant of 1 Kcal/mol·Å^2; (v) 10 ns NpT simulation with a 2.0 fs timestep using harmonic positional restraints on all protein backbone atoms and crystallographic ions with a force constant of 1 Kcal/mol·Å^2; (vi) 10 ns NpT simulation with a 2.0 fs timestep and a gradual release of harmonic positional restraints on all protein backbone atoms keeping the crystallographic ions fixed with a force constant of 1 Kcal/mol·Å^2; (vii) 300 ns NpT equilibration with a 2.0 fs timestep, all crystallographic ions constrained with harmonic positional restraints using a force constant of 1 Kcal/mol·Å^2 and distance harmonic restraints on opposing carbons of the carbonyl moieties of the selectivity filter with a force constant of 10 Kcal/mol·Å^2 [312]; (viii) 50 ns NpT equilibration with a 2.0 fs timestep and a gradual release of harmonic positional restraints and distance harmonic restraints. Then, the 350 ns equilibrated structure having 150 mM KCl was subjected to the addition of ions to reach an ionic strength I of 500 mM KCl using the CHARMM GUI Membrane builder for the calculation of the number of K+ and Cl- ions to be added and the Autoionize plugin of VMD 1.9.3; (ix) 5000 steps of energy minimization followed by a 20 ns NpT equilibration of the new ionized structure without harmonic positional restraints and distance harmonic restraints; and (x) 300 ns NpT production run with an applied electric field generating a membrane potential of 1 V with distance harmonic restraints using force constants of 1, 0.5 and 0.25 Kcal/mol·Å^2 on opposing carbon atoms of carbonyl groups of the selectivity filter (residues 367 to 372) for 10 ns, another 10 ns and the remaining of the production run, respectively. The center of mass motion removal was employed in all simulations. All simulations of NpT equilibration runs were carried out at a constant physiological temperature of 310.15 K using a Langevin dynamics scheme and at 1 atm pressure using a Langevin-Nosè-Hoover piston method[313,314]. All production runs were performed at a constant physiological temperature of 310.15 K in an NVT ensemble applying a homogeneous external electric field (Ez) along the z-axis (Lz) perpendicular to the membrane proportional to defined voltages (V) of 0.5 V and 1 V (Ez = -V/Lz) [315].

8.2.3 Data analysis

Sequence alignments were performed with Clustal 2 [316,317] using the graphical user interface ClustalX version 2.0 [318–320] in order to produce Figure 8.2. All sequences were aligned by performing a complete alignment in the multiple alignment mode. The pore radius was measured with the HOLE program [83]. The number of permeation events were measured with in house script, which divided the simulation box in three different main regions, the first one was before the intracellular side of the lipid membrane, the second one was including the selectivity filter and the third one was after the extracellular side of the lipid membrane in the bulk. The first and last two regions were interspaced by buffer regions spanning the areas occupied by the cavity and the interface between the selectivity filter and the bulk solution, respectively. The conductance, C, of K+ ions, with units in Siemens (S = 1A/1V) defined as the number of electron charges per nanosecond, was calculated by using the conversion factor of 160.217 x N e / ns, corresponding to 1 pA, and the following equation: Conductance = 160.217 x Number of permeation events/time of simulation in ns. The water coordination number and the distribution of K+ ions were estimated using the home made script. The electrostatic potential was calculated using the PME Electrostatics plugin of VMD and the adjusted potential was obtained using a homemade script. The analysis of contact maps and distances were performed with Gromacs 5.0.7 built-in analytical tools. Images, movies and trajectory analyses were performed using graphical tools, analytical plugins and Tcl scripts in VMD 1.9.3 [263].

8.3 Results

Recently, a few inherited mutations, among which there are the M373I and S390N single mutations, have been suggested to cause the onset of spinocerebellar ataxia type 19/22 (SCA19/22) through Purkinje cell loss and progressive neurodegeneration [286]. In this work, we are investigating for the first time the molecular basis of the M373E point mutation (methionine (M) to glutamic acid (E)) in comparison to wild type (WT) and inherited mutation M373I (methionine (M) to Isoleucine (I)) Kv4.3 channels.

8.3.1 Wild-type Kv4.3

The structural model of WT Kv4.3 TMD was generated using the protocol described in the Methods section. The Kv4.3 channel from Homo sapiens shares a ~47 % sequence identity with the Kv1.2 channel from Rattus norvegicus, which has a full length X-ray crystal structure in its open state [287,290].The sequence alignment of PD TMDs of Kv4.3 from Homo sapiens and Kv1.2 from Rattus norvegicus reveals that both proteins must possess very similar type of secondary structure pattern in their corresponding transmembrane helices (Figure 8.2a). Moreover, the PD of human Kv4.3 channel shares also a high sequence similarity with the same domain of other Kv channels from Homo sapiens (Figure 8.2b). In particular, the SF of Kv4.3 (TLGYGD, residues 367-372) shows high sequence similarity with the SF of all human Kv channels, indicating that this domain constitute a highly conserved and common structural feature of Kv channels (Figure 8.2b). In our open state model of human WT Kv4.3 TMD (residues 165-411) each VSD (S1-S4) (residues 182-307) has the typical architecture observed in Kv channels and has a modular structure linked to helices S5 and S6, which form the ion selective PD (residues 321-402) and SF (residues 367-372) of the channel (Figure 8.1).

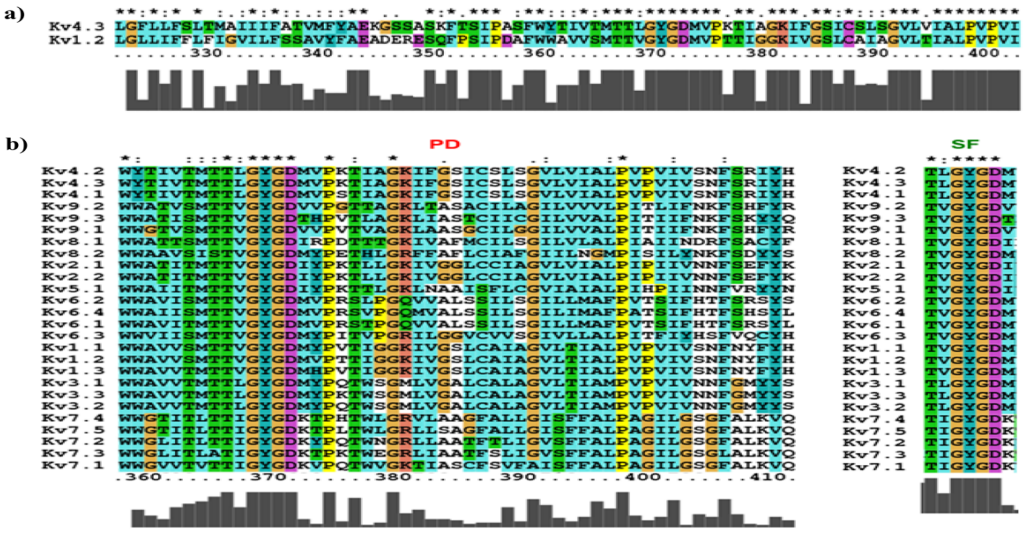

Figure 8.2: (*a*) Sequence alignment of the transmembrane PD (residues 321-402) of human wild-type Kv4.3 with Kv1.2 PD from *Rattus norvegicus* shows high sequence similarity. (*b*) Sequence alignment of the transmembrane PD domains (residues 359-411) of human wild-type Kv4.3 with different Kv channels from *Homo sapiens*. The SF domain of Kv4.3 exhibits high sequence similarity with all human Kv channels, indicating that this region of the protein is highly conserved.

8.3.2 Comparison of WT, M373I and M373E

The difference in channel activity for WT, M373I and M373E Kv4.3 TMDs embedded in a POPC lipid bilayer and subjected to an applied voltage of 1 V can be monitored by measuring the average pore radius over the first 350 ns of each simulation. The average pore radius between WT, M373I and M373E is shown in Figure 8.3. The average pore radius profiles are clearly indicating that the M373E Kv4.3 TMD adopts a conformation where the pore radius is increased compared to M373I and is quite similar to WT. This is the reason that allowed increased permeation of ions in M373E compared to M373I but somewhat similar to WT Kv4.3 TMD. The number of permeation events and the conductance of K^+ ions for WT, M373I and M373E from MD simulations and electrophysiological measurements at single-channel level are listed in Table 8.1. It is worth noting that the simulated mutant model M373I shows a reduction in permeation events and conductance as compared to both WT and M373E channels, whereas in the M373E mutant there is a significant increase in both conductance and permeation events as compared to WT and M373I Kv4.3 TMDs. The conductance values (expressed in pS) observed from MD simulations are in good agreement with experiments.

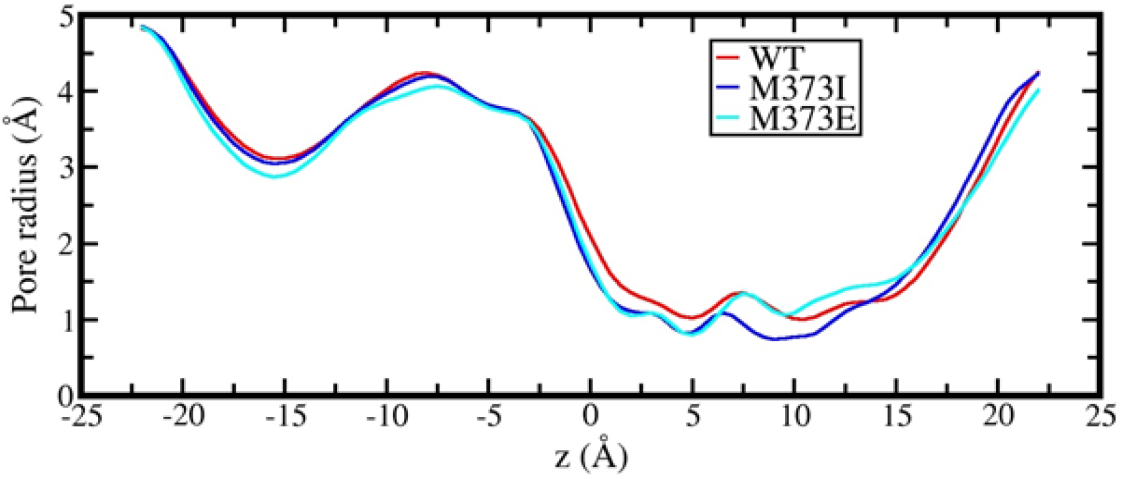

Figure 8.3: Average pore radius along the channel axial position (z-coordinate) for human WT, M373I and M373E Kv4.3 TMDs embedded in a POPC lipid bilayer and simulated with an applied voltage of 1 V. The S6 gating helices become increasingly constricted in mutated forms of Kv4.3 as it can be seen from the structural alignment of PDs for WT (red), M373I (blue) and M373E (cyan).

Table 8.1: Number of permeation events and conductance of K^+ ions for WT, M373I and M373E Kv4.3 estimated from MD simulations and electrophysiological measurements at single-channel level.

Kv4.3	Permeation events	Conductance (pS) simulations	Conductance (pS) experiments
WT	45	7.1	9.5 ± 1.95 (n = 6)
M373I	24	3.8	9.3 ± 0.52 (n = 4)
M373E	26	8.3	24.8 ± 1.4 (n = 5)

The conductance and number of permeation events both were calculated for the entire production run.

The water coordination number and the distribution of K+ ions shown in Figure 8.4 serves as another indicator of the differences between WT, M373I and M373E models. It has been observed that K+ ions are less hydrated in M373I than in WT, mainly in the SF region of the channel, while K+ ions are on average more hydrated in M373E. Remarkably, this effect was significant when we specifically considered ion solvation during K^+ translocation events, as displayed by the decrease in water coordination number in WT along the channel axis with respect to M373E whenever a potassium ion approached the SF region (Figure 8.4). The loss of coordinating water molecules appeared even more significant towards the exit of the SF (about 2 water molecules), where K^+ ions become again fully hydrated and are released into the extracellular environment, thus indicating a more favorable ion translocation pathway in M373E compared to WT model.

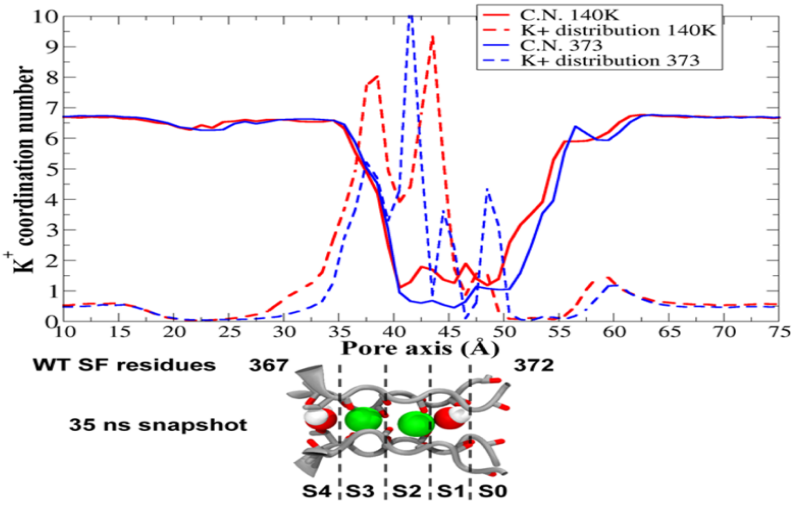

Figure 8.4: Water coordination number and distribution of K^+ ions of human WT and M373E Kv4.3 TMDs embedded in a POPC lipid bilayer and simulated with an applied voltage of 1 V at 310.15 K for 1 µs. The SF of WT Kv4.3 TMD is shown in silver with highlighted carbonyl groups and T367 sidechains in licorice representation. Water molecules and permeating K^+ ions (green) are shown in space filling representation. The different binding sites inside the SF are separated by dashed lines. The analysis was performed over the whole trajectory.

Contact maps of a region of the transmembrane PD domain in close proximity of the SF (residues 350-375) of human WT and M373I Kv4.3 TMD show how M373I and M373E are structurally similar to the WT model as shown in Figure 8.5.

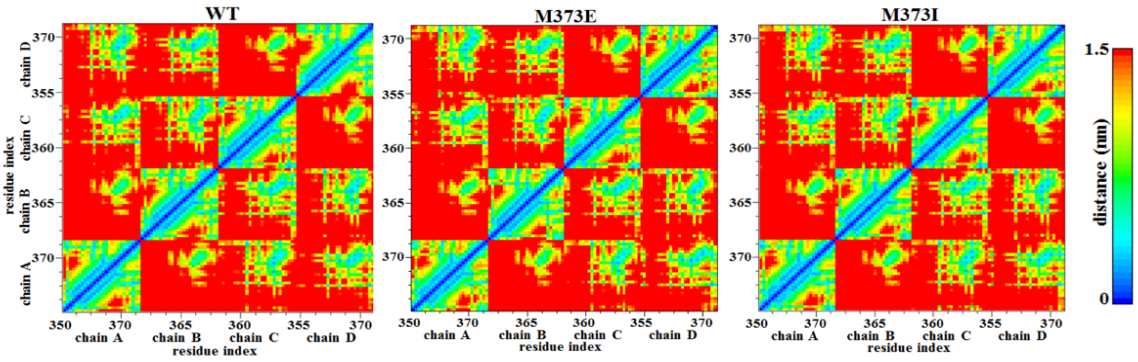

Figure 8.5: Contact maps of a region of the transmembrane PD domain in close proximity of the SF (residues 350-375) of human WT, M373E and M373I Kv4.3 TMDs embedded in a POPC lipid bilayer and simulated with an applied voltage of 1 V at 310.15 K for 350 ns.

The comparison of the number of contacts of residue 373 with residues from a region of the transmembrane PD in close proximity of the SF (residues 350-375) of human WT and M373I Kv4.3 TMD highlights that in M373I the mutated residue 373 exhibits more contacts to

residues 350-375 than in the WT and M373E models shown in Figure 8.6. The residue 373 in M373I has an average number of contacts higher than in the WT model, this result is in good agreement with the differences observed in the contact maps reported in Figure 8.5. The analysis of the number of contacts of residue 373 with other residues of the PD shows that there are almost no contacts with residues 321-349 and 376-402.

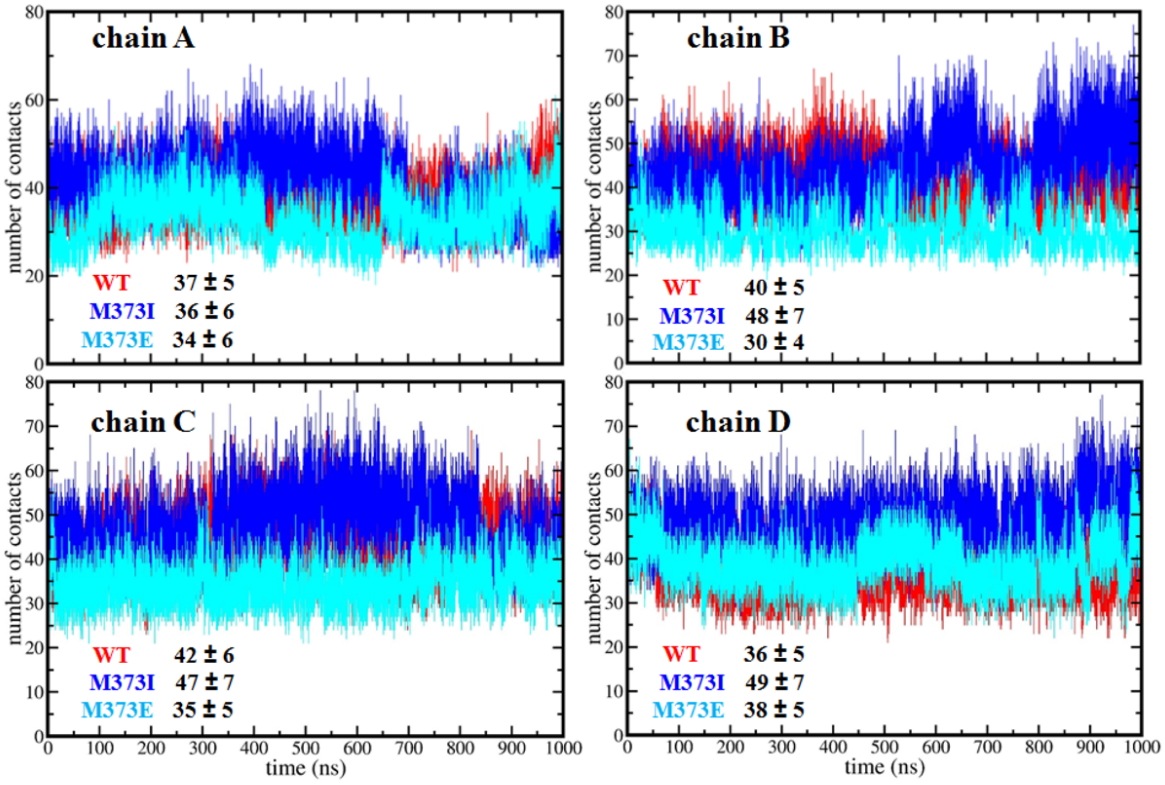

Figure 8.6: Number of contacts residue 373 with residues 350-375 of human WT, M373E and M373I Kv4.3 TMDs embedded in a POPC lipid bilayer and simulated with an applied voltage of 1 V at 310.15 K for 710 ns. In M373I the mutated residue 373 exhibits a higher average number of contacts to residues 350-375 than in the WT and M373E model. The cutoff used for the calculation of the number of contacts was 3.0 Å. Averages and standard deviations of the number contacts for each chain are measured over the last 40% of each trajectory.

It is remarkable that residue 373 interacts preferentially with specific residues of the protein domain containing residues 350-375 in both WT and M373I models reported in Figure 8.7. In particular, the isoleucine residue 373 of M373I exhibits more contacts with residues K350, F351, V363, G369 and G371 if compared to the WT methionine residue 373. This result is a

consequence of the higher hydrophobicity of the amino acid isoleucine compared to the methionine amino acid. Moreover, residue 373 of M373E has less contacts with residues 350-373 compared to both WT and M373I shown in Figure 8.6 and Figure 8.7. Generally, it is exhibiting fewer contacts with hydrophobic residues compared to WT and M373I, while it has more contacts with K350 compared to WT.

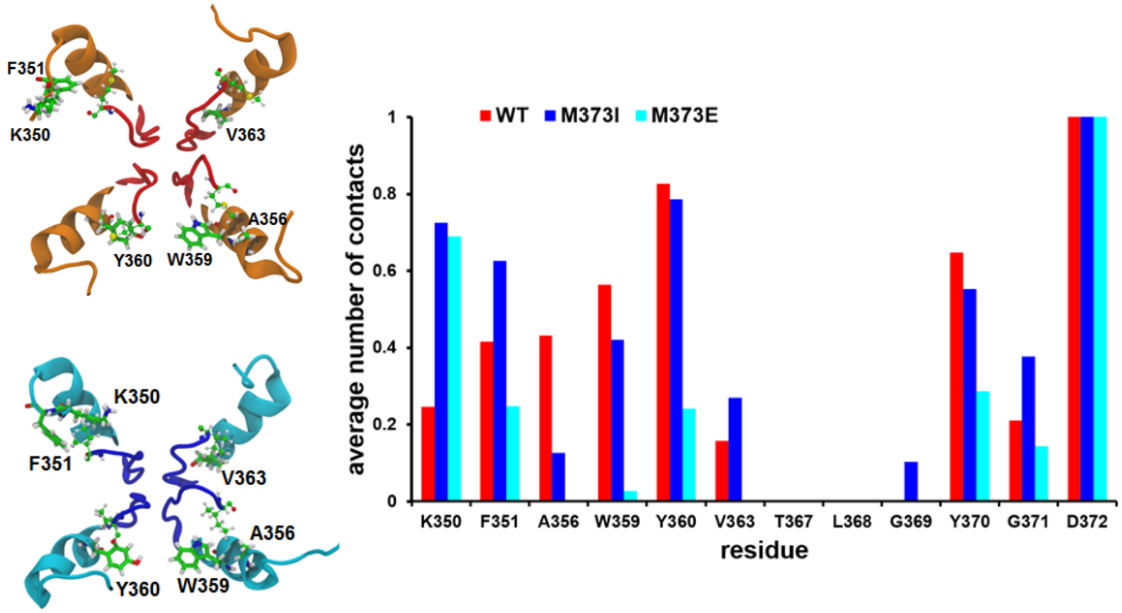

Figure 8.7: The average number of contacts of residue 373 of human WT, M373E and M373I Kv4.3 TMD with residues 350-372. The average number of contacts was measured by averaging the total number of contacts over the four chains and it was normalized dividing by the total number of frames from the whole trajectory. Top views of WT (red), M373E (cyan) and M373I (blue) SFs are shown with residues 350-363 (WT: orange and M373I: cyan). In the inset a side view of M373I SF shows the interaction of I373 with Y360. The cutoff for considering a residue in contact with residue 373 was 3.0 Å. The analysis was performed over the whole trajectory.

In order to better monitor the effect of the mutation in position 373 on the SF stability we have also measured the average distances of Cα atoms of residues 373 for WT, M373I and M373E models. Interestingly, the average distances of Cα atoms of residues 373 in M373I are shorter than those observed in WT, but in M373E the average distances of Cα atoms of residues 373 are longer than the M373I but in comparison to WT the average distances are slightly shorter this observation is reported in Figure 8.8. The average distances of Cα atoms of residues 373

in M373I and M373E TMDs indicate a much tighter packing of the SF in proximity of residue 373 in WT. However, M373E has a slightly flexible packing of the SF compared to M373I. Moreover, the comparison of solvent accessible surface areas (SASAs) of residues 367-373 reported in Figure 8.9a and only residue 373 of human WT, M373I and M373E Kv4.3 TMD shown in Figure 8.9b reports that in the WT and M373E models the SF including residue 373 exhibits larger SASAs than in the M373I system, indicating the presence and influence of the hydrophobic mutation i.e isoleucine mutation. The root mean square fluctuation (RMSF) of alpha carbons of M373I and M373E models show differences in VSD, PD and SF regions compared to WT. Though M373E RMSF of the SF domain is more similar to WT than M373I RMSF shown in Figure 8.10.

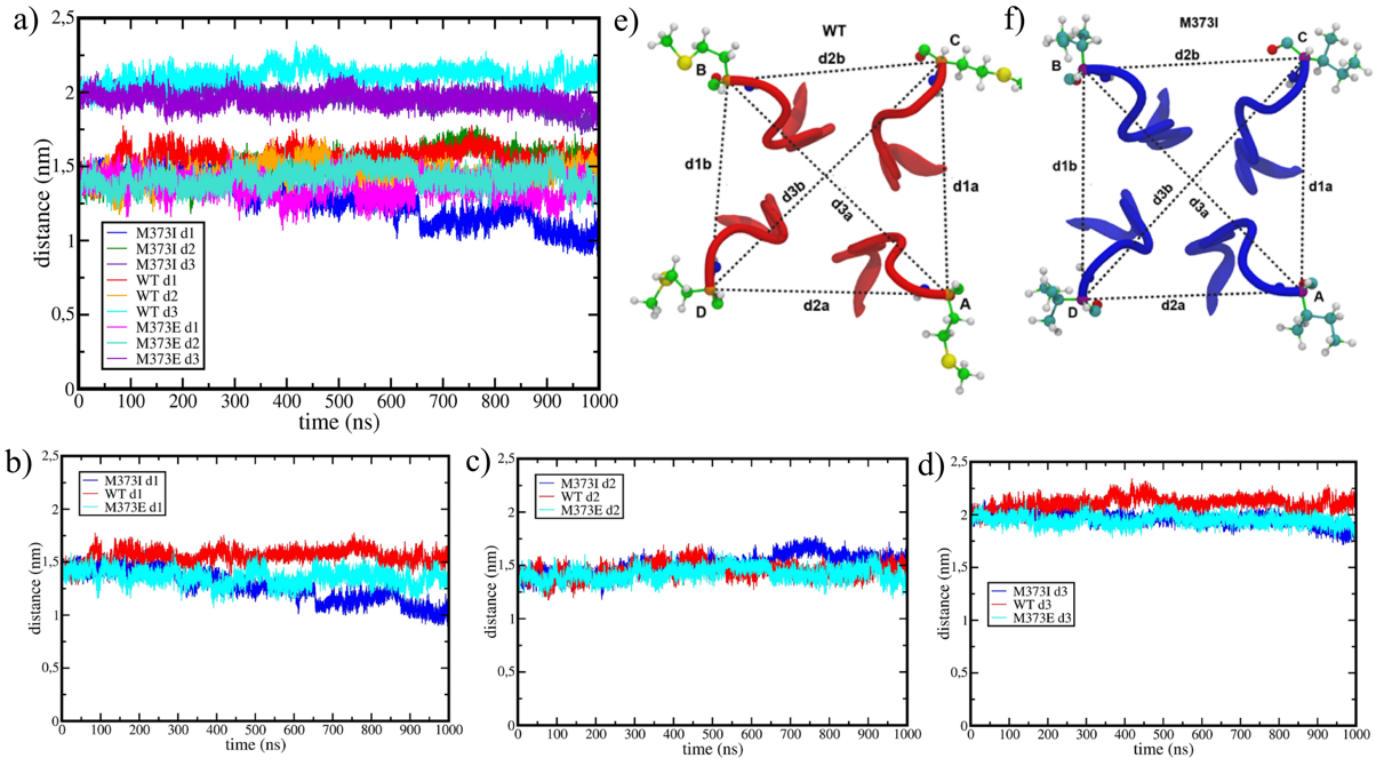

Figure 8.8: a) Average distances of residue 373 Cαs of human WT, M373E and M373I Kv4.3 TMDs embedded in a POPC lipid bilayer and simulated with an applied voltage of 1 V at 310.15 K for 710 ns. b-d) indicating average distance between SF of chains A, B, C and D for all three Kv models, in the M373I model the average distances d1 and d3 are shorter than those in the WT and M373E models, indicating a tighter packing of the SF in proximity of residue 373. (e,f) A top view of the SF is shown together with a

CPK representation of residue 373 and the set of distances of residue 373 Cαs in WT (red) and M373I (blue) models. Cαs are shown in orange and purple for WT and M373I models, respectively. The average distances were measured over the last 40% of each trajectory.

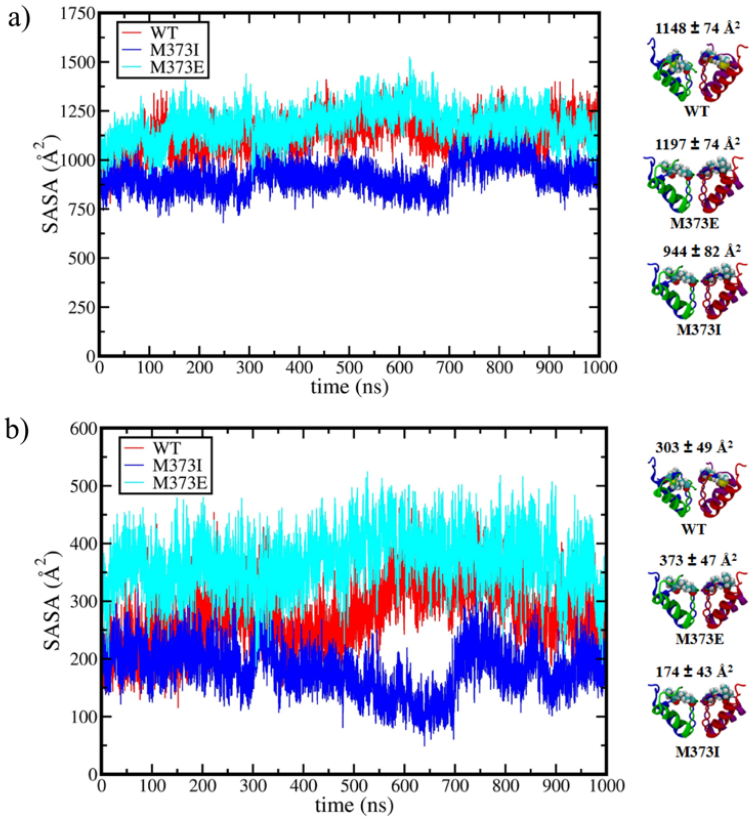

Figure 8.9: Solvent accessible surface areas (SASAs) of (a) residues 367-373 and (b) residue 373 of human WT, M373E and M373I Kv4.3 TMD embedded in a POPC lipid bilayer and simulated with an applied voltage of 1 V at 310.15 K for 710 ns. In both WT and M373E model the SF including residue 373 show larger SASAs compared to the M373I system, whereas the SASA for residue 373 in M373E is also larger than WT model indicating that the presence of the mutation affects the overall SF hydration. Average SASAs for residues 367-373 and residue 373 with their errors estimated as standard deviations over the

analyzed trajectory are reported in the right panel of the figure. The probe radius used for the calculation of SASAs was 1.4 Å. The analysis was performed over the last 40% of each trajectory.

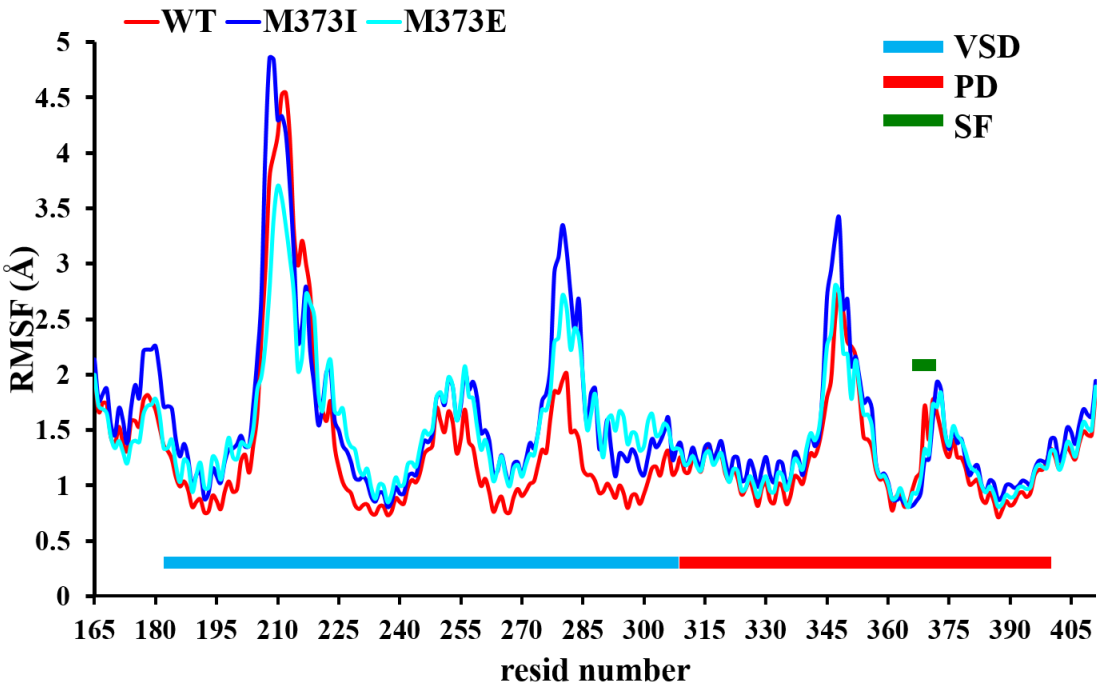

Figure 8.10: RMSF of alpha carbons of human WT (RED), M373I (blue) and M373E (Cyan) Kv4.3 models calculated for VSD, PD and SF region of the Kv4.3 channel TMD.

8.4 Discussion

Channelopathies are disorders caused by malfunctioning of ion channels. With recent advancements in gene sequencing technologies, many ion channel mutations have been identified and associated with human disorders, providing the opportunity to study the disease mechanisms and learn about the original physiological function in much higher detail by learning the malfunctioning of the mutated ion channels at the molecular level. Here we elucidate the functional and structural consequences of two neuropathogenic mutations of human Kv4.3 ion channel by employing molecular biology and electrophysiology methodologies in combination with structural modeling and full-atomistic molecular dynamics simulations.

The main effect of the physiologically mild mutation at position 373 methionine to isoleucine is that the channel conducts slightly fewer potassium ions. Our homology model and full

atomic simulations show that M373I and WT Kv4.3 channels are essentially structurally similar in their pore gate (P-gate) (residues 350-375) including the SF. However, the presence of a more hydrophobic amino acid residue (isoleucine in place of methionine) at the exit of SF of M373I leads to local dehydration mainly responsible for the reduction in the number of K^+ ion permeation events, lowering the overall conductance of the channel. Whereas The increased average pore radius in the region of SF of M373E as compared to WT suggests that the type of mutation in the PD from hydrophobic to more polar and charged glutamic acid could lead to an increase in the number of permeation events resulted from the access of solvated K^+ ions in the SF region, and therefore, finally the permeation of K+ ions. Moreover, a rather less pronounced decrease of the average pore radius in the region of the entrance of Kv4.3 is observed for M373I compared to the WT pore radius profile. This reduction combined with the effects of having a mutation with a more hydrophobic residue at the top of the SF of Kv4.3 most probably contribute to the 71% reduction in the number of permeation events observed over the first 350 ns of simulation. This reduction in permeation events drops to about 47% if the whole 1 μs trajectory is taken into account. Another interesting feature of the average pore radius profiles is how the SF region is affected by the presence of a mutation. Interestingly, the SF in M373I is less distorted than in the WT model, while in in the same region of M373E and WT a larger distortion can be observed as compared to the M373I channel (Figure 8.5).
This increased distortion of the WT and M373E SF compared to the less distorted SF of the mutated M373I model is probably associated with a different hydration and hydrophobicity of individual amino acids at the membrane interface[321]. According to Wimley and White hydrophobicity scale of amino acids, the free energies of transfer from water to a POPC lipid bilayer interface (ΔG_{wif}) for isoleucine (I) and methionine (M) are - 0.31 and - 0.23 kcal/mol, respectively, while ΔG_{wif} for glutamic acid (E) is 2.02 kcal/mol, supporting the reduction in hydrophobic interactions of the residue 373 in the M373E mutant [321,322]. However, the packing of residues in the PD region next to the SF affects the hydration level of the system filtering the permeation of K^+ ions, which has been previously shown in the literature to have remarkable effects on the flexibility and the stability of the SF in Kv channels.

8.5 Conclusions

Since the current atomistic model of Kv4.3 is able to reproduce with a good approximation experimental results, it could be employed for the study and the prediction of the effects of other inherited, and eventually de novo, mutations on the channel structure and function. Furthermore, our molecular model of Kv4.3 could also be used to test the effects of inhibitors and blockers of the channel with the final aim of developing drugs for the treatment of SCA 19/22. Our findings stress the importance to study the effect of pathogenic mutations on the channel function in relation to their regulatory proteins. Furthermore, it shows the strength of combining functional and structural studies in order to pinpoint the molecular determinant which causes the channel to be dysfunctional. Isoleucine affects the overall SF hydration while mutating the residue 373 with polar and charged amino acid i.e glutamic acid greatly enhances the function of the channel including permeation and conductance. Moreover, in the WT model the SF residues and residue 373 exhibit larger RMSFs compared to the M373I and M373E systems confirming that the presence of the mutations affects the overall flexibility of the SF which in the case of M373I is the reduced overall function of the channel and in the case of M373E it is the profound increase in the function and activity of the Kv4.3 potassium ion channel.

Chapter 9 In silico investigation of the interaction between the voltage-gated potassium channel Kv4.3 and its auxiliary protein KChIP1

9.1 Introduction

Voltage-gated potassium channels (Kv) are tetrameric membrane proteins containing α-helical subunits gated to the membrane voltage through voltage sensor domains (VSDs), which act like molecular voltmeters that control the opening and closing of the pore domain (PD)[282,323]. Inside the PD a selectivity filter (SF) regulates which ions can pass through the pore. Each of the four identical monomers contains six transmembrane subunits: S1-S4 comprise the VSD and S5-S6 the PD. Kv channels are involved in the production of electrical impulses, which are transient fluctuations in the membrane voltage (action potential), that allow neurons to transmit electric signals very rapidly over their length. The molecular mechanism of voltage-dependent gating, which is still not completely understood, has been investigated for many decades and it has been described as a process in which the opening and closing of these ion channels is associated with the movement of charged amino acids, which are known as gating charges, within the cell membrane[324].The depolarization of the plasma membrane, which corresponds to a less negative potential on the intracellular side of the membrane, is activating Kv channels and leading to the opening of the channel and to the translocation of K+ ions throughout the PD and the SF of the channel. The presence of mutations in genes coding voltage-gated K+ ion channels impairs the cellular function and leads to certain inherited channelopathies, such as epilepsy, long QT syndrome, and paralyses.

Shal-type Kv4 channels are expressed in a variety of tissues, particularly in the brain and heart [48] where these channels contribute essentially to the subthreshold-activating somato-dendritic A-type current (I_A) in neurons[325] and the transient outward current (I_{to}) in cardiomyocytes,[326]

respectively. Specifically, the Kv4 channels repolarize the action potential in cardiac and neuronal cells. Pathogenic mutations in Kv4.3, for example, have been reported to be associated with heart disorders such as atrial fibrillation[327] and Brugada syndrome [328], and brain disorders such as spinocerebellar ataxia, intellectual disability and epilepsy[283–286]. Kv channel-interacting proteins (KChIPs) are a family of cytosolic proteins, which are essential auxiliary β-subunits of the Kv4 channel for properly encoding its physiological current[329]. Indeed, coexpression with Kv4 increases current density, modulates channel inactivation kinetics and accelerates recovery from inactivation,[330–332] whereas loss of KChIP function may lead to pathological states.[333] Importantly, results suggest that binding and complex formation precede trafficking to cell surface.[334] KChIPs have different isoforms with variable lengths and belong to the neuronal calcium sensor (NCS) family of calcium binding EF-hand proteins[330,331]. In contrast to other β-subunits of the *Shaker*-type Kv1 channels, the KChIP–Kv4 complex forms a cross-shaped octamer at the cytoplasmic side of the channel Figure 9.1a,b, as seen in the X-ray crystal structure of the Kv4.3 channel tetramerization (T1) domain complexed with KChIP1,[291,292] where each KChIP1 subunit has two main interaction sites with the Kv4 intracellular domain Figure 9.1c: the first interface represents the main binding mode of KChIP1 with Kv4 and is formed between the Kv4 N-terminal segment and an adapted hydrophobic pocket of KChIP1; the second interface comprises interactions between KChIP1 and a Kv4 monomer adjacent to the one involved in the first interface. Mutagenesis and functional studies have suggested that the first interface influences mostly channel trafficking to the plasma membrane, while the second one modulates channel assembly and gating kinetics. [292,334] In particular, the specific binding of KChIPs to the Kv4 N-terminus has the effect of greatly enhancing the surface expression of the channel (~8x). Moreover, KChIPs facilitate the assembly of Kv4 subunits and regulate the functional gating properties of the channel. KChIPs can also rescue the function of the channel with mutations affecting the Zn^{2+} binding sites of the Kv4 T1 domain by promoting the binding of mutated monomers and by stabilizing the tetrameric assembly[335].

Here, using all-atom molecular dynamics (MD) simulations, we have carefully investigated the structure and stability of the wild-type (WT) Kv4.3 T1-KChIP1 complex and of five complex variants characterized by specific mutations either on Kv4.3 or KChIP1 or on both proteins, namely Y57A KChIP1, Y57A-K61A KChIP1, E70A-F73E Kv4.3, W8-P10E-A15E Kv4.3 and E70A-F73E Kv4.3 / L39E-Y57A-K61A KChIP1. These mutants were selected since they can

alter, to a different extent, the two known interaction sites between Kv4 channels and KChIP1 auxiliary subunits, and, in turn, they can affect the channel function with known and variable electrophysiology signatures. Structural deviations and instability of the above complex mutants were evaluated through tailored analysis and, in some cases, steered MD simulations. Besides, our MD simulation study has highlighted the existence of a third interface of interaction between Kv4.3 T1 and the H2 helix of KChIP1 Figure 9.1c, which seems to further enforce Kv4.3 tetramerization and calls for additional investigation through mutagenesis and functional analysis.

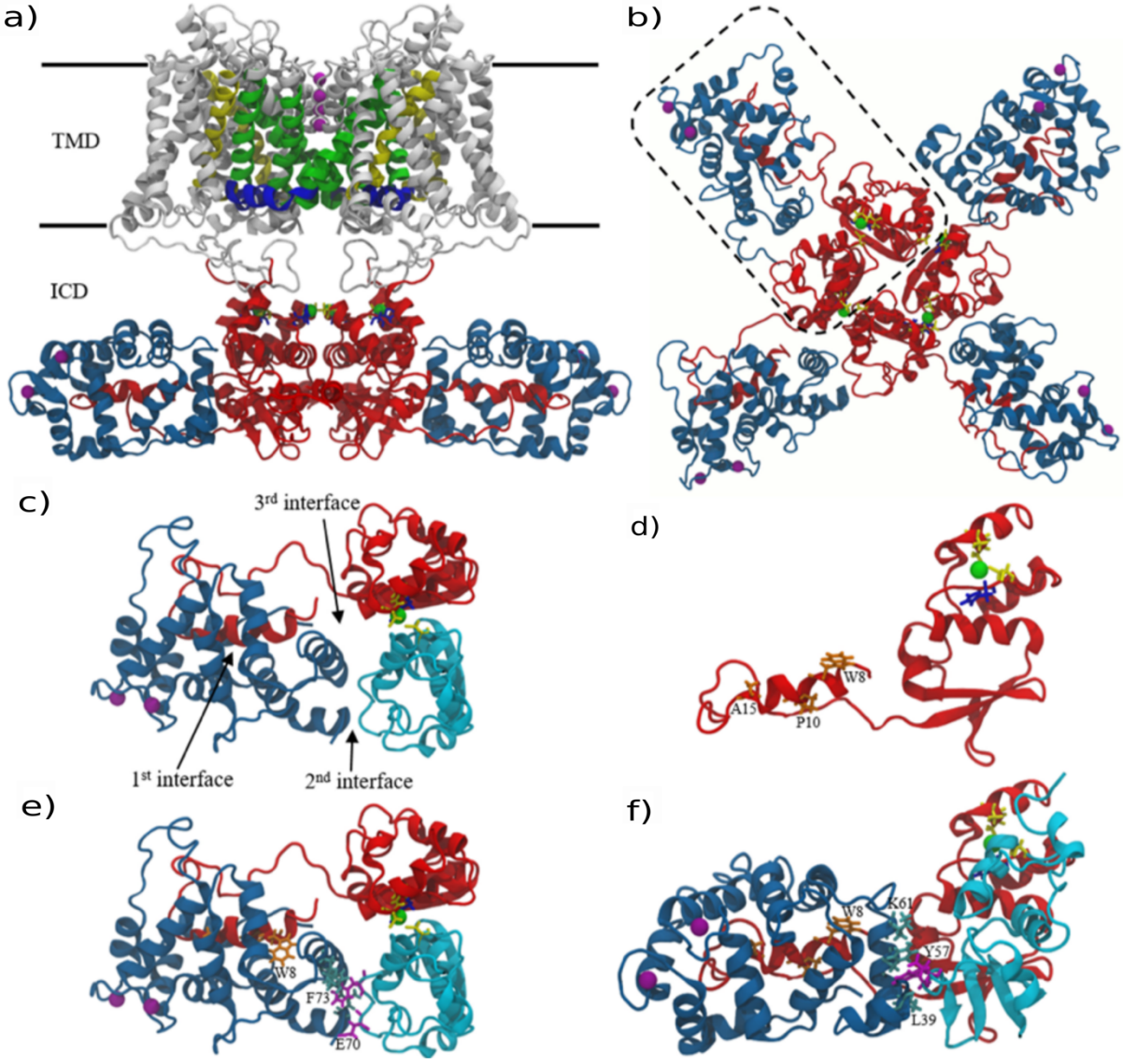

Figure 9.1: a) Side view of the full-length atomistic model of human wild-type (WT) Kv4.3 open state in its tetrameric form showing transmembrane (TMD), intracellular (ICD) domains and KChIP1 auxiliary subunits. Black lines indicate the lipid bilayer. S4, S4-S5 linker and S5/S6 helices are shown in yellow, blue

and green, respectively. Crystallographic potassium, zinc and calcium ions are shown in magenta, green and purple space filling representations, respectively. Kv4.3 TMD (residues 165-411) and Kv4.3 residues 142-164 are shown in white. KChIP1 residues are shown in skyblue. For clarity, only two of the four KChIP1 auxiliary subunits are shown. Kv4.3 T1 domain and KChIP1 auxiliary subunits are shown in red and skyblue ribbon representations, respectively. b) Top view of the WT Kv4.3 T1-KChIP1 complex with a dashed line enclosing a c) zoomed view of two Kv4.3 monomers (red and light blue) interacting with one KChIP1 auxiliary subunit (blue). First, second and third sites of interaction between Kv4.3 and KChIP1 are indicated by arrows. d) Side view of Kv4.3 T1 domain (red) showing residues involved in the W8E-P10E-A15E Kv4.3 triple mutant complex (orange). e) Top and f) side views showing sites of mutations in the first (orange) and second (Kv4.3 and KChIP1 residues are shown in magenta and cyan, respectively) interfaces.

9.2 Computational Details

9.2.1 Kv4.3 T1-KChIP1 complex model

A model of the full-length WT Kv4.3 *Shal* K^+ channel open state with its auxiliary subunits KChIP1 was built using a combination of homology modeling and molecular modeling. Because there is a ~47 % sequence identity in the transmembrane domain (TMD: helices S1-S6) between the Kv4.3 *Shal* K^+ channel and the high resolution X-ray crystal structure of the Kv2.1 paddle-Kv1.2 chimera channel (PDB ID 2R9R)[287]. The homology modeling of a Kv4.3 single monomer was performed with the SWISS-MODEL server and Swiss-PdbViewer[336–340]. Then, a full length tetrameric form of the WT Kv4.3 channel in its open state was also built with the monomeric form of the homology model of the Kv4.3 TMD and the X-ray crystal structure of the intracellular domain (ICD) of Kv4.3 complexed with KChIP1 auxiliary subunits[291,292] Figure 9.1a. The starting model of WT Kv4.3 T1 domain in complex with KChIP1 auxiliary subunit was generated from the X-ray crystal structure of the human complex released by Wang et al. in 2007 (PDB ID 2NZ0)[292]. Few missing residues were taken from the X-ray crystal structure of the Kv4.3 T1-KChIP1 complex reported by Pioletti et al. in 2006 (PDB ID 2I2R)[291]. The initial Kv4.3 T1-KChIP1 complex model Figure 9.1b was subject to the capping of the Kv4.3 C-terminus using a N-methylated residue (-CONH-CH_3: CT3). The variant E70A-F73E Kv4.3, W8E-P10E-A15E Kv4.3, Y57A KChIP1, Y57A-K61A KChIP1, and E70A-F73E Kv4.3 + L39E-Y57A-K61A KChIP1 complex models were generated from

an equilibrated structure of the WT model. Total number of atoms of each Kv4.3 T1-KChIP1 complex, including water and ions, was about 213,000.

9.2.2 Molecular dynamic simulation parameters

All simulations were performed with the NAMD 2.12 molecular dynamics software package[341]. The CHARMM36 force fields were used for the protein and lipids[306,342], and the TIP3P model was used for water[307]. The smooth Particle Mesh Ewald (PME) method was used to calculate electrostatic interactions[308,343]. Short-range real-space interactions were cut off at 12 Å using a switching function. A reversible multiple time-step algorithm was used to integrate the equations of motion with a time step of 4 fs for electrostatic forces, 2 fs for short-range non-bonded forces, and 1 fs for bonded force[310]. All bond lengths involving hydrogen atoms were held fixed using the SHAKE algorithm[344]. The Solvate and Autoionize plugins of VMD 1.9.3 were used to solvate the system and to adjust its ionic strength to 150 mM KCl. Extra bonds, using distance harmonic restraints, were applied to keep the Zn^{2+} ions bound to CYM (cysteine) and HSE (histidine) residues (force constant: 1.0 kcal/mol·Å^2), along with position harmonic restraints on Cα atoms of the Kv4.3 T1 domain (residues 41 to 50 and 102 to 141) (force constant: 0.25 kcal/mol·Å^2). The latter were maintained throughout the MD simulations to ensure stability of the core Kv4.3 T1 tetrameric assembly, while keeping flexible the known Kv4.3-KChIP1 interfacial regions under investigation. Then, 5000 steps of energy minimization were performed and followed by a 25 ns NpT equilibration and 100 ns NVT production run with the same restraints used in the equilibration step. All variant models were subject to an additional 20 ns NpT equilibration before performing NVT production run (100 ns). Additionally, the simulation of the W8E-P10E-A15E Kv4.3 T1-KChIP1 complex was extended up to 1 μs in order to investigate the stability of this system. All simulations were carried out at a constant temperature of 310.15 K using a Langevin dynamics scheme and at 1 atm pressure using a Langevin-Nosè-Hoover piston method[345,346]. Steered molecular dynamics (SMD) simulations were performed on WT, E70A-F73E Kv4.3, Y57A-K61A KChIP1 and W8E-P10E-A15E Kv4.3 Kv4.3 T1-KChIP1 complex models, which were initially solvated with an additional water layer of 40 Å in both directions along the x-dimension and ionized to maintain the physiological KCl ionic strength, by pulling one KChIP1 subunit using a constant velocity (0.1 and 0.25 Å/ns) and a harmonic constraint force constant of 5 kcal/mol·Å^2. The

center of mass of KChIP1 backbone atoms was employed for the pulled subunit. In order to estimate the pulling force for the first interface, the center of mass of the Cα atoms of Kv4.3 N-terminus (residues 1-34) was kept fixed. Moreover, Kv4.3 T1 domain residues 41-130 (i.e., Cα atoms) were kept fixed with a force constant of 1 kcal/mol·Å^2 to evaluate the pulling force in the analysis of the second interface. The total number of atoms of each Kv4.3 T1-KChIP1 complex subject to SMD protocol, including water and ions, was about 307,000.

9.2.3 Data analysis

The analysis of contacts, salt bridges, root mean square deviations (RMSDs), interaction energies and solvent accessible surface areas (SASAs) were performed with built-in analytical tools in VMD 1.9.3[347]. Images and trajectory analyses were performed using graphical tools, analytical plugins and Tcl scripts in VMD. A contact with a specific amino acid was counted as one when at least one atom of the amino acid of interest was within a cutoff distance of 3 Å. The electrostatic potential was calculated using PDB2PQR[348,349] and APBS (Adaptive Poisson-Boltzmann Solver)[350,351] software packages within the APBS plugin version 1.3 of VMD. Then, electrostatic potential surfaces were generated using the molecular surface program MSMS[352] within the Chimera software package version 1.13.1[353].

9.3 Results

9.3.1 Wild-type Kv4.3 T1-KChIP1 complex

A structural model of the WT Kv4.3 T1-KChIP1 complex Figure 9.1b, an octamer displaying four-fold rotational symmetry, was generated using the X-ray crystal structure obtained by Wang et al.[292], following the protocol described in the Methods section. The complex is characterized by two sites of interaction Figure 9.1c, which were originally described in refs[291,292]: the first interface is formed between the hydrophobic N-terminal segment of T1, an α-helix spanning residues 6-17, and a large hydrophobic pocket formed by KChIP1 upon binding, which is the result of a significant outward shift of the H10 helix Figure 9.2 with respect to the isolated protein[291].The T1 N-terminus is also known as the autoinhibitory peptide domain for its capability to favor N-type inactivation in Kv channels[354]. The remaining Kv4.3

N-terminal end (i.e., residues 20-40) forms a loop with no defined secondary structure that is folded back in an anti-parallel orientation and connected to the T1 core domain Figure 9.1d. Deletion of the N-terminal segment (residues 2-20) led to a drastic reduction of KChIP interaction with Kv4 channels[355].Hence, the first interface is not only important as an anchoring site for KChIP, thus allowing an enhanced expression of Kv4 channels on the plasma membrane, but it also helps to modulate Kv4 function by sequestering the inactivating N-terminal peptide domain. The second interaction site is mostly formed between the H1 and H2 helices of KChIP1 and the so-called "docking loop" of the Kv4.3 T1 domain (residues 70-78) and it has both an electrostatic and a hydrophobic nature Figure 9.1c. Importantly, in this case the Kv4.3-KChIP1 interaction occurs with an adjacent Kv4.3 T1 subunit, then it was suggested that the second interface has a special role in promoting and stabilizing Kv4 tetramerization.

Furthermore, our study has highlighted the existence of relevant interactions between the H2 helix and both of the Kv4.3 T1 subunits involved in the first and second interfaces. Indeed, each H2 helix is oriented approximately along the Kv4 longitudinal axis and faces one lateral side of the T1 tetramer in correspondence of the Kv4 intersubunit binding region Figure 9.1b,c. Therefore, in addition to the second interface reported in previous crystallographic studies, [291,292] each KChIP forms, via the H2 helix, a few salt bridges with the same Kv4 monomer tethering the T1 N-terminus to which it is bound (i.e., the first interface). Hereafter, we refer to this interaction site as the third Kv4.3 T1-KChIP1 binding interface Figure 9.1c.

In the following, the results issuing from extended MD simulations about the main interaction sites of the Kv4.3 T1-KChIP1 complex are presented, considering also a number of variants on both Kv4.3 and KChIP1: for the first interface, we considered the W8E-P10E-A15E Kv4.3 triple mutant and, for the second interface, the Kv4.3 mutations E70A and F73E and the KChIP1 mutations L39E, Y57A and K61A Figure 9.1e,f. Overall, six variants of the Kv4.3-KChIP1 octameric complex were generated and simulated along with WT. Such variants were chosen since the availability of biochemical and electrophysiology data.

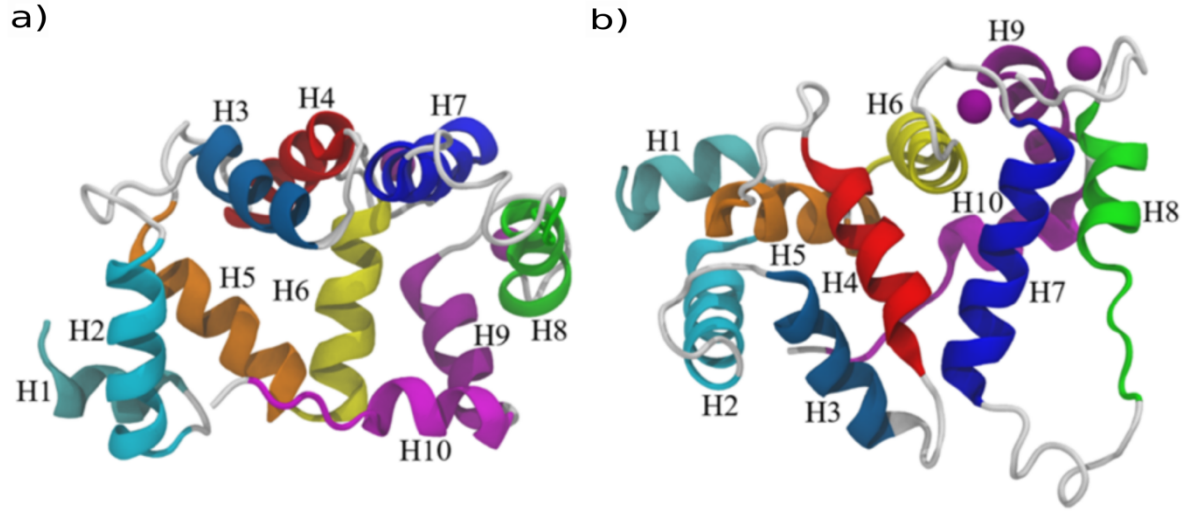

Figure 9.2: a) Side and b) top views of a KChIP1 auxiliary subunit showing all its α-helical domains in different colors. H1 (residues 39-45) and H2 helices (residues 50-63) mainly mediate the second interface interaction among Kv4.3 residues 70-78 and KChIP1. H1, H2, H3, H4, H5, H6, H7, H8, H9, H10 are shown in cyan, celeste, skyblue, red, orange, yellow, blue, green, purple and magenta, respectively. The remaining residues are in white. Calcium ions are shown in purple spacefilling representation.

9.3.2 The first interface and its destabilization by the W8E-P10E-A15E Kv4.3 triple mutant

Our MD simulation of the WT Kv4.3 T1-KChIP1 complex showed a very stable binding mode of the conserved T1 N-terminal segment within the hosting groove on the KChIP1 auxiliary subunit (about 30 Å long and 10 Å wide), with minimal deviations with respect to the starting crystallographic structure (i.e. root-mean-square deviation (RMSD) of Kv4.3 T1 N-terminus was 1.5 Å). In particular, we have examined the hydrophobic interactions and contacts formed by the Kv4.3 N-terminus residues W8, F11 and W19, as they have been considered particularly important for the interaction with KChIP1[291,292].The two tryptophan residues, which are highly conserved across the Kv4 channel family, support the α-helical domain of the Kv4.3 N-terminus (residues 4-17) within the KChIP1 elongated pocket. It is worth noting that during the MD simulation of the WT Kv4.3 T1-KChIP1 complex W8, F11 and W19 showed interactions with the same residues observed in both X-ray crystal structures reported in the literature, as confirmed by the average number of contacts obtained from the MD trajectory Figure 9.3. W8 interacts mostly with ten KChIP1 residues, namely G59, F60, C64, V69, F74,

I77, Y78, F81, F98 and F111, while (Kv4.3) F11 displays hydrophobic contacts with Y78, Y90, L94, F98, F111, A114, L115, L118 and W129 of KChIP1. Moreover, W19 makes van der Waals contacts with seven KChIP1 residues, i.e., Y134, M147, V151, I154, Y155, H174 and F178. Altogether, such hydrophobic interactions contribute to the stabilization of the first interface of the Kv4.3 T1-KChIP1 complex, playing an important role both in the inactivation gating and in the elimination of the open state inactivation of Kv4.3 by KChIP1[354,356].

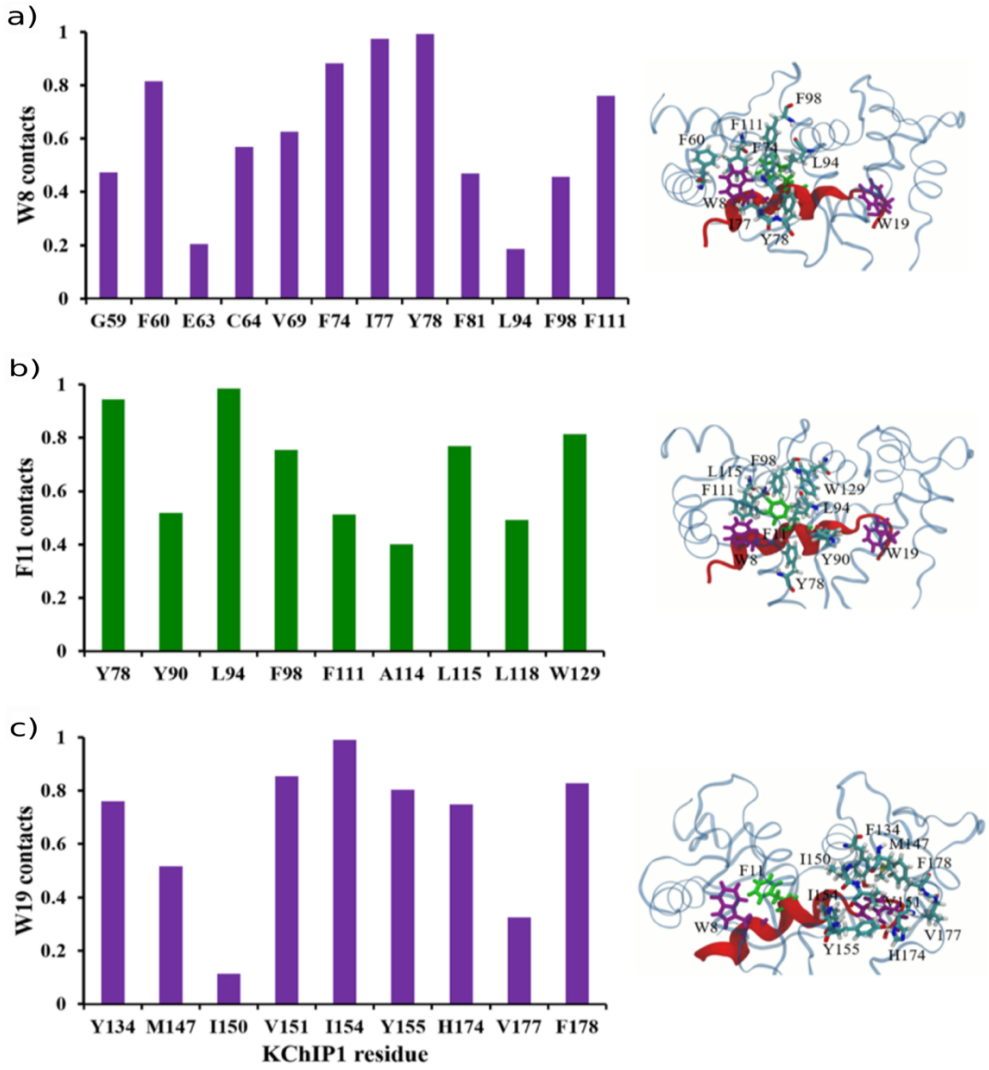

Figure 9.3: Average number of contacts of a) W8 (purple), b) F11 (green) and c) W19 (purple) residues of the WT Kv4.3 T1-KChIP1 complex. The cutoff used to define a contact was 3 Å. The Kv4.3 N-terminus (residues 1-20) and the KChIP1 subunit of the starting model are shown in red and transparent skyblue ribbon representations, respectively. W8, W19 and F11 amino acids are shown in purple and green licorice representations, respectively. Residues displaying the largest average number of contacts are also shown for W8 (top right, panel a), F11 (middle right, panel b) and W19 (bottom right, panel c).

Experimentally, the W8E-P10E-A15E Kv4.3 triple mutant was observed to drastically destabilized the first interaction site, basically inhibiting the Kv4.3-KChIP1 complex formation, as a result of the unfavorably gained hydrophilicity by the T1 N-terminus. Starting from an equilibrated bound configuration of the complex, we generated a model of the Kv4.3 triple mutant and investigated the energy stability and the time evolution of the complex with respect to WT. Note that although it is highly unlikely that a Kv4.3-KChIP1 complex can be formed when Kv4.3 bears the above triple mutation, we nevertheless decided to perform MD simulations of this variant complex for the sake of comparison and to gain a qualitative understanding of the large destabilization effect caused by the introduction of acidic residues in an otherwise hydrophobic pocket. To characterize the different energy stability of the first interface in the two complex systems, we evaluated the interaction energy of the Kv4.3 T1 N-terminus (residues 8-15) with KChIP1 for both WT and W8E-P10E-A15E Kv4.3 Figure 9.4, as issuing from 100 ns MD simulations. As expected, the latter exhibited a dramatic change in the electrostatic interaction energy and a reduction of the van der Waals energy as compared to WT, thus leading to an overall unstable configuration of the first interaction site (i.e., total interaction energy >> 0). The marked change in the hydrophobic nature of the T1 N-terminus caused by the mutations is also apparent from the electrostatic potential maps, as depicted in Figure 9.4b-c.

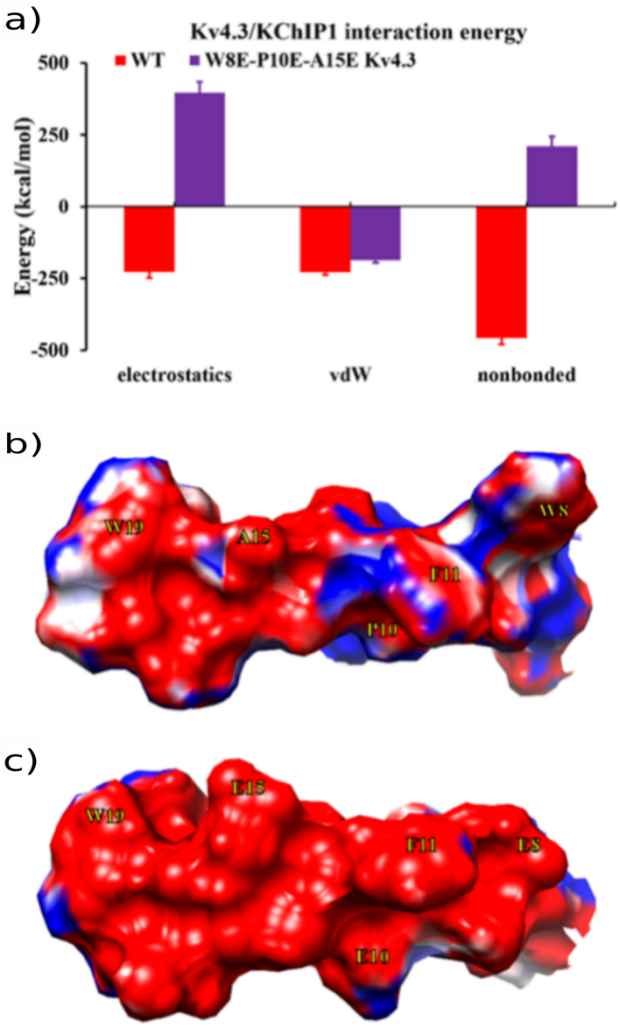

Figure 9.4: a) Average interaction energy of Kv4.3 residues 8-15 with KChIP1 from 100 ns MD simulations of WT (red) and W8E-P10E-A15E (purple) Kv4.3 T1-KChIP1 complex models. Energies were computed and averaged over the whole trajectory, saved every 50 ps. Errors correspond to one standard deviation. Electrostatic potential surfaces of the Kv4.3 N-terminus (residues 3-20) of b) WT and c) W8E-P10E-A15E Kv4.3 T1-KChIP1 complex models.

Moreover, we followed the time evolution of the first interaction region in the complex bearing the Kv4.3 triple mutant through a 1 μs long MD simulation. Though the time interval was not sufficient to observe the full detachment of the auxiliary subunit from the Kv4.3 T1 domain, we noticed a relevant distortion of the complex structure Figure 9.5, leading to a RMSD of up to 8.0 Å when considering the Cα atoms of the Kv4.3 T1 N-terminus (for WT, RMSD was 1.5 Å). Since the complete loss of Kv4.3-KChIP1 interaction upon mutation could not be observed within this time interval, we applied steered molecular dynamics (SMD) simulations in order

to further compare the different stability between WT and W8E-P10E-A15E Kv4.3 in the two complex models. During the SMD simulations, one auxiliary subunit was pulled away from the Kv4.3 T1 domain at a constant velocity of 0.25 $Å \cdot ns^{-1}$ and the resulting pulling force was recorded as a function of the distance between KChIP1 and Kv4.3 T1 centers of mass. The force profiles exhibit essentially three main peaks for both systems, as reported in Figure 9.6. The first peak is basically due to the breaking of the second interface interactions and the pulling force resulted rather similar for WT and W8E-P10E-A15E Kv4.3-KChIP1 systems. On the other hand, for the Kv4.3 triple mutant a smaller force was required to completely overcome the energy barrier associated with the first interface, second peak in Figure 9.6. In particular, the second barrier, which is related to the unbinding of the initial N-terminal segment (around residue 4-8) and peaked at about 60 Å, displays a noticeable smaller height for W8E-P10E-A15E Kv4.3 as compared to WT (Δ(force) ~150 pN). Then, the pulling force is progressively reduced until KChIP1 is completely unbound (~90 Å).

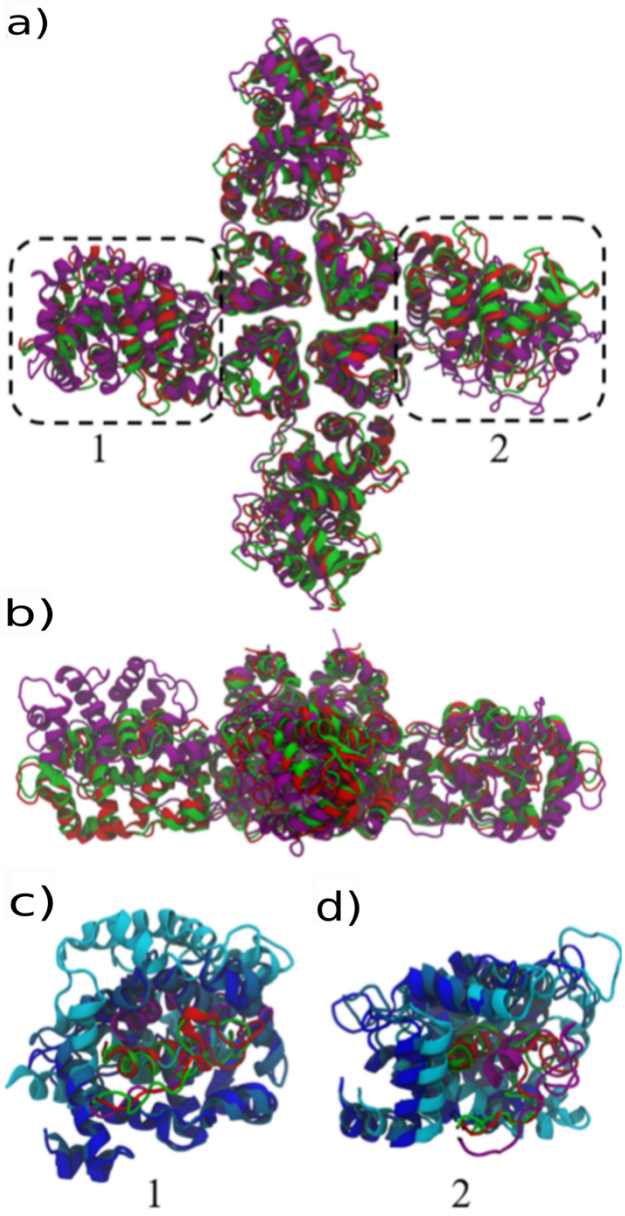

Figure 9.5: a) Average interaction energy of Kv4.3 residues 8-15 with KChIP1 from 100 ns MD simulations of WT (red) and W8E-P10E-A15E (purple) Kv4.3 T1-KChIP1 complex models. Energies were computed and averaged over the whole trajectory, saved every 50 ps. Errors correspond to one standard deviation. Electrostatic potential surfaces of the Kv4.3 N-terminus (residues 3-20) of b) WT and c) W8E-P10E-A15E Kv4.3 T1-KChIP1 complex models.

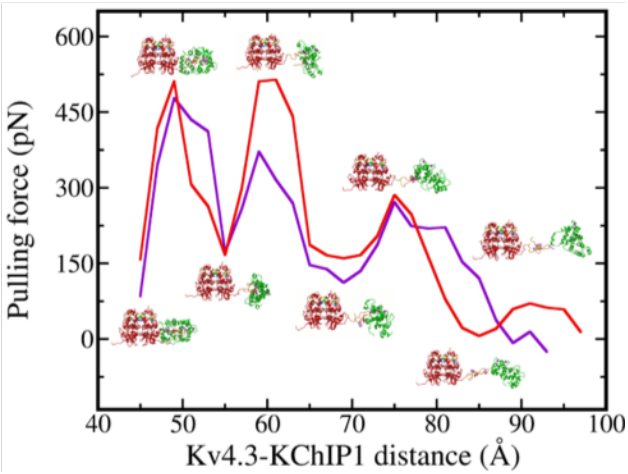

Figure 9.6: Average pulling forces applied to move a single KChIP1 subunit out of a Kv4.3 T1-KChIP1 octameric complex from 100 ns SMD simulations of WT (red) and W8E-P10E-A15E (purple) Kv4.3 T1-KChIP1 complex models using a constant velocity pulling of 0.25 Å·ns^{-1}. Pulling force is reported as a function of Kv4.3-KChIP1 distance. The Kv4.3 T1 domain (red) and the pulled KChIP1 subunit (green) structures are shown as insets at different distances. The overall force profile is given as an average over two SMD simulations. Standard deviation is 35 pN.

9.3.3 The second interface: structure, energy stability and effect of mutations

The second interface of the Kv4.3 T1-KChIP1 complex, burying an area of ~900 Å^2, is mostly characterized by the interaction of H1 (residues 39-45) and H2 helices (residues 50-63) and residue F108 of KChIP1 with the Kv4.3 T1 region spanning residues 70-78 Figure 9.1c,e. Apart a few salt bridges, the core of the interface shows a hydrophobic "lock" between residue F73 of Kv4.3, which is highly conserved among the members of the Kv4 family, and a hydrophobic cavity formed by residues L39, L42, L53, Y57 and F108 of KChIP1 in which F73 can nicely fit into, as observed in the X-ray crystal structures[291,292]. Four variants of the Kv4.3-KChIP1 complex were investigated along with WT, which have been divided in two groups based on their consequences on Kv4 channel function. In the first group, two variants, the Y57A KChIP1 single and Y57A-K61A KChIP1 double mutants, present mutations only on the β-subunit and have small to moderate effects on Kv4.3-KChIP1 electrophysiology, affecting particularly inactivation and/or recovery from inactivation kinetics. Second group's variants, namely E70A-F73E Kv4.3-KChIP1 and E70A-F73E Kv4.3 / L39E-Y57A-K61A KChIP1, have

mutations either on Kv4.3 or on both proteins and are found to alter more severely WT function, including both channel expression and inactivation/recovery kinetics. All such variants were recently tested in the laboratory, to gain further insights into the functional significance of the second interaction site of the Kv4.3-KChIP1 complex. In this work, we performed a comparative study of all the above variant models in order to complement available experimental data and provide additional structural information.

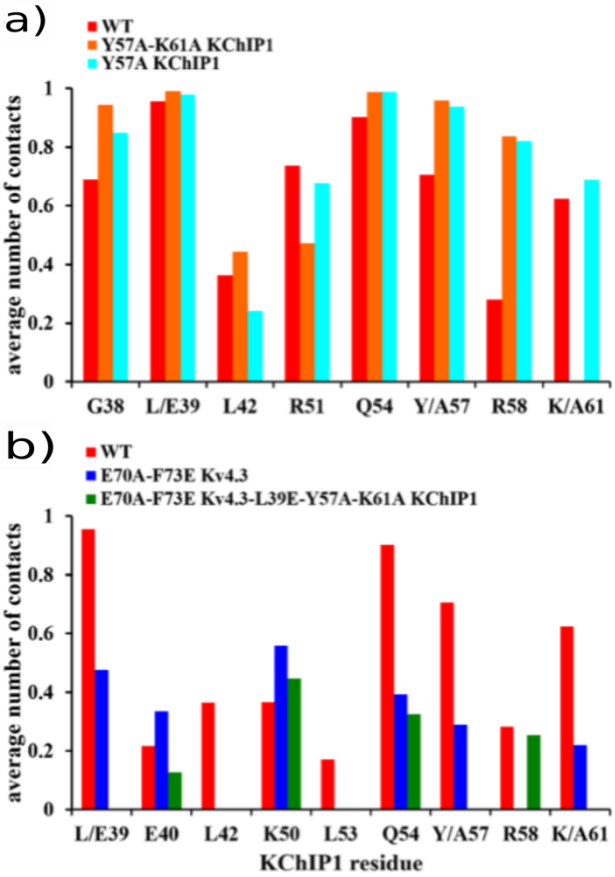

Figure 9.7: The average number of contacts of Kv4.3 amino acid residues 70-78 with KChIP1 residues 37-61 from 100 ns AA MD simulations of Kv4.3 T1-KChIP1 complexes: a) WT (red), Y57A-K61A KChIP1 (orange) and Y57A KChIP1 (cyan); b) WT (red), E70A-F73E Kv4.3 (blue) and E70A-F73E Kv4.3 + L39E-Y57A-K61A KChIP1 (green). The number of contacts were measured and averaged over the whole trajectory. The cutoff used to define a contact was 3 Å.

First, we analyzed the average number of contacts between Kv4.3 residues 70-78, taken collectively, and specific residues of KChIP1. In Figure 9.7, we report the contacts of WT and the two KChIP1 mutant models bearing mild effects: overall, we noted a similar network of contacts with the exception of KChIP1 residue 61 which is mutated in the one β-subunit

variant. Besides, both hydrophobic and hydrophilic KChIP1 residues are involved in the site contacts. When mutations are affecting the Kv4.3 side of the second interface, as in E70A-F73E Kv4.3 and E70A-F73E Kv4.3 + L39E-Y57A-K61A KChIP1 complex models, a dramatic decrease of contacts with hydrophobic residues is observed, which is even more relevant in the latter case Figure 9.7b. On the other hand, a significant number of contacts with KChIP1 hydrophilic residues E40, K50, Q54 and R58 is still preserved as compared to WT.

To better highlight the possible changes occurring upon mutation at the pivotal residue 73 of Kv4.3, we analyzed specifically the contacts between the latter and all relevant KChIP1 residues. In the WT complex, F73 exhibits mainly contacts with H1 and H2 helices and F108 of KChIP1 (i.e., the hydrophobic cavity), including a few minor contacts with hydrophilic residues among which the more relevant is Q54 Figure 9.8. Again, we observed similar contacts in the first group's variants, while in both systems displaying the F73E mutation, most of the hydrophobic contacts are lost in favor of stronger interactions with residues K50 and either R58 or K61: in particular, residue E73 interacts with KChIP1 lysine K50 and K61 in the Kv4.3 double mutant, while it shows only contacts with K50 and R58 in the E70A-F73E Kv4.3 + L39E-Y57A-K61A KChIP1 complex. This predictable result is ascribed to the replacement of phenylalanine with glutamate at position 73, an acidic and negatively charged residue. Note that when the Kv4.3 double mutant is associated with a KChIP1 triple mutant, the overall loss of contacts becomes very significant. Besides, in the WT Kv4.3 T1-KChIP1 complex KChIP1 residue Y57 interacts strongly with Kv4.3 F73 and F74 residues, while it displays less contacts with Kv4.3 F120 and Y121 amino acids Figure 9.8. In the Kv4.3 double mutant, the replacement of F73 with a glutamic acid decreases not only the contacts of this mutated residue with KChIP1 residue Y57, but also interactions with Kv4.3 F74 and Y121 residues. The presence of a double mutation seems to promote hydrophobic interactions between Kv4.3 F120 and KChIP1 Y57 residues. When the Kv4.3 double mutation E70A-F73E coexists with the KChIP1 triple mutation L39E-Y57A-K61A, hydrophobic contacts of KChIP1 residue A57 with all Kv4.3 residues are not observed Figure 9.8, indicating that this mutant is most probably destabilized by the lack of key residues involved in both van der Waals and electrostatics interactions. In the KChIP1 single and double mutants, A57 shows contacts with residues F73, F74 and F120 of Kv4.3, similarly to the WT system, suggesting once more that hydrophobic interactions are mainly regulated by the presence of the Kv4.3 F73 residue.

Table 9.1: Salt bridges of the second interface from MD simulations of WT and mutated Kv4.3 T1-KChIP1 complexes.

Kv4.3[a]	KChIP1[a]	WT [b]	Kv4.3 DM [b]	Kv4.3 DM + KChIP1 TM [b]	KChIP1 DM [b]	KChIP1 M [b]
E70	K61	16.4	0	0	0	0
K71	E40	0	25.6	11.3	0	0
K71	E39	0	0	23.4	0	0
K71	E109	0	0	0	32.3	30.5
K71	E43	0	6.7	19.0	0	0
E72	K50	0	14.4	0	0	5.4
E72	R51	0	0	43.1	0	0.4
E72	R58	0	0	84.5	0	0
E73	K50	0	26.4	42.9	0	0
E73	R58	0	0	21.4	0	0
E73	K61	0	21.9	0	0	0
E77	K50	35.6	17.7	0	14.4	4.5
E77	R51	59.9	14.4	22.5	44.1	63.8
D78	R51	73.0	43.4	0	1.6	20.5
D85	R58	0	0	0	23.6	0
D85	K61	0	0	0	0	24.9

[a] All charged residues (Arg, Lys, Glu, Asp) whose side-chain distance (i.e., N--O) was found below 5 Å were considered in the analysis. The more persistent salt bridges, those with an average percentage of >10% over the total simulation time, are reported. Percentages are also averaged over the four monomers.

[b] Legend of simulated Kv4.3 T1-KChIP1 complexes. WT: wild type, Kv4.3 DM: E70A-F73E Kv4.3, Kv4.3 DM + KChIP1 TM: E70A-F73E Kv4.3 + L39E-Y57A-K61A KChIP1, Kv4.3 TM: W8E-P10E-A15E Kv4.3, KChIP1 DM: Y57A-K61A KChIP1 and KChIP1 M: Y57A KChIP1.

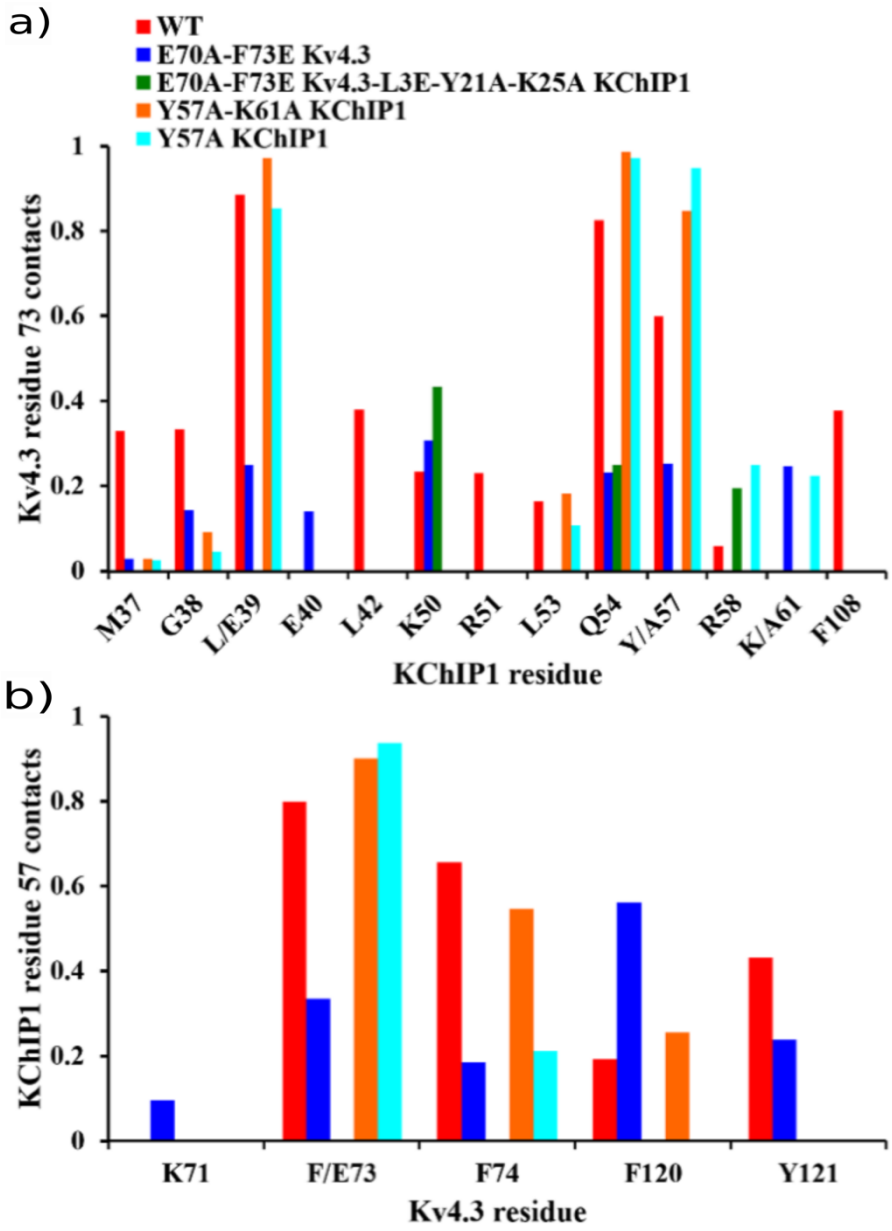

Figure 9.8: a) Average number of contacts of Kv4.3 residue 73 with KChIP1 residues from MD simulations of WT (red), E70A-F73E Kv4.3 (blue), E70A-F73E Kv4.3 + L39E-Y57A-K61A KChIP1 (green), Y57A-K61A KChIP1 (orange) and Y57A KChIP1 (cyan) Kv4.3 T1-KChIP1 complexes. b) Average number of contacts of KChIP1 residue 57 with Kv4.3 residues from MD simulations of WT and mutated Kv4.3 T1-KChIP1 complex models. The cutoff used to define a contact was 3 Å.

Since in the WT Kv4.3 T1-KChIP1 complex the stability of the second interface depends also on specific salt bridge interactions, we monitored the formation of close interactions between acidic and basic residues throughout the MD simulation of all variant models. Results are reported in Table 9.1 and depicted in Figure 9.9. In WT, we observed the formation of salt

bridges at the bottom (i.e., E77-K50, E77-R51 and D78-R51), and at the top (i.e., E70-K61) of the interaction site, thus surrounding the previously seen hydrophobic contacts at the middle of the interface, in good agreement with those reported by Wang et al. in 2007. In particular, concerning the other variants, the same salt bridges observed at the bottom of the interface were basically preserved in all systems, except the E70A-F73E Kv4.3 + L39E-Y57A-K61A KChIP1 model, whereas no E70-K61 interaction was observed in both variants missing lysine at position 61, due to the K61A mutation. It is worth noting that both E77-K50 and D78-R51 salt bridges were not formed when the E70A-F73E Kv4.3 double mutant and the L39E-Y57A-K61A KChIP1 triple mutant coexisted in the Kv4.3 T1-KChIP1 complex, suggesting that the combined absence of sufficient hydrophobic and salt bridges interactions inhibits effectively the surface expression of the Kv4.3 channel as previously reported in the literature (15). In the case of the E70A-F73E Kv4.3 double mutant, new salt bridges (i.e., E73-K50 and E73-K61) are formed with respect to WT, due to the second mutation (F73E) in the Kv4.3.

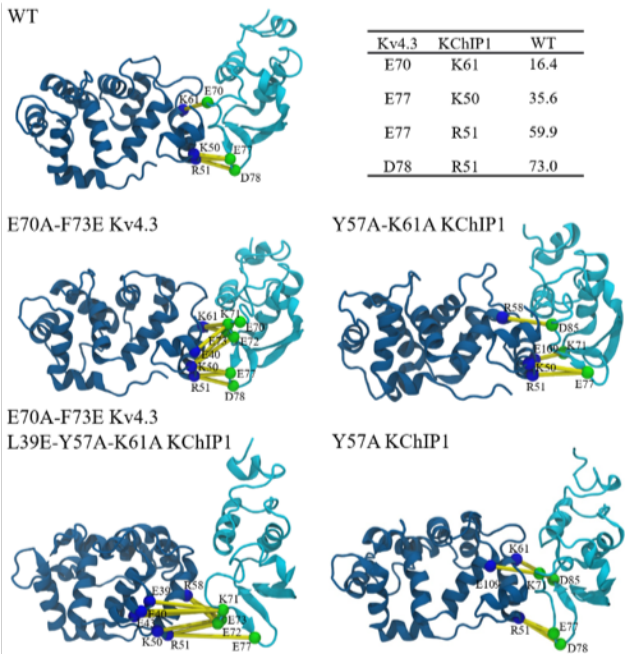

Kv4.3	KChIP1	WT
E70	K61	16.4
E77	K50	35.6
E77	R51	59.9
D78	R51	73.0

Figure 9.9: Salt bridges of the second interface formed between Kv4.3 (green) and KChIP1 (blue) amino acid residues from MD simulations of WT, E70A-F73E Kv4.3, E70A-F73E Kv4.3 + L39E-Y57A-K61A KChIP1, Y57A-K61A KChIP1, and Y57A KChIP1 Kv4.3 T1-KChIP1 complexes displayed on the 100 ns structure. The cutoff used to define a salt bridge was 5 Å. Kv4.3 monomers (omitting residues 3-40) and KChIP1 subunits of each model are shown with the same color code of Fig. 1. Salt bridges are shown in

yellow connecting alpha carbons of Kv4.3 and KChIP1 residues. The percentage of persistence of salt bridges of the WT Kv4.3 T1-KChIP1 complex are reported in the top, right table (see also Table 9.1).

Another feature highlighting the different interaction in the second surface of WT and variant complex models is the solvent accessible surface area (SASA) of the residues forming this interaction site, namely Kv4.3 residues E70, F73, F74 and D78 and KChIP1 residues M37-E40, L42, K50, R51, L53, Q54, Y57, R58, K61 and F108, which were selected on the basis of the previously discussed analysis of the contacts. The average SASA in the second interface of the WT Kv4.3 T1-KChIP1 complex is 892 ± 33 $Å^2$ Figure 9.10. When a double mutation is introduced in the Kv4.3 T1 domain (E70A-F73E Kv4.3 system) the average SASA per subunit increases to 1018 ± 31 $Å^2$, indicating that the observed reduction of hydrophobic interactions is also associated with an increase in the surface area accessible to the solvent. Moreover, if the Kv4.3 double mutation coexists with a KChIP1 triple mutant (E70A-F73E Kv4.3 + L39E-Y57A-K61A KChIP1 system), affecting both Kv4.3 and KChIP1 residues involved in the second surface hydrophobic interaction, the average SASA per subunit increases even more and reaches a value of 1235 ± 45 $Å^2$, which is again a consequence of a further reduction in the number of hydrophobic interactions. Interestingly, mutations on KChIP1 second interface do not increase the average SASA per subunit as observed in Y57A-K61A KChIP1 (i.e., 853 ± 30 $Å^2$) and Y57A KChIP1 (i.e., 880 ± 40 $Å^2$) Kv4.3 T1-KChIP1 complexes with respect to the WT system. This result further supports that the main contribution to the SASA of the second interface derives from mutations in Kv4.3 residues.

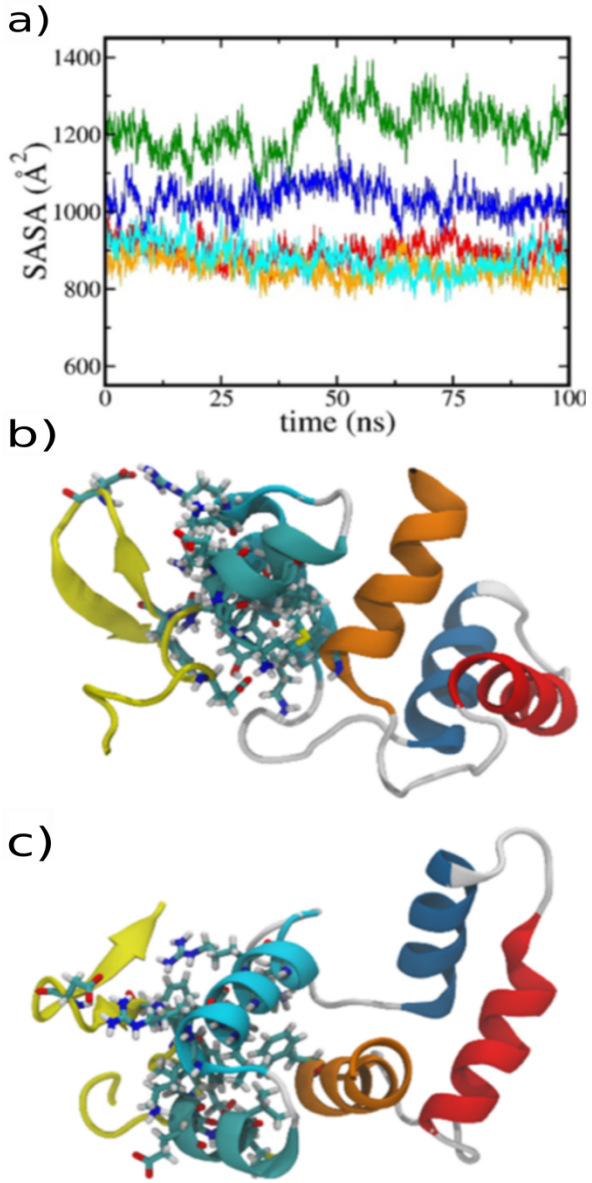

Figure 9.10: a) Solvent accessible surface areas (SASAs) of residues interacting in the second interface, namely Kv4.3 residues E70, F73, F74 and D78 and KChIP1 residues M37-E40, L42, K50, R51, L53, Q54, Y57, R58, K61 and F108, from 100 ns AA MD simulations of WT (red, 892 ± 33 Å^2), Y57A-K61A KChIP1 (orange, 853 ± 30 Å^2), Y57A KChIP1 (cyan, 880 ± 40 Å^2), E70A-F73E Kv4.3 (blue, 1018 ± 31 Å^2) and E70A-F73E Kv4.3 + L39E-Y57A-K61A KChIP1 (green, 1235 ± 45 Å^2), Kv4.3 T1-KChIP1 complexes. Mutations in the second interface side of Kv4.3 induce an increase in the SASA as compared to WT, KChIP1 mutants and Kv4.3 triple mutant systems. All SASAs were computed over the last 40% of each trajectory, saved every 50 ps. The errors are reported as standard deviations. b) Side and c) top views of residues interacting in the second interface. The same color code of Fig. S1 is used for helices of the KChIP1 subunit. The region of the Kv4.3 T1 domain interacting with H2 helix of KChIP1 is shown in yellow.

All previous analyses have consistently pointed towards a weakly interacting second interface in the case of mutations occurring on both Kv4.3 and KChIP1 protein (i.e., E70A-F73E Kv4.3 + L39E-Y57A-K61A KChIP1 complex). The destabilization of this interdomain interaction is also apparent from the superposition of two equilibrated structures issuing from the WT and variant complex models, as depicted in Figure 9.11. Indeed, in this mutant, the H2 helix of KChIP1 becomes loosely bound to Kv4.3 and can easily adopt rather distorted configurations with respect to the WT model, as shown in Figure 9.11b. Not surprisingly, electrophysiology measurements reported that the E70A-F73E Kv4.3 + L39E-Y57A-K61A KChIP1 complex displays similar electric features than WT Kv4.3 in absence of the KChIP1 auxiliary protein. Hence, our results support well the view of a second interaction that is basically lost in this variant complex.

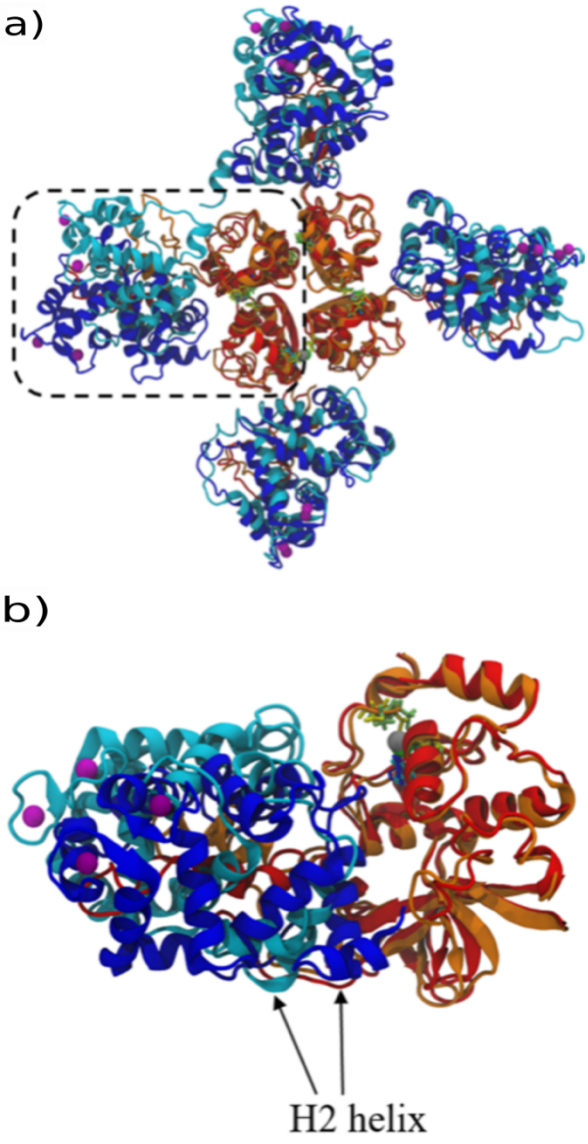

Figure 9.11: a) Top view of the structural alignment of starting and 100 ns structures of the E70A-F73E Kv4.3-L39E-Y57A-K61A KChIP1 Kv4.3 T1-KChIP1 complex. The starting structure is shown with the same color code of Fig. 1 except for KChIP1 auxiliary subunits, which are shown in blue. In the 100 ns structure, Kv4.3 T1 domain and KChIP1 auxiliary subunits are shown in orange and celestial blue ribbon representations, respectively. Cysteine and histidine amino acid residues involved in the Zn^{2+} ion (silver) binding site are highlighted in lime and celestial blue licorice representations, respectively. Two Kv4.3 monomers interacting with one KChIP1 subunit are enclosed with a dashed line and a b) zoomed view of them highlights the loss of second interface interactions, as confirmed by the large average C_α atoms RMSD of KChIP1 auxiliary subunits.

Furthermore, in order to further assess the effects of the mutations at the second interaction site, we evaluated the average interaction energy of Kv4.3 (residues 70-78) with KChIP1

(residues 37-61) for all Kv4.3 T1-KChIP1 complexes under study Figure 9.12a. The present analysis, which was mostly performed for the sake of comparison, provided an overwhelming contribution of the electrostatic energy with respect to the van der Waals term, as due to the neglect of screening effects by the surrounding aqueous solution. As expected, the WT Kv4.3 T1-KChIP1 complex resulted more stable energetically, while the Kv4.3 double mutant associated with the KChIP1 triple mutant was the least stable. Within the first group of mild-effect mutants, the Y57A-K61A KChIP1 model showed a more positive van der Waals energy as compared to the WT Kv4.3 T1-KChIP1 complex, indicating a destabilization of this system due to the reduced number of hydrophobic interactions Figure 9.12a. This reduction in the van der Waals term of the interaction energy is even more pronounced when the Kv4.3 double mutant is associated with the KChIP1 triple mutant, in which the electrostatics contribution undergoes a dramatic decrease if compared to WT and Kv4.3 double mutant Kv4.3 T1-KChIP1 complexes. These results confirm that both E70A-F73E Kv4.3 double mutant and the E70A-F73E Kv4.3 double mutant coexisting with the L39E-Y57A-K61A KChIP1 triple mutant are less stable than the WT Kv4.3 T1-KChIP1 complex Figure 9.12a.

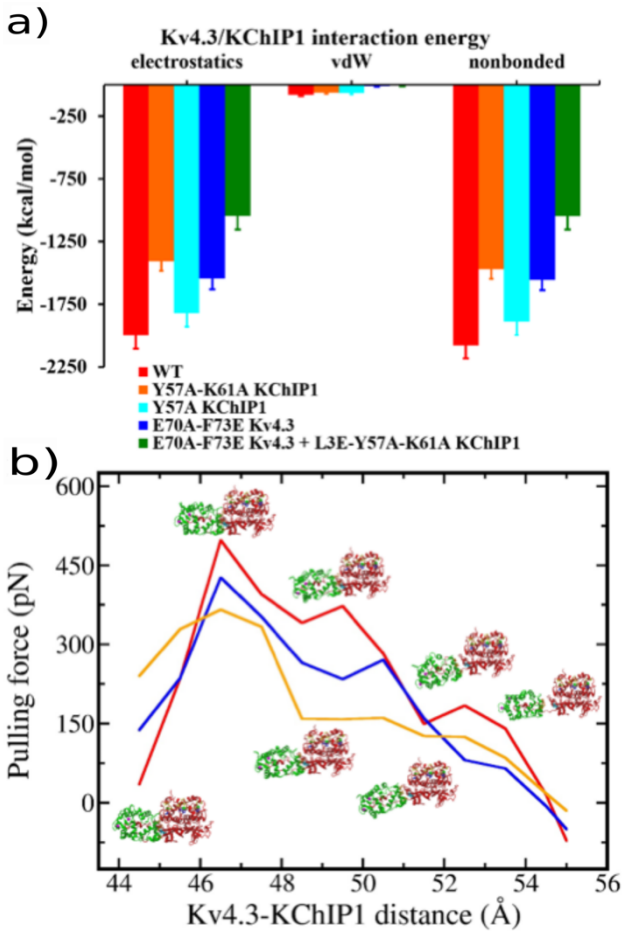

Figure 9.12: a) Average interaction energy of Kv4.3 amino acid residues 70-78 with KChIP1 residues 37-61 from MD simulations of WT (red), Y57A-K61A KChIP1 (orange), Y57A KChIP1 (cyan), E70A-F73E Kv4.3 (blue) and E70A-F73E Kv4.3 + L39E-Y57A-K61A KChIP1 (green) complex models. All energies were computed and averaged over the whole trajectory, saved every 50 ps. The errors are reported as standard deviations. b) Average pulling forces applied to move a single KChIP1 subunit out of a Kv4.3 T1-KChIP1 complex from 100 ns SMD simulations of WT (red), E70A-F73E Kv4.3 (blue) and Y57A-K61A KChIP1 (orange) complex models using a constant velocity pulling of 0.1 Å·ns^{-1}. Pulling forces are reported as a function of the Kv4.3-KChIP1 distance. Kv4.3 T1 domain (red) and the pulled KChIP1 subunit (green) are shown in the insets at different distances. The overall force profile is given as an average over two SMD simulations. Standard deviation is 25 pN.

To obtain a better estimate of the relative stability of the second interface within the context of the whole octameric complex and in the aqueous solution, we carried out SMD simulation focusing only on the WT, E70A-F73E Kv4.3 and Y57A-K61A KChIP1 models, since the E70A-F73E Kv4.3 + L39E-Y57A-K61A KChIP1 was already observed to led to unstable second interfaces and the Y57A KChIP1 is only marginally different with respect to WT. From

Figure 9.12b, it is apparent that the WT second interface is the harder to break among the systems considered, followed by E70A-F73E Kv4.3 and Y57A-K61A KChIP1 models. In particular, the estimated energy barrier for breaking the second interface in the case of WT is about 6 and 8 kcal/mol higher than E70A-F73E Kv4.3 and Y57A-K61A KChIP1 model, respectively.

9.3.4 The third interface

Analysis of the salt bridges between WT Kv4.3 T1 and KChIP1 auxiliary subunit highlighted the existence of three stable interactions formed among residues D39 and R60 on Kv4.3 and residues R51, R58 and E63 on KChIP1(Figure 9.13and Table 9.2). D39 is located on the loop following the Kv4.3 T1 N-terminal end, on the so-called T1N linker, and does interact with two arginines at the beginning and middle point of the H2 helix (i.e., R51 and R58), while R60 is part of a small α-helix structure of the T1 domain and points toward the top of the H2 helix in correspondence of the glutamate at position 63 (Figure 9.13). Such a further set of salt bridges essentially defines another site of interaction of the complex, not described previously [19,20], which we named as the third interaction site to better distinguish it from the other known two sites Figure 9.1c. Interestingly, all KChIP1 residues (i.e., R51, R58 and E63) taking part into the third interface belong to the same structural element (i.e., the H2 helix), which is also involved in the second site of interaction of the complex, whereas their counterparts on Kv4.3 are located on an adjacent T1 monomer with respect to the one defining the second interface, thus making H2 doubly interacting with Kv4.3 through two of the T1 α-subunits. The third interaction site is less extended than the other two sites, being essentially constituted by the above salt bridges, however it appears rather stable since the observed salt bridges were retained in all of our MD simulations (Table 9.2), even when the Kv43-KChIP1 second interface was significantly weakened upon mutations (e.g., in the case of the E70A-F73E Kv4.3 + L39E-Y57A-K61A KChIP1 complex model).

In light of these findings, we believe that it would be interesting to further investigate the possible functional role of the third interface through tailored mutagenesis and electrophysiology studies. In a previous experimental study [291] a partial test not designed for the investigation of the third interface was carried out by considering the Kv4.3 R51A single

mutation, which abolishes one of the three possible salt bridges observed in this work, but minor effects were noted with respect to WT complex.

Table 9.2: Salt bridges of the third interface from MD simulations of WT and mutated Kv4.3 T1-KChIP1 complexes.

Kv4.3[a]	KChIP1[a]	WT[b]	Kv4.3 DM[b]	Kv4.3 DM + KChIP1 TM[b]	KChIP1 DM[b]	KChIP1 M[b]
D39	R51	21.4	69.9	49.8	47.5	24.8
D39	R58	80.5	93.7	72.0	49.8	64.3
R60	E63	43.7	66.9	53.3	65.5	86.5

[a] All charged residues (Arg, Lys, Glu, Asp) whose side-chain distance (i.e., N--O) was found below 5 Å were considered in the analysis. The more persistent salt bridges, those with an average percentage of >10% over the total simulation time, are reported. Percentages are also averaged over the four monomers.

[b] Legend of simulated Kv4.3 T1-KChIP1 complexes. WT: wild type, Kv4.3 DM: E70A-F73E Kv4.3, Kv4.3 DM + KChIP1 TM: E70A-F73E Kv4.3 + L39E-Y57A-K61A KChIP1, Kv4.3 TM: W8E-P10E-A15E Kv4.3, KChIP1 DM: Y57A-K61A KChIP1 and KChIP1 M: Y57A KChIP1.

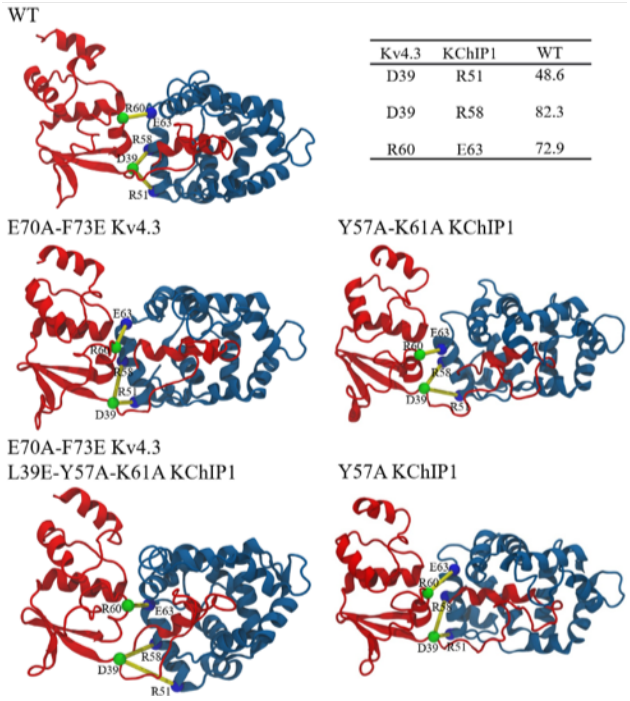

Figure 9.13: Salt bridges of the third interface formed between Kv4.3 (red) and KChIP1 (blue) residues from MD simulations of WT, E70A-F73E Kv4.3, E70A-F73E Kv4.3 + L39E-Y57A-K61A KChIP1, Y57A-K61A KChIP1, and Y57A KChIP1 complex models. The cutoff used to define a salt bridge was 5 Å. Salt bridges are shown as yellow bond connecting Kv4.3 and KChIP1 residues. The percentage of persistence of the salt bridges of the WT Kv4.3 T1-KChIP1 complex are reported in the top, right table (see also Table 9.2).

9.4 Discussion

In this work structure, energy stability and effect of mutations have been studied on the interaction sites of Kv4.3 T1-KChIP1 complex and on the various variants of Kv4.3 and KChIP1 through combinations of MD simulations and experiments. The three interfaces/interaction sites of the Kv4.3-KChIP1 complex that provides overall binding stability were analysed throughout the study. The hydrophobic interactions by Kv4.3 N-terminus residues W8, F11 and W19 with KChIP1 residues signifies the importance of such interactions in stabilization of the first interface of the complex. This was further proved by the interaction energies coming out of the WT and mutant Kv4.3-KChIP1 complex as there was significant decrease in the electrostatic interaction energy and van der Waals energy for the mutant variant than the WT. while observing the single and double mutants in the KChIP1 the

residue A57 showed similar contacts a in the WT system with residues F73, F74 and F120 of Kv4.3. The double and triple mutant coexistence in the Kv4.3 T1-KChIP1 complex affected the formation of the salt bridges interactions and also the formation of the hydrophobic interactions as the average SASA per subunit increases and also the electrostatic interactions were decreased, this combined loss of the formation of important interactions in turn inhibits the surface expression of the Kv4.3 channel, also this implies that this coexisting mutation is effectively less stable. This study reveals the importance of the third interface site which was previously overlooked. This interfacial region was maintained even in the complex mutant systems when second interface was completely destabilized. The three salt bridges indeed provided the stability to the Kv4.3-KChip1 complex. Although the light was shed on the importance and the role of the third interface but there is a need to further investigate its functional role in the future.

In our computational study, the interaction between the Kv4.3 T1 domain and the auxiliary subunit KChIP1 was carefully analyzed, especially considering those interfacial regions that confer binding stability to the overall Kv4.3-KChIP1 complex and, importantly, enable the observed modulation effect of the β-subunit which is essential for the physiology of A-type potassium channels. The structural basis of the Kv4.3-KChIP1 interaction, as originally found in recently resolved X-ray crystal structures, was basically confirmed by our MD simulation of the octameric complex in aqueous solution. Hence, inclusion of thermal and solvent effects has not significantly altered the nature and structural configuration of the first and second interaction sites of the complex. Our analysis, however, helped to highlight a previously overlooked third site of interaction of the Kv4.3-KChIP1 complex, which appears to play a relevant role in providing further stability to the Kv4.3 tetrameric intracellular domain. Indeed, the three salt bridges forming such a third interfacial region were maintained in all complex mutants, even when the second interface was completely destabilized. We predict that the cooperative double interaction of KChIP1, through the H2 helix, with two adjacent Kv4.3 T1 monomers could be the determining factor at the origin of the surprising capability of KChIP to rescue the functional expression of otherwise impaired *Shal*-type channel mutants[335].A clear assessment of the role of the third interface, however, could be obtained only by a comparative functional analysis of purposely selected mutants.

Furthermore, four different Kv4.3-KChIP1 mutants were considered, which display relevant structural alteration in key residues involved in the second interaction site of the complex. Remarkably, our results have provided an order of stability among these mutants with respect to the WT complex in consistent agreement with the extent of functional impairment observed in controlled electrophysiology analysis of the same variants. These findings support the view that a small set of specific interactions effectively modulate the A-type potassium channel current, not only in terms of current density but also for what concerns the timing of inactivation or recovery from inactivation, despite the detailed mechanism through which KChIP affects Kv4 channel function remains still unknown.

Overall, the present work has provided further valuable insights for the comprehension, at molecular level, of a very important protein complex, which is of primarily importance for controlling excitability in nerve and muscle cells. Beyond the context of basic biophysical and biochemical knowledge, we believe that this information may also contribute, along with tailored functional studies, to predict the possible pathological effects of the rapidly increasing number of inherited and de novo mutations linked to human channelopathies.

9.5 Conclusions

The voltage-gated potassium channel Kv4.3 plays a vital role in shaping the timing, frequency, and backpropagation of electrical signals in the brain and heart by generating fast transient currents at subthreshold membrane potentials in repetitive firing neurons. To achieve its physiological function, Kv4.3 is assisted by auxiliary β-subunits which become integral part of the native A-type potassium channels, among which there are the Kv channel-interacting proteins (KChIPs). KChIPs are a family of cytosolic proteins that, when coexpressed with Kv4, lead to higher current density, modulation of channel inactivation and faster recovery from inactivation. Indeed, loss of KChIPs function may lead to severe pathological states. Recently, the structural basis of KChIP1-Kv4.3 interaction was reported by two similar X-ray crystallographic structures, which supported a crucial role for KChIP1 on enhancing the stability of the Kv4.3 tetrameric assembly, thus helping the trafficking of the channel to the plasma membrane. Here, we investigate through fully atomistic simulations the structure and stability of the human Kv4.3 tetramerization (T1) domain in complex with KChIP1 upon

specific mutations located in the first and second interface of the complex, as compared to wild-type (WT).

Our results nicely complement the available structural and biophysical information collected so far on these complex variants. In particular, the degree of structural deviations and energetic instability observed in the complex variants, from small to substantial, with respect to the WT model seems to parallel well the level of channel dysfunction as known from electrophysiology data. Moreover, we confirm the overall structure of the octameric WT KChIP1-Kv4.3 assembly, as observed in the crystal structures, and, at the same time, we highlight the importance of another site of interaction between KChIP1 and the T1 domain, which was previously overlooked.

Chapter 10 Conclusions

The structural and dynamical properties of the lipid membranes are challenging to study solely through experimental techniques, thus molecular dynamic simulations, as reported in this thesis, represent a very valuable tool to complement experiments by providing atomic scale details for molecular phenomena otherwise not easily accessible. In the present thesis work, a great effort has been made to signify the importance of the fluorophores used in widespread studies of biological membranes and to elucidate their perturbing effect and the direct effect the fluorophore have on the structure and dynamics of the membranes.

In chapter 4 of this thesis, in the work related to Rhodamine labelled lipids, our findings supported a somewhat non-neutral and perturbing effect played by the dye-labeled lipids in diffusion experiments, quantitatively estimating a decrease in lipid mobility of up to 20% with respect to the unlabeled species. Moreover, our results highlighted the fact that, with increasing concentration of the Rhodamine, these fluorophores have the ability to form self-aggregates which resulted in increased water permeability and decreased lateral diffusion, the hydrodynamic drag because of the bulky Rhodamine head groups which could also be the reason for the slower dynamics and the increased water permeability. In contrast to these dynamical properties the structure of both labelled and unlabeled variants of the bilayer do not show significant changes.

In chapter 5, the structural and dynamic properties of the Rhodamine B-labeled lipid inserted into DOPC membrane was studied at different temperatures i.e. 293 K, 303 K and 320 K. The introduction of the RHB molecule in general has a negligible effect on area per lipid, bilayer thickness and on the order parameter of the DOPC molecules at different temperatures. On the other hand, lipid lateral diffusion was greatly decreased in labeled variant of the lipids, which was also previously described as the effect coming out of the hydrodynamic drag because of bulky Rhodamine head groups. The orientation study and partial density profiles of the RHB

headgroups within the lipid bilayer implied the amphiphilic nature of the RHB moiety. This study at all temperatures suggested the non-neutral role of the tagged lipids thus an important implication and a careful use of these molecules for optical microscopic or biophysical studies of lipid bilayers.

In chapter 6 of this thesis, FMR DPAP as a molecular probe was analyzed for detecting ordered and disordered phases in plasma membranes. The work is integration of both experimental and computational techniques and unravel the complex phenomenon occurring because of the interactions between lipids and the fluorophore molecules. In this work the novel force field has been developed for the first time for the excited state of the DPAP molecule and the force field has been validated in various liquid solutions such as acetonitrile, cyclohexane and o-xylene. MD simulations were performed to investigate the internal and global dynamics of the excited state of the DPAP probe affected by the viscosity of the surrounding environments. The theoretical optical computations reproduced in this work confirmed the solvatochromic trend of the emission signals with fair agreement with the Stock shift values. DPAP has also been studied in this work when embedded within two different lipid membranes, one with pure DOPC and one with DPPC and cholesterol. Using confocal fluorescence lifetime imaging microscopy (ph-FLIM), different signals have been measured when going from a liposome solution to the other one, owing to the different membrane phases experienced by the probe. MD simulations in the two membrane systems revealed that both flexible dihedral angles and global rotations are significantly retarded in the presence of cholesterol, thus further confirming the high sensitivity of DPAP to its local environment as well as its capability in detecting different structures and level of plasma membranes organization.

In chapter 7 of this thesis an *in-silico* study was performed on TAT peptide which works as CPP. This study provided some further insights on a very complex and challenging cellular process, namely CPPs direct transduction through plasma membranes, this understanding of the CPP action mechanism has direct application in cell biophysics and therapeutic development. During the course of this particular work related to CPP remarkable differences have been unraveled between Tat_{11} peptide in its monomeric and dimeric forms.

A lipid bilayer pore was created to investigate specifically the translocation kinetics of the CPP once inserted into the pore and the interactions with the surrounding lipids at molecular level were investigated. With the help of MD simulations much slower kinetics were observed for Tat_{11} aggregated form with respect to its monomeric counterpart. which is the explanation to

the results gathered in the study that Tat_{11} in its aggregated form has higher interaction energy and more hydrogen bonding between the peptide and the lipids shaping the translocation pore, in addition to its larger inertial mass. The data coming out of the MD simulations has shown clearly that Tat_{11} dimer, which has double the number of arginine residues than the monomer, was able to stabilize the membrane pore over a prolonged period of time (>1 μs). This enhanced pore stabilization effect by the Tat_{11} dimer has strongly pointed to the strong Coulomb interactions between arginine residues and surrounding lipid head groups. This was further proved further with the help of SMD simulations in this work. It was confirmed with SMD simulation results that the force required to pull the dimer out of the pore by breaking up such electrostatic interactions was significantly larger (i.e., x2) than in the case of the monomer. These strong interactions were the reason that interrupted the process of lipid diffusion required by the pore to close back and significantly extend the membrane defect lifetime.

The data in this study, coupled with previous experimental evidence, allows to propose for TAMRA a "supporting actor" role towards peptide transduction, the dye being able to promote effectively self-aggregation at micromolar concentration, though not adding any relevant contribution to lipid interaction. This work may provide supportive ideas to peptide design and engineering in a large number of targeted applications aiming at improving CPP-mediated delivery inside the cells inturn which could lead to the new paths in therapeutics.

In chapter 8 of this thesis de-novo mutations have been studied to understand the molecular behavior of the KV 4.3ion channel. The mutations have involvement in various developmental and heart disorders, the molecular behavior of these channels could lead to understand the structure and function of the ion channels and could possibly pave the way to further investigate the inherited and developmental disorders. The molecular model of Kv4.3 presented in this work could also be used to test the effects of inhibitors and blockers of the channel with the final aim of developing drugs for the treatment of SCA 19/22 and various other diseases directly caused by the over or under activation of these channels. The findings in this work stresses the importance to study the effect of pathogenic mutations on the channel function in relation to their regulatory proteins. Furthermore, it shows the strength of combining functional and structural studies in order to pinpoint the molecular determinant which causes the channel to be dysfunctional. The main result coming out of the MD simulations in this work was that mutating the residue 373 with charged and polar amino acid e.g. glutamic acid the function of the channel was greatly enhanced also the permeation and the conductance was increased

which was alos proved with the help of experiments mentioned in the study. This enhanced function of the channel and conductance had a great impact on the hydration of the SF also. The results coming out of WT in comparison to the mutations in this particular work confirms the presence of the mutations affects the overall flexibility of the SF, which in case of M373I the function of the channel was significantly reduced while in both S390N and M373E the function and activity of the channel were greatly enhanced. Since the current atomistic model of Kv4.3 is able to reproduce with a good approximation and the experimental results have also proved to be in accordance with the computational study in chapter 7 of this thesis, these findings could be employed for the study and the prediction of the effects of other inherited, and eventually de novo, mutations on the channel structure and function.

Finally, in chapter 9 of this thesis the study is devised to study the structure and stability of the human Kv4.3 tetramerization (T1) domain in complex with KChIP1 along with specific mutations in the first and second interface of the complex. The fully atomistic simulations of the complex compared to the WT in this study contributes towards the understanding of the pathological effects of the denovo mutations linked to the channelopathies and also enhancing the basic biophysical and biochemical knowledge of the channels. This study reveals the importance of another interaction site between KChIP1 and T1 domain and also the overall complex octameric structural assembly of the WT KChIP1-Kv4.3 was confirmed computationally as was observed in the crystal structures.

References

1. Singer, S. J. & Nicolson, G. L. The fluid mosaic model of the structure of cell membranes. *Science* **175**, 720–731 (1972).
2. Nicolson, G. L. The Fluid—Mosaic Model of Membrane Structure: Still relevant to understanding the structure, function and dynamics of biological membranes after more than 40years. *Biochimica et Biophysica Acta (BBA) - Biomembranes* **1838**, 1451–1466 (2014).
3. Mouritsen, O. G. & Bloom, M. Mattress model of lipid-protein interactions in membranes. *Biophys. J.* **46**, 141–153 (1984).
4. Simons, K. & Ikonen, E. Functional rafts in cell membranes. *Nature* **387**, 569–572 (1997).
5. Sonnino, S. & Prinetti, A. Membrane domains and the 'lipid raft' concept. *Curr. Med. Chem.* **20**, 4–21 (2013).
6. Schmid, F. Physical mechanisms of micro- and nanodomain formation in multicomponent lipid membranes. *Biochimica et Biophysica Acta (BBA) - Biomembranes* **1859**, 509–528 (2017).
7. Laude, A. J. & Prior, I. A. Plasma membrane microdomains: organisation, function and trafficking. *Mol Membr Biol* **21**, 193–205 (2004).
8. Truong Quang, B.-A. & Lenne, P.-F. Membrane microdomains: from seeing to understanding. *Front. Plant Sci.* **5**, (2014).

9. Berg, J. M., Tymoczko, J. L. & Stryer, L. There Are Three Common Types of Membrane Lipids. *Biochemistry. 5th edition* (2002).
10. Alberts, B. *et al.* The Lipid Bilayer. *Molecular Biology of the Cell. 4th edition* (2002).
11. Woodman, S. & Kim, K. Membrane Lipids: Implication for Diseases and Membrane Trafficking. 5
12. Simons, K. & Sampaio, J. L. Membrane Organization and Lipid Rafts. *Cold Spring Harb Perspect Biol* **3**, a004697 (2011).
13. Coskun, Ü. & Simons, K. Cell Membranes: The Lipid Perspective. *Structure* **19**, 1543–1548 (2011).
14. Chen, L., Johnson, M. L. & Biltonen, R. L. A macroscopic description of lipid bilayer phase transitions of mixed-chain phosphatidylcholines: chain-length and chain-asymmetry dependence. *Biophys J* **80**, 254–270 (2001).
15. Feigenson, G. W. Phase behavior of lipid mixtures. *Nat Chem Biol* **2**, 560–563 (2006).
16. Heberle, F. A. & Feigenson, G. W. Phase Separation in Lipid Membranes. *Cold Spring Harb Perspect Biol* **3**, a004630 (2011).
17. Kranenburg, M. & Smit, B. Phase Behavior of Model Lipid Bilayers. *J. Phys. Chem. B* **109**, 6553–6563 (2005).
18. Raghunathan, null & Katsaras, null. L beta '-->Lc' phase transition in phosphatidylcholine lipid bilayers: A disorder-order transition in two dimensions. *Phys Rev E Stat Phys Plasmas Fluids Relat Interdiscip Topics* **54**, 4446–4449 (1996).
19. Scott, H. L. A model for phase transitions in lipid bilayers and biological membranes. *Journal of Theoretical Biology* **46**, 241–253 (1974).
20. Watson, H. Biological membranes. *Essays In Biochemistry* **59**, 43–69 (2015).

21. Mäe, M. & Langel, U. Cell-penetrating peptides as vectors for peptide, protein and oligonucleotide delivery. *Curr Opin Pharmacol* **6**, 509–514 (2006).

22. Foged, C. & Nielsen, H. M. Cell-penetrating peptides for drug delivery across membrane barriers. *Expert Opin Drug Deliv* **5**, 105–117 (2008).

23. Kerkis, A., Hayashi, M. A. F., Yamane, T. & Kerkis, I. Properties of cell penetrating peptides (CPPs). *IUBMB Life* **58**, 7–13 (2006).

24. Lundberg, P. & Langel, U. A brief introduction to cell-penetrating peptides. *J. Mol. Recognit.* **16**, 227–233 (2003).

25. Milletti, F. Cell-penetrating peptides: classes, origin, and current landscape. *Drug Discovery Today* **17**, 850–860 (2012).

26. Frankel, A. D. & Pabo, C. O. Cellular uptake of the tat protein from human immunodeficiency virus. *Cell* **55**, 1189–1193 (1988).

27. Madani, F., Lindberg, S., Langel, Ü., Futaki, S. & Gräslund, A. Mechanisms of Cellular Uptake of Cell-Penetrating Peptides. *Journal of Biophysics* (2011). doi:10.1155/2011/414729

28. Li, Z. *et al.* Transporting carriers for intracellular targeting delivery via non-endocytic uptake pathways. *Drug Delivery* **24**, 45–55 (2017).

29. Derakhshankhah, H. & Jafari, S. Cell penetrating peptides: A concise review with emphasis on biomedical applications. *Biomedicine & Pharmacotherapy* **108**, 1090–1096 (2018).

30. Hewlett, L. J., Prescott, A. R. & Watts, C. The coated pit and macropinocytic pathways serve distinct endosome populations. *J. Cell Biol.* **124**, 689–703 (1994).

31. Kerr, M. C. & Teasdale, R. D. Defining macropinocytosis. *Traffic* **10**, 364–371 (2009).

32. Sarkar, K., Kruhlak, M. J., Erlandsen, S. L. & Shaw, S. Selective inhibition by rottlerin of macropinocytosis in monocyte-derived dendritic cells. *Immunology* **116**, 513–524 (2005).

33. Luzio, J. P., Parkinson, M. D. J., Gray, S. R. & Bright, N. A. The delivery of endocytosed cargo to lysosomes. *Biochem. Soc. Trans.* **37**, 1019–1021 (2009).

34. Parton, R. G. & del Pozo, M. A. Caveolae as plasma membrane sensors, protectors and organizers. *Nat. Rev. Mol. Cell Biol.* **14**, 98–112 (2013).

35. Nichols, B. Caveosomes and endocytosis of lipid rafts. *Journal of Cell Science* **116**, 4707–4714 (2003).

36. Underhill, D. M. & Goodridge, H. S. Information processing during phagocytosis. *Nat. Rev. Immunol.* **12**, 492–502 (2012).

37. Champion, J. A. & Mitragotri, S. Role of target geometry in phagocytosis. *Proc. Natl. Acad. Sci. U.S.A.* **103**, 4930–4934 (2006).

38. Derossi, D. *et al.* Cell internalization of the third helix of the Antennapedia homeodomain is receptor-independent. *J. Biol. Chem.* **271**, 18188–18193 (1996).

39. Deshayes, S. *et al.* Formation of transmembrane ionic channels of primary amphipathic cell-penetrating peptides. Consequences on the mechanism of cell penetration. *Biochimica et Biophysica Acta (BBA) - Biomembranes* **1758**, 1846–1851 (2006).

40. Herce, H. D. & Garcia, A. E. Molecular dynamics simulations suggest a mechanism for translocation of the HIV-1 TAT peptide across lipid membranes. *Proc. Natl. Acad. Sci. U.S.A.* **104**, 20805–20810 (2007).

41. Herce, H. D. *et al.* Arginine-Rich Peptides Destabilize the Plasma Membrane, Consistent with a Pore Formation Translocation Mechanism of Cell-Penetrating Peptides. *Biophys J* **97**, 1917–1925 (2009).

42. Pouny, Y., Rapaport, D., Mor, A., Nicolas, P. & Shai, Y. Interaction of antimicrobial dermaseptin and its fluorescently labeled analogues with phospholipid membranes. *Biochemistry* **31**, 12416–12423 (1992).

43. Lee, M.-T., Hung, W.-C., Chen, F.-Y. & Huang, H. W. Many-Body Effect of Antimicrobial Peptides: On the Correlation Between Lipid's Spontaneous Curvature and Pore Formation. *Biophys J* **89**, 4006–4016 (2005).

44. Lindahl, E. & Sansom, M. S. Membrane proteins: molecular dynamics simulations. *Current Opinion in Structural Biology* **18**, 425–431 (2008).

45. Jo, S., Kim, T. & Im, W. Automated Builder and Database of Protein/Membrane Complexes for Molecular Dynamics Simulations. *PLOS ONE* **2**, e880 (2007).

46. MacKinnon, R. Potassium channels. *FEBS Letters* **555**, 62–65 (2003).

47. Bezanilla, F. Voltage-Gated Ion Channels. *IEEE Transactions on Nanobioscience* **4**, 34–48 (2005).

48. Birnbaum, S. G. *et al.* Structure and Function of Kv4-Family Transient Potassium Channels. *Physiological Reviews* **84**, 803–833 (2004).

49. Grizel, A. V., Glukhov, G. S. & Sokolova, O. S. Mechanisms of Activation of Voltage-Gated Potassium Channels. *Acta Naturae* **6**, 10–26 (2014).

50. Veltman, J. A. & Brunner, H. G. *De novo* mutations in human genetic disease. *Nature Reviews Genetics* **13**, 565–575 (2012).

51. Bouvrais, H., Pott, T., Bagatolli, L. A., Ipsen, J. H. & Méléard, P. Impact of membrane-anchored fluorescent probes on the mechanical properties of lipid bilayers. *Biochim. Biophys. Acta* **1798**, 1333–1337 (2010).

52. Loura, L. M. S. & Ramalho, J. P. P. Recent Developments in Molecular Dynamics Simulations of Fluorescent Membrane Probes. *Molecules* **16**, 5437–5452 (2011).

53. Faller, R. Molecular modeling of lipid probes and their influence on the membrane. *Biochim. Biophys. Acta* **1858**, 2353–2361 (2016).

54. Kyrychenko, A. Using fluorescence for studies of biological membranes: a review. *Methods Appl. Fluoresc.* **3**, 042003 (2015).

55. Klymchenko, A. S. & Kreder, R. Fluorescent Probes for Lipid Rafts: From Model Membranes to Living Cells. *Chemistry & Biology* **21**, 97–113 (2014).

56. Beija, M., Afonso, C. A. M. & Martinho, J. M. G. Synthesis and applications of Rhodamine derivatives as fluorescent probes. *Chem. Soc. Rev.* **38**, 2410–2433 (2009).

57. Owen, D. M., Neil, M. A. A., French, P. M. W. & Magee, A. I. Optical techniques for imaging membrane lipid microdomains in living cells. *Semin. Cell Dev. Biol.* **18**, 591–598 (2007).

58. Macchiagodena, M. *et al.* Computational study of the DPAP molecular rotor in various environments: from force field development to molecular dynamics simulations and spectroscopic calculations. *Phys Chem Chem Phys* **19**, 30590–30602 (2017).

59. Koenig, M. *et al.* Unraveling the peculiar modus operandi of a new class of solvatochromic fluorescent molecular rotors by spectroscopic and quantum mechanical methods. *Chem. Sci.* **4**, 2502–2511 (2013).

60. Parasassi, T., Gratton, E., Yu, W. M., Wilson, P. & Levi, M. Two-photon fluorescence microscopy of laurdan generalized polarization domains in model and natural membranes. *Biophysical Journal* **72**, 2413–2429 (1997).

61. Azam, S. S. & Akhunzada, M. J. Structure and dynamic studies of lunatic, manic and radical fringe. *Journal of Molecular Liquids* **188**, 186–195 (2013).

62. McCammon, J. A., Gelin, B. R. & Karplus, M. Dynamics of folded proteins. *Nature* **267**, 585 (1977).

63. Allen, M. P. & Tildesley, author.), D. J. *Computer simulation of liquids*. (Oxford : Oxford University Press, 2017).

64. Huang, K. *Statistical Mechanics, 2nd Edition by Kerson Huang*. (Wiley, 1713).

65. Chandler, J. H., Clark, J. S., Cooper, M. a. R. & Stirling, D. M. Analytical Photogrammetry Applied to Nepalese Slope Morphology. *The Photogrammetric Record* **12**, 443–458 (1987).

66. Hinchliffe, A. Molecular Modelling for Beginners. 430

67. Industrial Applications of Molecular Simulations. *CRC Press* Available at: https://www.crcpress.com/Industrial-Applications-of-Molecular-Simulations/Meunier/p/book/9781439861011. (Accessed: 7th June 2019)

68. Leach, D. A. *Molecular Modelling: Principles and Applications*. (Prentice Hall, 2001).

69. Griebel, M., Knapek, S. & Zumbusch, G. *Numerical Simulation in Molecular Dynamics: Numerics, Algorithms, Parallelization, Applications*. (Springer-Verlag, 2007).

70. *Biomolecular Simulations: Methods and Protocols*. (Humana Press, 2013).

71. Rapaport, D. C. The Art of Molecular Dynamics Simulation by D. C. Rapaport. *Cambridge Core* (2004). doi:10.1017/CBO9780511816581

72. Grubmüller, H., Heller, H., Windemuth, A. & Schulten, K. Generalized Verlet Algorithm for Efficient Molecular Dynamics Simulations with Long-range Interactions. *Molecular Simulation* **6**, 121–142 (1991).

73. Vianello, R., Domene, C. & Mavri, J. The Use of Multiscale Molecular Simulations in Understanding a Relationship between the Structure and Function of Biological Systems of the Brain: The Application to Monoamine Oxidase Enzymes. *Front. Neurosci.* **10**, (2016).

74. Perilla, J. R. & Schulten, K. Physical properties of the HIV-1 capsid from all-atom molecular dynamics simulations. *Nature Communications* **8**, 15959 (2017).

75. Antunes, D. A. *et al.* New Insights into the In Silico Prediction of HIV Protease Resistance to Nelfinavir. *PLOS ONE* **9**, e87520 (2014).

76. Jabbarzadeh Kaboli, P., Ismail, P. & Ling, K.-H. Molecular modeling, dynamics simulations, and binding efficiency of berberine derivatives: A new group of RAF inhibitors for cancer treatment. *PLoS One* **13**, (2018).

77. Tsigelny, I. F., Kurzrock, R., Skjevik, Å. A., Kouznetsova, V. L. & Ikeda, S. Molecular dynamics use in personalized cancer medicine: Example of MET Y501C mutation. in *2016 6th International Conference on Simulation and Modeling Methodologies, Technologies and Applications (SIMULTECH)* 1–4 (2016).

78. Barreca, M. L., Lee, K. W., Chimirri, A. & Briggs, J. M. Molecular Dynamics Studies of the Wild-Type and Double Mutant HIV-1 Integrase Complexed with the 5CITEP Inhibitor: Mechanism for Inhibition and Drug Resistance. *Biophys J* **84**, 1450–1463 (2003).

79. Wang, J. & Li, Z. C. and S. Molecular Dynamics Simulations of Intrinsically Disordered Proteins in Human Diseases. *Current Computer-Aided Drug Design* (2009). Available at: http://www.eurekaselect.com/70258/article. (Accessed: 7th June 2019)

80. Ode, H., Nakashima, M., Kitamura, S., Sugiura, W. & Sato, H. Molecular dynamics simulation in virus research. *Front Microbiol* **3**, (2012).

81. Hollingsworth, S. A. & Dror, R. O. Molecular Dynamics Simulation for All. *Neuron* **99**, 1129–1143 (2018).

82. Heller, H., Schaefer, M. & Schulten, K. Molecular dynamics simulation of a bilayer of 200 lipids in the gel and in the liquid crystal phase. *J. Phys. Chem.* **97**, 8343–8360 (1993).

83. Smart, O. S., Neduvelil, J. G., Wang, X., Wallace, B. A. & Sansom, M. S. P. HOLE: A program for the analysis of the pore dimensions of ion channel structural models. *Journal of Molecular Graphics* **14**, 354–360 (1996).

84. Edidin, M. Lipids on the frontier: a century of cell-membrane bilayers. *Nat Rev Mol Cell Biol* **4**, 414–418 (2003).

85. Di Rienzo, C., Gratton, E., Beltram, F. & Cardarelli, F. Fast spatiotemporal correlation spectroscopy to determine protein lateral diffusion laws in live cell membranes. *Proceedings of the National Academy of Sciences* **110**, 12307–12312 (2013).

86. Eggeling, C. *et al.* Direct observation of the nanoscale dynamics of membrane lipids in a living cell. *Nature* **457**, 1159–1162 (2009).

87. Fujiwara, T., Ritchie, K., Murakoshi, H., Jacobson, K. & Kusumi, A. Phospholipids undergo hop diffusion in compartmentalized cell membrane. *The Journal of Cell Biology* **157**, 1071–1082 (2002).

88. Kusumi, A., Shirai, Y. M., Koyama-Honda, I., Suzuki, K. G. N. & Fujiwara, T. K. Hierarchical organization of the plasma membrane: Investigations by single-molecule tracking vs. fluorescence correlation spectroscopy. *FEBS Letters* **584**, 1814–1823 (2010).

89. Macháň, R. & Hof, M. Lipid diffusion in planar membranes investigated by fluorescence correlation spectroscopy. *Biochimica et Biophysica Acta (BBA) - Biomembranes* **1798**, 1377–1391 (2010).

90. Kachel, K., Asuncion-Punzalan, E. & London, E. The location of fluorescence probes with charged groups in model membranes. *Biochimica et Biophysica Acta (BBA) - Biomembranes* **1374**, 63–76 (1998).

91. Johnson, I. D. *Molecular Probes Handbook: A Guide to Fluorescent Probes and Labeling Technologies*. (Life Technologies Corporation, 2010).

92. Lindblom, G. & Orädd, G. Lipid lateral diffusion and membrane heterogeneity. *Biochimica et Biophysica Acta (BBA) - Biomembranes* **1788**, 234–244 (2009).

93. Akhunzada, M. J. *et al.* The role of Tat peptide self-aggregation in membrane pore stabilization: insights from a computational study. *Phys. Chem. Chem. Phys.* **19**, 27603–27610 (2017).

94. Macchi, S. *et al.* Self-aggregation propensity of the Tat peptide revealed by UV-Vis, NMR and MD analyses. *Phys. Chem. Chem. Phys.* **19**, 23910–23914 (2017).

95. Chiantia, S., Ries, J., Kahya, N. & Schwille, P. Combined AFM and Two-Focus SFCS Study of Raft-Exhibiting Model Membranes. *ChemPhysChem* **7**, 2409–2418 (2006).

96. Woodward, X., Stimpson, E. E. & Kelly, C. V. Single-lipid tracking on nanoscale membrane buds: The effects of curvature on lipid diffusion and sorting. *Biochimica et Biophysica Acta (BBA) - Biomembranes* **1860**, 2064–2075 (2018).

97. Kahya, N. & Schwille, P. How Phospholipid-Cholesterol Interactions Modulate Lipid Lateral Diffusion, as Revealed by Fluorescence Correlation Spectroscopy. *J Fluoresc* **16**, 671–678 (2006).

98. Guo, L. *et al.* Molecular Diffusion Measurement in Lipid Bilayers over Wide Concentration Ranges: A Comparative Study. *ChemPhysChem* **9**, 721–728 (2008).

99. Skaug, M. J., Longo, M. L. & Faller, R. The Impact of Texas Red on Lipid Bilayer Properties. *J. Phys. Chem. B* **115**, 8500–8505 (2011).

100. Skaug, M. J., Longo, M. L. & Faller, R. Computational Studies of Texas Red−1,2-Dihexadecanoyl-sn-glycero-3-phosphoethanolamine—Model Building and Applications. *J. Phys. Chem. B* **113**, 8758–8766 (2009).

101. do Canto, A. M. T. M. *et al.* Diphenylhexatriene membrane probes DPH and TMA-DPH: A comparative molecular dynamics simulation study. *Biochimica et Biophysica Acta (BBA) - Biomembranes* **1858**, 2647–2661 (2016).

102. Camley, B. A., Lerner, M. G., Pastor, R. W. & Brown, F. L. H. Strong influence of periodic boundary conditions on lateral diffusion in lipid bilayer membranes. *The Journal of Chemical Physics* **143**, 243113 (2015).

103. Venable, R. M. *et al.* Lipid and Peptide Diffusion in Bilayers: The Saffman–Delbrück Model and Periodic Boundary Conditions. *J. Phys. Chem. B* **121**, 3443–3457 (2017).

104. Klauda, J. B., Brooks, B. R. & Pastor, R. W. Dynamical motions of lipids and a finite size effect in simulations of bilayers. *The Journal of Chemical Physics* **125**, 144710 (2006).

105. Reddy, A. S., Warshaviak, D. T. & Chachisvilis, M. Effect of membrane tension on the physical properties of DOPC lipid bilayer membrane. *Biochim. Biophys. Acta* **1818**, 2271–2281 (2012).

106. Wu, E. L. *et al.* CHARMM-GUI Membrane Builder toward realistic biological membrane simulations. *Journal of Computational Chemistry* **35**, 1997–2004 (2014).

107. Pettersen, E. F. *et al.* UCSF Chimera--a visualization system for exploratory research and analysis. *J Comput Chem* **25**, 1605–1612 (2004).

108. Frisch, M. J. *et al.* J., Fox, DJ, 2009. Gaussian 09, Re vision B. 01. *Wallingford CT* (2009).

109. Wang, J., Wolf, R. M., Caldwell, J. W., Kollman, P. A. & Case, D. A. Development and testing of a general amber force field. *Journal of Computational Chemistry* **25**, 1157–1174 (2004).

110. Cossi, M., Rega, N., Scalmani, G. & Barone, V. Energies, structures, and electronic properties of molecules in solution with the C-PCM solvation model. *J Comput Chem* **24**, 669–681 (2003).

111. Nitschke, W. K., Vequi-Suplicy, C. C., Coutinho, K. & Stassen, H. Molecular Dynamics Investigations of PRODAN in a DLPC Bilayer. *J. Phys. Chem. B* **116**, 2713–2721 (2012).

112. Vanommeslaeghe, K. *et al.* CHARMM general force field: A force field for drug-like molecules compatible with the CHARMM all-atom additive biological force fields. *J. Comput. Chem.* **31**, 671–690 (2010).

113. Venable, R. M., Luo, Y., Gawrisch, K., Roux, B. & Pastor, R. W. Simulations of Anionic Lipid Membranes: Development of Interaction-Specific Ion Parameters and Validation Using NMR Data. *J. Phys. Chem. B* **117**, 10183–10192 (2013).

114. Phillips, J. C. *et al.* Scalable molecular dynamics with NAMD. *J. Comput. Chem.* **26**, 1781–1802 (2005).

115. Klauda, J. B. *et al.* Update of the CHARMM all-atom additive force field for lipids: Validation on six lipid types. *J Phys Chem B* **114**, 7830–7843 (2010).

116. Ryckaert, J.-P., Ciccotti, G. & Berendsen, H. J. C. Numerical integration of the cartesian equations of motion of a system with constraints: molecular dynamics of n-alkanes. *Journal of Computational Physics* **23**, 327–341 (1977).

117. Darden, T., York, D. & Pedersen, L. Particle mesh Ewald: An N·log(N) method for Ewald sums in large systems. *The Journal of Chemical Physics* **98**, 10089–10092 (1993).

118. Feller, S. E., Zhang, Y., Pastor, R. W. & Brooks, B. R. Constant pressure molecular dynamics simulation: The Langevin piston method. *The Journal of Chemical Physics* **103**, 4613–4621 (1995).

119. Parasassi, T., De Stasio, G., Ravagnan, G., Rusch, R. M. & Gratton, E. Quantitation of lipid phases in phospholipid vesicles by the generalized polarization of Laurdan fluorescence. *Biophys J* **60**, 179–189 (1991).

120. Michaud-Agrawal, N., Denning, E. J., Woolf, T. B. & Beckstein, O. MDAnalysis: A toolkit for the analysis of molecular dynamics simulations. *J. Comput. Chem.* **32**, 2319–2327 (2011).

121. Pronk, S. *et al.* GROMACS 4.5: a high-throughput and highly parallel open source molecular simulation toolkit. *Bioinformatics* **29**, 845–854 (2013).

122. Case, D. A. *et al.* AMBER 2015. *University of California, San Francisco* (2015).

123. Kučerka, N. *et al.* Lipid Bilayer Structure Determined by the Simultaneous Analysis of Neutron and X-Ray Scattering Data. *Biophys J* **95**, 2356–2367 (2008).

124. Kucerka, N., Tristram-Nagle, S. & Nagle, J. Structure of fully hydrated fluid phase lipid bilayers with monounsaturated chains. *The Journal of membrane biology* 193–202 (2005). doi:10.1007/s00232-005-7006-8

125. Nagle, J. F. & Tristram-Nagle, S. Structure of lipid bilayers. *Biochim Biophys Acta* **1469**, 159–195 (2000).

126. Vermeer, L. S., de Groot, B. L., Réat, V., Milon, A. & Czaplicki, J. Acyl chain order parameter profiles in phospholipid bilayers: computation from molecular dynamics simulations and comparison with 2H NMR experiments. *Eur. Biophys. J.* **36**, 919–931 (2007).

127. Jämbeck, J. P. M. & Lyubartsev, A. P. An Extension and Further Validation of an All-Atomistic Force Field for Biological Membranes. *J. Chem. Theory Comput.* **8**, 2938–2948 (2012).

128. Warschawski, D. E. & Devaux, P. F. Order parameters of unsaturated phospholipids in membranes and the effect of cholesterol: a 1H–13C solid-state NMR study at natural abundance. *Eur Biophys J* **34**, 987–996 (2005).

129. Falck, E., Róg, T., Karttunen, M. & Vattulainen, I. Lateral Diffusion in Lipid Membranes through Collective Flows. *J. Am. Chem. Soc.* **130**, 44–45 (2008).

130. Böckmann, R. A., Hac, A., Heimburg, T. & Grubmüller, H. Effect of Sodium Chloride on a Lipid Bilayer. *Biophysical Journal* **85**, 1647–1655 (2003).

131. Vácha, R. *et al.* Effects of Alkali Cations and Halide Anions on the DOPC Lipid Membrane. *J. Phys. Chem. A* **113**, 7235–7243 (2009).

132. Terdale, S. & Tantray, A. Spectroscopic study of the dimerization of rhodamine 6G in water and different organic solvents. *Journal of Molecular Liquids* **225**, 662–671 (2017).

133. Zehentbauer, F. M. *et al.* Fluorescence spectroscopy of Rhodamine 6G: Concentration and solvent effects. *Spectrochimica Acta Part A: Molecular and Biomolecular Spectroscopy* **121**, 147–151 (2014).

134. Parasassi, T., De Stasio, G., Ravagnan, G., Rusch, R. M. & Gratton, E. Quantitation of lipid phases in phospholipid vesicles by the generalized polarization of Laurdan fluorescence. *Biophysical journal* **60**, 179–189 (1991).

135. Parasassi, T., Krasnowska, E. K., Bagatolli, L. & Gratton, E. Laurdan and Prodan as Polarity-Sensitive Fluorescent Membrane Probes. *Journal of Fluorescence* **8**, 365–373 (1998).

136. Edidin, M. Lipids on the frontier: a century of cell-membrane bilayers. *Nature Reviews Molecular Cell Biology* **4**, 414–418 (2003).

137. Simons, K. & Ikonen, E. Functional rafts in cell membranes. *Nature* **387**, 569–572 (1997).

138. Klymchenko, A. S. & Kreder, R. Fluorescent Probes for Lipid Rafts: From Model Membranes to Living Cells. *Chemistry & Biology* **21**, 97–113 (2014).

139. Schlebach, J. P. *et al.* Topologically Diverse Human Membrane Proteins Partition to Liquid-Disordered Domains in Phase-Separated Lipid Vesicles. *Biochemistry* **55**, 985–988 (2016).

140. Kusumi, A., Tsunoyama, T. A., Hirosawa, K. M., Kasai, R. S. & Fujiwara, T. K. Tracking single molecules at work in living cells. *Nature Chemical Biology* **10**, 524–532 (2014).

141. Brancato, G. *et al.* Dual Fluorescence through Kasha's Rule Breaking: An Unconventional Photomechanism for Intracellular Probe Design. *J. Phys. Chem. B* **119**, 6144–6154 (2015).

142. Koenig, M. *et al.* A fluorescent molecular rotor showing vapochromism, aggregation-induced emission, and environmental sensing in living cells. *J. Mater. Chem. C* **4**, 3018–3027 (2016).

143. Macchiagodena, M. *et al.* Computational Study of DPAP Molecular Rotor in Various Environments: From Force Field Development to Molecular Dynamics Simulations and Spectroscopic Calculations. *Phys Chem Chem Phys* **19**, 30590–30602 (2017).

144. Loura, L. M. S. & Prates Ramalho, J. P. Fluorescent membrane probes' behavior in lipid bilayers: insights from molecular dynamics simulations. *Biophys Rev* **1**, 141 (2009).

145. *Molecular Probes Handbook, A Guide to Fluorescent Probes and Labeling Technologies, 11th Edition*. (Life Technologies, 2010).

146. Bacalum, M. *et al.* A Blue-Light-Emitting BODIPY Probe for Lipid Membranes. *Langmuir* **32**, 3495–3505 (2016).

147. Lindblom, G. & Orädd, G. Lipid lateral diffusion and membrane heterogeneity. *Biochimica et Biophysica Acta (BBA) - Biomembranes* **1788**, 234–244 (2009).

148. Juhasz, J., Davis, J. H. & Sharom, F. J. Fluorescent probe partitioning in giant unilamellar vesicles of 'lipid raft' mixtures. *Biochem. J.* **430**, 415–423 (2010).

149. Castro, B. M., de Almeida, R. F. M., Fedorov, A. & Prieto, M. The photophysics of a Rhodamine head labeled phospholipid in the identification and characterization of membrane lipid phases. *Chemistry and Physics of Lipids* **165**, 311–319 (2012).

150. Akhunzada, M. J. *et al.* Interplay between lipid lateral diffusion, dye concentration and membrane permeability unveiled by a combined spectroscopic and computational study of a model lipid bilayer. *Scientific Reports* **9**, 1508 (2019).

151. Böckmann, R. A., Hac, A., Heimburg, T. & Grubmüller, H. Effect of Sodium Chloride on a Lipid Bilayer. *Biophysical Journal* **85**, 1647–1655 (2003).

152. Kyrychenko, A. A molecular dynamics model of rhodamine-labeled phospholipid incorporated into a lipid bilayer. *Chemical Physics Letters* **485**, 95–99 (2010).

153. Ileri Ercan, N., Stroeve, P., Tringe, J. W. & Faller, R. Molecular Dynamics Modeling of Methylene Blue−DOPC Lipid Bilayer Interactions. *Langmuir* **34**, 4314–4323 (2018).

154. Filipe, H. A. L., Pokorná, Š., Hof, M., Amaro, M. & Loura, L. M. S. Orientation of nitro-group governs the fluorescence lifetime of nitrobenzoxadiazole (NBD)-labeled lipids in lipid bilayers. *Phys. Chem. Chem. Phys.* **21**, 1682–1688 (2019).

155. Luo, Y. & Roux, B. Simulation of osmotic pressure in concentrated aqueous salt solutions. *J. Phys. Chem. Lett.* **1**, 183–189 (2010).

156. Lewis, R. N. A. H., Sykes, B. D. & McElhaney, R. N. Thermotropic phase behavior of model membranes composed of phosphatidylcholines containing cis-monounsaturated acyl chain homologs of oleic acid: differential scanning calorimetric and phosphorus-31 NMR spectroscopic studies. (1988). doi:10.1021/bi00403a007

157. Abraham, M. J. *et al.* GROMACS: High performance molecular simulations through multi-level parallelism from laptops to supercomputers. *SoftwareX* **1–2**, 19–25 (2015).

158. Stachura, S. S., Malajczuk, C. J., Kuprusevicius, E. & Mancera, R. L. Influence of Bilayer Size and Number in Multi-Bilayer DOPC Simulations at Full and Low Hydration. *Langmuir* **35**, 2399–2411 (2019).

159. Liu, Y. & Nagle, J. F. Diffuse scattering provides material parameters and electron density profiles of biomembranes. *Phys. Rev. E* **69**, 040901 (2004).

160. Kučerka, N. *et al.* Lipid bilayer structure determined by the simultaneous analysis of neutron and X-ray scattering data. *Biophys J* **95**, 2356–2367 (2008).

161. Pan, J., Tristram-Nagle, S., Kučerka, N. & Nagle, J. F. Temperature Dependence of Structure, Bending Rigidity, and Bilayer Interactions of Dioleoylphosphatidylcholine Bilayers. *Biophysical Journal* **94**, 117–124 (2008).

162. Mashl, R. J., Scott, H. L., Subramaniam, S. & Jakobsson, E. Molecular Simulation of Dioleoylphosphatidylcholine Lipid Bilayers at Differing Levels of Hydration. *Biophysical Journal* **81**, 3005–3015 (2001).

163. Vácha, R. *et al.* Effects of Alkali Cations and Halide Anions on the DOPC Lipid Membrane. *J. Phys. Chem. A* **113**, 7235–7243 (2009).

164. Siu, S. W. I., Vácha, R., Jungwirth, P. & Böckmann, R. A. Biomolecular simulations of membranes: Physical properties from different force fields. *J. Chem. Phys.* **128**, 125103 (2008).

165. Nagle, J. F. & Tristram-Nagle, S. Structure of lipid bilayers. *Biochimica et Biophysica Acta (BBA) - Reviews on Biomembranes* **1469**, 159–195 (2000).

166. Amaro, M., Filipe, H. A. L., Ramalho, J. P. P., Hof, M. & Loura, L. M. S. Fluorescence of nitrobenzoxadiazole (NBD)-labeled lipids in model membranes is connected not to lipid mobility but to probe location. *Phys. Chem. Chem. Phys.* **18**, 7042–7054 (2016).

167. Filipe, H. A. L., Santos, L. S., Ramalho, J. P. P., Moreno, M. J. & Loura, L. M. S. Behaviour of NBD-head group labelled phosphatidylethanolamines in POPC bilayers: a molecular dynamics study. *Phys. Chem. Chem. Phys.* **17**, 20066–20079 (2015).

168. Flynn, K. R., Sutti, A., Martin, L. L., Leigh Ackland, M. & Torriero, A. A. J. Critical effects of polar fluorescent probes on the interaction of DHA with POPC supported lipid bilayers. *Biochimica et Biophysica Acta (BBA) - Biomembranes* **1860**, 1135–1142 (2018).

169. Capponi, S., Freites, J. A., Tobias, D. J. & White, S. H. Interleaflet mixing and coupling in liquid-disordered phospholipid bilayers. *Biochimica et Biophysica Acta (BBA) - Biomembranes* **1858**, 354–362 (2016).

170. Loura, L. M. S. & Ramalho, J. P. P. Recent Developments in Molecular Dynamics Simulations of Fluorescent Membrane Probes. *Molecules* **16**, 5437–5452 (2011).

171. Polat, B. E. *et al.* Experimental and Molecular Dynamics Investigation into the Amphiphilic Nature of Sulforhodamine B. *J. Phys. Chem. B* **115**, 1394–1402 (2011).

172. Kung, C. E. & Reed, J. K. Fluorescent molecular rotors: a new class of probes for tubulin structure and assembly. *Biochemistry* **28**, 6678–6686 (1989).

173. Borisov, S. M. & Wolfbeis, O. S. Optical Biosensors. *Chem. Rev.* **108**, 423–461 (2008).

174. Haidekker, M. A. & Theodorakis, E. A. Environment-sensitive behavior of fluorescent molecular rotors. *J Biol Eng* **4**, 11 (2010).

175. Kuimova, M. K. Mapping viscosity in cells using molecular rotors. *Phys Chem Chem Phys* **14**, 12671–12686 (2012).

176. Haidekker, M. A. & Theodorakis, E. A. Molecular rotors--fluorescent biosensors for viscosity and flow. *Org. Biomol. Chem.* **5**, 1669–1678 (2007).

177. Lee, S.-C. *et al.* Fluorescent Molecular Rotors for Viscosity Sensors. *Chemistry – A European Journal* **24**, 13706–13718 (2018).

178. Karpenko, I. A. *et al.* Push-pull dioxaborine as fluorescent molecular rotor: far-red fluorogenic probe for ligand-receptor interactions. *J Mater Chem C Mater* **4**, 3002–3009 (2016).

179. Mika, J. T. *et al.* Measuring the Viscosity of the Escherichia coli Plasma Membrane Using Molecular Rotors. *Biophys. J.* **111**, 1528–1540 (2016).

180. Ning, P. *et al.* A two-photon fluorescent probe for viscosity imaging in vivo. *J. Mater. Chem. B* **5**, 2743–2749 (2017).

181. Klymchenko, A. S. & Kreder, R. Fluorescent probes for lipid rafts: from model membranes to living cells. *Chem. Biol.* **21**, 97–113 (2014).

182. Jacobson, K., Mouritsen, O. G. & Anderson, R. G. W. Lipid rafts: at a crossroad between cell biology and physics. *Nat. Cell Biol.* **9**, 7–14 (2007).

183. Lingwood, D. & Simons, K. Lipid rafts as a membrane-organizing principle. *Science* **327**, 46–50 (2010).

184. Brown, D. A. & London, E. Structure and function of sphingolipid- and cholesterol-rich membrane rafts. *J. Biol. Chem.* **275**, 17221–17224 (2000).

185. Simons, K. & Toomre, D. Lipid rafts and signal transduction. *Nat. Rev. Mol. Cell Biol.* **1**, 31–39 (2000).

186. Kuimova, M. K., Yahioglu, G., Levitt, J. A. & Suhling, K. Molecular Rotor Measures Viscosity of Live Cells via Fluorescence Lifetime Imaging. *J. Am. Chem. Soc.* **130**, 6672–6673 (2008).

187. López-Duarte, I., Vu, T. T., Izquierdo, M. A., Bull, J. A. & Kuimova, M. K. A molecular rotor for measuring viscosity in plasma membranes of live cells. *Chem. Commun.* **50**, 5282–5284 (2014).

188. Stöckl, M., Plazzo, A. P., Korte, T. & Herrmann, A. Detection of Lipid Domains in Model and Cell Membranes by Fluorescence Lifetime Imaging Microscopy of Fluorescent Lipid Analogues. *J Biol Chem* **283**, 30828–30837 (2008).

189. Stöckl, M. T. & Herrmann, A. Detection of lipid domains in model and cell membranes by fluorescence lifetime imaging microscopy. *Biochimica et Biophysica Acta (BBA) - Biomembranes* **1798**, 1444–1456 (2010).

190. Nipper, M. E. *et al.* Characterization of changes in the viscosity of lipid membranes with the molecular rotor FCVJ. *Biochimica et Biophysica Acta (BBA) - Biomembranes* **1778**, 1148–1153 (2008).

191. Valeur, B. & Berberan-Santos, M. N. *Molecular fluorescence : principles and applications*. (Weinheim, Germany : Wiley-VCH Verlag GmbH & Co. KGaA, 2013).

192. Förster, Th. & Hoffmann, G. Die Viskositätsabhängigkeit der Fluoreszenzquantenausbeuten einiger Farbstoffsysteme. *Zeitschrift für Physikalische Chemie* **75**, 63–76 (2011).

193. Haidekker, M. A., Brady, T. P., Lichlyter, D. & Theodorakis, E. A. Effects of solvent polarity and solvent viscosity on the fluorescent properties of molecular rotors and related probes. *Bioorg. Chem.* **33**, 415–425 (2005).

194. Wang, K., Shi, W., Jia, J., Chen, S. & Ma, H. Characterization of 2-phenylbenzo[g]quinoxaline derivatives as viscosity-sensitive fluorescent probes. *Talanta* **77**, 1795–1799 (2009).

195. Cowan, A. E. *et al.* Lipids in the inner membrane of dormant spores of Bacillus species are largely immobile. *PNAS* **101**, 7733–7738 (2004).

196. Chandramouli, B., Silvestri, V., Scarno, M., Ottini, L. & Chillemi, G. Smyd3 open & closed lock mechanism for substrate recruitment: The hinge motion of C-terminal domain

inferred from μ-second molecular dynamics simulations. *Biochim. Biophys. Acta* **1860**, 1466–1474 (2016).

197. Chandramouli, B., Del Galdo, S., Mancini, G. & Barone, V. Mechanistic insights into metal ions transit through threefold ferritin channel. *Biochim Biophys Acta Gen Subj* **1863**, 472–480 (2019).
198. Akhunzada, M. J. *et al.* Interplay between lipid lateral diffusion, dye concentration and membrane permeability unveiled by a combined spectroscopic and computational study of a model lipid bilayer. *Scientific Reports* **9**, 1508 (2019).
199. Ramadass, R. & Bereiter-Hahn, J. Photophysical Properties of DASPMI as Revealed by Spectrally Resolved Fluorescence Decays. *J. Phys. Chem. B* **111**, 7681–7690 (2007).
200. *Advanced Fluorescence Reporters in Chemistry and Biology I: Fundamentals and Molecular Design*. (Springer-Verlag, 2010).
201. Atsbeha, T., Mohammed, A. M. & Redi-Abshiro, M. Excitation wavelength dependence of dual fluorescence of DMABN in polar solvents. *J Fluoresc* **20**, 1241–1248 (2010).
202. Minei, P. *et al.* Reversible vapochromic response of polymer films doped with a highly emissive molecular rotor. *J. Mater. Chem. C* **2**, 9224–9232 (2014).
203. Cacelli, I. & Prampolini, G. Parametrization and Validation of Intramolecular Force Fields Derived from DFT Calculations. *J. Chem. Theory Comput.* **3**, 1803–1817 (2007).
204. Marenich, A. V., Jerome, S. V., Cramer, C. J. & Truhlar, D. G. Charge Model 5: An Extension of Hirshfeld Population Analysis for the Accurate Description of Molecular Interactions in Gaseous and Condensed Phases. *J. Chem. Theory Comput.* **8**, 527–541 (2012).
205. Kaminski, G. A., Friesner, R. A., Tirado-Rives, J. & Jorgensen, W. L. Evaluation and Reparametrization of the OPLS-AA Force Field for Proteins via Comparison with

Accurate Quantum Chemical Calculations on Peptides. *J. Phys. Chem. B* **105**, 6474–6487 (2001).

206. Barone, V., Cimino, P. & Stendardo, E. Development and Validation of the B3LYP/N07D Computational Model for Structural Parameter and Magnetic Tensors of Large Free Radicals. *J. Chem. Theory Comput.* **4**, 751–764 (2008).
207. Barone, V. & Cimino, P. Validation of the B3LYP/N07D and PBE0/N07D Computational Models for the Calculation of Electronic g-Tensors. *J. Chem. Theory Comput.* **5**, 192–199 (2009).
208. Barone, V. & Cossi, M. Quantum Calculation of Molecular Energies and Energy Gradients in Solution by a Conductor Solvent Model. *J. Phys. Chem. A* **102**, 1995–2001 (1998).
209. Improta, R., Barone, V., Scalmani, G. & Frisch, M. J. A state-specific polarizable continuum model time dependent density functional theory method for excited state calculations in solution. *J. Chem. Phys.* **125**, 054103 (2006).
210. Pronk, S. *et al.* GROMACS 4.5: a high-throughput and highly parallel open source molecular simulation toolkit. *Bioinformatics* **29**, 845–854 (2013).
211. Wang, J., Wolf, R. M., Caldwell, J. W., Kollman, P. A. & Case, D. A. Development and testing of a general amber force field. *J Comput Chem* **25**, 1157–1174 (2004).
212. Mahoney, M. W. & Jorgensen, W. L. A five-site model for liquid water and the reproduction of the density anomaly by rigid, nonpolarizable potential functions. *J. Chem. Phys.* **112**, 8910–8922 (2000).
213. Vanommeslaeghe, K. *et al.* CHARMM general force field: A force field for drug-like molecules compatible with the CHARMM all-atom additive biological force fields. *J Comput Chem* **31**, 671–690 (2010).

214. Catte, A., White, G. F., Wilson, M. R. & Oganesyan, V. S. Direct Prediction of EPR Spectra from Lipid Bilayers: Understanding Structure and Dynamics in Biological Membranes. *Chemphyschem* **19**, 2183–2193 (2018).

215. Marrink, S. J., Risselada, H. J., Yefimov, S., Tieleman, D. P. & de Vries, A. H. The MARTINI Force Field: Coarse Grained Model for Biomolecular Simulations. *J. Phys. Chem. B* **111**, 7812–7824 (2007).

216. Jo, S., Lim, J. B., Klauda, J. B. & Im, W. CHARMM-GUI Membrane Builder for mixed bilayers and its application to yeast membranes. *Biophys. J.* **97**, 50–58 (2009).

217. Humphrey, W., Dalke, A. & Schulten, K. VMD: Visual molecular dynamics. *Journal of Molecular Graphics* **14**, 33–38 (1996).

218. Bussi, G., Donadio, D. & Parrinello, M. Canonical sampling through velocity rescaling. *J. Chem. Phys.* **126**, 014101 (2007).

219. Berendsen, H. J. C., Postma, J. P. M., van Gunsteren, W. F., DiNola, A. & Haak, J. R. Molecular dynamics with coupling to an external bath. *J. Chem. Phys.* **81**, 3684–3690 (1984).

220. Hess, B., Bekker, H., Berendsen, H. J. C. & Fraaije, J. G. E. M. LINCS: A linear constraint solver for molecular simulations. *Journal of Computational Chemistry* **18**, 1463–1472 (1997).

221. Darden, T., Perera, L., Li, L. & Pedersen, L. New tricks for modelers from the crystallography toolkit: the particle mesh Ewald algorithm and its use in nucleic acid simulations. *Structure* **7**, R55-60 (1999).

222. Domenicano, A. & Murray-Rust, P. Geometrical substituent parameters for benzene derivatives: inductive and resonance effects. *Tetrahedron Letters* **20**, 2283–2286 (1979).

223. Koenig, M. *et al.* Ultrasound-induced transformation of fluorescent organic nanoparticles from a molecular rotor into rhomboidal nanocrystals with enhanced emission. *Chem. Commun.* **50**, 12955–12958 (2014).

224. Digman, M. A., Caiolfa, V. R., Zamai, M. & Gratton, E. The phasor approach to fluorescence lifetime imaging analysis. *Biophys. J.* **94**, L14-16 (2008).

225. Clayton, A. H. A., Hanley, Q. S. & Verveer, P. J. Graphical representation and multicomponent analysis of single-frequency fluorescence lifetime imaging microscopy data. *J Microsc* **213**, 1–5 (2004).

226. Hirshfield, K. M., Toptygin, D., Packard, B. S. & Brand, L. Dynamic fluorescence measurements of two-state systems: applications to calcium-chelating probes. *Anal. Biochem.* **209**, 209–218 (1993).

227. Campanelli, A. R., Domenicano, A., Macchiagodena, M. & Ramondo, F. Electronegativity and resonance parameters from the geometry of monosubstituted benzene rings. *Struct Chem* **22**, 1131 (2011).

228. *Lange's handbook of chemistry*. (McGraw-Hill, 1999).

229. Bechara, C. & Sagan, S. Cell-penetrating peptides: 20 years later, where do we stand? *FEBS Letters* **587**, 1693–1702 (2013).

230. Brock, R. The Uptake of Arginine-Rich Cell-Penetrating Peptides: Putting the Puzzle Together. *Bioconjugate Chem.* **25**, 863–868 (2014).

231. Jones, A. T. & Sayers, E. J. Cell entry of cell penetrating peptides: tales of tails wagging dogs. *Journal of Controlled Release* **161**, 582–591 (2012).

232. Takeuchi, T. & Futaki, S. Current Understanding of Direct Translocation of Arginine-Rich Cell-Penetrating Peptides and Its Internalization Mechanisms. *Chemical and Pharmaceutical Bulletin* **64**, 1431–1437 (2016).

233. Duchardt, F., Fotin-Mleczek, M., Schwarz, H., Fischer, R. & Brock, R. A Comprehensive Model for the Cellular Uptake of Cationic Cell-penetrating Peptides. *Traffic* **8**, 848–866 (2007).

234. Cleal, K., He, L., D. Watson, P. & T. Jones, A. Endocytosis, Intracellular Traffic and Fate of Cell Penetrating Peptide Based Conjugates and Nanoparticles. (2013). Available at: https://www.ingentaconnect.com/contentone/ben/cpd/2013/00000019/00000016/art00005. (Accessed: 10th June 2019)

235. El-Andaloussi, S., Johansson, H. J., Lundberg, P. & Langel, Ü. Induction of splice correction by cell-penetrating peptide nucleic acids. *J. Gene Med.* **8**, 1262–1273 (2006).

236. Fittipaldi, A. *et al.* Cell Membrane Lipid Rafts Mediate Caveolar Endocytosis of HIV-1 Tat Fusion Proteins. *J. Biol. Chem.* **278**, 34141–34149 (2003).

237. Kaplan, I. M., Wadia, J. S. & Dowdy, S. F. Cationic TAT peptide transduction domain enters cells by macropinocytosis. *Journal of Controlled Release* **102**, 247–253 (2005).

238. Nakase, I. *et al.* Cellular Uptake of Arginine-Rich Peptides: Roles for Macropinocytosis and Actin Rearrangement. *Molecular Therapy* **10**, 1011–1022 (2004).

239. Richard, J. P. *et al.* Cellular Uptake of Unconjugated TAT Peptide Involves Clathrin-dependent Endocytosis and Heparan Sulfate Receptors. *J. Biol. Chem.* **280**, 15300–15306 (2005).

240. Säälik, P. *et al.* Protein Cargo Delivery Properties of Cell-Penetrating Peptides. A Comparative Study. *Bioconjugate Chem.* **15**, 1246–1253 (2004).

241. Verdurmen, W. P. R., Thanos, M., Ruttekolk, I. R., Gulbins, E. & Brock, R. Cationic cell-penetrating peptides induce ceramide formation via acid sphingomyelinase: Implications for uptake. *Journal of Controlled Release* **147**, 171–179 (2010).

242. Goñi, F. M. & Alonso, A. Sphingomyelinases: enzymology and membrane activity. *FEBS Letters* **531**, 38–46 (2002).

243. Lamazière, A. *et al.* Non-Metabolic Membrane Tubulation and Permeability Induced by Bioactive Peptides. *PLOS ONE* **2**, e201 (2007).

244. Persson, D. *et al.* Vesicle size-dependent translocation of penetratin analogs across lipid membranes. *Biochimica et Biophysica Acta (BBA) - Biomembranes* **1665**, 142–155 (2004).

245. Swiecicki, J.-M. *et al.* The Efficacies of Cell-Penetrating Peptides in Accumulating in Large Unilamellar Vesicles Depend on their Ability To Form Inverted Micelles. *ChemBioChem* **15**, 884–891 (2014).

246. Di Pisa, M., Chassaing, G. & Swiecicki, J.-M. Translocation Mechanism(s) of Cell-Penetrating Peptides: Biophysical Studies Using Artificial Membrane Bilayers. *Biochemistry* **54**, 194–207 (2015).

247. Macchi, S. *et al.* Self-aggregation propensity of the Tat peptide revealed by UV-Vis, NMR and MD analyses. *Phys. Chem. Chem. Phys.* **19**, 23910–23914 (2017).

248. Chugh, A. & Eudes, F. Translocation and nuclear accumulation of monomer and dimer of HIV-1 Tat basic domain in triticale mesophyll protoplasts. *Biochimica et Biophysica Acta (BBA) - Biomembranes* **1768**, 419–426 (2007).

249. Erazo-Oliveras, A. *et al.* Protein delivery into live cells by incubation with an endosomolytic agent. *Nat Meth* **11**, 861–867 (2014).

250. Pepper, J. T., Maheshwari, P. & Eudes, F. Adsorption of cell-penetrating peptide Tat2 and polycation luviquat FC-370 to triticale microspore exine. *Colloids and Surfaces B: Biointerfaces* **157**, 207–214 (2017).

251. Rudolph, C. *et al.* Application of Novel Solid Lipid Nanoparticle (SLN)-Gene Vector Formulations Based on a Dimeric HIV-1 TAT-Peptide in Vitro and in Vivo. *Pharm Res* **21**, 1662–1669 (2004).

252. Monreal, I. A. *et al.* Branched dimerization of Tat peptide improves permeability to HeLa and hippocampal neuronal cells. *Chem. Commun.* **51**, 5463–5466 (2015).

253. Jain, A., Shah, S. G. & Chugh, A. Cell penetrating peptides as efficient nanocarriers for delivery of antifungal compound, natamycin for the treatment of fungal keratitis. *Pharm Res* **32**, 1920–1930 (2015).

254. Moss, J. A. *et al.* A Dimerization "Switch" in the Internalization Mechanism of a Cell-Penetrating Peptide. *J. Am. Chem. Soc.* **127**, 538–539 (2005).

255. Hoyer, J., Schatzschneider, U., Schulz-Siegmund, M. & Neundorf, I. Dimerization of a cell-penetrating peptide leads to enhanced cellular uptake and drug delivery. *Beilstein J Org Chem* **8**, 1788–1797 (2012).

256. Macchi, S. *et al.* Spontaneous membrane-translocating peptides: influence of peptide self-aggregation and cargo polarity. *Scientific Reports* **5**, 16914 (2015).

257. Brancato, G. *et al.* Dual Fluorescence through Kasha's Rule Breaking: An Unconventional Photomechanism for Intracellular Probe Design. *J. Phys. Chem. B* **119**, 6144–6154 (2015).

258. Koenig, M. *et al.* Unraveling the peculiar modus operandi of a new class of solvatochromic fluorescent molecular rotors by spectroscopic and quantum mechanical methods. *Chemical Science* **4**, 2502 (2013).

259. Koenig, M. *et al.* A fluorescent molecular rotor showing vapochromism, aggregation-induced emission, and environmental sensing in living cells. *J. Mater. Chem. C* **4**, 3018–3027 (2016).

260. Koenig, M. *et al.* Ultrasound-induced transformation of fluorescent organic nanoparticles from a molecular rotor into rhomboidal nanocrystals with enhanced emission. *Chem. Commun.* **50**, 12955–12958 (2014).

261. Minei, P. *et al.* Reversible vapochromic response of polymer films doped with a highly emissive molecular rotor. *J. Mater. Chem. C* **2**, 9224–9232 (2014).

262. Di Carlo, M. G. *et al.* Thioflavin T templates amyloid β(1–40) conformation and aggregation pathway. *Biophysical Chemistry* **206**, 1–11 (2015).

263. Humphrey, W., Dalke, A. & Schulten, K. VMD: visual molecular dynamics. *J Mol Graph* **14**, 33–38, 27–28 (1996).

264. Martyna, G. J., Tobias, D. J. & Klein, M. L. Constant pressure molecular dynamics algorithms. *The Journal of Chemical Physics* **101**, 4177–4189 (1994).

265. Kneller, G. R., Baczynski, K. & Pasenkiewicz-Gierula, M. Communication: Consistent picture of lateral subdiffusion in lipid bilayers: Molecular dynamics simulation and exact results. *The Journal of Chemical Physics* **135**, 141105 (2011).

266. Kučerka, N., Tristram-Nagle, S. & Nagle, J. F. Structure of Fully Hydrated Fluid Phase Lipid Bilayers with Monounsaturated Chains. *J Membrane Biol* **208**, 193–202 (2006).

267. Herce, H. D. *et al.* Arginine-Rich Peptides Destabilize the Plasma Membrane, Consistent with a Pore Formation Translocation Mechanism of Cell-Penetrating Peptides. *Biophysical Journal* **97**, 1917–1925 (2009).

268. Yesylevskyy, S., Marrink, S.-J. & Mark, A. E. Alternative Mechanisms for the Interaction of the Cell-Penetrating Peptides Penetratin and the TAT Peptide with Lipid Bilayers. *Biophysical Journal* **97**, 40–49 (2009).

269. Chandramouli, B., Di Maio, D., Mancini, G. & Brancato, G. Introducing an artificial photo-switch into a biological pore: A model study of an engineered α-hemolysin. *Biochimica et Biophysica Acta (BBA) - Biomembranes* **1858**, 689–697 (2016).

270. Akabori, K. *et al.* HIV-1 Tat membrane interactions probed using X-ray and neutron scattering, CD spectroscopy and MD simulations. *Biochimica et Biophysica Acta (BBA) - Biomembranes* **1838**, 3078–3087 (2014).

271. Sun, D., Forsman, J. & Woodward, C. E. Atomistic Molecular Simulations Suggest a Kinetic Model for Membrane Translocation by Arginine-Rich Peptides. *J. Phys. Chem. B* **119**, 14413–14420 (2015).

272. Sun, D., Forsman, J., Lund, M. & Woodward, C. E. Effect of arginine-rich cell penetrating peptides on membrane pore formation and life-times: a molecular simulation study. *Phys. Chem. Chem. Phys.* **16**, 20785–20795 (2014).

273. Salomone, F. *et al.* High-yield nontoxic gene transfer through conjugation of the CM_{18}-Tat_{11} chimeric peptide with nanosecond electric pulses. *Mol Pharm* **11**, 2466–2474 (2014).

274. Fasoli, A. *et al.* Mechanistic Insight into CM18-Tat11 Peptide Membrane-Perturbing Action by Whole-Cell Patch-Clamp Recording. *Molecules* **19**, 9228–9239 (2014).

275. Salomone, F. *et al.* A novel chimeric cell-penetrating peptide with membrane-disruptive properties for efficient endosomal escape. *J Control Release* **163**, 293–303 (2012).

276. Salomone, F., Cardarelli, F., Signore, G., Boccardi, C. & Beltram, F. In Vitro Efficient Transfection by CM18-Tat11 Hybrid Peptide: A New Tool for Gene-Delivery Applications. *PLOS ONE* **8**, e70108 (2013).

277. Mishra, A., Gordon, V. D., Yang, L., Coridan, R. & Wong, G. C. L. HIV TAT Forms Pores in Membranes by Inducing Saddle-Splay Curvature: Potential Role of Bidentate Hydrogen Bonding. *Angewandte Chemie International Edition* **47**, 2986–2989 (2008).

278. Futaki, S. *et al.* Arginine-rich Peptides AN ABUNDANT SOURCE OF MEMBRANE-PERMEABLE PEPTIDES HAVING POTENTIAL AS CARRIERS FOR INTRACELLULAR PROTEIN DELIVERY. *J. Biol. Chem.* **276**, 5836–5840 (2001).

279. Schmidt, N., Mishra, A., Lai, G. H. & Wong, G. C. L. Arginine-rich cell-penetrating peptides. *FEBS Letters* **584**, 1806–1813 (2010).

280. MacKinnon, R. Potassium Channels and the Atomic Basis of Selective Ion Conduction (Nobel Lecture). *Angewandte Chemie International Edition* **43**, 4265–4277 (2004).

281. Grandi, E. *et al.* Potassium channels in the heart: structure, function and regulation. *The Journal of Physiology* **595**, 2209–2228 (2017).

282. Bezanilla, F. How membrane proteins sense voltage. *Nature Reviews Molecular Cell Biology* **9**, 323 (2008).

283. Lee, Y.-C. *et al.* Mutations in KCND3 Cause Spinocerebellar Ataxia Type 22. *Ann. Neurol.* **72**, 859–869 (2012).

284. Smets, K. *et al.* First de novo KCND3 mutation causes severe Kv4.3 channel dysfunction leading to early onset cerebellar ataxia, intellectual disability, oral apraxia and epilepsy. *BMC Medical Genetics* **16**, 1–7 (2015).

285. Duarri, A. *et al.* Mutations in Potassium Channel KCND3 Cause Spinocerebellar Ataxia Type 19. *Ann. Neurol.* **72**, 870–880 (2012).

286. Duarri, A. *et al.* Spinocerebellar ataxia type 19/22 mutations alter heterocomplex Kv4.3 channel function and gating in a dominant manner. *Cellular and Molecular Life Sciences* **72**, 3387–3399 (2015).

287. Long, S. B., Tao, X., Campbell, E. B. & MacKinnon, R. Atomic structure of a voltage-dependent K+ channel in a lipid membrane-like environment. *Nature* **450**, 376–382 (2007).

288. Banerjee, A., Lee, A., Campbell, E. & MacKinnon, R. Structure of a pore-blocking toxin in complex with a eukaryotic voltage-dependent K+ channel. *eLife Sciences* **2**, e00594 (2013).

289. Tao, X., Lee, A., Limapichat, W., Dougherty, D. A. & MacKinnon, R. A Gating Charge Transfer Center in Voltage Sensors. *Science* **328**, 67–73 (2010).

290. Chen, X., Wang, Q., Ni, F. & Ma, J. Structure of the full-length Shaker potassium channel Kv1.2 by normal-mode-based X-ray crystallographic refinement. *PNAS* **107**, 11352–11357 (2010).

291. Pioletti, M., Findeisen, F., Hura, G. L. & Daniel L Minor, J. Three-dimensional structure of the KChIP1–Kv4.3 T1 complex reveals a cross-shaped octamer. *Nature Structural and Molecular Biology* **13**, 987–995 (2006).

292. Wang, H. *et al.* Structural basis for modulation of Kv4 K^+ channels by auxiliary KChIP subunits. *Nature Neuroscience* **10**, 32–39 (2007).

293. Catte, A., Tiecher, C., Bhattacharjee, N., Brancato, G. & Kocer, A. The effect of two disease-causing mutations on the function and structure of the voltage-gated potassium channel Kv4.3. *Submitted* (2019).

294. Biasini, M. *et al.* SWISS-MODEL: modelling protein tertiary and quaternary structure using evolutionary information. *Nucleic Acids Res.* **42**, W252-258 (2014).

295. Bienert, S. *et al.* The SWISS-MODEL Repository—new features and functionality. *Nucleic Acids Res* **45**, D313–D319 (2017).

296. Guex, N., Peitsch, M. C. & Schwede, T. Automated comparative protein structure modeling with SWISS-MODEL and Swiss-PdbViewer: a historical perspective. *Electrophoresis* **30 Suppl 1**, S162-173 (2009).

297. Benkert, P., Biasini, M. & Schwede, T. Toward the estimation of the absolute quality of individual protein structure models. *Bioinformatics* **27**, 343–350 (2011).

298. Bertoni, M., Kiefer, F., Biasini, M., Bordoli, L. & Schwede, T. Modeling protein quaternary structure of homo- and hetero-oligomers beyond binary interactions by homology. *Sci Rep* **7**, (2017).

299. Ebejer, J.-P., Hill, J. R., Kelm, S., Shi, J. & Deane, C. M. Memoir: template-based structure prediction for membrane proteins. *Nucleic Acids Res.* **41**, W379-383 (2013).

300. Hill, J. R. & Deane, C. M. MP-T: improving membrane protein alignment for structure prediction. *Bioinformatics* **29**, 54–61 (2013).

301. Kelm, S., Shi, J. & Deane, C. M. MEDELLER: homology-based coordinate generation for membrane proteins. *Bioinformatics* **26**, 2833–2840 (2010).

302. Jo, S., Kim, T., Iyer, V. G. & Im, W. CHARMM-GUI: A web-based graphical user interface for CHARMM. *J. Comput. Chem.* **29**, 1859–1865 (2008).

303. Wu, E. L. *et al.* CHARMM-GUI Membrane Builder toward realistic biological membrane simulations. *J. Comput. Chem.* **35**, 1997–2004 (2014).

304. Jo, S., Kim, T. & Im, W. Automated Builder and Database of Protein/Membrane Complexes for Molecular Dynamics Simulations. *PLOS ONE* **2**, e880 (2007).

305. Phillips, J. C. *et al.* Scalable Molecular Dynamics with NAMD. *J Comput Chem* **26**, 1781–1802 (2005).

306. Best, R. B. *et al.* Optimization of the Additive CHARMM All-Atom Protein Force Field Targeting Improved Sampling of the Backbone ϕ, ψ and Side-Chain χ1 and χ2 Dihedral Angles. *J. Chem. Theory Comput.* **8**, 3257–3273 (2012).

307. Jorgensen, W. L., Chandrasekhar, J., Madura, J. D., Impey, R. W. & Klein, M. L. Comparison of simple potential functions for simulating liquid water. *The Journal of Chemical Physics* **79**, 926–935 (1983).

308. Essmann, U. *et al.* A smooth particle mesh Ewald method. *The Journal of Chemical Physics* **103**, 8577–8593 (1995).

309. Darden, T., York, D. & Pedersen, L. Particle mesh Ewald: An N·log(N) method for Ewald sums in large systems. *The Journal of Chemical Physics* **98**, 10089–10092 (1993).

310. Grubmüller, H., Heller, H., Windemuth, A. & Schulten, K. Generalized Verlet Algorithm for Efficient Molecular Dynamics Simulations with Long-range Interactions. *Molecular Simulation* **6**, 121–142 (1991).

311. Ryckaert, J.-P., Ciccotti, G. & Berendsen, H. J. C. Numerical integration of the cartesian equations of motion of a system with constraints: molecular dynamics of n-alkanes. *Journal of Computational Physics* **23**, 327–341 (1977).

312. Starek, G., Freites, J. A., Berneche, S. & Tobias, D. J. Gating energetics of a voltage-dependent K+ channel pore domain. *J. Comput. Chem.* **38**, 1472–1478 (2017).

313. Feller, S. E., Zhang, Y., Pastor, R. W. & Brooks, B. R. Constant pressure molecular dynamics simulation: The Langevin piston method. *The Journal of Chemical Physics* **103**, 4613–4621 (1995).

314. Martyna, G. J., Tobias, D. J. & Klein, M. L. Constant pressure molecular dynamics algorithms. *The Journal of Chemical Physics* **101**, 4177–4189 (1994).

315. Chandramouli, B., Maio, D. D., Mancini, G., Barone, V. & Brancato, G. Breaking the Hydrophobicity of the MscL Pore: Insights into a Charge-Induced Gating Mechanism. *PLOS ONE* **10**, e0120196 (2015).

316. Chenna, R. *et al.* Multiple sequence alignment with the Clustal series of programs. *Nucleic Acids Res* **31**, 3497–3500 (2003).

317. Larkin, M. A. *et al.* Clustal W and Clustal X version 2.0. *Bioinformatics* **23**, 2947–2948 (2007).

318. Higgins, D. G., Thompson, J. D. & Gibson, T. J. Using CLUSTAL for multiple sequence alignments. in *Methods in Enzymology* **266**, 383–402 (Academic Press, 1996).

319. Jeanmougin, F., Thompson, J. D., Gouy, M., Higgins, D. G. & Gibson, T. J. Multiple sequence alignment with Clustal X. *Trends in Biochemical Sciences* **23**, 403–405 (1998).

320. Thompson, J. D., Gibson, T. J., Plewniak, F., Jeanmougin, F. & Higgins, D. G. The CLUSTAL_X Windows Interface: Flexible Strategies for Multiple Sequence Alignment Aided by Quality Analysis Tools. *Nucleic Acids Res* **25**, 4876–4882 (1997).

321. Capener, C. E., Proks, P., Ashcroft, F. M. & Sansom, M. S. P. Filter Flexibility in a Mammalian K Channel: Models and Simulations of Kir6.2 Mutants. *Biophys J* **84**, 2345–2356 (2003).

322. Wimley, W. C. & White, S. H. Experimentally determined hydrophobicity scale for proteins at membrane interfaces. *Nat. Struct. Biol.* **3**, 842–848 (1996).

323. Börjesson, S. I. & Elinder, F. Structure, Function, and Modification of the Voltage Sensor in Voltage-Gated Ion Channels. *Cell Biochem Biophys* **52**, 149 (2008).

324. Tombola, F., Pathak, M. M. & Isacoff, E. Y. How Does Voltage Open an Ion Channel? *Annual Review of Cell and Developmental Biology* **22**, 23–52 (2006).

325. Jerng, H. H., Pfaffinger, P. J. & Covarrubias, M. Molecular physiology and modulation of somatodendritic A-type potassium channels. *Molecular and Cellular Neuroscience* **27**, 343–369 (2004).

326. Patel, S. P. & Campbell, D. L. Transient outward potassium current, 'Ito', phenotypes in the mammalian left ventricle: underlying molecular, cellular and biophysical mechanisms. *The Journal of Physiology* **569**, 7–39 (2005).

327. Olesen, M. S. *et al.* A novel KCND3 gain-of-function mutation associated with early-onset of persistent lone atrial fibrillation. *Cardiovasc. Res.* **98**, 488–495 (2013).

328. Giudicessi, J. R. *et al.* Novel mutations in the KCND3-encoded Kv4.3 K+ channel associated with autopsy-negative sudden unexplained death. *Hum. Mutat.* **33**, 989–997 (2012).

329. Rhodes, K. J. *et al.* KChIPs and Kv4 α Subunits as Integral Components of A-Type Potassium Channels in Mammalian Brain. *J. Neurosci.* **24**, 7903–7915 (2004).

330. An, W. F. *et al.* Modulation of A-type potassium channels by a family of calcium sensors. *Nature* **403**, 553–556 (2000).

331. Holmqvist, M. H. *et al.* Elimination of fast inactivation in Kv4 A-type potassium channels by an auxiliary subunit domain. *PNAS* **99**, 1035–1040 (2002).

332. Patel, S. P., Parai, R., Parai, R. & Campbell, D. L. Regulation of Kv4.3 voltage-dependent gating kinetics by KChIP2 isoforms. *J Physiol* **557**, 19–41 (2004).

333. Kuo, H.-C. *et al.* A Defect in the Kv Channel-Interacting Protein 2 (KChIP2) Gene Leads to a Complete Loss of Ito and Confers Susceptibility to Ventricular Tachycardia. *Cell* **107**, 801–813 (2001).

334. Cui, Y. Y., Liang, P. & Wang, K. W. Enhanced Trafficking of Tetrameric Kv4.3 Channels by KChIP1 Clamping. *Neurochem Res* **33**, 2078–2084 (2008).

335. Kunjilwar, K., Strang, C., DeRubeis, D. & Pfaffinger, P. J. KChIP3 Rescues the Functional Expression of Shal Channel Tetramerization Mutants. *J. Biol. Chem.* **279**, 54542–54551 (2004).

336. Biasini, M. *et al.* SWISS-MODEL: modelling protein tertiary and quaternary structure using evolutionary information. *Nucleic Acids Research* **42**, W252–W258 (2014).

337. Bienert, S. *et al.* The SWISS-MODEL Repository—new features and functionality. *Nucleic Acids Research* **45**, D313–D319 (2017).

338. Guex, N., Peitsch, M. C. & Schwede, T. Automated comparative protein structure modeling with SWISS-MODEL and Swiss-PdbViewer: A historical perspective. *ELECTROPHORESIS* **30**, S162–S173 (2009).

339. Benkert, P., Biasini, M. & Schwede, T. Toward the estimation of the absolute quality of individual protein structure models. *Bioinformatics* **27**, 343–350 (2011).

340. Bertoni, M., Kiefer, F., Biasini, M., Bordoli, L. & Schwede, T. Modeling protein quaternary structure of homo- and hetero-oligomers beyond binary interactions by homology. *Scientific Reports* **7**, (2017).

341. Phillips, J. C. *et al.* Scalable molecular dynamics with NAMD. *J. Comput. Chem.* **26**, 1781–1802 (2005).

342. Klauda, J. B. *et al.* Update of the CHARMM All-Atom Additive Force Field for Lipids: Validation on Six Lipid Types. *J. Phys. Chem. B* **114**, 7830–7843 (2010).

343. Darden, T., York, D. & Pedersen, L. Particle mesh Ewald: An N·log(N) method for Ewald sums in large systems. *The Journal of Chemical Physics* **98**, 10089–10092 (1993).

344. Ryckaert, J., Ciccotti, G. & Berendsen, H. Numerical-Integration of Cartesian Equations of Motion of a System with Constraints - Molecular-Dynamics of N-Alkanes. *J. Comput. Phys.* **23**, 327–341 (1977).

345. Feller, S. E., Zhang, Y., Pastor, R. W. & Brooks, B. R. Constant pressure molecular dynamics simulation: The Langevin piston method. *The Journal of Chemical Physics* **103**, 4613–4621 (1995).

346. Martyna, G. J., Tobias, D. J. & Klein, M. L. Constant pressure molecular dynamics algorithms. *The Journal of Chemical Physics* **101**, 4177–4189 (1994).

347. Humphrey, W., Dalke, A. & Schulten, K. VMD: Visual molecular dynamics. *Journal of molecular graphics & modelling, Journal of molecular graphics & modelling.* **14**, 33–38 (1996).

348. Dolinsky, T. J., Nielsen, J. E., McCammon, J. A. & Baker, N. A. PDB2PQR: an automated pipeline for the setup of Poisson–Boltzmann electrostatics calculations. *Nucleic Acids Res* **32**, W665–W667 (2004).

349. Dolinsky, T. J. *et al.* PDB2PQR: expanding and upgrading automated preparation of biomolecular structures for molecular simulations. *Nucleic Acids Res* **35**, W522–W525 (2007).

350. Jurrus, E. *et al.* Improvements to the APBS biomolecular solvation software suite. *Protein Science* **27**, 112–128 (2018).

351. Baker, N. A., Sept, D., Joseph, S., Holst, M. J. & McCammon, J. A. Electrostatics of nanosystems: Application to microtubules and the ribosome. *PNAS* **98**, 10037–10041 (2001).

352. Sanner, M. F., Olson, A. J. & Spehner, J.-C. Reduced surface: An efficient way to compute molecular surfaces. *Biopolymers* **38**, 305–320 (1996).

353. Pettersen, E. F. *et al.* UCSF Chimera--a visualization system for exploratory research and analysis. *J Comput Chem* **25**, 1605–1612 (2004).

354. Gebauer, M. *et al.* N-type Inactivation Features of Kv4.2 Channel Gating. *Biophysical Journal* **86**, 210–223 (2004).

355. Bähring, R. *et al.* Conserved Kv4 N-terminal Domain Critical for Effects of Kv Channel-interacting Protein 2.2 on Channel Expression and Gating. *Journal of Biological Chemistry* **276**, 23888–23894 (2001).

356. Beck, E. J., Bowlby, M., An, W. F., Rhodes, K. J. & Covarrubias, M. Remodelling inactivation gating of Kv4 channels by KChIP1, a small-molecular-weight calcium-binding protein. *The Journal of Physiology* **538**, 691–706 (2002).